University of California
Santa Barbara

Forward and Inverse Modeling Frameworks for Nondestructive Evaluation of Materials with Resonant Ultrasound Spectroscopy

A dissertation submitted in partial satisfaction
of the requirements for the degree

Doctor of Philosophy
in
Materials

by

Brent Richard Goodlet

Committee in charge:

Professor Tresa M. Pollock, Chair
Professor Carlos G. Levi
Professor Matthew R. Begley
Professor Kimberly L. Foster

June 2018

The dissertation of Brent Richard Goodlet is approved.

Professor Carlos G. Levi

Professor Matthew R. Begley

Professor Kimberly L. Foster

Professor Tresa M. Pollock, Committee Chair

May 2018

Forward and Inverse Modeling Frameworks for Nondestructive Evaluation of Materials with Resonant Ultrasound Spectroscopy

by

Brent Richard Goodlet

Dedicated to:

All who helped me get this far,

you know exactly who you are.

Curriculum Vitæ

Brent Richard Goodlet

Education

2018 Ph.D. in Materials, University of California, Santa Barbara.

2012 B.S. in Metallurgical & Materials Engineering, Colorado School of Mines

Publications

5. **B.R. Goodlet**, L. Mills, B. Bales, M.A. Charpagne, S.P. Murray, W.C. Lenthe, L. Petzold and T.M. Pollock. "Elastic Properties of Novel Co and CoNi-Based Superalloys Determined through Bayesian Inference and Resonant Ultrasound Spectroscopy," *Metallurgical and Materials Transactions A* 49 (2018) pp. 2324-2339. [DOI]

4. B. Bales, **B.R. Goodlet**, W.C. Lenthe, L. Petzold and T.M. Pollock. "Bayesian Inference of Elastic Properties with Resonant Ultrasound Spectroscopy," *Journal of the Acoustical Society of America* 143 (2018) pp. 71-83. [DOI]

3. **B.R. Goodlet**, C.J. Torbet, E.J. Biedermann, L.M. Jauriqui, J.C. Aldrin, and T.M. Pollock. "Forward Models for Extending the Mechanical Damage Evaluation Capability of Resonant Ultrasound Spectroscopy," *Ultrasonics* 77 (2017) pp. 183-196. [DOI]

2. L.H. Rettberg, **B.R. Goodlet**, and T.M. Pollock. "Detecting Recrystallization in a Single Crystal Ni-base Alloy using Resonant Ultrasound Spectroscopy," *NDT&E International* 83 (2016) pp. 68-77. [DOI]

1. **B.R. Goodlet**, L.H. Rettberg, and T.M. Pollock. "Resonant Ultrasound Spectroscopy for Defect Detection in Single Crystal Superalloy Castings," *Superalloys 2016* pp. 303-312. [DOI]

Abstract

Forward and Inverse Modeling Frameworks for Nondestructive Evaluation of Materials with Resonant Ultrasound Spectroscopy

by: Brent Richard Goodlet

The objective of this dissertation is the development of both forward and inverse modeling frameworks that extend the nondestructive evaluation (NDE) capability of resonant ultrasound spectroscopy (RUS) for materials science applications through utilization of modern computational resources and a rigorous application of the fundamental physics of mechanical resonance. First, a forward modeling framework (FMF) based on 3D linear-elastic finite element models is developed to explain the complex manner in which resonance frequencies of a specimen change as damage is accumulated. Numerous examples of damage common to Ni-based superalloys for structural applications in extreme thermo-mechanical environments, like those found in turbine engines, are specifically addressed including: creep, fatigue and recrystallization. Then, an inverse modeling framework (IMF) devised with the goal of quantitative NDE of materials based on RUS measured resonance frequencies is introduced. Built upon a full-Bayesian approach to the inverse problem, the novel IMF devised here affords substantially simplified experimental methods by estimating elastic constants and crystal orientation parameters simultaneously. The potential of the IMF is demonstrated by evaluating a series of novel Co and CoNi-based single crystal superalloys, with robust convergence behavior as compared to optimizer-based approaches described in the literature. Together, the finite element-based FMF and the Bayesian IMF demonstrate the immense value and insight gained by coupling experiments with physics-based models for state-of-the-art materials characterization and NDE.

Contents

List of Figures

List of Tables

Chapter 1

Nondestructive Materials Characterization

1.1 Early Ultrasonic Methods

Ultrasonic techniques have numerous engineering applications across materials science and condensed matter physics that are founded on the simple relationship between the velocity of elastic wave propagation and the material properties of the propagation medium. In 1942, Floyd A Firestone of the University of Michigan patented what he called the "supersonic reflectoscope", and in conjunction with his publication in 1946 [1], demonstrated the ability to detect sub-surface flaws in welds using ultrasound. Rapid emergence and diversification of ultrasonic techniques followed soon after, with considerable pioneering research conducted at Bell Telephone Laboratories starting in the late 1940s by WP Mason, HJ McSkimin, et al. [2–7]. In this early work, piezoelectric crystals were bonded to specimens and excited with short duration electrical pulses in order to propagate shear or longitudinal elastic waves through a material. Commonly referred to as "pulse methods", these investigations probed elastic properties and attenuation losses of single and polycrystalline metals, ceramics, glass, and polymers, and laid the groundwork for modern day pulse-transmission and pulse-echo ultrasonic methods that are still employed today.

1.1.1 Origin of Resonance-based Ultrasonic Methods

Early resonance-based ultrasonic methods were also developed at Bell Laboratories by Fraser and LeCraw, who in 1964 published on a novel method for evaluating elastic properties using the resonance frequencies of spherical samples [8]. However, their methods were limited by the fact that only special cases of the forward problem—for the calculation of resonance frequencies of a 3D elastic body—could be solved as of 1964. Despite the governing physics of waves being known since the middle of the 18th century when mathematician Jean le Rond d'Alembert first described the one-dimensional wave equation of motion after studying the vibration of strings, and Leonhard Euler's extension

of the wave equation to 3 dimensions by 1766 [9], general solution methods for the 3D forward problem remained elusive through all of the 19th and most of the 20th century. Using an analytical solution to the forward problem for homogeneous isotropic spheres derived by Sato and Usame two years earlier [10], Fraser and LeCraw demonstrated in 1964 the viability of determining elastic properties from simple resonance frequency measurements, and named their method the Resonant Sphere Technique (RST) [8, 11]. Of course, fabricating spherical samples is far from a trivial task, but until forward calculation methods amenable to specimen geometries of lower symmetry, the RST was the only viable resonance-based method of determining elastic properties.

By the late 1960s considerable advances were made towards developing a generalized solution of the forward problem, first by Holland in 1967 [12] and then Demarest in 1969 [13]. Both Holland and Demarest utilized a variational approach and formulated the forward problem as a general eigenvalue problem which was then solved using Rayleigh-Ritz numerical methods [12, 13]. This formulation unlocked a forward calculation procedure for rectangular parallelepiped geometry samples with isotropic and cubic elastic symmetry, with the latter being possible so long as the crystal reference frame was aligned with the specimen reference frame. These advances gave rise to what would be known as the Rectangular Parallelepiped Resonance (RPR) method [11], which along with the RST, were commonly employed to characterize elastic properties through the 1980's and into the 1990's [11, 14].

Further developing the variational approach of Holland and Demarest, Ichiro Ohno in 1976 expanded the forward calculation methods of the RPR technique from cubic (3 elastic degrees of freedom) to orthorhombic (9 elastic DOF) crystal symmetry, devised a classification scheme for parallelepiped resonance modes using group theory, leveraged matrix splitting to reduce evaluation time, and detailed an optimization inversion procedure for determining elastic constants from resonance frequencies [15]. With resonance mode identification being "the most important and difficult step" of the inversion proce-

dure according to Ohno, accurate initial guess values of elastic constants were essential to a successful inversion of elastic properties [15]. In 1986, Ohno et al. expanded the RPR technique again to now accept trigonal (6 elastic DOF) symmetry crystals [16]. However, Ohno's methods still required that the crystal reference frame be aligned with the specimen reference frame, which substantially complicated specimen preparation procedures and added potential sources of experimental error. Of course this also required the use of additional measurement modalities, typically x-ray diffraction [15], capable of identifying the orientation of the crystal reference frame such that one could cut the rectangular parallelepiped specimen from the parent single crystal with the faces aligned with the crystal axes.

1.1.2 The Origin of RUS

In the early 1990's, motivated by efforts to measure the elastic properties of small (approximately 1 mm^3) superconducting ceramic samples at low temperatures, Albert Migliori and a team of researchers at LANL modernized many experimental aspects of the RPR method of Ohno, Anderson, and others in the geophysics community [11,17,18]. Perhaps the most important advance came in 1991 when Visscher et al. extended the forward calculation methods to allow for most simple geometry specimens and fully anisotropic elastic bodies through insightful changes of the basis functions used by the Rayleigh-Ritz method to describe the specimen. Visscher's method, also known as the xyz-algorithm, is named after the polynomial basis functions that expand the displacements of the specimen as a product of powers of the Cartesian coordinates with the form: $x^l\ y^m\ z^n$ [19]. While incurring a slight computational penalty as compared to an orthonormal set of basis functions as used previously by Ohno and Demarest [13,19], Visscher's method allowed for a single set of basis functions to be applied towards a range of simple specimen geometries given straightforward modifications of the basis functions. These possible

geometries include hemispheres, spheroids, ellipsoids, cylinders, cones, pyramids, prisms, tetrahedra, octahedra, and others [19]. Further discussion of Visscher's method will come in later chapters, but as the forward calculation methods no longer required specimen geometries be rectangular parallelepipeds, Migliori et al. coined the modern terminology of resonant ultrasound spectroscopy (RUS), which has largely superseded the RST and RPR methods.

Today, RUS is probably the most common name given to resonance-based ultrasonic methods, but by no means has the community coalesced on a set of terminology, or even agreed upon a naming convention. Alternative nomenclature has been suggested for differentiating between resonance-based ultrasonic methods according to the size of a specimen, with Ostrovsky et al. referring to resonance methods investigating large specimens—which exhibit low-frequency resonances within the audible regime—as resonant acoustic spectroscopy (RAS) instead of RUS [20]. Such distinctions may be unnecessary, as nothing about the underlying physics is affected by the resonances falling within or beyond the audible regime of human hearing. A more persuasive argument might be to differentiate resonance-based ultrasonic methods into two broad categories involving contacting and contactless excitation methods. As RUS most-often relies on piezoelectric transducers for specimen excitation, it would fall under the category of contacting resonance-based ultrasonic methods, along with those employing hammer strikes [21, 22] and mechanical oscillators [23]. With a more recent alternative to traditional RUS being laser-based RUS (LRUS), which relies on the thermoacoustic effect and lasers for contactless excitation and measurement of resonances [24–26]. These laser-based excitation setups demonstrate considerable potential for future application, as laser vibrometry measurements supply sufficient data for solving the mode identification problem that simple RUS methods struggle with [25–27]. It is possible that RUS may some day be superseded by a technique like LRUS, or renamed as novel capabilities are developed. But given the considerable cost and time associated with these laser-based systems—particularly as

compared to traditional RUS setups consisting of contacting piezoelectric transducers, in conjunction with the growing body of literature around the RUS technique—both RUS and LRUS are likely to enjoy broad use across the fields of materials, geology, and physics for many years to come.

1.2 Background

Before delving into the finer details, this section strives to orient a broad audience of readers to the definitions, terminology, and background information relevant to this dissertation. Starting with the field of study which encompasses the RUS technique, ultrasonics is generally defined and discussed along with related fields of study. Key features and details of the forward and inverse problems are discussed in the context of determining elastic properties. Ending with broad discussions of the limits and potential of RUS, in the context of alternative nondestructive evaluation (NDE) techniques.

1.2.1 Ultrasonics, Acoustics, and Resonance

Ultrasonics refers to sound waves with a frequency above the audible limits of human hearing of 20,000 Hz, i.e. ultra-sound, while infrasound waves are below the audible limits of human hearing around 20 Hz [28]. Acoustics as a field of scientific study generally spans the audible range, though acoustics and ultrasonics are often used interchangeably. In this dissertation RUS is considered an ultrasonic technique, although larger specimens will exhibit low-frequency resonances within the audible range. Ultrasonics is concerned with the science and application of ultrasonic waves across both solid and fluid media. While fluids like a gas or a liquid propagate compressional waves only, solid matter is capable of transmitting both compressional and shear waves [29]. Transmission of waves across solid-liquid interfaces is also an important area of study for medical ultrasound [30], as well as immersion ultrasonic testing techniques [31], which leverage fluids like water,

oil, or gels as a couplant to facilitate the transmission of ultrasonic energy between an ultrasonic transducer and the inspected material. Even air-coupled ultrasonic methods exist [32], though are far less common due to the inferior coupling provided by air, and gases in general.

Ultrasonics ultimately studies how elastic waves travel through matter, and how the properties of elastic wave propagation, reflection, refraction, and attenuation can be used to interrogate the propagation medium. This dissertation will focus only on ultrasonics of solid matter, ignoring completely the transmission of ultrasonic energy between specimens and surrounding fluids. Such things can be ignored because under typical RUS measurement conditions, the effect of air pressure and other external forces on the specimen can be managed such that they do not appreciably affect the measured resonance frequencies [33]. Further, RUS does not rely on a couplant to facilitate the transmission of energy from transducers to specimens. Instead, RUS is generally concerned with the free vibrations of a specimen where external forces are ignored [33, 34].

Ultrasonic waves are created through a concentrated input of kinetic energy which perturbs the propagation medium from its equilibrium position. This initially concentrated input energy is then disbursed throughout the matter over a period of time, with the spacial and temporal characteristics of propitiation governed by the wave equation of motion [34]. The input energy can be expressed in terms of an initial force applied to, or an initial displacement of, the propagation medium. As long as the initial energy input does not exceed the elastic limit of the material, the energy is dispersed nondestructively via elastic waves. RUS almost exclusively employs contacting piezoelectric transducers to generate these elastic waves [33], though hammer strikes [21, 22], mechanical oscillators [23], lasers [25], and electro-magnetic fields [35] are also viable means of excitation for resonance-based ultrasonic evaluation.

Resonance methods are a specific subset of ultrasonic techniques which rely on the excitation of mechanical resonance modes of a specimen, across a range of excitation

frequencies, for purposes of evaluation. Resonance occurs when the frequency of the ultrasonic excitation force approaches a natural vibrational mode frequency of the specimen, and opposite-traveling elastic waves constructively interfere to develop a standing wave across the specimen [33, 36]. This standing wave results in deflections of the specimen specimen surface that are magnified in amplitude, potentially thousands of times greater than the drive amplitude—depending on the quality factor of the resonance/material [37]—which greatly facilitates the observation of resonance modes above background vibrations [33]. When collecting a broadband resonance measurement, the lowest-frequency mode is often first identified before the specimen is excited through a continuous range of greater frequencies until a desired quantity of resonance modes are collected. While the relationships between the properties of a 3D specimen and its resonance frequencies are complicated [34, 38], these characteristic resonance frequencies provide indirect measurements of a variety of specimen attributes. Attributes such as elastic properties, crystal orientation, and specimen geometry, which can all be determined with a high degree of precision given RUS measurements are combined with powerful computational methods.

1.2.2 Ultrasonic Methods for Measuring Elastic Properties

Ultrasonic techniques are capable of providing the most accurate characterizations of elastic properties in solid media [33, 34], as well as superior precision and repeatability as compared to static methods [39]. Pulse-echo ultrasonic methods assess characteristic elastic wave propagation velocities of a material via time-of-flight measurements, and with a plane-wave assumption, provide simply-defined relationships for the elastic properties of isotropic media [34, 40]. However, when the material is elastically anisotropic, pulse-echo experimental methods become more complicated. They require multiple pulse-echo measurements be collected between parallel planes of a specimen that are coincident to

specific planes of crystal symmetry [34, 40]; and may require multiple specimens when the elastic symmetry is lower than cubic [34]. For the number of independent wave velocities equals the number of independent elastic constants necessary to characterize the material.

The experimental procedures for RUS evaluation of elastic properties of anisotropic materials are simpler than those required by pulse-echo methods. Partially because RUS computational methods do not require plane-wave assumptions [34], instead relying on a rigorous treatment of the governing physics. This rigorous treatment allows for a single RUS broadband measurement from a single specimen to fully characterize its elastic properties, regardless of the elastic symmetry exhibited by the specimen. Thus, the experimental advantages provided by RUS are more pronounced when the elastic symmetry of the material is lower [41]. Moreover, in order to collect pulse-echo measurements from a specimen, the specimen faces must be larger than the face of the transducer in order for the plane-wave assumptions to be valid [34]. While RUS transducers only require contact with the specimen sufficient to excite and record resonance modes, which may be accomplished through weak contact along the specimen faces, edges, or corners [42]. This means that RUS can be applied to smaller specimens than pulse-echo methods [41], which can be particularly important considering larger single crystal specimens are more difficult and expensive to fabricate.

1.2.2.1 The Forward Problem

The "forward problem" refers to calculating the resonance frequencies of a specimen, given all of the requisite information including its geometry, density, boundary conditions, and elastic properties [33, 42]. Historically, solving the forward problem has been a serious impediment to the broad application of resonance-based ultrasonic methods [33]. For without a generalized method of solving the forward problem, only simple cases of the problem, e.g. cubes and spheres with uniform elastic properties exhibiting relatively

high elastic symmetries, could be solved by the end of the 1960's [12, 13]. Key developments towards solving the forward problem were introduced in Section 1.1.1, while Section 6.3.1 gives detailed discussion of how Visscher's xyz-algorithm is implemented with the Rayleigh-Ritz method to actually solve the forward problem [19]. The problem is readily solved today with the benefit of powerful computational resources, employing either finite element [43] or Rayleigh-Ritz methods [19]. The key difference between these two methods is that the Rayleigh-Ritz method requires the use of continuous polynomial functions to describe the geometry of the specimen, while FE methods do not have such restrictions. In 2004, Plesek, Kolman, and Landa first demonstrated that the inverse problem could be modified to utilize FE forward problem evaluations [43], while Liu and Maynard in 2012 gave a particularly insightful demonstration of the FE method applied to an arbitrarily shaped specimen [44]. Although, the flexibility of FE methods come at a cost, as FE evaluations are computationally less efficient as compared to Rayleigh-Ritz evaluations, requiring greater computational time [43, 44]. The additional time required is highly dependent on the number of finite elements used versus the order of the polynomial functions used by the Rayleigh-Ritz method. But for simple geometries (for which both FE and Rayleigh-Ritz methods may be used), prior experience suggest FE methods are an order of magnitude slower, while Plesek et al. suggest two orders of magnitude slower when FE methods are integrated into an inversion framework [43]. Though given a modern desktop computer and sufficient time, either method is capable of providing accurate and precise predictions of resonance frequencies for both forward and inverse modeling efforts. With the Rayleigh-Ritz approach often preferred for inverse modeling efforts, which are heavily dependent on numerous fast and accurate forward problem evaluations [33, 37].

1.2.2.2 The Inverse Problem

The RUS "inverse problem" as it has come to be known, is the process by which the elastic constants (or other unknown parameters) of a specimen are quantified based upon an input of measured resonance frequencies. As no direct solution to this problem exists [38, 45], indirect optimization-based methods as first outlined by Ohno were developed [15]. Since Ohno in 1976, the basic formulation of the inverse problem has remained relatively consistent. Beginning with an "initial guess set of elastic constants", which are typically informed by prior measurements or from values in the literature. These guess values are used to solve the first iteration of the forward problem, most often using Rayleigh-Ritz numerical methods, which gives an initial list of modeled resonance frequencies. Next, an optimization algorithm is employed to iteratively improve the guess set of elastic constants as judged by the minimization of an objective (i.e. cost) function that calculates the difference between the modeled and measured lists of frequencies. Often this function is a sum of squared errors:

$$F = \sum_{i=1}^{N} \left(f_{R,i}^{exp.} - f_{R,i}^{calc.} \right)^2 \tag{1.1}$$

with $f_{R,i}^{exp.}$ being the list of N experimentally determined frequencies, and $f_{R,i}^{calc.}$ the calculated frequencies from the forward model [26,38,45,46]. Different optimization algorithms have been used over time, with the Levenberg-Marquardt (LM) algorithm popularized by Migliori et al. being the most common [33,38]. Effectively performing a least-squares regression of an over determined system, whereby more resonance frequencies are used than elastic constants are sought. The optimization proceeds in a loop, improving the guess set of elastic constants until some convergence or termination criteria are met [46]. At which point, the current guess values of elastic constants are returned, and the optimization terminated.

Section 1.3.2 further discusses the inverse problem and previews the novel Bayesian methods developed in Chapter 6 that reformulate the inverse problem as a statistical inference, instead of an optimization. Such formulations have only recently become viable through the advent of cheap and powerful computational resources. A single optimization may require 10^2–10^4 forward problem evaluations, depending on the quality of the initial guess values and the optimization algorithm used, while collecting a significant number of independent samples to perform a Bayesian inference may require upwards of 10^6 forward problem evaluations [47]. Clearly, efficiently solving the forward problem is of key importance when a full Bayesian inference takes 12 or more hours to complete. Though given the Bayesian formulation substantially simplifies both the experimental and the computational procedures required of the user—while providing capabilities unmatched by optimization-based approaches—longer computation times are deemed an appropriate trade-off.

1.2.3 Broad Potential and Limits of RUS

One of the key attributes distinguishing RUS from other nondestructive evaluation techniques—like eddy-current testing, dye penetrant inspection, magnetic particle inspection, as well as other ultrasonic techniques like pulse-echo or phased-array methods—is that the entire volume of a specimen is excited during a single broadband RUS measurement. This feature allows for indirect measurements of: geometry, temperature, density, defect concentrations, linear and nonlinear elastic properties, including damping, as well as the orientation dependence of these properties. All from a single measurement that can be collected in a short period of time, using relatively inexpensive equipment, with a near-zero cost per measurement [38]. When considering other NDE methods which evaluate an entire specimen with a single measurement, radiography comes to mind. While there are instances where radiographic techniques are likely superior to RUS, e.g. searching

for porosity or inclusions at the center of cast metal parts [48]. Such high fidelity radiographic techniques work through the use of high energy x-rays that are dangerous to human health. They require large capital investments in x-ray equipment, and are considerably more expensive to operate on a per-measurement basis as compared to RUS, which all conspire to substantially limit broad evaluation potential.

As a limitation, the fact that RUS is simultaneously sensitive to many properties across the entire volume of a specimen does leave many avenues for uncontrolled experimental or material conditions to bias results. Particularly in the context of statistical sorting techniques applied to large populations of mass produced parts, where uncontrolled variability in specimen properties can overwhelm the indirect observations that are desired by the NDE with RUS framework [49]. Specifically, the problem of natural variability in a part population, as discussed further in Section 1.3.1, is one of the key limiting features of historical RUS for NDE methods for which this dissertation works to resolve. Section 1.3.2 will preview how this historical issue can be addressed by tracking the changes in resonance frequency over time and by comparing these results to a part-specific baseline response that removes benign variations affecting f_R.

Additional limits include the fact that free vibrations of the specimen are being modeled, such that the specimen itself needs to be mechanically isolated from its surroundings during any RUS measurement [49]. Otherwise, the boundary conditions must be well understood and appropriately represented by any forward modeling efforts if the measured and modeled resonance characteristics are to be compared. Generally this precludes RUS inspection of things like civil engineering structures, or anything fixed to the ground, as well as assembled pieces of machinery. Though it is possible to account for fixed boundary conditions during resonance, efforts to do so fall outside the scope of this dissertation. Furthermore, this work generally assumes that a specimen be capable of excitation to a resonant condition, which generally precludes soft or lossy materials like rubber and cork from investigation [50]. Though considerable progress has been made recently by

Remillieux et al. [51] and Bernard et al. [52, 53] towards investigating highly attenuative and anisotropic materials like bone and rock using RUS inversion. Most metals, ceramics, and other structural materials exhibit high stiffness and relatively low mechanical losses during elastic wave propagation, making these materials ideal for investigating with RUS [49].

One final limitation for the development and broad use of modeling frameworks for NDE of damage is that model results are neither broadly applicable, nor readily converted to similar NDE problems where the geometry or material properties have changed. However, the fact that model results are not applicable for much beyond the specific scenario being modeled, as long as the modeling methods are simple and parameterizable, then the modeling methods themselves should have broad potential. Take for example an FMF for NDE of damage in turbine blades. If the design of the blade were to be updated, or if a thermal/environmental barrier coating were to be applied, either would have the potential to change the baseline f_R behavior significantly enough that would require a new series of forward models detailing how damage evolution affects the resonance characteristics of this new blade design. While no methods currently exist for converting previously-modeled results from earlier turbine blade designs, for use towards evaluating a new turbine blade design. But as long as the modeling framework utilizes relatively simple and easily parameterizable models—of which finite element models are particularly well suited—the baseline and damaged specimen models should be readily repeated.

1.3 Motivation and Introductory Concepts

This dissertation details the development and the application of both forward and inverse modeling frameworks—abbreviated as FMF and IMF for short—for extending the nondestructive evaluation and materials characterization capability of RUS. These fun-

damental concepts and terminology are being introduced here as a primer for the main body chapters of this dissertation, given the historical framing provided by Section 1.1 and the background of Section 1.2. After a discussion of the historical use of RUS for NDE applications in Section 1.3.1, motivation for inclusion of models for expanded NDE potential is given in Section 1.3.1.1. Then Section 1.3.2 will preview key and novel concepts of the FMF covered by Chapters 4 and 5, and the IMF covered by Chapters 6 and 7 of this dissertation.

1.3.1 Historical Use of RUS for NDE

Until quite recently, most RUS for NDE efforts that have reached industrial application could generally be described as population statistics sorting (PSS) methods. PSS methods generally seek to identify outliers from a population of nominally identical parts and rely on a database of f_R collected from parts previously classified into pass/fail conditions [49]. These previously classified parts comprise a "teaching set", against which future components are evaluated. The goal of building a teaching set is to develop a database that encompasses the entire range of f_R variation resulting from: natural variability in manufacturing, acceptable levels of damage acquired throughout the service life of the component, and a variety of benign defects and imperfections that may lead to changes in f_R but would not cause the component to be removed from service [49]. In addition to a population of acceptable parts, teaching sets for PSS methods will often take into account the f_R profiles of failed parts as well. Ranging from critically flawed to marginal failures, in theory, the larger the variety of failed components supplied to the teaching set, the better the database will become at qualifying future parts [49]. However, the the methods by which the condition of the teaching set parts are classified are not always well defined. With the teaching set of parts of known condition used to divide the the f_R landscape into acceptable and unacceptable regimes, against which

parts of unknown condition can be judged; the ultimate utility of a teaching set is highly dependent on the quality of the input data.

PSS methods are the founding principle behind the commercially relevant NDE with RUS technique: Process Compensated Resonance Testing (PCRT) [49, 54], of the Vibrant Corporation of Albuquerque, New Mexico. Today, Vibrant's PCRT has advanced considerably beyond simple PSS methods through the inclusion of both forward and inverse modeling methods. However, PSS methods are still commonly employed for NDE with RUS in many industrial settings, both for damage evaluation and manufacturing processes control.

1.3.1.1 Motivation for Integration of Models

Many of the obstacles first encountered by empirical PSS methods continue to hinder NDE efforts today. For example, PSS methods are prone to reject parts that exhibit anomalous resonance characteristics—including benign anomalies that may arise from a change in the manufacturing process [33]. While any error in qualifying parts used to develop the original teaching set, either identifying false positives or misidentifying failed parts as acceptable, can greatly hinder future capabilities at qualifying parts of unknown quality [49]. Clearly, the process of building a comprehensive teaching set of measured data is a difficult task, which may ultimately require that serviceable parts be purposefully damaged or destroyed in order to generate the relevant data for statistical analysis. However, the process of imparting controlled levels of damage to a series of parts may itself be a difficult task.

Take for example the goal of creating a PSS database capable of sorting service-exposed turbine blades into pass/fail conditions based on whether they have sustained a "critical level" of creep strain as defined by the manufacturer. It is likely that a majority of the service-exposed turbine blades will exhibit some amount of creep strain, though most will likely fall below the "critical level", and can safely be returned to service. So

in order to develop a comprehensive PSS database to sort blades of unknown condition, one first needs to qualify a teaching set of turbine blades using alternative nondestructive means. Creep strain may be easily quantified in a simple geometry test specimen with precise measurements of the specimen length, however the localization of creep strain in a complex geometry turbine blade would be far less amenable to simple measurements. But assuming some means of qualifying a teaching set is available, acquiring a series of blades with varying levels of creep strain—without alternative damage mechanisms that could confound the NDE process—is also likely to be difficult. As there are no simple laboratory setups that can impart creep strain to turbine blades in a controlled manner, one would most likely have to create the teaching set from service exposed parts that may contain further unidentified defects or damage. Clearly, the task of creating a PSS database for evaluation of creep damage in turbine blades through empirical means is fraught with difficulties and potential for error; while many of these problems could be averted by creating the teaching set using validated modeled data instead of empirical data. Of course, forward models alone do not comprise the full extent of a forward modeling framework for NDE. For further explanation of key aspects, the following section introduces terminology that will be helpful in preview of additional concepts key to the development of FMFs for NDE with RUS.

1.3.2 Preview of Key Concepts

In Chapters 4 and 5 of this dissertation, and in the publications upon which these chapters are based [55–57], an NDE with RUS framework is developed and presented. Understanding the issue of mode identification that can plague piezoelectric transducer-based RUS measurement schemes, and in lieu of expensive and slow laser vibrometry measurements for reliable mode identification, a key concept behind FMF development is outlined here. Unlike traditional inverse modeling efforts, where RUS measured f_R are compared directly

with precise forward models of f_R ; models and measurements of a FMF are compared through mode-specific changes in resonance frequency ($\triangle f_R$), defined as:

$$\Delta f_R = \frac{f_R^{damaged} - f_R^{baseline}}{f_R^{baseline}} \times 100\% \ . \tag{1.2}$$

Here $f_R^{baseline}$ refers to the measured and modeled resonance frequencies of the undamaged state, while $f_R^{damaged}$ are of course from the damaged state, with a $\triangle f_R$ signature calculated for both the measured and the modeled data. The key point being "mode-specific" changes in f_R, meaning that FE modeled results—where mode shape information is available for mode identification—should be used to ensure that $\triangle f_R$ are calculated for each specific mode.

In this work, the FE model baseline frequency order is conserved, and the f_R calculated from the specimen modeled with damage are reordered as necessary to match the order of the baseline model. The same procedure should be attempted with the measured modes, as it is sometimes possible to track modes changing in frequency order over successive RUS measurements. Though without an ability to positively identify the measured modes, the process is admittedly prone to error. Fortunately, a process for correcting these errors is provided in Section 4.4.2, which first starts by calculating the "residual" between the measured $\triangle f_R$ and the modeled $\triangle f_R$ as:

$$Residual = \Delta f_R^{Measured} - \Delta f_R^{Modeled} \ . \tag{1.3}$$

If the measured $\triangle f_R$ are in good agreement with the modeled $\triangle f_R$, then the residual for most modes should be near zero. If a significant residual remains that cannot be explained by changing the magnitude or extent of the primary mechanisms being modeled, then its important to consider additional mechanisms affecting resonance that may be operable in the measured specimen. An example is demonstrated in Chapter 4, when creep damage

in a polycrystalline dog-bone of Ni-based superalloy is investigated. Generally, additional damage mechanisms affecting resonance should be considered until a near-zero residual for a majority of the lower-frequency modes is achieved. As RUS measurement errors for repeated measurements of a single specimen are routinely less than ±0.1% for each mode, a residual exceeding this amount should be considered potentially significant [55, 56].

A key implication of calculating $\triangle f_R$ for the specimen and the model individually, is that each $\triangle f_R$ signature can remove anomalies affecting resonance that may be present in the baseline model or specimen. Take for example a situation where the actual specimen and the specimen model exhibit elastic properties that differ from each other by $\approx 1\%$. Admittedly this difference is small, but it is likely to result in modeled f_R to differ from measured f_R by $\approx \pm 0.5\%$. Recursive modeling efforts could focus considerable effort towards tuning the model properties to account for this disagreement—and the countless other potential sources of disagreement between a given specimen and a given model—but these efforts would be largely wasted. As comparisons of $\triangle f_R$ are blind to such differences between measured and modeled baselines, and only require a reasonable match between the measured and modeled baselines. Though the fewer instances of disagreement in mode ordering between the two baselines, the more straightforward the analysis will ultimately be.

Chapters 6 and 7, and the publications upon which these chapters are based [47, 58], cover the development and application of a novel approach to solving the RUS inverse problem. Instead of relying upon quality initial guess values and optimization algorithms to perform a least-squares regression [46], the Bayesian approach developed herein does not require any resemblance of quality initial guess values. In fact, reformulation the inverse problem as a Bayesian inference means the initial guess values are randomly generated based on weakly informative priors that simply help guide the sampler towards initial conditions that are physically possible [47, 58]. Further differentiating from optimizer-based inversions, Bayesian inferences involve computing a Bayesian posterior

which yields probability distributions for the unknown parameters, instead of just point estimates [47, 58]. From these probability distributions, the mean value of a normal distribution corresponds to the maximum likelihood estimate of the parameter, while the standard deviation of the distribution corresponds to the uncertainty of the estimate. Thus, Bayesian methods provide built-in estimates of uncertainty based on a theoretical framework that takes into account measurement and model-based uncertainty [47]. The posterior distributions are calculated via Hamiltonian Monte Carlo (HMC) sampling, which is an efficient form of Markov Chain Monte Carlo (MCMC). With its efficiency due to Hamiltonian dynamics that use partial derivatives of the Bayesian likelihood (similar to the objective function given in Equation (1.1)) with respect to the estimated parameters to facilitate progression of the Markov Chain towards the higher-likelihood regions of the posterior [59]. Together, this Bayesian approach with efficient HMC sampling forms the core of a powerful and robust inverse modeling framework, with capabilities beyond those of historical optimization-based approaches.

In addition to the powerful and robust capabilities already discussed, the IMF as developed in Chapter 6 also affords the ability to simultaneously estimate the crystal lattice orientation of anisotropic crystals. Employing a rigorous treatment of 3D rotations and elastic symmetries, the IMF code allows for dramatically simplified experimental and computational procedures. The full extent of these benefits will be discussed later, and form the basis of one of the key conclusions of this work. With additional benefits, functionality, and usability gained through integration of the core IMF code into a custom distribution of the open-sourced probabilistic programing language of Stan [60], detailed by Chapter 7 of this dissertation. Recent efforts have only begun to explore the capabilities and opportunities afforded by the library of Stan functions, diagnostic tools, built-in optimizers, and other key features [61]. This IMF code is given the name CmdStan-RUS [62], and is proudly provided free of charge[1] under an open-source license.

[1] CmdStan-RUS [62] can be downloaded at: https://github.com/bbbales2/cmdstan-rus

Chapter 2

Fundamental Theory: Elasticity, Resonance, and 3D Rotations

Chapter Abstract

Beginning with an introduction of constitutive equations that relate two (or more) kinetic quantities through a material-specific constant of proportionality, discussion soon proceeds to the various forms and characteristics of Hooke's law for linear elasticity. From the most basic isotropic properties and transformations, to the tensorial notation of anisotropic elastic properties exhibited by single crystals, composites, and textured polycrystalline materials, elastic constitutive behavior is explored as it pertains to ultrasonic methods. Then under the guise of governing laws, discussion covers the derivation and application of the wave equation of motion. With this powerful governing equation describing the propagation of all wave phenomena, further details are provided about how the equation of motion is solved, and the implications of the theory as it applies to the fundamental aspects of mechanical resonance. Finally, the chapter concludes with theory of rotations in 3D, how these rotations are applied to anisotropic elastic bodies, and the implications of a rotated stiffness tensor when seeking the elastic properties of a specimen with misaligned specimen-crystal reference frames.

2.1 Constitutive Equations

2.1.1 Isotropic Elasticity

Constitutive equations describe material-specific responses to external forces, and are almost entirely phenomenologically determined[1], i.e. determined through physical measurements [63]. Constitutive equations relate two physical quantities, and are often combined in sets to fully describe the complex response of a given material. The very first constitutive equation was formulated in the late 17th century by Robert Hooke, with his pronouncement "ut tensio sic vis" which translates from Latin to "as the extension, so the force" [64]. Today this constitutive equation is known as Hooke's law, and in scalar form relates the two kinematic quantities of stress (σ) and strain (ε) through a material-specific constant of proportionality defined as the elastic modulus (E):

$$E = \frac{\sigma}{\varepsilon} \ . \tag{2.1}$$

This simple scalar representation will ultimately need to be expanded to a full tensorial representation in order to capture the behavior of single crystal materials, but before that point some additional terminology should first be defined.

Stress is a physical quantity describing the internal forces that particles of a continuous medium exert on each other, and is generally defined as "the force per cross-sectional area". Specifically, engineering stress is defined as the normal force (F_N) divided by the unstressed cross-sectional area (A_0) over which the force is applied:

$$\sigma = \frac{F_N}{A_0} \ . \tag{2.2}$$

[1] Ab initio calculations applying first principles to estimate single crystal elastic constants based on quantum mechanical interactions at atomic scales have been demonstrated, though these calculations are still in their infancy do not always agree with experimentally determined values.

Strain is a physical quantity describing the change in shape, i.e. deformation, of material as a result of an applied stress. As depicted in Figure 2.1, engineering strain is defined as the change in height (Δh) divided by the original height (h) of the material subvolume:

$$\varepsilon = \frac{\Delta h}{h} \ . \tag{2.3}$$

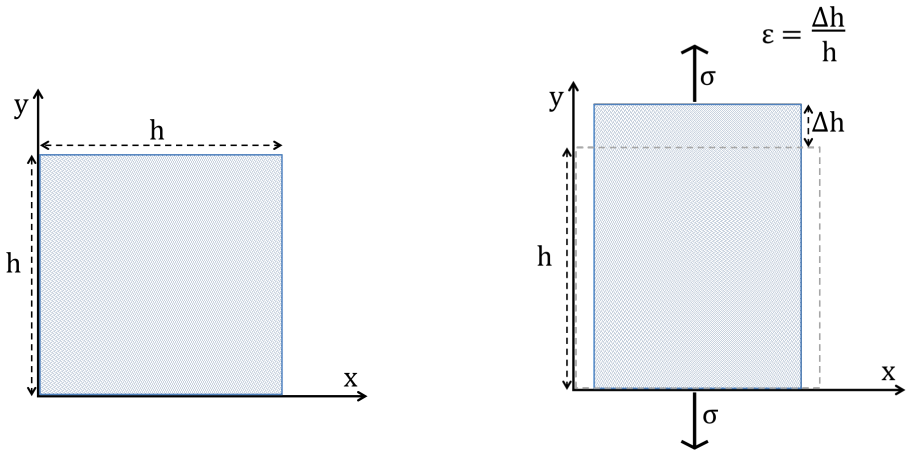

(a) before applied stress

(b) after applied normal stress

Figure 2.1: Depiction of engineering strain ε in 2D using a square subvolume of material (a) before and (b) after the application of a normal stress σ.

When the material is elastically isotropic (i.e. the same in all directions), and the stresses and strains are uniaxial, the the proportionality defined by Hooke's Law (Equation (2.1)) is known as Young's modulus (E). Note that herein E will exclusively be used to represent Young's modulus, while the elastic modulus in Equation (2.1) could pertain to any of a number of elastic moduli depending on the state of the stress and strain being related. For example, the elastic modulus relating shear stresses (τ) to shear strains (γ) is known as the shear modulus (G):

$$G = \frac{\tau}{\gamma} \ . \tag{2.4}$$

With engineering shear stress defined as the coplanar force transverse to the cross-sectional plane normal (F_T), divided by the unstrained cross-sectional area A_0:

$$\tau = \frac{F_T}{A_0} \ . \tag{2.5}$$

As depicted in Figure 2.2, engineering shear strain is defined as the shear displacement (Δx) divided by the height perpendicular to the shear displacement (h):

$$\gamma = \frac{\Delta x}{h} \ . \tag{2.6}$$

Note that a clockwise rigid body rotation equal to one-half θ was applied to the subvolume so as to align it with the x-axis and to demonstrate that $\gamma = tan(\theta)$.

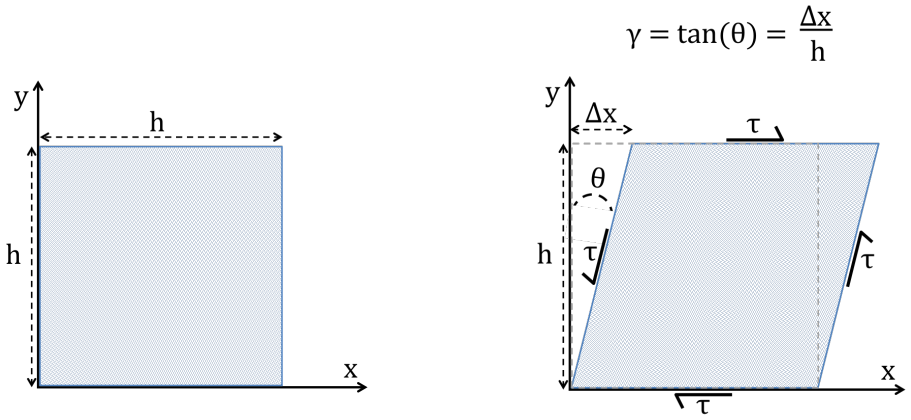

(a) before applied stress (b) after applied shear stress

Figure 2.2: Depiction of engineering shear strain γ in 2D using a square subvolume of material (a) before and (b) after the application of a shear stress τ.

Given Equations (2.1) and (2.4) and the assumption of isotropy, the complete elastic response (i.e. the complete constitutive model of the material) is fully defined by the two elastic moduli E and G [63]. Common units for E and G are given in gigapascals (GPa), with typical values of E for metals with low stiffness ranging from 45 to 69 GPa for magnesium and aluminum, respectively [65]. Higher stiffness metals like nickel and

steel have a Youngs modulus around 207 GPa, while Tungsten has a very high stiffness at 407 GPa [65].

Indeed, there are more than two possible parameterizations that can be used to fully define the isotropic constitutive model. Through simple parameter transformations, the constitutive behavior can be represented in alternate forms that may be useful for different situations. For example, returning to the case of uniaxial stress applied to a material subvolume as depicted in Figure 2.1. The negative ratio of strain in the transverse direction ε_T to the strain in the normal direction ε_N is defined as Poissons ratio (ν) [65]:

$$\nu = \frac{-\varepsilon_T}{\varepsilon_N} \ . \tag{2.7}$$

Note the negative sign in the definition of ν is because most materials exhibit a negative ε_T and a positive ε_N, which makes the negative ratio of these strains a positive value. While the full range of possible values for ν is not restricted to be positive, the instances where a material exhibits a negative ν is extremely rare because it requires a uniaxial tensile σ to result in an increase in cross-sectional area transverse to the σ. Most polycrystalline metals have a Poissons ratio between the range of 0.25–0.35 [65]. However, in order to ensure stability of an isotropic linear elastic material, $-1 < \nu < 0.5$ is the extent of possible values as required through the restriction of E, G and the bulk modulus (K) to be positive. Whereby the bulk modulus of a material describes its resistance to hydrostatic (i.e. isotropic) pressure, as depicted by Figure 2.3. With a definition for K being the constant of proportionality equal to the hydrostatic stress (σ_H):

$$\sigma_H = \sigma_x = \sigma_y, \tag{2.8}$$

divided by the resultant volumetric strain (ε_V) :

$$\varepsilon_V = \frac{\Delta V}{V_0} = \frac{\Delta h^2}{{h_0}^2}, \tag{2.9}$$

thus [66]:

$$K = \frac{\sigma_H}{\varepsilon_V} \ . \tag{2.10}$$

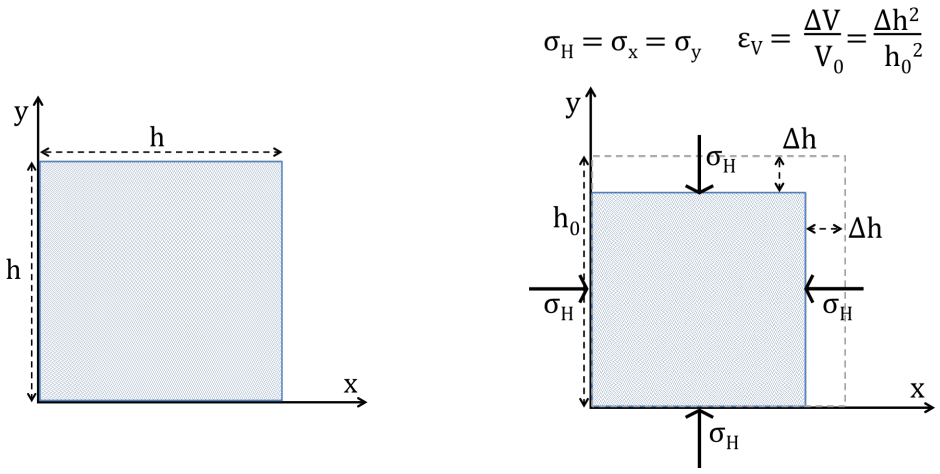

(a) before applied stress (b) after hydrostatic stress

Figure 2.3: Depiction of volumetric strain ε_V in 2D using a square subvolume of material, (a) before and (b) after the application of a hydrostatic stress σ_H.

As stated previously, one only needs two elastic parameters (E, G, ν, K, etc.) in order to fully define the constitutive behavior of an isotropic solid. This of course means

that parameter transformations are simply defined [63], such that:

$$E = \frac{9KG}{3K+G} = 2G(1+\nu) = 3K(1-2\nu)\ , \tag{2.11}$$

$$\nu = \frac{3K-2G}{2(3K+G)} = \frac{3K-E}{6K} = \frac{E}{2G}-1\ , \tag{2.12}$$

$$G = \frac{3K(1-2\nu)}{2(1+\nu)} = \frac{3KE}{9K-E} = \frac{E}{2(1+\nu)}\ , \tag{2.13}$$

$$K = \frac{EG}{3(3G-E)} = \frac{E}{3(1-2\nu)} = \frac{2G(1+\nu)}{3(1-2\nu)}\ . \tag{2.14}$$

Now of course there are materials with anisotropic, i.e. non-isotropic, properties which vary with direction. Single crystals for instance have elastic properties that vary based on crystallographic direction [33, 63], while polycrystalline metals that have undergone deformation processing like rolling often exhibit elastic properties that vary according to the normal or rolling directions [67–69]. Wood is also a common example of elastically anisotropic material, where the properties vary based on the direction of the wood fibers which leads to orthotropic elastic behavior characterized by 9 independent elastic parameters. In order to discuss these situations and materials further, it is necessary to use full three dimensional representations of stress, strain, and elastic parameters as given in the following section.

2.1.2 Anisotropic Elasticity

The full anisotropic (tensorial) form of Hooke's law relating σ and ε in three Cartesian dimension is given as:

$$\sigma_{ij} = C_{ijkl}\varepsilon_{kl}, \tag{2.15}$$

where C_{ijkl} is the rank-four stiffness tensor, σ_{ij} and ε_{kl} are rank-two tensors, and where summation has been assumed over repeated indices. The Cauchy stress tensor σ_{ij} consists of nine components that fully define the state of stress using an orthogonal basis (e_1, e_2, e_3), such that:

$$\sigma_{ij} = \begin{bmatrix} \sigma_{11} & \sigma_{12} & \sigma_{13} \\ \sigma_{21} & \sigma_{22} & \sigma_{23} \\ \sigma_{31} & \sigma_{32} & \sigma_{33} \end{bmatrix} . \tag{2.16}$$

Figure 2.4 depicts these nine components of stress on a cubic subvolume of material, which could also be expressed using the (x, y, z) coordinates and σ/τ variables from Section 2.1.1 as:

$$\sigma_{xy} = \begin{bmatrix} \sigma_x & \tau_{xy} & \tau_{xz} \\ \tau_{yx} & \sigma_y & \tau_{yz} \\ \tau_{zx} & \tau_{zy} & \sigma_z \end{bmatrix} . \tag{2.17}$$

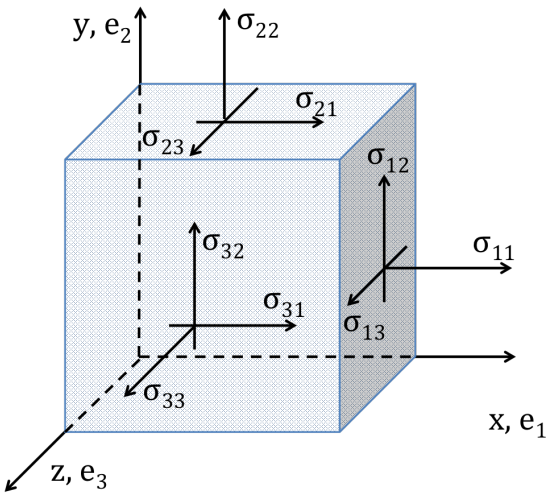

Figure 2.4: Depiction of stresses on a cubic subvolume of material in three Cartesian dimensions.

The infinitesimal strain tensor ε_{ij} is formulated in the same way as the stress tensor,

with displacements u mapped according to $\varepsilon_{ij} = \frac{1}{2}\left(u_{i,j} + u_{j,i}\right)$ as:

$$\varepsilon_{ij} = \begin{bmatrix} \frac{\partial u_1}{\partial x_1} & \frac{1}{2}\left(\frac{\partial u_1}{\partial x_2} + \frac{\partial u_2}{\partial x_1}\right) & \frac{1}{2}\left(\frac{\partial u_1}{\partial x_3} + \frac{\partial u_3}{\partial x_1}\right) \\ \frac{1}{2}\left(\frac{\partial u_2}{\partial x_1} + \frac{\partial u_1}{\partial x_2}\right) & \frac{\partial u_2}{\partial x_2} & \frac{1}{2}\left(\frac{\partial u_2}{\partial x_3} + \frac{\partial u_3}{\partial x_2}\right) \\ \frac{1}{2}\left(\frac{\partial u_3}{\partial x_1} + \frac{\partial u_1}{\partial x_3}\right) & \frac{1}{2}\left(\frac{\partial u_3}{\partial x_2} + \frac{\partial u_2}{\partial x_3}\right) & \frac{\partial u_3}{\partial x_3} \end{bmatrix}. \tag{2.18}$$

Maintaining consistency with the definition of engineering shear strain (γ) as defined by Equation (2.6) necessitates the factor of $\frac{1}{2}$ be used to equate the off-diagonal tensorial strain components (ε_{ij}) as:

$$\varepsilon_{ij} = \begin{bmatrix} \varepsilon_{11} & \varepsilon_{12} & \varepsilon_{13} \\ \varepsilon_{21} & \varepsilon_{22} & \varepsilon_{23} \\ \varepsilon_{31} & \varepsilon_{32} & \varepsilon_{33} \end{bmatrix} = \begin{bmatrix} \varepsilon_{xx} & \varepsilon_{xy} & \varepsilon_{xz} \\ \varepsilon_{yx} & \varepsilon_{yy} & \varepsilon_{yz} \\ \varepsilon_{zx} & \varepsilon_{zy} & \varepsilon_{zz} \end{bmatrix} = \begin{bmatrix} \varepsilon_{xx} & \gamma_{xy}/2 & \gamma_{xz}/2 \\ \gamma_{yx}/2 & \varepsilon_{yy} & \gamma_{yz}/2 \\ \gamma_{zx}/2 & \gamma_{zy}/2 & \varepsilon_{zz} \end{bmatrix} \tag{2.19}$$

because γ_{xy} was effectively defined as: $\left(\frac{\partial u_y}{\partial x} + \frac{\partial u_x}{\partial y}\right)$, and not $\frac{1}{2}\left(\frac{\partial u_y}{\partial x} + \frac{\partial u_x}{\partial y}\right)$.

The C_{ijkl} stiffness tensor has $3\times3\times3\times3 = 81$ components. However, "minor symmetry" of the 9 component stress and strain tensors require:

$$\begin{aligned} \sigma_{ij} = \sigma_{ji} \quad &\Rightarrow \quad C_{ijkl} = C_{jikl} \\ \varepsilon_{kl} = \varepsilon_{lk} \quad &\Rightarrow \quad C_{ijkl} = C_{ijlk} \end{aligned} \tag{2.20}$$

reducing the number of unique components of these rank-two tensors to 6, and the number of unique components of the rank-four C_{ijkl} tensor to 36. As such, the C_{ijkl} tensor can

be reprsented as a 6×6 matrix as:

$$\begin{bmatrix} \sigma_{11} \\ \sigma_{22} \\ \sigma_{33} \\ \sigma_{23} \\ \sigma_{31} \\ \sigma_{12} \end{bmatrix} = \begin{bmatrix} C_{1111} & C_{1122} & C_{1133} & C_{1123} & C_{1131} & C_{1112} \\ C_{2211} & C_{2222} & C_{2233} & C_{2223} & C_{2231} & C_{2212} \\ C_{3311} & C_{3322} & C_{3333} & C_{3323} & C_{3331} & C_{3312} \\ C_{2311} & C_{2322} & C_{2333} & C_{2323} & C_{2331} & C_{2312} \\ C_{3111} & C_{3122} & C_{3133} & C_{3123} & C_{3131} & C_{3112} \\ C_{1211} & C_{1222} & C_{1233} & C_{1223} & C_{1231} & C_{1212} \end{bmatrix} \begin{bmatrix} \varepsilon_{11} \\ \varepsilon_{22} \\ \varepsilon_{33} \\ 2\varepsilon_{23} \\ 2\varepsilon_{31} \\ 2\varepsilon_{12} \end{bmatrix}, \tag{2.21}$$

while Voigt provides a short-hand notation that uses the definition of engineering shear strain (for ε_{23}, ε_{13}, and ε_{12}) and maps the components $ij \to p$ and $kl \to q$ as follows:

$$\sigma = \begin{bmatrix} \sigma_{11} \to \sigma_1 \\ \sigma_{22} \to \sigma_2 \\ \sigma_{33} \to \sigma_3 \\ \sigma_{23} \to \sigma_4 \\ \sigma_{13} \to \sigma_5 \\ \sigma_{12} \to \sigma_6 \end{bmatrix} \quad \varepsilon = \begin{bmatrix} \varepsilon_{11} \to \varepsilon_1 \\ \varepsilon_{22} \to \varepsilon_2 \\ \varepsilon_{33} \to \varepsilon_3 \\ 2\varepsilon_{23} \to \varepsilon_4 \\ 2\varepsilon_{13} \to \varepsilon_5 \\ 2\varepsilon_{12} \to \varepsilon_6 \end{bmatrix}. \tag{2.22}$$

This Voigt short-hand simplifies Equation (2.21) to:

$$\begin{bmatrix} \sigma_1 \\ \sigma_2 \\ \sigma_3 \\ \sigma_4 \\ \sigma_5 \\ \sigma_6 \end{bmatrix} = \begin{bmatrix} C_{11} & C_{12} & C_{13} & C_{14} & C_{15} & C_{16} \\ C_{21} & C_{22} & C_{23} & C_{24} & C_{25} & C_{26} \\ C_{31} & C_{32} & C_{33} & C_{34} & C_{35} & C_{36} \\ C_{41} & C_{42} & C_{43} & C_{44} & C_{45} & C_{46} \\ C_{51} & C_{52} & C_{53} & C_{54} & C_{55} & C_{56} \\ C_{61} & C_{62} & C_{63} & C_{64} & C_{65} & C_{66} \end{bmatrix} \begin{bmatrix} \varepsilon_1 \\ \varepsilon_2 \\ \varepsilon_3 \\ \varepsilon_4 \\ \varepsilon_5 \\ \varepsilon_6 \end{bmatrix}. \tag{2.23}$$

Then, just as the "minor symmetries" of Equation (2.20) allowed us to say, e.g. $\sigma_{12} =$

σ_{21}, $\sigma_{23} = \sigma_{32}$, *etc*, the "major symmetry" of the stiffness tensor means it is also symmetric, i.e. $C_{pq} = C_{qp}$, and that there are at most 21 independent stiffness values

$$C_{pq} = \begin{bmatrix} C_{11} & C_{12} & C_{13} & C_{14} & C_{15} & C_{16} \\ C_{12} & C_{22} & C_{23} & C_{24} & C_{25} & C_{26} \\ C_{13} & C_{23} & C_{33} & C_{34} & C_{35} & C_{36} \\ C_{14} & C_{24} & C_{34} & C_{44} & C_{45} & C_{46} \\ C_{15} & C_{25} & C_{35} & C_{45} & C_{55} & C_{56} \\ C_{16} & C_{26} & C_{36} & C_{46} & C_{56} & C_{66} \end{bmatrix}. \tag{2.24}$$

2.1.2.1 Anisotropic Elasticity of Crystals

Equation (2.24) represents the stiffness tensor of single crystals with the lowest elastic symmetry, triclinic [34,40]. Triclinic crystals have no planes or axes of symmetry, making all of the 21 stiffness constants non-zero [70]. The implications of this are that even uniaxial stresses, e.g. $\sigma_1 \neq 0$ and $\sigma_2 = \sigma_3 = \sigma_4 = \sigma_5 = \sigma_6 = 0$, produce both normal and shear strains (ε_1, ε_2, ε_3, ε_4, ε_5, $\varepsilon_6 \neq 0$) in the crystal.

Whereas a single plane of reflection symmetry gives a crystal monoclinic symmetry [70], which can be fully characterized by 13 independent stiffness constants:

$$C_{pq} = \begin{bmatrix} C_{11} & C_{12} & C_{13} & 0 & 0 & C_{16} \\ C_{12} & C_{22} & C_{23} & 0 & 0 & C_{26} \\ C_{13} & C_{23} & C_{33} & 0 & 0 & C_{36} \\ 0 & 0 & 0 & C_{44} & C_{45} & 0 \\ 0 & 0 & 0 & C_{45} & C_{55} & 0 \\ C_{16} & C_{26} & C_{36} & 0 & 0 & C_{66} \end{bmatrix}. \tag{2.25}$$

With the plane of reflection symmetry about the e_3 axis, any elastic constant expressed

in the tensorial C_{ijkl} representation that contains an odd number of components with the value of three (be there one or three threes) must be equal to zero as the material is invariant upon reflections about the e_3 axis [70]. Therefore, in referencing Equation (2.21), it is clear that:

$$\begin{Bmatrix} C_{1123} = C_{14} \\ C_{1131} = C_{15} \\ C_{2223} = C_{24} \\ C_{2231} = C_{25} \\ C_{3323} = C_{34} \\ C_{3331} = C_{35} \\ C_{2312} = C_{46} \\ C_{3112} = C_{56} \end{Bmatrix} = 0 \tag{2.26}$$

The next highest symmetry are orthorhombic crystals, also commonly described as having orthotropic symmetry [71], with three mutually orthogonal planes of reflection symmetry that reduce the number of independent stiffness values to 9:

$$C_{pq} = \begin{bmatrix} C_{11} & C_{12} & C_{13} & 0 & 0 & 0 \\ C_{12} & C_{22} & C_{23} & 0 & 0 & 0 \\ C_{13} & C_{23} & C_{33} & 0 & 0 & 0 \\ 0 & 0 & 0 & C_{44} & 0 & 0 \\ 0 & 0 & 0 & 0 & C_{55} & 0 \\ 0 & 0 & 0 & 0 & 0 & C_{66} \end{bmatrix}. \tag{2.27}$$

Orthotropic materials, which are invariant to reflections about any of the e_1, e_2, or e_3 axes, must therefore have zero-value elastic constants whenever an odd number of i, j, k, or l components are present in the C_{ijkl} representation, Equation (2.21). Note that a

material with only two orthogonal planes of elastic symmetry is physically impossible as the inclusion of two requires the third [72]. Orthotropic elastic symmetry includes many important classes of materials, including many composites [73] and rolled cubic metals e.g. steel [66].

Table 2.1: Single crystal elastic constants for various hexagonal metals, data from [74].

Material	C_{11} (GPa)	C_{12} GPa	C_{13} (GPa)	C_{33} (GPa)	C_{44} (GPa)
Be	292.3	26.7	14.0	336.4	162.5
Co	307.0	165.0	103.0	358.1	78.3
Mg	59.7	26.2	21.7	61.7	16.4
Ti	162.4	92.0	69.0	180.7	46.7
Zn	161.0	34.2	50.1	61.0	38.3
Zr	143.4	72.8	65.3	164.8	32.0

Besides planes of reflection symmetry, it is also possible for crystals to exhibit transverse isotropy about an axis, e.g. hexagonal crystals exhibit such symmetry about the c-axis of the material. Elastically indistinguishable from the case of 6-fold rotational symmetry about the c-axis [72], complete rotational symmetry implies that the material is elastically isotropic when stressed perpendicular to the c-axis, which we will assume to be collinear to the e_3 axis. This requires that $C_{11} = C_{22}$, $C_{13} = C_{23}$, and $C_{44} = C_{55}$, in addition to the invariance of reflections about any of the e_1 and e_2 axes, reducing the stiffness tensor to:

$$C_{pq} = \begin{bmatrix} C_{11} & C_{12} & C_{13} & 0 & 0 & 0 \\ C_{12} & C_{11} & C_{13} & 0 & 0 & 0 \\ C_{13} & C_{13} & C_{33} & 0 & 0 & 0 \\ 0 & 0 & 0 & C_{44} & 0 & 0 \\ 0 & 0 & 0 & 0 & C_{44} & 0 \\ 0 & 0 & 0 & 0 & 0 & C^*_{66} \end{bmatrix} \tag{2.28}$$

containing 5 independent elastic parameters as $C^*_{66} = (C_{11} - C_{12})/2$. A variety of single crystal metals exhibit hexagonal elastic symmetry including: Mg, Zn, α-Ti, α-Be, α-Co,

α-Zr, and α-Y [75], with example values provided in Table 2.1. In addition to single crystals, directionally solidified cubic materials like Ni-based superalloys exhibit fiber textures with hexagonal symmetry [76], as well as unidirectional composites [77,78], and layered geological formations [79].

A special case of orthotropic symmetry is that of cubic symmetry, which has three mutually orthogonal planes of reflection symmetry like orthorhombic crystals, with the added condition of the properties along the three axes e_1, e_2, and e_3 being identical. This symmetry requires: $C_{11} = C_{22} = C_{33}$, $C_{12} = C_{13} = C_{23}$, and $C_{44} = C_{55} = C_{66}$, which reduces the stiffness tensor to

$$C_{pq} = \begin{bmatrix} C_{11} & C_{12} & C_{12} & 0 & 0 & 0 \\ C_{12} & C_{11} & C_{12} & 0 & 0 & 0 \\ C_{12} & C_{12} & C_{11} & 0 & 0 & 0 \\ 0 & 0 & 0 & C_{44} & 0 & 0 \\ 0 & 0 & 0 & 0 & C_{44} & 0 \\ 0 & 0 & 0 & 0 & 0 & C_{44} \end{bmatrix} \tag{2.29}$$

and the number of independent elastic constants to 3. Single crystal Ni-based superalloys, and its two constituent phases of γ and γ', possess cubic crystal structures and cubic elastic symmetry [80]. As do all cubic single crystals which includes a majority of structural and technically relevant metals such as: Al, Fe, Cu, Au, Ag, Pb, Cr, Nb, etc. Table 2.2 provides a list of single crystal stiffness values for various cubic metals.

The case of greatest elastic symmetry belongs to isotropic media, which could be considered a special case of cubic symmetry when $C_{44} = (C_{11} - C_{12})/2$. As such, isotropic materials can be considered to exhibit rotational symmetry, like that of transversely isotropic (e.g. hexagonal) materials, about each of the three mutually orthogonal e_1, e_2, and e_3 axes. With the stiffness matrix for an isotropic material containing only two

Table 2.2: Single crystal elastic constants for various cubic metals, data from [81] .

Material	C_{11} (GPa)	C_{12} GPa	C_{44} (GPa)	A (unitless)
Al	107.3	60.9	28.3	1.22
Au	192.9	163.8	41.5	2.85
Ag	124.0	93.4	46.1	3.01
Cu	168.4	121.4	75.4	3.21
Fe	231.4	134.7	116.4	2.41
Ni	246.5	147.3	127.4	2.57
Pb	49.5	42.3	14.9	4.14
Cr	339.8	58.6	99.0	0.70
Pt	346.7	250.7	76.5	1.59
Nb	240.2	125.6	28.2	0.49
Si	166.2	64.4	79.8	1.57

[1] Reported values can vary considerably based on differences in crystal growth methods, defect concentrations, chemical purity, and testing methods.

independent elastic constants:

$$C_{pq} = \begin{bmatrix} C_{11} & C_{12} & C_{12} & 0 & 0 & 0 \\ C_{12} & C_{11} & C_{12} & 0 & 0 & 0 \\ C_{12} & C_{12} & C_{11} & 0 & 0 & 0 \\ 0 & 0 & 0 & (C_{11}-C_{12})/2 & 0 & 0 \\ 0 & 0 & 0 & 0 & (C_{11}-C_{12})/2 & 0 \\ 0 & 0 & 0 & 0 & 0 & (C_{11}-C_{12})/2 \end{bmatrix}. \tag{2.30}$$

While isotropic elasticity is commonly assumed for structural materials, the highest intrinsic symmetry exhibited by crystalline materials is cubic, not isotropic [72]. The isotropy exhibited by many structural metals and alloys is a direct result of their polycrystalline grain structure, and depends on a variety of factors including the intrinsic elastic anisotropy of the constituent material, the grain size and shape, as well as the crystallographic orientation of each grain. Therefore, the following section will discuss in further detail the conditions required for a material to exhibit isotropy, and the means by

which isotropic elastic properties are calculated using polycrystalline averaging schemes and single crystal elastic properties.

2.1.3 Polycrystalline Averaging Schemes: Calculating Isotropic Moduli

When consisting of a large volume of randomly oriented grains, polycrystalline materials act as elastically isotropic bodies with no directional dependence of constitutive elastic behavior [82]. While the assumption of isotropy may not be appropriate for many instances including: deposited films and coatings [83], hot and cold worked metals [84,85], or microelectronic devices [83,86]; the assumption is appropriate in many instances as will be demonstrated herein.

Through a series of FE models, Nygårds [87] was able to determine the number of grains necessary to achieve an effectively isotropic response from an aggregate of cubic crystals. What he found was that the number of equaixed grains necessary for effective isotropy depends strongly on the definition of "effectively isotropic", as well as the elastic anisotropy (A) of the material which Zener [88] first defined in 1947 as:

$$A = \frac{2C_{44}}{C_{11} - C_{12}}. \tag{2.31}$$

Single crystals of Al and W are nearly isotropic with A approximately equal to 1, while other metals such as Ni, Fe, and Cu are more anisotropic with A ranging from 2.3–3.2 [63]. The more anisotropic a material is, the more grains that will be necessary to produce an isotropic aggregate response. While "effectively isotropic" behavior was defined by comparing the stress response of a 3D volume of grains under uniaxial tension ($\varepsilon_{xx} = \varepsilon$, with all other $\sigma_{ij} = 0$), biaxial loading ($\varepsilon_{xx} = \varepsilon_{yy} = \varepsilon$, with all other $\sigma_{ij} = 0$), and biaxial shear ($\varepsilon_{xx} = -\varepsilon_{yy} = \varepsilon$, with all other $\sigma_{ij} = 0$), to the stress response of a 500 grain

aggregate [87].

Using the properties of a typical Ni-based superalloy[2], an isotropic response equivalent to 98% the isotropic limit would be expected from a aggregate volume containing 200 or more randomly oriented grains. Thus, a cubic volume of superalloy comprised of equiaxed grains 500 µm in diameter would need to have side lengths of 3 mm or greater in order to exhibit 98% effectively isotropic behavior. While this analysis by Nygårds is relatively simple, and one could easily argue with the particular definition of "effectively isotropic". The study does make clear the general length scales at which a volume of randomly oriented grains transitions to effectively isotropic behavior. A conservative rule of thumb one could take away from this analysis would be: whenever a specimen or structural component has dimensions within two orders of magnitude of the average grain diameter, the assumption of effective isotropy should not be carelessly applied.

When a material is effectively isotropic, it means that $A = 1$ in Equation (2.31), and that an elastic degree of freedom is fixed such that only two (isotropic) moduli fully define the response. As detailed extensively in Section 2.1.1, common isotropic moduli include: Young's modulus (E), bulk modulus (K), shear modulus (G) and Poisson's ratio (ν) [63]. The specific moduli one uses is often based on the context of problem like the loading conditions, with straightforward conversions between them enumerated in Equations (2.11) to (2.14). It is not possible to determine the single crystal elastic constants of a material from measurements of its isotropic response in a polycrystalline form, however it is quite possible to go the opposite direction.

Isotropic moduli can be determined through a variety of averaging schemes, e.g. Voigt-Reuss-Hill [89], Hashin [90], Kröner [91], and Gairola-Kröner [92]). All of these averaging schemes make different assumptions about how the material is modeled, but they all start

[2]Cast Ni-based superalloys, be they single crystal, directionally solidified, or polycrystalline variants all exhibit relatively similar stiffness values when studied in a single crystal form. For instances where typical stiffness values are necessary, properties of Mar-M247 (Table 3.6) are appropriate.

off with the same definition for the isotropic bulk modulus (K):

$$K = \frac{C_{11} + 2C_{12}}{3} \ . \tag{2.32}$$

With half of the isotropic response defined, the various theories differ in their calculation of the isotropic shear modulus (G). The very first averaging scheme was devised by Voigt in 1928 (G_{Vo}) whereby:

$$G_{Vo} = \frac{2C' + 3C_{44}}{5}, \tag{2.33}$$

and with

$$C' = \frac{C_{11} - C_{12}}{2} \tag{2.34}$$

denoted herein as the tetragonal shear modulus. Voigt was followed soon after by Reuss in 1929 who devised G_{Re} as:

$$G_{Re} = \frac{5C'C_{44}}{3C' + 2C_{44}}. \tag{2.35}$$

Voigt and Reuss' first-order averaging schemes provide an upper and lower bound on G, respectively, but they do not take into account any statistical distribution of grain orientations, any grain interactions, or surface strains [93]. Instead their averaging schemes can be seen as analogous to Kirchhoff-rules for electrical resistivity. Where Voigt employs a serial connection of grains along alternating elastically stiff and elastically compliant directions with all grains in a state of uniform strain, while Reuss employs a parallel connection of grains under uniform stress [90, 93]. However, these upper and lower bounds diverge for materials with significant elastic anisotropy ($A > 2$) necessitating the use of higher-order averaging schemes.

A simple and commonly employed scheme devised by Hill [89] is to average the upper and lower bound values of G_{Vo} and G_{Re} to produce a Voigt-Reuss-Hill average shear modulus (G_{VRH}), which often agrees well with empirical values and is far simpler than self-consistent schemes. While extensive studies by Kuhn and Sockel [93–95] found that

for significantly anisotropic material like Ni, higher-order averaging schemes (e.g. [90–92]) be used. Finding the Gairola-Kröner average (G_{GK}) [92] to be superior, with a definition of:

$$G_{GK} = G_{Vo}\left[1 - \left(\frac{12}{125}\right)\frac{\eta\left(\frac{C_{44}-C'}{G_{Vo}}\right)^2}{1 - \left(\frac{2\eta}{25}\right)\left(\frac{C_{44}-C'}{G_{Vo}}\right) - \left(\frac{24\eta^2}{625}\right)\left(\frac{C_{44}-C'}{G_{Vo}}\right)^2}\right], \tag{2.36}$$

where $\eta = (3K + 6G_{Vo})/(3K + 4G_{Vo})$. At various times in this dissertation, the 3rd order Gairola-Kröner averaging scheme will be employed to calculate self-consistent elastic properties for modeling both cast polycrystalline material, as well as thin polycrystalline layers of recrystallized grains. Offering vastly simplified modeling procedures as compared to modeling discrete anisotropic grains, and with very comparable results.

2.1.4 Cubic Directionally Dependent Engineering Moduli

For linking C_{pq} values to the elastic response of a single-crystal casting, and later to facilitate comparisons to isotropic moduli, it is useful to define a set of engineering moduli that describe the directionally-dependent elastic response with respect to the casting's crystallographic reference frame. Single crystal Ni-base superalloy castings are typically solidified along the <001> crystallographic direction since growth is preferred on the {100} family of planes, and the low modulus along this direction is favorable for strain-controlled fatigue [80]. For linking C_{pq} values to the elastic response of a single-crystal casting, and later to facilitate comparisons to isotropic moduli, it is useful to define a set of engineering moduli that describe the directionally-dependent elastic response with respect to the casting's crystallographic reference frame. The directionally-dependent Young's modulus ($E_{[hkl]}$) relates normal stresses to normal strains as applied parallel to a crystallographic direction $[hkl]$. This constitutive behavior is in the same form as

(Equation (2.15)), except C_{ijkl} is replaced by $E_{[hkl]}$, with the definition:

$$E_{[hkl]} = \frac{C_{44}(C_{11} - C_{12})(C_{11} + 2C_{12})}{C_{44}(C_{11} + C_{12}) + (C_{11} + 2C_{12})\alpha J_{hkl}}. \tag{2.37}$$

The direction cosine (J_{hkl}) corresponds to the angle between the plane normal to the applied stress and the nearest <100> crystallographic direction; J_{hkl} is zero along <100>, maximum when $J_{111} = 1/3$, and median for $J_{110} = 1/4$. The anisotropy factor (α)—which should not be confused with the anisotropy ratio—is negative and goes to zero as the material becomes isotropic ($A \rightarrow 1$), defined as: $\alpha = C_{11} - C_{12} - 2C_{44}$ [96, 97]. From (Equation (2.37)) it is clear that $E_{[111]}$ is the highest directionally-dependent Young's modulus and $E_{[100]}$ is the minimum modulus [98].

The directionally-dependent shear modulus ($G_{(mno)[hkl]}$) is also useful to consider, where (mno) is the plane normal and $[hkl]$ is the direction of shear on (mno). $G_{(mno)[hkl]}$ has rotational symmetry on {100} and {111} planes allowing for the direction of shear to be expressed as an arbitrary perpendicular direction ($[\perp]$) contained in the plane. While loading on all other planes will exhibit $G_{(mno)[hkl]}$ that varies with the direction of shear. For $G_{\{100\}[\perp]}$ and $G_{\{111\}[\perp]}$ the directional shear modulus is given as:

$$G_{\{mno\}[\perp]} = \frac{C_{44}(C_{11} - C_{12})}{C_{11} - C_{12} - 2\alpha J_{mno}}. \tag{2.38}$$

with the maximum and near minimum values corresponding to the <100> and <111> crystallographic directions, respectively.

2.2 Governing Equations

Governing equations provide a mathematical model to represent physical phenomena governing the system at hand, and often consist of balance (or conservation) equations

that are ubiquitous in physics. From conservation of mass, to the balance of: energy, linear and angular momentum, electric charge, and magnetic flux, governing equations provide the principle structures upon which physics is based. And with the language of continuum mechanics, it is from these principles that the fields of acoustics and ultrasonics are ultimately derived. Even the time dependent behavior of a system, perturbed from an equilibrium condition, can be explained through these governing equations. With the most important equation governing acoustics and ultrasonics being the wave equation of motion, a second-order linear partial differential equation, defined in Section 2.2.1.

The discovery of the wave equation is discussed in the preceding chapter, while Section 2.2.1 focuses on how the wave equation is obtained from the initial balance of linear momentum using Newton's second law. Following this is an introductory discussion of how the forward problem is solved by formulating a Lagrangian equation that represents the total energy of the specimen as a sum of kinetic and potential energy terms, with a full treatment covered by Chapter 6. Finally, relationships between the wave equation and fundamental aspects of resonance are discussed.

2.2.1 The Wave Equation of Motion

The link between the elastic constitutive behavior of a material and its acoustic properties, from shear and compressional wave velocities to resonance characteristics, is through the wave equation of motion. Applying Newtons 2nd law of motion to a cubic volume (V), while assuming body forces and spatial variations of stress (σ_{ij}) are zero, the net force in the i direction can be written as:

$$\frac{\partial \sigma_{ij}}{\partial x_i} = \rho\left(\frac{\partial^2 u_i}{\partial t^2}\right), \tag{2.39}$$

where u_i is the ith Cartesian component of the displacement vector of each point in V, and ρ is the mass density. As such, these displacements are a function of both position (x)

and time (t) [34, 40]. Combining the infinitesimal strain tensor (Equation (2.18)), with Hooke's law in 3D (Equation (2.15)), and Newton's 2nd Law (Equation (2.39)) yields the differential wave equation describing the motion of elastic waves in the material as:

$$\frac{C_{ijkl}\,\partial^2 u_k}{\partial x_j \partial x_l} = \rho\left(\frac{\partial^2 u_i}{\partial t^2}\right). \tag{2.40}$$

Alternatively, Equation (2.40) is also written as:

$$\frac{\partial^2 u_k}{\partial x_i^2} = \frac{1}{c_0^2}\left(\frac{\partial^2 u_i}{\partial t^2}\right) \tag{2.41}$$

where c_0 represents the multiple independent wave velocities of the material, with as many wave velocities as there are elastic constants because $c_0 = f(C_{ijkl}, \rho)$. For isotropic materials there are two independent wave velocities, corresponding to shear and longitudinal waves, which are simply related to the isotropic moduli by:

$$c_T = \sqrt{\frac{G}{\rho}} \tag{2.42}$$

for shear waves and

$$c_L = \sqrt{\frac{K + \frac{4G}{3}}{\rho}} \tag{2.43}$$

for longitudinal waves [99]. Though the wave equation is applicable to far more than just isotropic materials, as all manifestations of wave motion from the 1D motion of strings, to the propagation of sound waves in anisotropic solids, to electromagnetic waves traveling through the vacuum of space are all described by it [100].

2.2.1.1 Solutions to the Wave Equation

Later in this dissertation, Section 6.3.1 provides a complete derivation of the forward problem in terms of the mechanical Lagrangian ($\mathscr{L}$). Herein, this section introduces

the basic form of $\mathscr{L}$, and discuss how the extrema of $\mathscr{L}$ correspond to the resonance frequencies and resonance modes sought by the forward problem. As such, the total energy of a specimen of volume V can be stated as the combination of the kinetic energy (KE) and potential energy (PE) of the specimen [33]:

$$\mathscr{L} = \int_V \big(KE - PE\big) dV \ . \tag{2.44}$$

Assuming simple harmonic motion with a time dependence of u_i given by $e^{i\omega t}$ [34], the PE of the specimen is given as:

$$PE \ = \ \frac{1}{2} C_{ijkl} \frac{\partial u_i}{\partial x_j} \frac{\partial u_k}{\partial x_l} \tag{2.45}$$

and the KE is given as:

$$KE \ = \ \frac{1}{2} \rho \omega^2 u_i^2, \tag{2.46}$$

with ω being the angular resonance frequencies and $f_R = \omega / 2\pi$.

Then using a variational approach pioneered by Holland and Demarest [12, 13], with the u_i allowed to vary arbitrarily in the volume V, the extrema of $\mathscr{L}$ are sought. With the Rayleigh-Ritz method applied to expand the displacements u_i in some basis such as:

$$u_i = \alpha_{i\lambda} \phi_\lambda \tag{2.47}$$

where λ is the function label, ϕ_λ are the Visscher basis functions, and $\alpha_{i\lambda}$ are the coefficients of the expansion [19,34]. The expansion of each of the three (x, y, z) components of u_i are made according to Equation (2.47), providing complete forms of Equations (2.45) and (2.46) which are then substituted into $\mathscr{L}$. The extrema are then determined by setting $\partial \mathscr{L} = 0$ and differentiating with respect to each of the expansion coefficients, results

in the generalized eigenvalue equation:

$$\omega^2 \boldsymbol{M} a = \boldsymbol{K} a \ . \tag{2.48}$$

In Equation (2.48), $\boldsymbol{M}$ is the mass matrix, $\boldsymbol{K}$ the stiffness matrix, and a the polynomial expansion coefficients, which can then be solved numerically for a set of N eigenvalues and eigenvectors that are the resonance frequencies and the resonance mode shapes, respectively, of the specimen described by $\mathscr{L}$ [34, 101].

2.2.1.2 Fundamentals of Mechanical Resonance

There are an infinite number of possible solutions to the wave equation (Equation (2.40)), any of which corresponds to a wave motion with velocity c_0 [100]. Of the infinite possible solutions to the wave equation, both standing and traveling wave solutions exist. With standing wave solutions representing the superposition of two identical waves that are traveling in opposite directions through the elastic body. In a simplified treatment of the underlying physics, each traveling wave can be said to exhibit a wavelength (λ) given as

$$\lambda = \frac{2\pi}{k} \ , \tag{2.49}$$

where k is the angular wave number [100]. Constructive interfere of these opposite-traveling waves in a specimen of finite dimensions (L) produce a standing wave with harmonic motion [41]. These standing wave solutions are a manifestation of the normal mode vibrations of the elastic body, i.e. the resonance modes of the specimen, with λ related to L by

$$L = \frac{n\lambda}{2}, \tag{2.50}$$

and n representing the resonance mode-order [102]. The resonance frequencies come from the fundamental relationship between c_0 of the opposite-traveling waves and λ as:

$$f_R = \frac{c_0}{\lambda}. \tag{2.51}$$

Thus demonstrating how the f_R of a specimen are linked to the wave speeds/elastic properties of the specimen through the fundamental properties of waves and the wave equation of motion.

2.3 Crystal Lattice Orientations

In materials science, the orientation of a crystal lattice is generally described by a set of rotations that are relative to a fixed external reference frame [103]. While Euler angles are probably the most commonly used, alternative parameterizations (e.g. rotation matrices, unit quaternions, Rodrigues-Frank vectors, homochoric vectors and cubochoric vectors) may be particularly useful depending on the context of the problem. This means that transformation between different parameterizations are also useful, just as a transformation of Cartesian coordinates to spherical coordinates can dramatically simplify the mathematics of a given problem. But before discussing specific parameterizations and transformations, it is necessary to first establish a series of conventions in order to eliminate ambiguity and to ensure that everything is handled properly. For anyone with experience in this area knows full well that there are many ways in which one can lose self-consistency by carelessly changing between conventions in a momentary lapse of attention. While replicating the results of others is very often a frustrating endeavor because of the various ways in which alternative conventions are implicitly (or inadvertently) used.

2.3.1 Conventions for Rotations

Ambiguity and disagreement can arise whenever conventions are not clearly delineated in the context of crystal lattice orientations. Therefore, no convention or assumption is considered trivial, particularly when implementing algorithms that require clear rules for every possible case, transition, or initial condition. The conventions listed below combines those established by a group of experienced materials scientists [103] with those provided to the author by colleague and collaborator W.C. Lenthe.

1. All Cartesian reference frames are assumed to be right-handed.

2. Counter clockwise rotations about an axes are taken to be positive when viewed from the end point of the axes to the origin.

3. Rotations will be interpreted as passive rotations, whereby a crystal reference frame rotated with respect to the specimen reference frame is brought into alignment by a passive rotation of the specimen reference frame to coincide with the crystal.

4. Euler angle triplets $\boldsymbol{\theta} = (\phi_1, \psi, \phi_2)$ utilize the Bunge convention with axis triplet zxz and corresponding rotation angles (ϕ_1, ψ, ϕ_2) with ranges $\phi_1 \in [0, 2\pi]$, $\psi \in [0, \pi]$, $\phi_2 \in [0, 2\pi]$

5. For axis-angle pairs $(\hat{\mathbf{n}}, \omega)$, the rotation angle ω about the axis $\hat{\mathbf{n}}$ is limited to the interval $[0, \pi]$.

6. Orientation matrices employ row major order.

7. Rotation axis $\hat{\mathbf{n}}$, rotated by π, is in the positive hemisphere.

8. Rotation axis $\hat{\mathbf{n}} = [0, 0, 1]$ for rotations of 0.

2.3.2 Definitions

2.3.2.1 Euler angles

Euler angles refer to any 3D rotation that is decomposed into three successive rotations around the xyz coordinate axes in which two of the three axis symbols are equal [103]. This means that there are six possible conventions (zxz, xzx, yzy, zyz, yxy, and xyx), with zxz—known as the Bunge convention—being one of the most common for materials science applications [103]. The Euler angle triplet $\boldsymbol{\theta} = (\phi_1, \psi, \phi_2)$ describes the successive rotations, applied from left to right, with the ranges for each angle specified in convention 4. Note that in accordance with convention 3 passive rotations are assumed, while an active rotation requires the rotations be applied with opposite sign and in opposite order: $(-\phi_2, -\psi, -\phi_1)$ [103].

2.3.2.2 Unit Quaternions

In the context of the inverse modeling framework developed in Chapter 6, the crystal orientation is parameterized as a passive unit quaternion ($q = [q_0, q_1, q_2, q_3]$), with components also referred to as (w, x, y, z) in the forms: [104]

$$\begin{aligned} q &= q_0 + iq_1 + jq_2 + kq_3 \\ &= [q_0, q_1, q_2, q_3] \\ &= [q_0, \mathbf{q}] \end{aligned} \tag{2.52}$$

Each q consists of two parts, a positive scalar q_0 and a unit vector axis $\hat{\boldsymbol{n}} = (q_1,\ q_2,\ q_3) = \mathbf{q}$, which together represent a point on the upper half of a unit sphere [105]. q_0 describes the rotation about $\hat{\mathbf{n}}$ by ω according to $q_0 = cos(\omega/2)$, while $\hat{\mathbf{n}}$ can be extracted from

$q = \hat{\mathbf{n}} sin(\omega/2)$ [105]. Therefore, the unit quaternion can always be expressed in the form:

$$q = cos\left(\frac{\omega}{2}\right) + sin\left(\frac{\omega}{2}\right)\left(c_1 i + c_2 j + c_3 k\right), \tag{2.53}$$

where c_i represent the direction cosines of $\hat{\mathbf{n}}$ [103]. The imaginary units (i, j, k) obey the following relations:

$$\begin{aligned} i^2 = j^2 = k^2 = -1 \\ ij = -ji = k \\ jk = -kj = i \\ ki = -ik = j \ , \end{aligned} \tag{2.54}$$

making quaternion multiplication non-commutative (i.e. $pq \neq qp$) [103]. Instead,

$$\begin{aligned} pq &= \left[p_0 q_0 - \mathbf{p}\cdot\mathbf{q},\ q_0\mathbf{p} + p_0\mathbf{q} + \mathbf{p}\times\mathbf{q}\right] \\ &= \left[p_0 q_0 - p_r q_r,\ q_0 p_i + p_0 q_i + \epsilon_{ijk} p_j q_k\right], \end{aligned} \tag{2.55}$$

where ϵ_{ijk} represents the permutation symbol with a value of +1 for even and −1 for odd permutations [103]. The norm of a quaternion is defined as:

$$|q| = \left[q_0^2 + q_1^2 + q_2^2 + q_3^2\right]^{1/2}. \tag{2.56}$$

2.3.2.3 Neo-Eulerian Vector Representations

Homochoric and Rodrigues-Frank vectors are two neo-Eulerian representations which take the form: $\hat{\boldsymbol{n}} f(\omega)$, with $\hat{\boldsymbol{n}}$ being a unit vector axis and f a monotonic function of the rotation angle ω [103]. The Rodrigues-Frank vector ($\boldsymbol{\rho}$) is obtained by setting

$f(\omega) = tan(\omega/2)$ for:

$$\boldsymbol{\rho} = \hat{\boldsymbol{n}}\ tan\left(\frac{\omega}{2}\right). \tag{2.57}$$

All rotations about the axis $\hat{\boldsymbol{n}}$ by ω over the interval $[0, \pi]$ are represented by points along a half-line formed by the unit vector [103]. For ω over the interval $[\pi, 2\pi]$, an equivalent rotation can be represented by setting $\hat{\boldsymbol{n}}$ equal to $-\hat{\boldsymbol{n}}$ and using the angle $2\pi - \omega$, while rotations of $\omega = \pi$ is represented by a point along the line at $+\infty$ [103].

The homochoric vector ($\boldsymbol{h} = [h_1, h_2, h_3]$) is a generalization of the Lambert equal-area mapping of a 2D sphere onto a 2D disk, providing an equal-volume mapping the 3D unit quaternion Northern hemisphere onto a 3D ball of radius $(3\pi/4)^{1/3}$ ensuring the volume of the ball ($V_{\boldsymbol{h}} = \pi^2$) is equal to the surface area of the hemisphere [103, 104]. For $\boldsymbol{h}$ the monotonic function f is

$$f(\omega) = \left[\frac{3}{4}\left(\omega - sin(\omega)\right)\right]^{1/3} \quad \text{for} \quad \omega \in [0, \pi] \tag{2.58}$$

and

$$f(\omega) = \left[\frac{3}{4}\left(2\pi - \omega - sin(\omega)\right)\right]^{1/3} \quad \text{for} \quad \omega \in]\pi, 2\pi[\ , \tag{2.59}$$

giving the homochoric vector a definition of [103]:

$$\boldsymbol{h} = \hat{\boldsymbol{n}}\left[\frac{3}{4}\left(\omega - sin(\omega)\right)\right]^{1/3}. \tag{2.60}$$

2.3.2.4 Cubochoric Representation

The cubochoric vector ($\boldsymbol{\kappa} = [\kappa_1, \kappa_2, \kappa_3]$) is derived from the homochoric vector ($\boldsymbol{h}$) via an equal-volume transformation from the homochoric ball ($V_{\boldsymbol{h}} = \pi^2$) to the cubochoric cube of edge length $\pi^{2/3}$ [104]. The ω dependence of $\boldsymbol{\kappa}$ is not of the simple form $\hat{\boldsymbol{n}} f(\omega)$, which is why it is not included a with the neo-Eulerian representations in the previous section [104]. Though an important feature of the homochoric and cubochoric repre-

sentations is that they are equal-volume representations of the unit quaternion hemisphere [104]. This feature ensures that random samples drawn from a homochoric or cubochoric space will uniformly sample that space [103, 104], and was important for stabilizing the Hamiltonian Monte Carlo (HMC) sampler employed by the IMF in Chapter 7. First, mapping the quaternion orientations of the code described in Chapter 6 onto an equal-volume homochoric ball created a uniform grid over the entire ball. Then transforming the homochoric vector to a cubochoric vector as described in the following section, the uniform grid over the homochoric ball was transformed into a uniform grid over the cubochoric cube. Not only does this equal-volume mapping provide readily refinable grids for sampling, the cubochoric representation is particularly well suited for implementation in modern computer programming with 2D and 3D arrays [106].

2.3.3 Coordinate Transformations

Direct analytical transformations between rotation representations exist for some—but not all—cases [103]. Though with indirect transformations and the occasional approximation, it is possible to transform between the various representations while maintaining numerical precision that is sufficient for most applications, including the applications of this dissertation. Herein a subset of the transformations most applicable to this work are provided, while Rowenhorst et al. provide [103] a complete set of instructions for transforming between: Euler angles, rotation matrices, axis-angle pairs, Rodriguez-Frank vectors, unit quaternions, Homochoric vectors, and cubochoric vectors. Most of the inverse modeling work utilizes the quaternion representation because of its superior stability and speed when implemented programmatically.

2.3.3.1 Euler Angle to Unit Quaternion: $\boldsymbol{\theta} = (\phi_1, \psi, \phi_2) \Rightarrow q = [q_0, q_1, q_2, q_3]$

With the Euler angles in radians, the following variables are defined:

$$\lambda = \frac{1}{2}\left(\phi_1 + \phi_2\right) ; \qquad \delta = \frac{1}{2}\left(\phi_1 - \phi_2\right) ; \qquad c = cos\left(\frac{\psi}{2}\right) ; \qquad s = sin\left(\frac{\psi}{2}\right) . \tag{2.61}$$

Giving the unit quaternion as:

$$q = \left[c\,cos(\lambda),\ -s\,cos(\delta),\ -s\,sin(\delta),\ -c\,sin(\lambda)\right] , \tag{2.62}$$

with the sign of the entire quaternion reversed if q_0 becomes negative to ensure the result lies in the Northern hemisphere of the unit quaternion sphere [103].

2.3.3.2 Unit Quaternion to Euler Angle: $q = [q_0, q_1, q_2, q_3] \ \Rightarrow \ \boldsymbol{\theta} = (\phi_1, \psi, \phi_2)$

Given a unit quaternion q, the following variables are defined:

$$q_{03} = q_0^2 + q_3^2 ; \qquad q_{12} = q_1^2 + q_2^2 ; \qquad \xi = \sqrt{q_{03}\ q_{12}} . \tag{2.63}$$

Then the Euler angles $\boldsymbol{\theta}$ are given by:

$$\boldsymbol{\theta} = \left(\alpha\left[-2q_0q_3,\ q_0^2 - q_3^2\right],\ 0,\ 0\right) \qquad \text{when} \ \ \xi = q_{12} = 0$$

$$\boldsymbol{\theta} = \left(\alpha\left[2q_1q_2,\ q_1^2 - q_2^2\right],\ 0,\ 0\right) \qquad \text{when} \ \ \xi = q_{03} = 0 \tag{2.64}$$

$$\boldsymbol{\theta} = \left(\alpha\left[\frac{q_1q_3 - q_0q_2}{\xi},\ -\frac{q_0q_1 - q_2q_3}{\xi}\right],\ \alpha\left[2\xi,\ q_{03} - q_{12}\right], \alpha\left[\frac{q_0q_2 + q_1q_3}{\xi},\ \frac{q_2q_3 - q_0q_1}{\xi}\right]\right) \tag{2.65}$$

$$\text{when} \ \ \xi \neq 0$$

with $\alpha(y, x)$ being the standard two-argument implementation of the $arctan(y/x)$ function.

2.3.3.3 Unit Quaternion to Homochoric Vector:

$$q = [q_0, q_1, q_2, q_3] \;\Rightarrow\; \boldsymbol{h} = [h_1, h_2, h_3]$$

Given a unit quaternion q, compute the following:

$$\omega = 2arccos(q_0) \;; \qquad b = \frac{1}{\sqrt{q_1^2 + q_2^2 + q_3^2}} \;; \qquad f = \frac{3}{4}\Big[\omega - sin(\omega)\Big] \;. \tag{2.66}$$

If $\omega = 0$, then $\boldsymbol{h} = 0$. Otherwise $\hat{\boldsymbol{n}} = [q_1, q_2, q_3]$, with $\boldsymbol{h}$ given as:

$$\boldsymbol{h} = b\hat{\boldsymbol{n}}f^{1/3} = \Bigg[bq_1, bq_2, bq_3\Bigg]\Bigg[\frac{3}{4}\Big(\omega - sin(\omega)\Big)\Bigg]^{1/3} \;. \tag{2.67}$$

2.3.4 Rotated Stiffness Tensors

The effective elastic constants (C'_{ijkl}, or C'_{pq} in Voigt notation) of any specimen with anisotropic elastic properties are a function of the intrinsic elastic properties (C_{ijkl}, or C_{pq} in Voigt notation) and the orientation of the crystal lattice with respect to the specimen axes. While the primary focus of this dissertation involves elastically anisotropic single crystals of cubic symmetry, textured polycrystalline materials and composites can also exhibit a range of elastic symmetries from cubic to triclinic. The Regardless of the material, anytime anisotropic elasticity is involved with ultrasonic methods, the orientation of the elastic body must be properly considered. This is accomplished by applying rotations to C_{ijkl}/C_{pq} equivalent to the misorientation angle between the specimen and crystal axes using the following procedure.

The rotation from the specimen axes to the crystal axes is represented as a passive unit quaternion $q = [q_0, q_1, q_2, q_3]$, with components referred to as $[w, x, y, z]$. These

components are used to construct a rotation matrix (R) with the following definition:

$$R = \begin{bmatrix} w^2 + x^2 - y^2 - z^2 & 2(xy - wz) & 2(xz + wy) \\ 2(yx + wz) & w^2 - x^2 + y^2 - z^2 & 2(yz - wx) \\ 2(zx - wy) & 2(zy + wx) & w^2 - x^2 - y^2 + z^2 \end{bmatrix} . \tag{2.68}$$

The rotations are applied and the effective elastic constants of the specimen C'_{ijkl} come from:

$$C'_{ijkl} = R_{ip} R_{jq} C_{pqrs} R_{kr} R_{ls} \ , \tag{2.69}$$

with Voigt mapping from C'_{ijkl} to C'_{pq} defined by Equation (2.22).

Applying rotations to a stiffness tensor, which is equivalent to fabricating a parallelepiped specimen with a misaligned crystal-specimen reference frame, has important implications for the RUS inversion efforts. These implications can best be explained with the aid of a few examples. First consider a notional cubic symmetry material (Equation (2.29)) with elastic properties similar to those of a Ni-based superalloy. The cubic symmetry allows for the intrinsic elastic behavior to be described with three independent stiffness values: $C_{11} = 250$ GPa, $C_{12} = 150$ GPa, $C_{44} = 140$ GPa, giving the full Voigt stiffness tensor as:

$$C_{pq} = \begin{bmatrix} 250.0 & 150.0 & 150.0 & 0.0 & 0.0 & 0.0 \\ 150.0 & 250.0 & 150.0 & 0.0 & 0.0 & 0.0 \\ 150.0 & 150.0 & 250.0 & 0.0 & 0.0 & 0.0 \\ 0.0 & 0.0 & 0.0 & 140.0 & 0.0 & 0.0 \\ 0.0 & 0.0 & 0.0 & 0.0 & 140.0 & 0.0 \\ 0.0 & 0.0 & 0.0 & 0.0 & 0.0 & 140.0 \end{bmatrix} . \tag{2.70}$$

Now assume a crystal reference frame that is rotated with respect to the specimen reference frame by an Euler angle triplet of $\boldsymbol{\theta} = (10.0, 0.0, 0.0)$ degrees. The equivalent

quaternion representation is $q = (0.996195, 0.0, 0.0, -0.087156)$, which is still only 3 rotational DOF because Equation (2.57). The effective stiffness tensor (C'_{pq}) of this specimen would be:

$$C'_{pq} = \begin{bmatrix} 260.5 & 139.5 & 150.0 & 0.0 & 0.0 & 28.93 \\ 139.5 & 260.5 & 150.0 & 0.0 & 0.0 & -28.93 \\ 150.0 & 150.0 & 250.0 & 0.0 & 0.0 & 0.0 \\ 0.0 & 0.0 & 0.0 & 140.0 & 0.0 & 0.0 \\ 0.0 & 0.0 & 0.0 & 0.0 & 140.0 & 0.0 \\ 28.93 & -28.93 & 0.0 & 0.0 & 0.0 & 129.5 \end{bmatrix} \tag{2.71}$$

The first implication of this rotation is that C'_{pq} has non-zero values of C'_{16} and C'_{26}, and one of each of the three repeated C_{pq} elastic constants are no longer equal (e.g. $C'_{44} = C'_{55} \neq C'_{66}$). If this specimen was measured via RUS and the cubic elastic properties were sought through inversion without simultaneously estimating the orientation, the inversion would have considerable difficulty finding a sufficient solution. With the best values capable of being returned by this inversion likely to be the average of the component values from Equation (2.71), e.g.:

$$\begin{aligned} C_{11} &= (C'_{11} + C'_{22} + C'_{33})/3 &&= 257.0\ GPa\ , \\ C_{12} &= (C'_{12} + C'_{13} + C'_{23})/3 &&= 146.5\ GPa\ , \\ C_{44} &= (C'_{44} + C'_{55} + C'_{66})/3 &&= 136.5\ GPa\ . \end{aligned} \tag{2.72}$$

Clearly these average values are biased by the misaligned specimen-crystal reference frame, but it is conceivable that an inversion would not be completely confounded by a misaligned crystal-specimen reference frame when $\boldsymbol{\theta} = (10.0, 0.0, 0.0)$ degrees.

Next assume the misalignment between the specimen and the crystal axes is increased to $\boldsymbol{\theta} = (10.0, 20.0, 30.0)$ degrees, and the measured resonances frequencies of this specimen

were used for an inversion. The C'_{pq} of this specimen would be:

$$C'_{pq} = \begin{bmatrix} 340.7 & 72.0 & 137.3 & 18.9 & 8.2 & 22.4 \\ 72.0 & 352.6 & 125.3 & 20.5 & 13.1 & -5.7 \\ 137.3 & 125.3 & 287.3 & -39.3 & -21.3 & -16.6 \\ 18.9 & 20.5 & -39.3 & 115.4 & -16.7 & 13.1 \\ 8.2 & 13.1 & -21.3 & -16.7 & 127.3 & 18.9 \\ 22.4 & -5.7 & -16.6 & 13.1 & 18.9 & 62.0 \end{bmatrix} \tag{2.73}$$

where all of the 21 matrix values are now non-zero, and many values vary greatly from Equation (2.70). If no orientation inversion capability were available, then the full triclinic (21 DOF) stiffness tensor would need to be estimated in order to characterize the 6 DOF specimen (with 3 elastic and 3 orientation DOF). Clearly, lacking an ability to deconvolve the effect of orientation from the intrinsic stiffness values of the specimen results in an incredibly more difficult inversion problem. For the volume of possible parameter space grows by the parameter range (R) to the power of the DOF, i.e. the volume $R^6 \ll R^{21}$. While attempting to estimate just three cubic stiffness values from a specimen exhibiting the effective stiffness values of Equation (2.73) would most surely fail, or return nonsensical results. Further complicating the RUS inversion problem is the fact that the frequency order of the resonance modes of a specimen with effective properties like Equation (2.73) would differ greatly from the frequency order of a specimen with an aligned crystal-specimen reference frame. Take for example an optimization-based inversion which requires "quality initial guess values", as introduced in Section 1.2.2.2. If referenced values from the literature suggest properties similar to those of the aligned specimen, even an optimization capable of estimating a full triclinic stiffness matrix would likely fail to reach the values of Equation (2.73).

Chapter 3

Experimental Overview: Equipment, Methods, and Materials

Chapter Abstract

Starting with a discussion of experimental materials and procedures by chapter, discussions cover basic details about the alloys, heat treatment conditions, specimen design, and ancillary procedures useful for reproduction. This detail of specific materials and procedures is followed by background information about the Ni-based superalloy Mar-M247—which is used extensively for experimental validation of forward models developed in Chapters 4 and 5—with discussions including material properties for modeling. Next, the RUS measurement setup is discussed, with measurement considerations for small and large specimens, and details about the individual components of the setup. Followed by sections detailing the procedures of iterative creep testing and iterative ultrasonic fatigue testing. Altogether, this chapter is intended as a primer to the main body chapters (Chapters 4 to 7), while also supplying details about specific experimental procedures and materials conditions that are not provided elsewhere.

3.1 Experimental Materials and Procedures

The work of this dissertation can be summarized as an effort towards materials characterization and NDE of damage, with a focus on structural metal alloys of technical significance to the aerospace industry. Though it should be noted that the methods, techniques, and procedures developed as part of the FMF work discussed in Chapters 4 and 5, as well as the IMF work as discussed in Chapters 6 and 7, require trivial—if any—modifications when substituting one alloy for another. In fact, broad applicability was a major goal of this dissertation work. As such, the main body chapters (Chapters 4 to 7) focused more on the development, validation, and implementation of modeling frameworks; while only providing basic details and background information about the specific materials and specimens used. Thus, the following sections provide some of the ancillary details and background information necessary for reproducing the experimental work, and guiding future studies. With a particular focus on: the condition of as-received and as-tested materials, the machining and design of test specimens, and the experimental methods not addressed by the main body chapters.

3.1.1 Chapter 4

Starting with the work covered in Chapter 4, both fatigue and creep damage were investigated in an effort towards extending the NDE of mechanical damage capability of RUS through the development of a FMF. Experimental work for model validation was conducted using the investment cast polycrystalline superalloy Mar-M247, with considerable details about this material provided in Section 3.2, including micrographs of the investment cast microstructure, as-received heat treatment conditions, and elastic properties for modeling. The investment cast bars of Mar-M247 were machined into a dual-purpose dog-bone geometry according to Figure 3.11, allowing the specimen to be ultrasonically

fatigued or crept.

RUS measurements were conducted on two dog-bone specimens prior to any iterative creep or fatigue tests, to first establish the baseline response of the as-received dog-bones. Then one dog-bone was iteratively crept, and the other iteratively fatigued, each for six iterations. Accumulating damage over each cycle, RUS measurements were collected from the unloaded dog-bone specimens between each iteration. The six iterative creep tests were conducted to a total strain of 8.81%, as summarized in Table 4.2. While the iterative fatigue tests summarized in Table 4.1 lasted a total of 12.3 million cycles before the dog-bone was deemed to have failed. Ultimately, the mode-specific changes in resonance frequency ($\triangle f_R$, Equation (1.2)) as a function of damage were determined, and the results for the lowest-frequency modes plotted in Figures 4.6 and 4.8. Further details about creep in Ni-based superalloys are discussed in Section 4.1.1, while the procedures for conducting iterative creep tests are given in Section 3.4. Fatigue in Ni-based superalloys is discussed in Section 4.1.2, while the capabilities of the ultrasonic fatigue setup and procedures for iterative fatigue testing are covered in Section 3.5.

In addition to the solution and aging heat treatments applied to the as-received Mar-M247 material summarized in Table 3.5, a second isothermal "pre-treatment" was applied to the dog-bone specimen prior to the iterative creep experiments. The rationale for this 13 hour 1080 °C pre-treatment in air was two-fold. First, the original heat treatments were conducted prior to machining the dog-bone specimen, so the pre-treatment should relieve residual stresses imparted to the specimen during the machining process. Second, the pre-treatment was conducted in air such that the surface developed a thin, mostly adherent, oxide layer. Both of these phenomena, oxidation and residual stress relaxation, were expected to have minor implications for the resonance characteristics of the specimen as compared to the shape change associated with creep. But in an attempt to isolate these effects, and gain understanding about the relative impact of these mechanisms on resonance, the specimen was measured via RUS before and after the isothermal pre-

treatment, as well as after each creep iteration.

3.1.2 Chapter 5

Chapter 5 looks at the problem of recrystallization and grain structure defects in single crystals of Ni-based superalloys. This work is broadly applicable to any Ni-based superalloy, as demonstrated through a companion study by Rettberg et al. [57] on single crystal dog-bones of Ni-based superalloy René N5. In fact, a wide range of single crystal materials would be prime candidates for RUS detection of recrystallization and grain structure defects, as detectability ultimately comes down to the elastic anisotropy (A defined in Equation (2.31)) of the single crystal material. As the data in Table 2.2 suggest, many technically relevant metals exhibit A values near or in excess of that exhibited by Ni with an A_{Ni} = 2.57; e.g. Cu exhibits an A_{Cu} = 3.21, while Fe has an A_{Fe} = 2.41. In fact, the only cubic symmetry metal with an A that would limit detectability is that of Al with an A_{Al} = 1.22. Ultimately, the recrystallization work covered by this dissertation employed the familiar Mar-M247 material in the solution treated and aged condition as discussed in Section 3.2, except now the material is in a single crystal form.

The specimen design for experimental validation of the surface recrystallization models started with a 3.00 in long 0.5 in diameter bar of single crystal bar of Mar-M247, machined according to Figure 3.10. This bar was then shot peened to induce plastic deformation uniformly over the surface of the bar, with the peening treatment provided by GE Power & Water courtesy of Jesse Keller, Art Peck, and Jon Schaeffer. The peening gas pressure was twice that of a "typical surface treatment" applied to Ni-based superalloys prior to coating treatments. Producing an 11 mil Almen strip deflection, the peening pressure was chosen with the intention of imparting a sufficient amount of deformation such that recrystallization would be likely to occur on subsequent heat treatments. Fixturing allowed for complete circumferential coverage during shot peening, as Figure 3.1

shows, however less than one-half inch of material at the top and bottom of the bar was not peened. Therefore, one-half of one inch was removed from both ends of the 3.00 in long bar, using a wire EDM (electrical discharge machining). Next, the 2.00 in long bar with a uniform peening treatment applied to the circumferential surface was sectioned longitudinally, again via EDM, into four equivalent "pie pieces" which are henceforth referred to as quarter-cylinder specimens.

Figure 3.1: Photo of shot-peened 3.00 in long, 0.5 in diameter bar specimen, showing the peened surface of the bar prior to removal of the unpeened ends.

Two of the quarter-cylinder specimens were then iteratively heat treated in air, one at 1150 °C and the other at 1225 °C, by charging them into the hot zone of a pre-heated tube furnace. Heat treatment times were for 2, 5, 10, 20, 80, 160, and 320 minutes, followed by air cooling to room temperature between each iteration. RUS measurements were conducted on the room temperature quarter cylinder specimens after each heat treatment, with the $\triangle f_R$ tracked across the iterative heat treatments. The 1225 °C $\triangle f_R$ results are plotted in Figure 5.4 and the 1150 °C $\triangle f_R$ results are plotted in Figure 5.12, both exhibiting a characteristics saw-tooth pattern which the FMF demonstrates is a result of surface recrystallization of the Mar-M247 single crystal quarter-cylinder specimens.

3.1.3 Chapter 6

Chapter 6 employs two different alloys for experimental validation of the IMF, which performs Bayesian inference for estimating elastic properties of materials using RUS measured resonance frequencies. The first alloy is Ti-6Al-4V, or Ti-64 for short, which is the most widely used Ti alloy [107], with particular importance to the aerospace

Table 3.1: Nominal composition (wt%) of the fine grained texture free Ti-64 alloy [110].

Al	**V**	**Fe**	**O**	**Si**	**Ti**
6.3	4.1	0.18	0.18	0.03	Bal

Table 3.2: Composition (wt%) of single crystal superalloy CMSX-4 according to [80].

Cr	**Co**	**Mo**	**W**	**Al**	**Ti**	**Ta**	**Re**	**Hf**	**Ni**
6.5	9.6	0.6	6.4	5.6	1.0	6.5	3.0	0.1	Bal

industry [107, 108]. The utility of Ti-64 for aerospace applications is largely a result of its low density, which affords the material superior specific strength and stiffness at room temperature as compared to other structural metals such as steel or Ni-based superalloys [109]. While some Ti alloys are even employed at moderately elevated temperatures ranging from 370–595 °C [109], depending on the alloy. The Ti-64 material used in this dissertation was provided courtesy of Lee Semiatin of the Air Force Research Lab, Wright-Patterson Air Force Base, OH. The Ti-64 has a chemical composition as specified by Table 3.1, and was specially forged (uniaxial upset "abc forged") to produce a sub-micron, texture free, grain structure [110]. This processing assured the material would exhibit an isotropic elastic symmetry, which was independently verified by the inversion results presented in Table 6.1. In preparation for conducting the RUS measurements, the Ti-64 material was cut into rectangular parallelepiped geometries, as required by the IMF code, with parallelepiped dimensions and fabrication details provided in Section 6.2.1. For further details about the forging and prior processing of the as-received Ti-64 material, readers are directed to the publication by Zherebtsov et al. [110].

The second alloy used in Chapter 6 was a common second-generation single crystal Ni-based superalloy, CMSX-4. This material has been studied for decades, since it was first developed by the Cannon-Muskegon Corporation of Muskegon, Michigan [111]. As the literature provides a wealth of information from its development [111], to its creep [112]

and recrystallization behavior [113], to its single crystal elastic properties [98], only a cursory description will be provided here. CMSX-4 is classified as a second-generation single crystal superalloy, along with PWA1484 and René N5, because they each contain approximately 3 wt. % of the element Re [80]. These Re-containing alloys followed first-generation single crystal alloys, which primarily benefited from the reduction of grain boundary strengthening elements of C and B that limited homogenization heat treatments because of their susceptibility for incipient melting [80, 114]. Re further benefited the second-generation alloys by slowing the coarsening kinetics of the strengthening γ' phase, while also affording a negative $\gamma - \gamma'$ misfit at elevated temperatures to facilitate rafting and improve creep resistance [115]. The CMSX-4 material used in this dissertation was not provided with a chemical certification, though Table 3.2 provides the nominal alloy composition [80]. Then, as with the Ti-64 material, the CMSX-4 material was cut into a rectangular parallelepiped specimen, with dimensions and fabrication details provided in Section 6.2.1. Notably, this parallelepiped specimen of single crystal CMSX-4 was cut from the parent single crystal without regard for the crystallographic orientation of the specimen—which dramatically simplifies the specimen preparation procedures. This was only possible because of novel functionality of the IMF code, capable of simultaneously estimating the misorientation between the specimen axes and the crystallographic axes, as well as the intrinsic single crystal elastic constants of the material. Finally, this novel functionality is validated with XRD (x-ray diffraction) measurements of the crystal orientation, demonstrating very good agreement between the measured and inverted orientation parameters.

3.1.4 Chapter 7

Elastic properties of novel Co and CoNi-based alloys were characterized in Chapter 7 using a more advanced version of the IMF detailed by Chapter 6. Stemming from a

discovery by Sato et al. in 2006 of a stable $\gamma - \gamma'$ two-phase field in the Co-Al-W ternary system [116], with morphologically identical microstructure to Ni-based $\gamma - \gamma'$ superalloys [117]. A class of Co-based quaternary alloys were soon developed from the Co-9.2Al-9W at% ternary composition [117], herein referred to as Co-Ternary, with elemental additions of Re, Ta, Ti, Mo/V, Ni, and Cr investigated for the myriad reasons discussed in Section 7.2.1. A vast majority of these novel Co-based quaternary alloys were soon shown to exhibit the characteristic superalloy microstructure, with a γ FCC solid solution matrix surrounding coherent cuboidal γ' precipitates with an ordered FCC ($L1_2$) crystal structure [117]. This spurred considerable research efforts [118–121] directed towards understanding the high temperature mechanical properties of these Co-based quaternary alloys, as well as a second series of CoNi-based alloys with approximately 30 at% Ni added for an expanded range of γ' stability. The focus of these initial investigations was to understand the creep and high temperature deformation characteristics of these novel Co and CoNi-based alloys [118–121]; though the elastic properties were not studied in any specific detail. Thus, using material leftover from these earlier investigations, with compositions and alloy names summarized in Table 7.1, the current research effort of this dissertation sought to apply the IMF developed in Chapter 6 to accurately characterize the single crystal elastic properties of these novel Co and CoNi-based superalloys.

In preparation for RUS measurements, two rectangular parallelepiped specimens were machined from each of the 9 parent single crystal alloy castings listed in Table 7.1 via wire EDM. All parallelepiped specimens were approximately the same dimensions at $9 \times 10 \times 11$ mm, though the exact dimensions of each specimen varied slightly as a result of removal of the EDM damage layer by hand grinding with 800 grit sandpaper. This $9 \times 10 \times 11$ mm rectangular parallelepiped geometry was intentionally chosen to provide specimens with a compact shape (i.e. low aspect ratio) with side lengths that were not integer or half-integer multiples of each other. Together these strategies help ensure that the lowest-frequency modes exhibit a variety of deflection characteristics (shear, bending,

Table 3.3: Heat treatment schedules for the various Co, Ni, and CoNi-based alloys investigated in Chapter 7.

Alloy	Solution Treatment	Age Treatment
CMSX-4	1277 °C, 4 h → 1287 °C, 2 h → 1296 °C, 3 h → 1304 °C, 2 h → 1313 °C, 2 h → 1316 °C, 2 h → 1318 °C, 2 h	1140 °C, 6 h → 871 °C, 20 h
Co-Ternary	1350 °C, 12 h	950 °C, 100 h
Co-2Ta	1350 °C, 12 h	1000 °C, 100 h
Co-6Ti	1225 °C, 14 h	1000 °C, 100 h
CoNi-based	1215 °C, 12 h	950 °C, 100 h

extensional, etc.) that will be sensitive to the different elastic moduli of the material. While also decreasing the likelihood of degenerate or nearly-degenerate modes that occur when the specimen geometry or elastic properties exhibit high degrees of symmetry.

Next the as-received material was solution heat treated and fully aged according to the treatment schedules outlined in Table 3.3. The solution heat treatment schedules for the novel alloys were devised based on solidus and solvus temperatures, which were previously measured, and conducted using a vacuum furnace with a Ti getter for a minimum of 12 hours in order to homogenize the as-cast microstructures. After the homogenization treatment was complete, the alloys were furnace cooled except for the Ni-based superalloy CMSX-4 material—included for comparison purposes—which was furnace quenched with gettered Ar according to industry standards [122]. Next, all of the alloys were individually sealed under vacuum in quartz tubes and aged in a box furnace for times ranging from 20–100 hours, allowing the γ' precipitates to grow to an optimal size. As the micrographs of Figure 7.1 demonstrate, consistent microstructures were achieved across the three (Ni, Co, and CoNi-based) alloy classes, with this filly-aged

condition being the as-characterized condition. In addition to reporting the results of the best inferences of elastic parameters for the two parallelepiped specimens of each alloy in the fully aged condition in Table 7.3, parallelepipeds of Co-6Ti, CoNi-A, and CMSX-4—constituting one alloy from each class—were also evaluated in the solution heat treated condition, with those results summarized in Table 7.4.

3.2 Background on Superalloy Mar-M247

The origin of the research effort covered by this dissertation grew from earlier investigations of first-stage turbine blades from Pratt and Whitney JT8D turbofan engines. As these turbine blades were investment cast from Ni-based superalloy Mar-M247, it was decided that Mar-M247 would be the primary material for experimental validation of the forward models. Therefore, this section provides a brief introduction to the Ni-based superalloy Mar-M247, with some introductory information that pertains to superalloys in general.

Ni-based superalloys like Mar-M247 maintain remarkable mechanical properties at high fractions of their melting temperature, even exhibiting an anomalous increase in yield strength between 500–900 °C [80, 123]. This high temperature strength, along with intrinsically high toughness, thermal stability, and reasonable oxidation resistance, all describe the properties which make this material well suited for use in the hot sections of land-based or aerospace turbine engines [124]. Finding broad use as a material for structural components such as combustors, blades, and disks; these materials are often coupled with coatings for improved resistance to oxidation and high temperatures [80, 124].

Mar-M247 is precipitate strengthened and comprised primarily of two cubic phases, the FCC matrix phase is referred to as γ and the $L1_2$ precipitate phase is γ'. The γ' precipitates often exhibit a cuboidal shape as a result of the relatively small lattice

misfit between the γ and γ' phases and the coherent boundary between them. Mar-M247, along with other Ni-based superalloys developed prior to single crystal alloys, also exhibits irregular and rosette eutectic γ' morphologies as the SEM micrographs in Figure 3.2 show. Together these various γ' morphologies comprise 50 to 70 % of the volume fraction of the alloy; though the particular volume fraction often depends on the alloy chemistry—i.e. the amount of γ'-forming elements Al, Ti, and Ta—as well as the heat treatment condition [80].

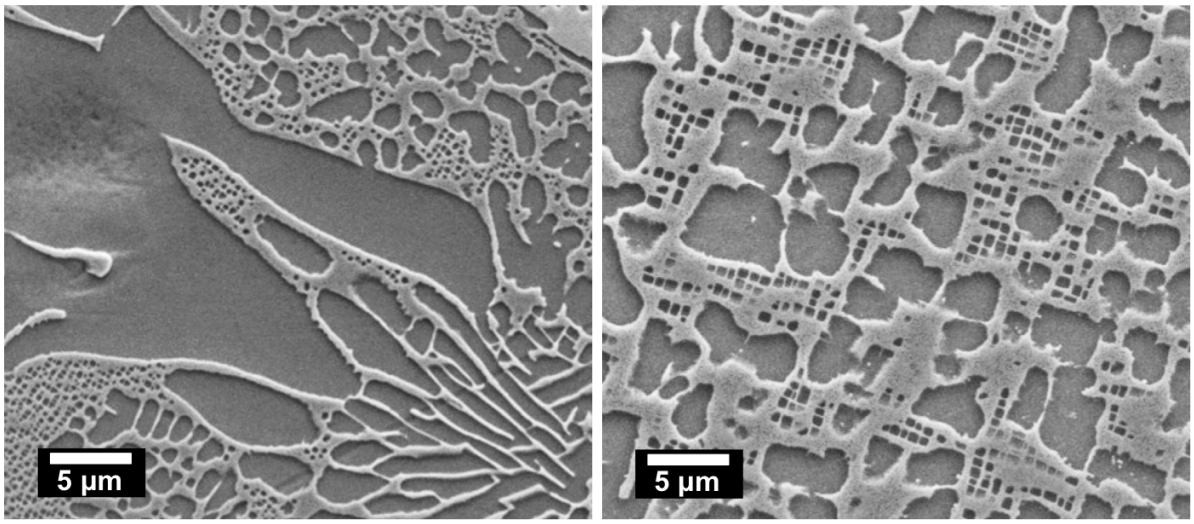

(a) Irregular and eutectic γ' (b) Generally cuboidal γ'

Figure 3.2: SEM micrographs showing Mar-M247 precipitate morphologies with (a) irregular and rosette eutectic as found in interdendritic regions, to (b) generally cuboidal morphologies closer to the core of the dendrites.

3.2.1 As-received Mar-M247 Material

All of the Mar-M247 material used in this dissertation was cast by PCC Airfoils of Beachwood, Ohio, with a master heat composition given in Table 3.4. This Ni-based superalloy was cast in both single crystal and polycrystalline forms, but the alloy as originally developed is a polycrystalline alloy as is clear from the C and B content. These additions are responsible for the nearly 1 volume percent of (the predominantly) metal

Table 3.4: Nominal composition (wt%) of Mar-M247 material.

Cr	Co	Mo	W	Al	Ti	Ta	Hf	C	B	Ni
8.2	9.8	0.75	9.9	5.6	0.90	3.1	1.6	0.16	0.013	Bal

carbide and (to a lesser extent) boride phases, which are primarily for strengthening the grain boundaries of the alloy against sliding while exposed to creep conditions [80, 124]. In total, 5 molds of bars approximately 16 cm long and 1.6 cm in diameter were cast. Three of the molds were investment cast to produce a polycrystalline grain structure, with each of these molds consisting of 16 bars for a total of 48 polycrystalline bars. One mold was directionally solidified with a polycrystalline seed producing a directionally solidified columnar grain structure, while the last mold was directionally solidified with a single crystal grain selector to produce a set of single crystal bars. The directionally solidified and single crystal bar molds each consisted of 7 bars.

Table 3.5: Heat treatment schedule for the Mar-M247 material.

Solution Treatment	Age Treatment
1185 °C, 12 h → cool to 899 °C in 12 min → 649 °C in 14 min	1080 °C, 4 h → air cool

After casting, all bars except one of each grain structure was solution heat treated then aged according to typical industry standards for the alloy. Table 3.5 outlines the treatment schedule, which consisted a 12 hour 1185 °C solution heat treatment for homogenization of compositional segregation upon solidification—which is particularly important for the directionally solidified material—and to reduce the volume fraction of eutectic γ'. After the 12 hour homogenization, the material was cooled in an accelerated manner to produce a supersaturated solid solution in preparation for the subsequent aging treatment. The 4 hour 1080 °C aging treatment was designed to produce an opti-

mal γ-γ' microstructure, with approximately 55% of the volume consisting of generally cuboidal γ' precipitates, 1 to 2 microns in size.

Figure 3.3 provides light optical microscopy (LOM) micrographs of the as-received polycrystalline Mar-M247 material in the solution treated and aged condition, after being polished and etched. With Figure 3.3a providing a representative view of both the dendritic and rosette solidification structures. The rosette structure is found between the dendrite arms, where the last liquid to solidify is of the eutectic composition [80]. This γ–γ' eutectic is more prolific in the as-received material with a volume fraction nearing 15%. While approximately 5% eutectic was observed in JT8D turbine blade material, suggesting longer or higher-temperature solution treatments, which reduce the volume fraction of eutectic. Figure 3.3b provides a higher magnification LOM micrograph of the interdendritic region, showing the rosette eutectic structure in greater detail with large and irregularly shaped γ' surrounded by γ. Figure 3.3c provides a detailed view of the dendrite core where the γ' precipitates are smaller, more consistent in size, and generally cuboidal; while also showing metal carbides (dark brown) which comprise 1% or less of the total volume with blocky or script morphologies.

3.2.2 Properties of Mar-M247 for Modeling

Given the Mar-M247 material as described above, the polycrystalline investment cast material used for experimental validation exhibits isotropic elastic properties. These properties can be referenced from a reputable source in the literature, calculated from single crystal elastic constants (C_{ij}) via polycrystalline averaging scheme as discussed in Section 2.1.3, or determined experimentally—e.g. using the methods discussed in Chapter 6. Specifically for the forward models in Chapter 4, literature values of the single crystal elastic constants representing the constituent γ [95] and γ' [125] phases were first gathered from the literature. Then, assuming a 55% volume fraction of γ' and

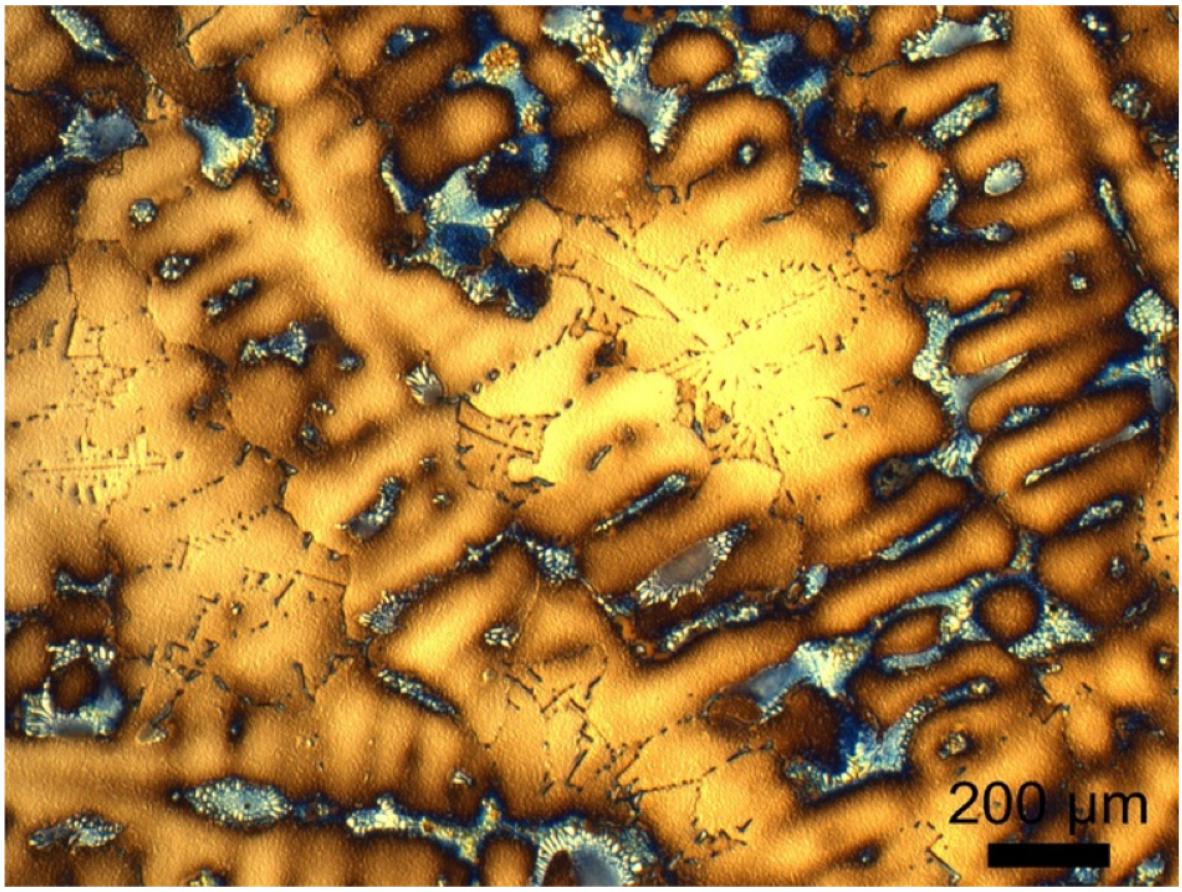

(a) Low magnification

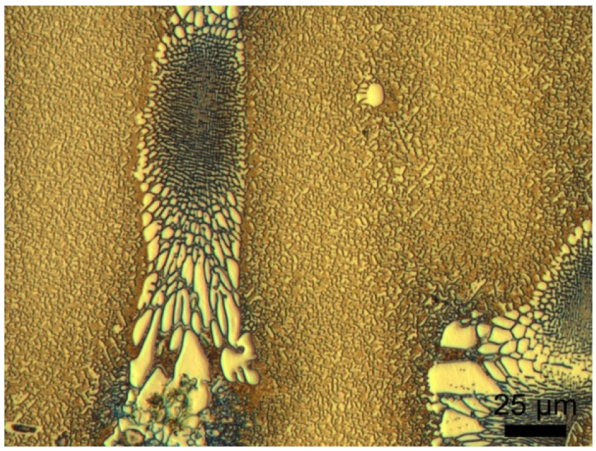

(b) Interdendritic region

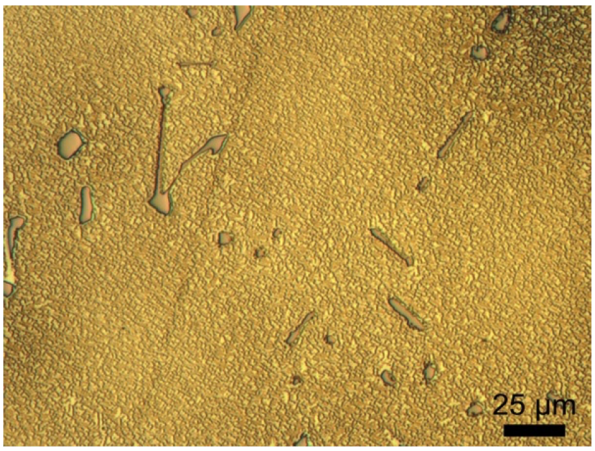

(c) Dendrite core

Figure 3.3: Light optical micrographs of an etched Mar-M247 alloy specimen detailing (a) a lower magnification view of the overall microstructure with approximately 10% remnant eutectic (white cellular structure), as well as higher magnification micrographs focusing of the (b) interdendritic region and the (c) dendrite core.

a 45% volume fraction of γ, a simple rule of mixtures (ROM) average was calculated as described by Kuhn [95]. Table 3.6 summarizes the single crystal elastic constants of the constituent phases, as well as ROM values representing the composite γ–γ' Mar-M247 single crystal material.

Some limitations of this ROM approach not discussed in the later chapters are given here for consideration. First, the simple concept of predicting the elastic response of a material comprised of multiple phases (or for the example of composites, multiple materials), based upon simply adding up the elastic properties of the constituent phases, while appealing, is inadequate under many conditions discussed by Kuhn and Sockel [95]. First, no elastic interaction between the two phases or materials is considered by a simple ROM analysis, which may or may not be an important factor in a given material system. Second, this analysis relies on the assumption that one can characterize the elastic properties of a bulk phase, and apply that property to describe the elastic response of a precipitate or matrix phase. However, it is obvious that compositional changes will affect the elastic properties of a given phase, while diffusion between the matrix and precipitate phases is also guaranteed. Yet, the only circumstance in which one could ignore the effect of compositional changes resulting from diffusion between the matrix and precipitate phases which will affect the elastic properties of the composite material, is if the elastic response to the compositional change of each phase is equal and opposite. This is almost certainty not the case for Ni-based superalloys, or almost any other precipitate strengthened materials. But again, these limitations may or may not preclude the use of a simple ROM analysis as a starting point for modeling the elastic properties of multi-phase alloys, they are simply offered a points for consideration.

Finally, to model the isotropic elastic response of the polycrystalline Mar-M247 material, the single crystal elastic constants from Table 3.6 were used along with Equation (2.36) to calculate the Gairola-Kröner average isotropic shear modulus (G_{GK}), and Equation (2.32) to calculate the isotropic bulk modulus (K). For elastically anisotropic

Table 3.6: Single crystal stiffness values of the Mar-M247 constituent phases, and rule of mixtures (ROM) values assuming 55% γ' and 45% γ.

Constant	**γ [95]**	**γ' [125]**	**ROM**
C_{11}	276 GPa	223 GPa	247 GPa
C_{12}	184 GPa	148 GPa	164 GPa
C_{44}	129 GPa	125 GPa	127 GPa

materials like Ni-based superalloys, third-order Gairola-Kröner average values provide a much better fit to experimental measurements than either of the first-order Voigt or Reuss bounds [93]. While these two isotropic moduli, G_{GK} and K, were later converted to a Gairola-Kröner average Young's modulus (E_{GK}) and Poisson's ratio (ν_{GK}) using the conversion equations Equations (2.11) and (2.12), as required for input into the ABAQUS FE models. Altogether, the Mar-M247 isotropic elastic constants for modeling are summarized in Table 3.7, along with the mass density (ρ), given as 8700 kg/m^3 according to [80].

Table 3.7: Gairola-Kröner average polycrystalline Mar-M247 properties used for forward FE models.

Constant	**Value (units)**
B	192 GPa
G_{GK}	82.3 GPa
E_{GK}	216 GPa
ν_{GK}	0.313
ρ	8700 kg/m^3

3.3 RUS Equipment and Measurement Procedures

RUS equipment is commercially available [50], or may be constructed without exceptional cost as described by Migliori and Maynard [126]. The RUS equipment utilized by this research was provided courtesy of the Vibrant Corporation of Albuquerque, New Mexico, with a diagram of the setup provided in Figure 3.4. Consisting of four primary

components, the RUS measurement setup includes: a desktop computer running control software, a transceiver unit for generating and receiving signals, a transducer cradle to position the piezoelectric transducers consisting of a vibration dampening breadboard and optical table fixtures, and finally a set of omni-directional piezoelectric transducers. Coaxial cables connect three IO ports on the transceiver to the three piezoelectric transducers, while a serial cable connects the computer and the transceiver. The three piezoelectric transducers are identical, custom built by Vibrant, with a detailed view provided in Figure 3.5. The transducers are omni-directional, responding to both normal and lateral displacements, and consist of a piezoelectric element encased with electrical leads in a brass and steel housing, with a silicon carbide tip to protect the piezoelectric element below.

To excite a specimen a swept sinusoidal frequency, with a variable step size of 1-10 hz and a dwell time of 1 to 100 μs, is generated by the transceiver and transmitted to one of the piezoelectric transducers (noted as the drive PT in Figure 3.4). As the drive frequency nears a resonance frequency of the specimen, it begins to resonate with amplified deflections hundreds to thousands of times greater than the displacements produced by the drive transducer. The magnitude of the amplification is roughly the quality factor ($Q = f_R / \Delta f$) of the peak [37], which is defined as the peak frequency (f_R) divided by the peak width at half height (Δf). Q is thus frequency dependent, and a function of the mechanical losses associated with maintaining the standing elastic wave developed during resonance. These amplified deflections of the specimen are then registered by the two receive piezoelectric transducers contacting the specimen, with the signal returned to the transceiver and visualized through the computer controller to produce a broadband resonance spectra like those depicted at the bottom of Figure 3.4. While the signal amplitudes are generally unreliable given the transducer cradle configuration that allows the specimen to freely lift off of the transducers during a measurement, the frequency values are often reliably measured to better than 0.02% precision, which is consistent

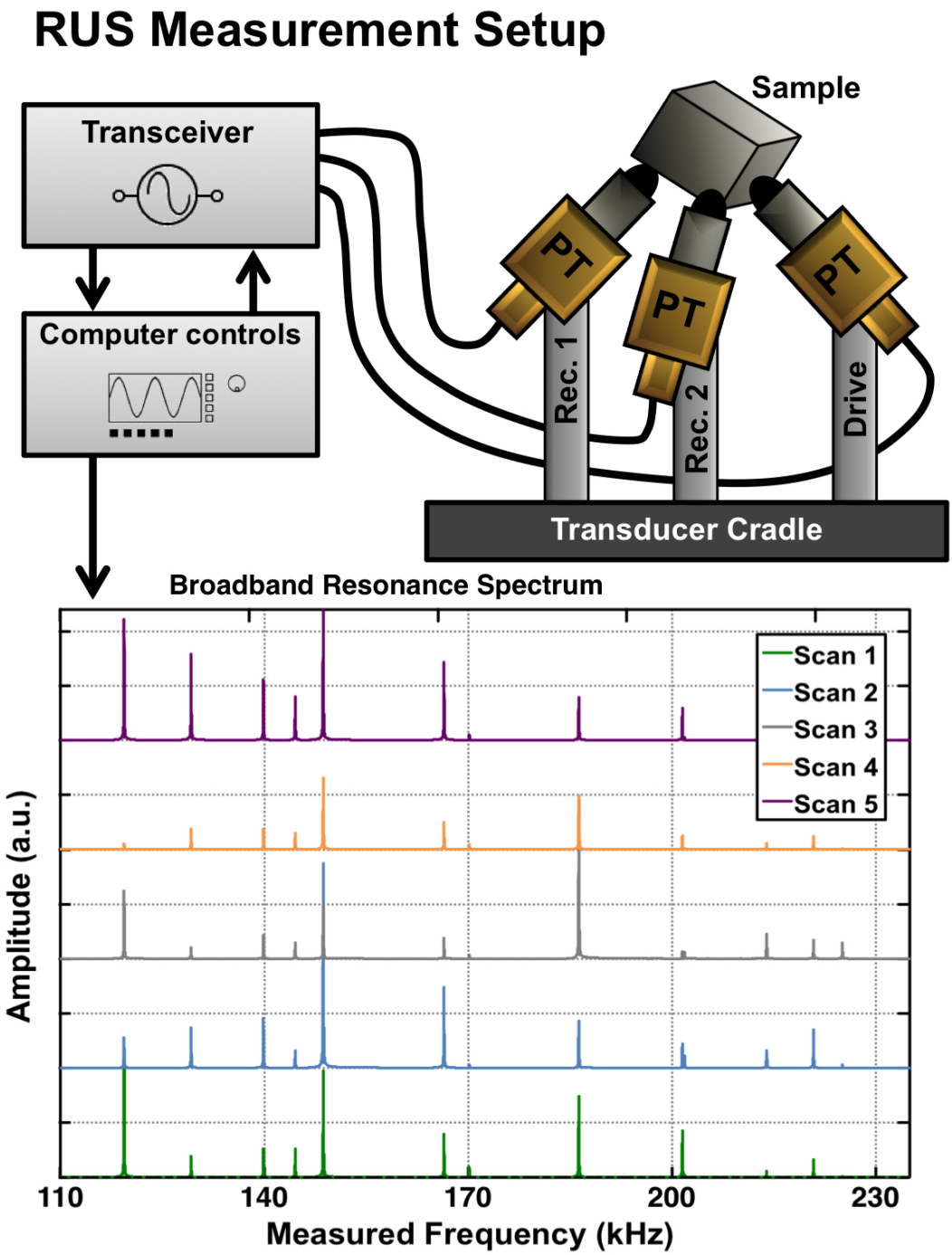

Figure 3.4: Diagram of RUS measurement setup and broadband RUS spectrum plots from 5 measurements of a parallelepiped specimen of Co-Ternary alloy. The spectrum plots are vertically offset to demonstrate the repeatability of the frequency measurement, while the amplitudes—which are not reliable given the cradle configuration—are plotted with arbitrary units (a.u.).

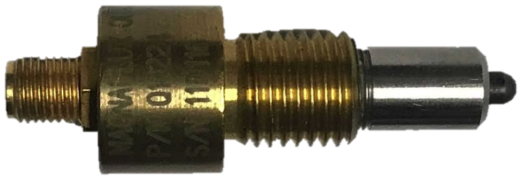

Figure 3.5: Photo of piezoelectric transducer custom built by Vibrant.

with other studies utilizing similar equipment [127].

For both the purpose of NDE and elastic property inversion, the advantages of multiple measurements and averaged f_R results adds considerable confidence to the measured data. For a reason as simple as a poor placement of the specimen on the transducer cradle where one of the piezoelectric transducers is insufficiently contacting the specimen may lead to multiple resonance modes being missed from a single measurement. Even when the specimen is in good contact with the piezoelectric transducers, a mode is still occasionally missed. While NDE efforts may choose to discard modes that are not reliably measured, inversion efforts are greatly benefited by the inclusion of all of the lowest-frequency modes. Typically, f_R utilized in this study are average values from at least 3 broadband scans, where the specimen is removed, rotated if possible, and then replaced on the transducer cradle between each measurement. A list of f_R characteristic of the specimen is then distiled from the broadband spectrum using automated peak picking available on the computer controller, though each scan is typically checked by the user to ensure that the automated peak picking was successful. Occasionally, background noise or ring down from a previous mode can be spuriously identified as a low amplitude mode, while modes in close proximity to each other can lead to the lower-amplitude mode being missed. Such shadowing of lower-amplitude modes is a problem often encountered during RUS measurements, which becomes particularly problematic when the material has a low Q [51]. Removing, rotating, and replacing the specimen is a great first step to resolving this issue too, while using a smaller step size and a longer dwell time can also provide assistance in isolating individual peaks.

3.3.1 Transducer Cradle Configuration

The transducer cradle configuration and the precise placement of the specimen will affect the relative signal amplitude of the broadband spectrum, particularly between measurements where the specimen is removed and then replaced on the transducer cradle. Individual resonance modes cause certain regions of the specimen to exhibit relatively large deflections, while other regions of the specimen will deflect far less. If a resonance mode exhibits near-zero surface displacements in close proximity to a receive piezoelectric transducer, that resonance peak will have a low amplitude on the broadband spectrum, or may be missed entirely. For this reason it is beneficial to have a second receive piezoelectric transducer contacting the specimen at a different location, as detailed by Figure 3.4. For it is far less likely that both of the receive piezoelectric transducers will be located at or near zero-displacement nodes for any individual resonance mode.

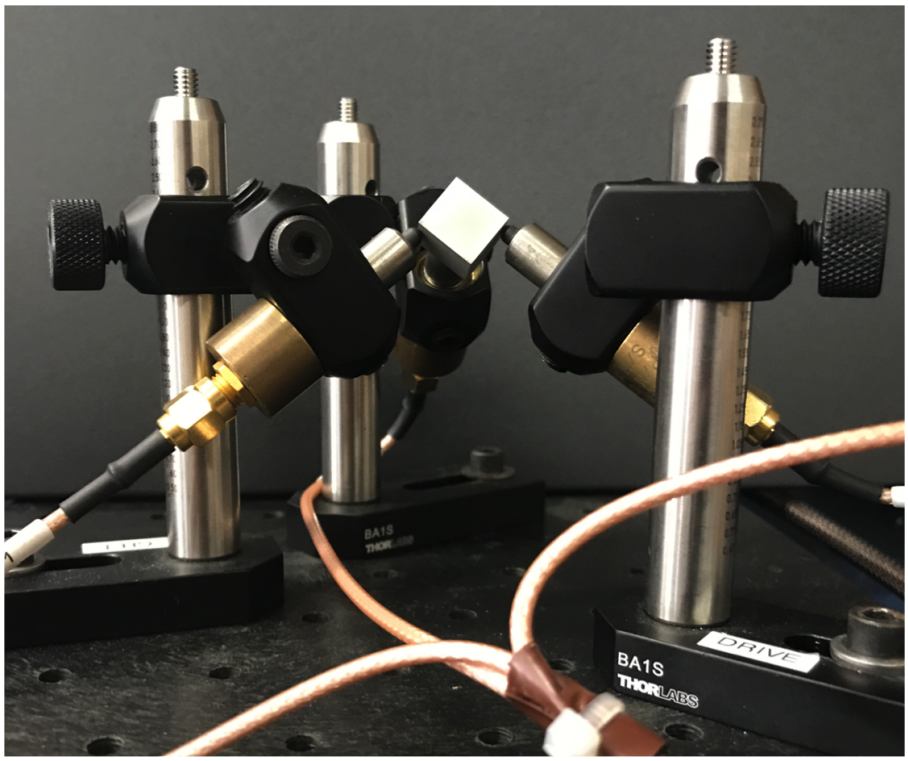

Figure 3.6: Photo of transducer cradle with a rectangular parallelepiped specimen supported along its faces near the corners of the specimen.

When measuring rectangular parallelepiped specimens for the purpose of estimating elastic constants, the contact location of the piezoelectric transducers should be given special consideration. The corners of a rectangular parallelepiped specimen are the points of lowest symmetry, making the corners of the specimen ideal for both exciting and detecting the most resonance modes [13,38,128,129]. The corners also provide the lowest elastic coupling/impedance for minimal biasing of the measured resonance frequencies due to loading from the transducers [38, 42]. However, contacting only the corners of a parallelepiped specimen is difficult, as some applied force is necessary to hold the specimen in place, while the application of excessive force can damage both the specimen and the transducer. Given the 3 transducer cradle configuration described above, it was found that contacting the parallelepiped specimen on its faces, nearest to the corners as reasonably possible, provides sufficient signal to noise ratio. Figure 3.6 provides a picture of the transducer cradle configured to support a rectangular parallelepiped specimen from these near-corner positions, which results in the consistent excitation and recording of modes. Furthermore, minimal variance in frequency is observed due to loading from the transducers across multiple measurements when the specimen is removed, rotated, and replaced upon the cradle, because the specimen rests via gravity instead of through a variable applied force. In a later publication by Migliori and Maynard [126], they both conclude that contacting rectangular parallelepiped specimens by their corners, while theoretically optimal, is often impractical due to the issues of variable loading and damage to the specimens and transducers. Ultimately, they simply suggest contacting the specimen by its faces [126], agreeing with the methods outlined above.

3.3.2 Consideration of Specimen Size

When properly designed, the configuration of the transducer cradle has little impact on the measured f_R . Although massive specimens in excess of 2 kg could have unintended in-

teractions with the measurement setup due simply to the force of gravity acting to couple the motion of the specimen and the cradle [50], such coupling does not preclude useful measurements. Based on considerable experience with the custom built piezoelectric transducers (Figure 3.5) and the transducer cradle configuration (Figure 3.6) described previously, the optimal specimen is one that exhibits a compact shape and has a mass between 0.005 and 5 kg. For these specimens, a transducer cradle can be configured such that the specimen freely rest upon the silicon carbide tipped piezoelectric transducers via gravity, without undue concern for biased frequency measurements or damage to the transducers. Particularly small specimens less than 0.005 kg in mass are often difficult to measure due to insufficient coupling with the transducers, while specimens smaller than 5 mm in dimension may preclude the use of three piezoelectric transducers in a cradle configuration. However, an RUS apparatus as described by Maynard works very well for tiny specimens as small as a few hundred micrometers in size [40]. In fact, given specially designed piezoelectric transducers fabricated with polyvinylidene fluoride (PVDF), a piezoelectric plastic film material, combined with a transducer cradle configuration that can pinch tiny specimens between two planar PVDF transducers—RUS is particularly well suited for tiny specimens where alternative ultrasonic methods become impracticable [33, 40]. As for particularly large or massive specimens, others have reported successfully measuring specimens in excess of 20 kg [50], though resting such large specimens atop the piezoelectric transducers used in this study may damage them. One possible strategy to avoid damaging the transducers would be to suspend large specimens via thin wires, which has the effect of both limiting the loss of vibrational energy to mechanically stiff supports, while progressing towards the stress-free boundary conditions assumed during modeling. When suspended, the piezoelectric transducers are either brought into contact with the specimen, or the specimen may be excited using non-contacting methods in a manner similar to that of Remillieux et al. [51]; who report excitation and measurement of resonance mode shapes and frequencies with 3D laser

vibrometry on a large cylindrical specimen suspended using strings [51].

3.4 Creep Testing Equipment and Procedures

Creep testing of polycrystalline Mar-M247 dog-bones, machined according to Figure 3.11, was conducted as part of a broader effort focused on extending the mechanical damage evaluation capability of RUS. Specifically, the collection of RUS data from iteratively crept dog-bone specimens is used for validation of a forward modeling framework (FMF) of creep damage as covered by Chapter 4 of this dissertation. While the information in this chapter provides details about the experimental setup and procedure as would be necessary for repeating the iterative creep experiments. Note that single crystal Mar-M247 dog-bones, machined according to Figure 3.12, were also tested as part of collaborative research efforts, but are not specifically discussed here. For details about the single crystal Mar-M247 creep work, including incremental creep levels and measured RUS results, readers are directed to publications: Heffernan et al. [130] and Mayes et al. [131].

3.4.1 Specimen and Load Train Design

All creep testing was conducted according to the general experimental procedure as follows. First, the dog-bone specimen was affixed between the upper and lower grips of the creep frame using creep resistant collars, constructed from a single crystal of CMSX-4, as shown in Figure 3.7. One face of the collar contacts the recessed end of the dog-bone shoulder (detailed in Figure 4.3), while the opposite face of the collar seats into a recess in the grip. Then the extensometer scaffolding is placed around the specimen, resting atop flat faces of the upper and lower grips. The creep frame grips, creep resistant collars, and extensometer scaffolding are all spray coated with boron nitride to prevent diffusion bonding, which gives these components a white appearance in Figure 3.7. Next,

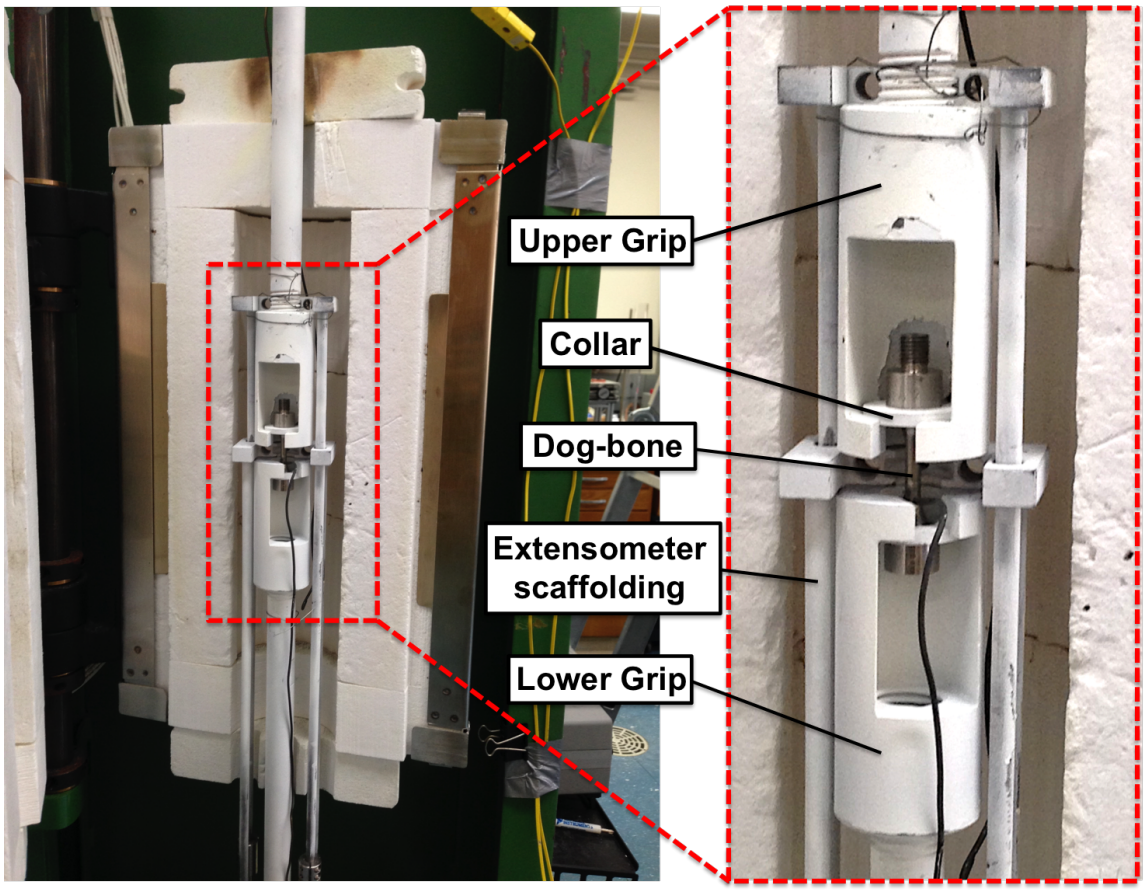

Figure 3.7: Picture of creep frame with a dog-bone specimen loaded just prior to testing.

three thermocouples are affixed near the upper grip, dog-bone gauge section, and lower grip using tungsten wire; as these thermocouples provide data for controlling the power supply to the three heating zones of the clamshell furnace. Finally, the clamshell furnace is carefully closed and latched around the specimen, grips, extensometer scaffolding, and load-bearing rods. Taking note that the ceramic foam insulation of the furnace may come into contact with the load-bearing rods as necessary to minimize heat loss, but that insulation should not contact or otherwise imped the free motion of the extensometer scaffolding extending past the bottom of the furnace to two digital extensometers below.

The creep test temperature of 950 °C, in air, was selected to simulate those experienced by aerospace turbine engine components [80], while a somewhat aggressive load of 300 MPa was applied to facilitate a quicker test. The target heating rate was set to 500 °C per hour, which would imply a 2 hour ramp to temperature. However, as a result of conservative furnace control settings intended to prevent overheating the specimen, heating from 900 °C to 950 °C would often take an additional hour. Once the target temperature was reached by the three heating zones of the furnace, a 30 minute hold at ± 5 °C is recorded for each zone of the furnace before the test is initiated. Once the 30 minute hold is complete, the extensometers are recalibrated to account for thermal expansion of the components, and the extensometer data collection is initiated. Finally, manually engaging a clutch and flipping the motor controller to automatic will add tension to the creep specimen by suspending a stack of weights at the back of the creep frame (at a 20:1 load:weight ratio). Occasionally throughout the duration of the test, due to of elongation of the specimen, the tension motor will automatically turn on to ensure that the stack of weights remains suspended a few inches above a load-bearing platform designed to catch the weights if the specimen breaks. If the specimen fails before the test is terminated by the steps outlined in the following section, the stack of weights will fall into contact with the load-bearing platform below and trigger the furnace to automatically shut down.

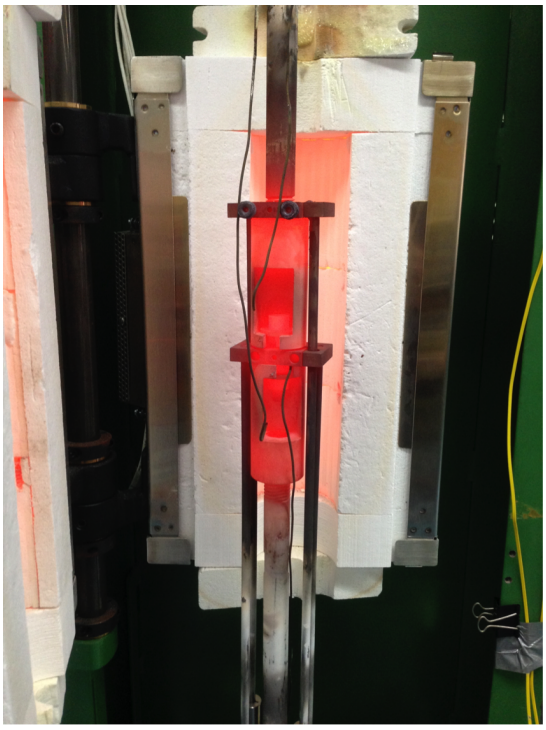

Figure 3.8: Picture of creep setup immediately after a test is terminated, after the clamshell furnace is opened and the specimen is air-cooled to room temperature.

After the desired level of creep strain was accumulated, generally 1–2% strain, the creep test was terminated with the following steps. First, data collection is halted along with the automatic tension control. Second, the manual clutch to the tension motor is disengaged and the load is manually removed by turning a hand-crank to raise a load bearing platform until the free hanging weights are fully supported. Special care is made to only raise the platform and weights as necessary to disengage the load applied to the specimen, which is judged by slack in the load bearing rod (connected to the lower grip in Figure 3.7) coming through the bottom of the clamshell furnace. Next, with a desire to cool the specimen to room temperature as quickly as reasonably possible, so as to preserve the as-crept microstructure and minimize the temperature exposure beyond the extent of the creep test. After ensuring that any temperature-sensitive equipment is safely out of the way, the clamshell furnace is slowly opened and rotated away from the specimen and grips to "air cool" the specimen, as demonstrated by Figure 3.8.

Importantly, while the specimen, extensometer scaffolding, grips, and load bearing rods of the creep frame are cooling to room temperature, the position of the load bearing platform at the back of the creep frame must be manually adjusted to ensure that slack remains in setup. Too much slack and the specimen can fall out of the grips before being fully cooled, while too little slack will put unwanted tension in the dog-bone specimen as the hot components contract upon cooling. While the overall cooling process lasts approximately 2 hours, maintaining slack in the load bearing components is only an issue during the first hour of cooling, at which point the vast majority of the contraction has taken place. Once everything has cooled, the dog-bone specimen is removed from the grips, the collars are removed from the dog-bone shoulders, and the specimen is allowed to fully equilibrate to room temperature before the RUS measurements are conducted. Note that because elastic properties are temperature dependent, it is very important to let the dog-bone specimen fully equilibrate to room temperature before its resonance frequencies are measured. After the RUS measurements are collected, the mass and height of the specimen are also recorded as a confirmation of the extensometer measurements, and as a check on the oxidation of the specimen. From this point the creep frame components are cleaned, checked, re-coated with boron nitride spray, before the procedure listed above is repeated until the desired number of creep increments are imparted to the dog-bone specimen. For the polycrystalline Mar-M247 dog-bone specimen iteratively crept as discussed in Chapter 4, this process was followed a total of six times.

3.5 Ultrasonic Fatigue Testing Equipment and Procedures

Iterative ultrasonic fatigue tests of polycrystalline Mar-M247 dog-bones, machined according to Figure 3.11, were conducted as part of a broader effort focused on extending

the mechanical damage evaluation capability of RUS. Specifically, the collection of RUS data from iteratively fatigued dog-bone specimens is used for validation of a forward modeling framework (FMF) of mechanical damage as covered by Chapter 4 of this dissertation. The information provided in this chapter focuses on the ultrasonic fatigue setup, and the testing procedures used to impart fatigue damage to the specimen. Single crystal Mar-M247 dog-bones were also machined according to Figure 3.12, such that they would exhibit an extensional resonance mode near 20 kHz as required for ultrasonic fatigue testing. Ultimately, these single crystal dog-bones were only used for the iterative creep experiments, and are therefore not further addressed in this section.

Fatigue tests conducted as part of this investigation employ a custom-built ultrasonic fatigue test rig capable of producing 20,000 Hz cyclic loading on specially designed dog-bones that have an extensional resonance mode near the 20 kHz operating frequency of the setup. As the 20 kHz resonant condition is reached, the ends of the specimen act like point masses connected via a linear elastic spring (the gauge section of the dog bone), with displacements of the ends in opposite directions creating the cyclic fatigue loading. One of the major obstacles to performing such rapid cycling is the mitigation of heat generated by frictional losses in the material as it is strained [132]. As the fatigue testing in this dissertation sought to probe the room temperature fatigue behavior, multiple controls are in place to mitigate unnecessary heating. E.g. the rig is programmed to fatigue the sample in pulses for tens to hundreds of milliseconds, followed by a rest period for a comparable length of time to allow the specimen to cool. Further details about this control, and others, are discussed in the following section. A picture of the ultrasonic fatigue setup with the major components labeled is provided in Figure 3.9, with an expanded view detailing the dog-bone specimen affixed to the lambda rod with a small strain gauge glued to the center of the dog-bone where the strains are at a maximum.

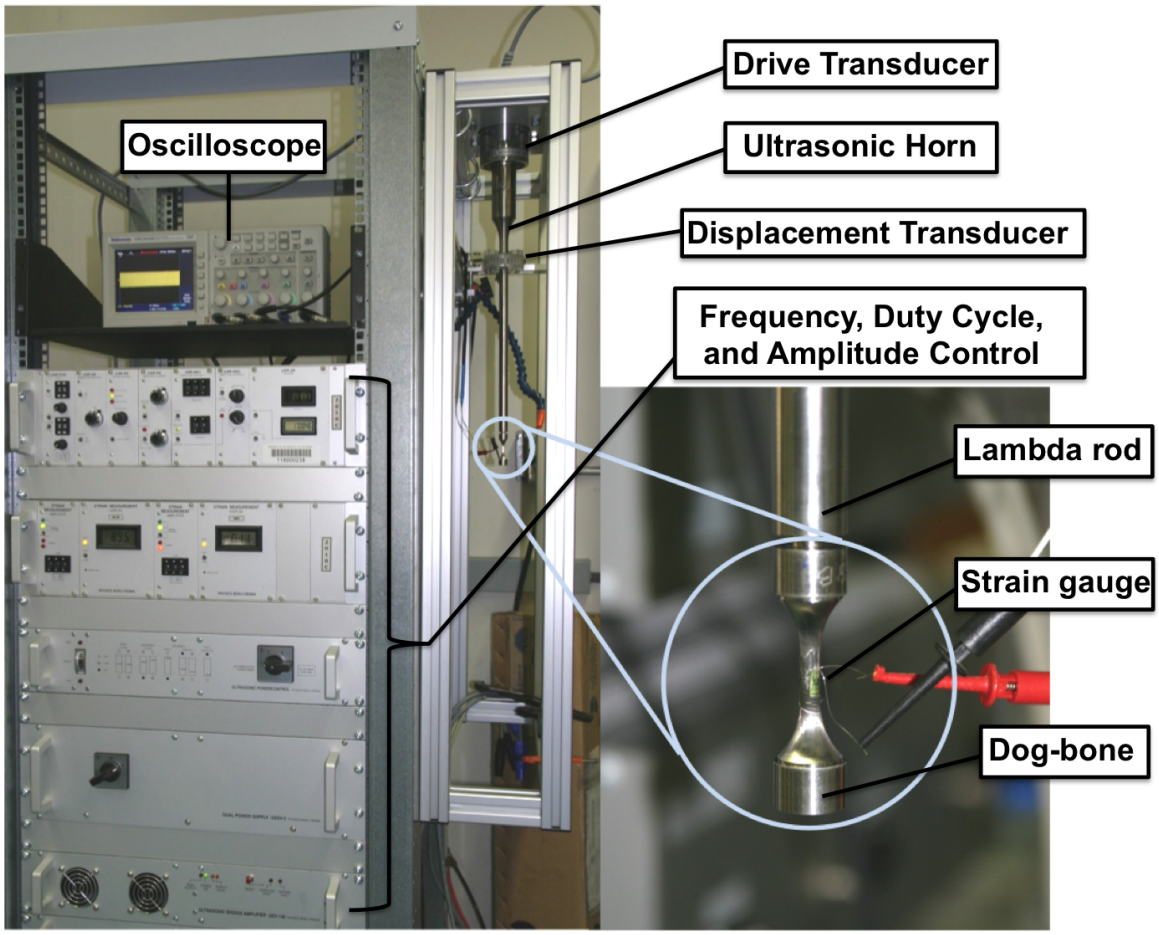

Figure 3.9: Picture of the ultrasonic fatigue setup, with a polycrystalline Mar-M247 dog-bone specimen and strain gauge visible in the expanded inset, and the major components labeled.

3.5.1 Ultrasonic Fatigue System Controls

Multiple controls were in place to ensure the resonance behavior of the specimen was always within specified tolerances. As a primary control on excessive frictional heating, the test rig was programmed to fatigue the dog-bone specimen in 50 to 150 millisecond pulses followed by a rest period ranging from 100 to 200 milliseconds. The specimen also had cooling air flowing across the surface of the gauge section during the experiment, ensuring the specimen temperature never exceeded 50 °C. As a tertiary control on excessive heating, any substantial increase in dog-bone temperature would decrease the stiffness of the specimen and trigger a resonance frequency monitoring control. Then after each rest period, the dog-bone must be capable of returning to a resonant condition within a fraction of a second in order for the cycling pulse to initiate. If a resonant condition could not be reached after multiple consecutive attempts, the test is terminated. Note that in addition to excessive heating, a dog-bone with a fatal crack may also fail to reach a resonant condition, at which point the specimen is deemed to have failed and the test terminated. In general, it was found that the resonance frequency of the dog-bone remained relatively consistent over a large portion of the fatigue life. This result is consistent with the general behavior predicted by FE models and simple first order calculations as outlined by Migliori and Sarrao [33], which require cracks of considerable length in relation to the overall dog-bone gauge section before significant shifts in resonance frequency are discernible. Note that the application of a small strain gauge to the gauge section of the dog-bone, which was necessary for calibrating the fatigue experiment, had a minimal affect on the RUS measured resonance behavior.

3.5.2 Nonlinear Ultrasonic Measurements

A technique for early detection of a small fatigue crack, which is unique to the ultrasonic fatigue setup, is through tracking nonlinear changes in the power spectrum of the feed-

back signal [133]. Unlike the RUS measurements where the resonating specimen is free to deflect away from the piezoelectric transducers of the cradle [55,56], the threaded end of the dog-bone is screwed into to the lambda rod of the fatigue setup, which allows for precise tracking of the displacements on an absolute scale. Starting with the drive transducer generating a longitudinal wave of frequency ω_0, corresponding to the fundamental extensional mode of the coupled specimen-rig system, with a tone burst amplitude of a_0 as recorded by the displacement transducer. The elastic wave propagates down from the drive transducer, through the ultrasonic horn, lambda rod, and into the specimen with a characteristic velocity c_0 dictated by the density and elastic properties of the individual components. The wave energy is then reflected off the bottom free surface of the dog-bone specimen before traveling back through the specimen and lambda rod, at which point the displacement transducer records the reduced amplitude a_1 of the wave at ω_0, along with the amplitudes a_2 and a_3 from the second and third harmonics at $2\omega_0$ and $3\omega_0$, respectively [133]. When the drive amplitude is large enough, the elastic response of the material is nonlinear, and the amplitude a_1 is reduced due to losses associated with the elastic wave being scattered as it propagates through the material. From the amplitudes a_1 and a_2, the material nonlinearity parameter β is first determined for the undamaged specimen. Then when tracked over the course of the fatigue test, changes in β can serve as an early indication of the initiation and growth of a fatigue crack [133]. With changes in β arising from the elastic discontinuity of a crack, the tensional phase of the fatigue cycle opens the crack and reduces the local modulus of the material, while the compressional phase closes the crack and returns the local modulus to near the continuum value. β is observed to increase monotonically throughout the fatigue test, likely due to changes in stress state as well as the dislocation substructure [134]. However, the rate of change increases as the crack grows, with a theoretical dependence of β on the crack radius r_C being $\beta \propto r_C^4$ explaining the rapid increase in β near the end of the fatigue lifetime [135].

This feature of the ultrasonic fatigue setup is specifically mentioned here because

it may offer insight as to the origins of an as-yet unexplained observation from the crept Mar-M247 dog-bone specimens in Chapter 4. For both the both single crystal and polycrystalline dog-bones, there exists an anomalous global increase in resonance frequency after the first creep test increment that cannot be explained by a change in dog-bone shape. While the nonlinear elastic behavior of these dog-bones were not measured before and after the first creep increment, it is possible that changes in β could be used to interrogate this anomalous behavior. Particularly, if changes in the dislocation density or residual stress state of the material can be quantified from changes in β according to the theoretical relationships proposed by Cantrell [136], then it is possible that the anomalous global increase in resonance frequency observed during the early stages of creep could also be explained.

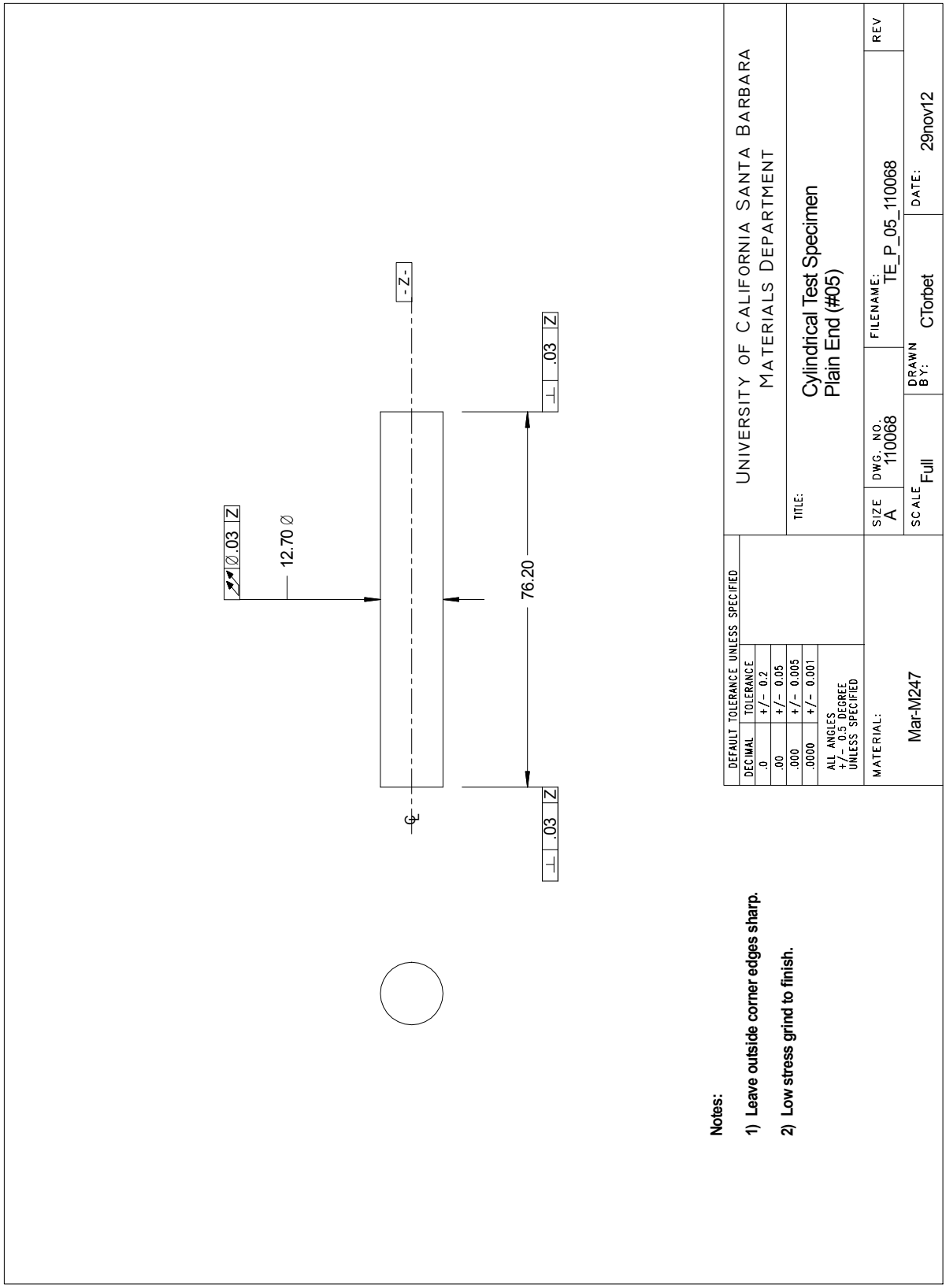

Figure 3.10: Mar-M247 cylinder specimen drawing.

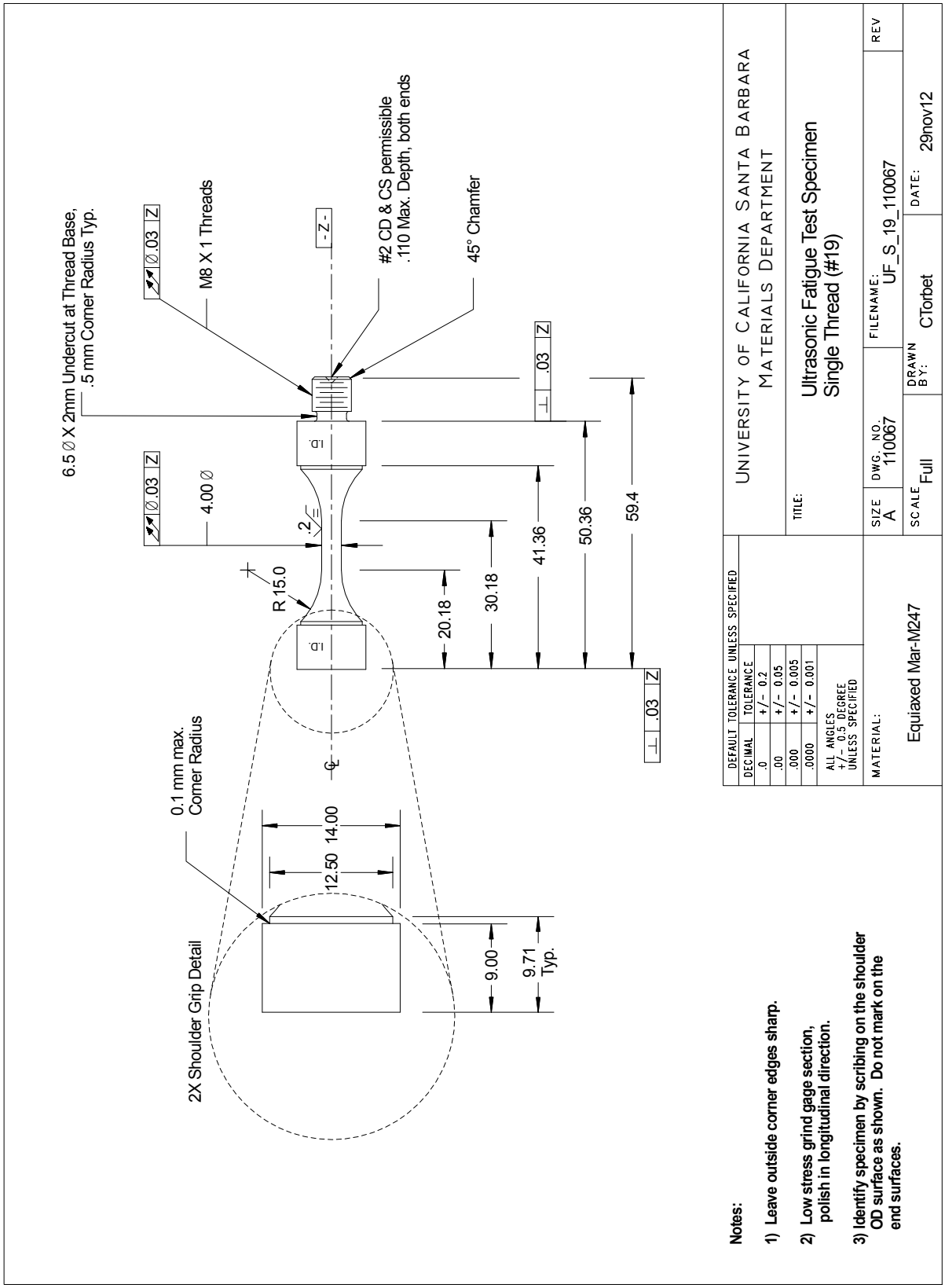

Figure 3.11: Polycrystalline Mar-M247 dog-bone specimen drawing.

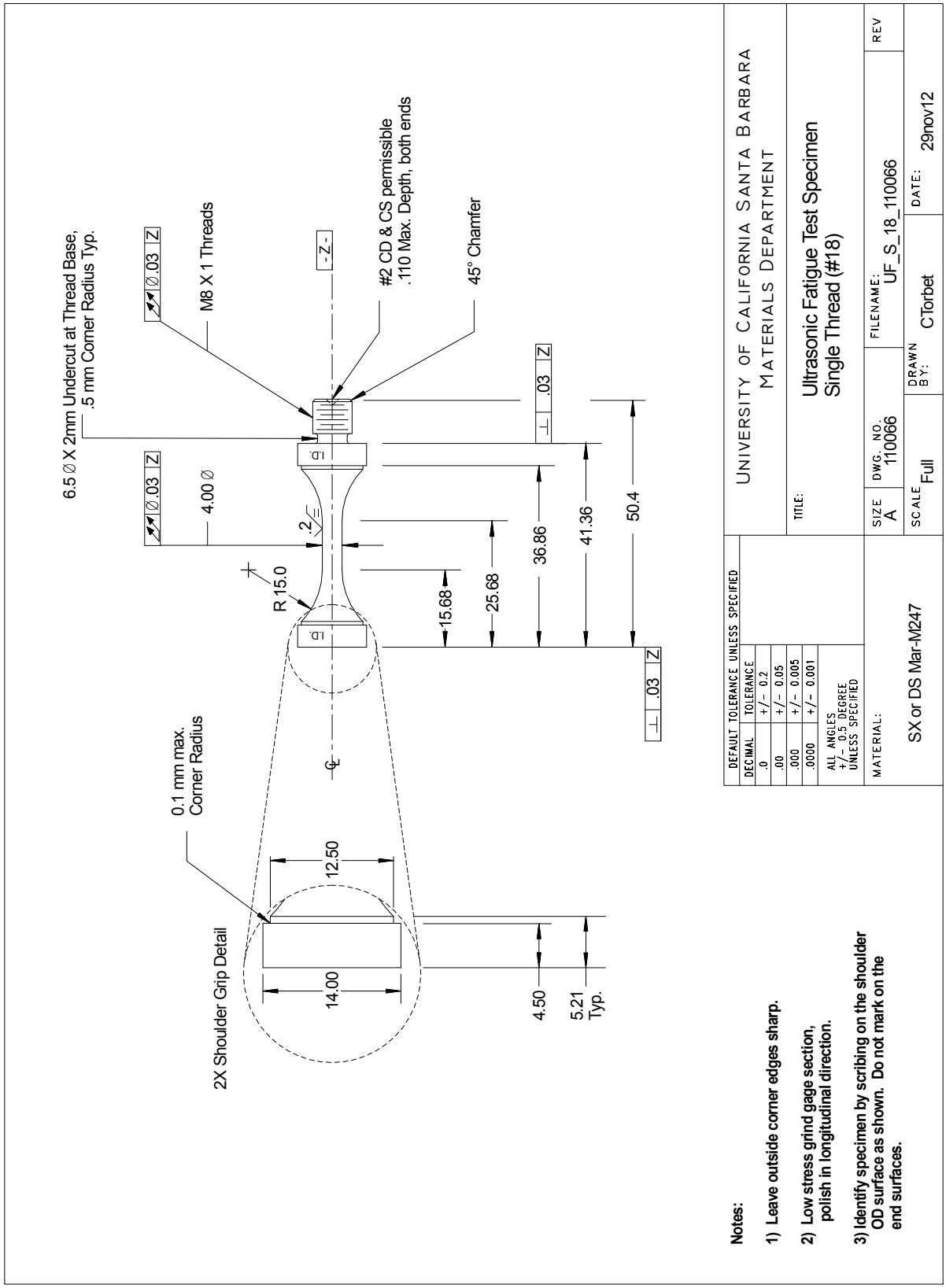

Figure 3.12: Single crystal Mar-M247 dog-bone specimen drawing.

Chapter 4

Forward Modeling Framework for NDE of Mechanical Damage

Chapter Abstract

Broadly this chapter, and the publication upon which this chapter is based[1] seeks to demonstrate how relatively simple forward finite element (FE) models, as part of a forward modeling framework (FMF), can practically be employed to quantify mechanical damage on a complex geometry (dog-bone) specimen. By varying the location, type, and severity of damage in the models, the unique resonance response can be assessed. These model results are then compared to RUS-measured experimental results from a dog-bone specimen subjected to fatigue and creep conditions, with the later exhibiting multiple concurrent damage mechanisms. Residual analysis comparing the measured and modeled changes in resonance frequencies demonstrate when the dominant mechanism affecting resonance is identified, and whether modeling secondary mechanisms is necessary. FE models also provide mode shape information to inform RUS measurements and assist in NDE efforts to identify diagnostic resonance modes. Such diagnostic modes are ones that are reliably measured and either particularly sensitive to damage, or relatively insensitive to damage making them useful markers to confirm or exclude the possibility of alternative mechanisms affecting resonance. The final sections of the chapter include discussion of distinguishing characteristics of the proposed FMF from historical methods and some key conclusions.

[1] [56] B.R. Goodlet, C.J. Torbet, E.J. Biedermann, L.M. Jauriqui, J.C. Aldrin, and T.M. Pollock. "Forward Models for Extending the Mechanical Damage Evaluation Capability of Resonant Ultrasound Spectroscopy," *Ultrasonics* 77 (2017) pp. 183-196. [doi:10.1016/j.ultras.2017.02.002]

4.1 Introduction

Mar-M247, a model polycrystalline Ni-based superalloy is used to investigate room temperature high cycle fatigue as well as creep at 950 °C. In both instances, iterative levels of damage are imparted to a dog-bone specimen with testing interrupted to conduct RUS measurements. FE models predict mode-specific changes in resonance frequencies ($\triangle f_R$) that inform RUS measurements of mode-type and elucidate the connections between damage evolution and $\triangle f_R$.

Mar-M247, along with most polycrystalline Ni-based superalloys, utilizes small additions of carbon to promote formation of grain boundary metal carbides to inhibit boundary sliding during creep. However, if these carbides are too large they may also serve as fatigue crack initiation sites [80]. A fully-aged two-phase γ–γ' microstructure of Mar-M247 is shown in Figure 4.1 (a), along with an etched micrograph of the cast dendritic structure in Figure 4.1 (b) which elucidates the polycrystalline nature of the material. The cuboidal γ' precipitates are an ordered FCC phase that strengthen the material and inhibit the motion of dislocations necessary for high temperature deformation. Ultimately, understanding the onset, location, and progressive growth of damage will be important to evaluating NDE techniques such as RUS and to the development of realistic FE models that can aid in the interpretation of measured RUS data.

4.1.1 Creep of Ni-based Superalloys

Creep is a time-dependent process of plastic deformation that occurs in metals and other materials at significant fractions of their homologous temperature [137]. Creep damage can manifest in a number of forms, from coarsening or dissolution of strengthening precipitates, to grain structure changes as a result of grain growth or dynamic recrystallization, to grain boundary damage such as sliding, void formation, and cracking [138].

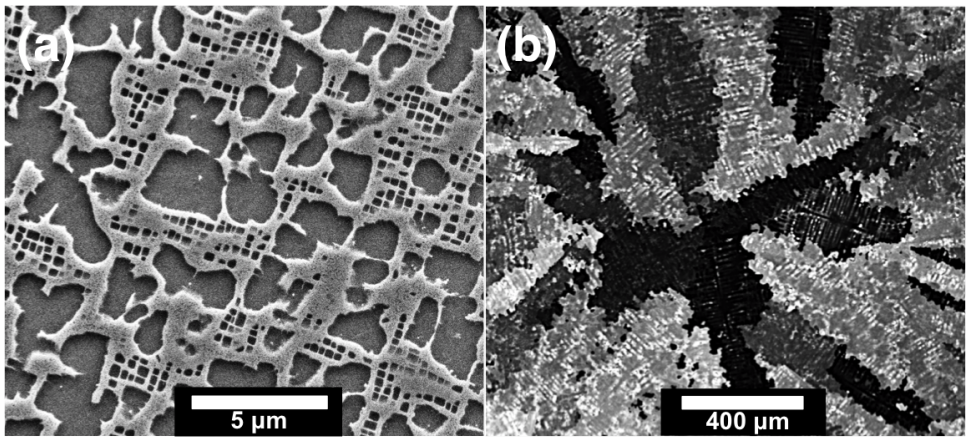

Figure 4.1: (a) Aged γ–γ' microstructure and (b) investment cast grain structure of Mar-M247.

Protracted exposure of the polycrystalline Ni-based superalloy Mar-M247 alloy to sustained mechanical loads at high temperatures will result in creep rupture. An example of an *uninterrupted* creep curve for polycrystalline Mar-M247, loaded at 300 MPa at 950 °C in air, is provided in Figure 4.2.

The creep curve in Figure 4.2 displays the three distinct creep regimes, with a majority of the creep life under the test conditions residing in the secondary regime. The primary creep regime is characterized by an initially high creep rate that quickly decays as mobile dislocations, driven by the applied load and facilitated by thermally activated mechanisms, are forced to glide through the γ channels [65, 80, 139]. Initially the dislocations are unable to shear the ordered γ' precipitates, instead bowing around the cuboidal precipitates, and building up strain energy in the process, which impedes further plasticity [139]. The secondary creep regime is characterized by a steady state creep rate, wherein the work hardening mechanisms of the primary regime are balanced by thermal annealing effects aiding dislocation recovery and annihilation [65, 80]. The γ–γ' microstructure can evolve considerably during creep as internal stresses drive directional diffusion of material to create a coarsened and ultimately rafted microstructure [124, 140]. As creep progresses, stresses build up necessary to shear the γ' precipitates, and the ac-

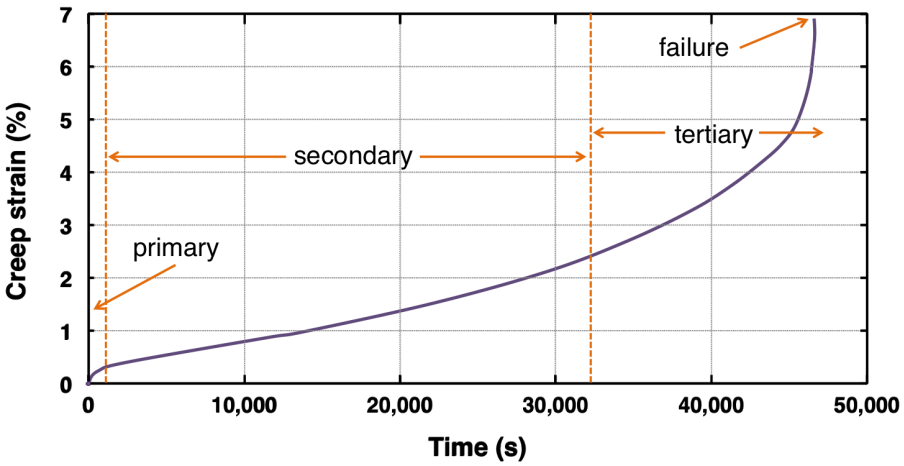

Figure 4.2: Primary, secondary and tertiary creep regimes depicted for a dog-bone specimen of Mar-M247 loaded to 300 MPa at 950 °C in air, crept until failure.

cumulation of vacancies coalescing into voids deteriorates the load carrying capacity of the material [138]. This accumulation of damage brings about the accelerated creep rate of the tertiary regime, with failure via creep rupture resulting soon after [80, 124].

4.1.2 Fatigue of Ni-based Superalloys

In addition to sustained loads at elevated temperatures resulting in creep damage, cyclic loading below the yield strength of the material, both at room temperature and at elevated temperatures also accumulates damage which can lead to failure [80]. Despite macroscopic loading at low strains, small regions of the material can experience loads that exceed the elastic limit due to localization of stresses around inclusions, pores, carbides, eutectic, and other microstructural features [124, 141]. Materials scientists often endeavor to reduce the size of these microstructural features in an effort to improve fatigue life [141], yet fatigue remains a serious concern for failure of critical components like turbine disks. Surface defects are particularly detrimental to low-cycle fatigue life, where the number of cycles to failure (N_f) is governed by fatigue crack propagation, typically $N_f < 10^5$ [80]. High-cycle fatigue, above 10^6 cycles, is dominated by the crack initiation process [80], typically at sub-surface features [142]. Regardless of the initiation

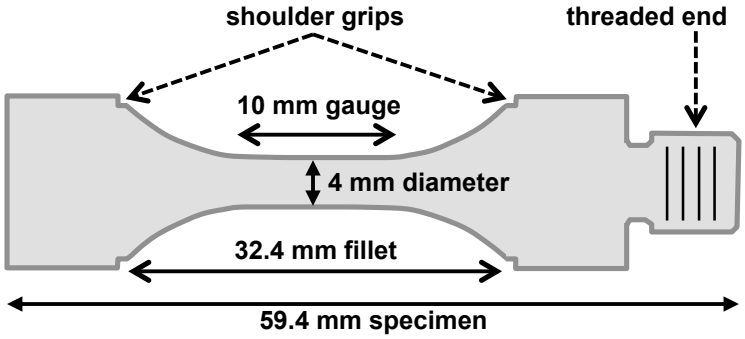

Figure 4.3: Dual-purpose creep and ultrasonic fatigue cylindrical dog-bone design, all dimensions are in mm.

mechanism, be it sustained-peak low-cycle fatigue which combines mechanisms of creep and fatigue [143,144], or low/high-cycle fatigue mechanisms acting independent of creep, the resulting cracks reduce the stiffness of a component and are generally expected to lead to a decrease in resonance frequencies.

4.2 Experimental Methods and Results

4.2.1 Fatigue Experiments

A diagram of the dual-purpose creep and ultrasonic fatigue cylindrical dog-bone specimen is depicted in Figure 4.3, with complete machining specifications provided in Section 3.5.2. The dog-bone specimens were machined from investment cast polycrystalline bars of Ni-based superalloy Mar-M247, with nominal composition given in Table 3.4. The fatigue tests employed a custom-built ultrasonic fatigue test rig [145], with considerable details about the setup, including pictures, provided in Section 3.5. The specially designed dog-bone is affixed via its threaded end to a lambda rod, which itself is affixed to an ultrasonic horn placed at the end of a powerful piezoelectric transducer capable of exciting the lambda rod and specimen to a resonant condition at 20 kHz. Specifically, this resonance mode exhibits extensional motion with maximum displacement produced at both ends

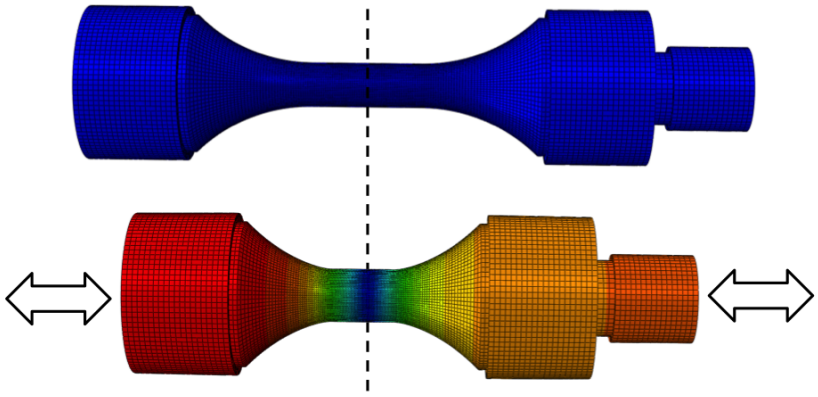

Figure 4.4: FE model of dog-bone 20 kHz extensional resonance mode used for fatigue testing, with blue indicating zero displacement and warmer colors (orange and red) indicating maximum displacement along the long axis of the dog-bone.

of the dog-bone in opposite directions, as Figure 4.4 illustrates. Blue indicates zero displacement, while warmer colors (orange and red) indicate maximum displacement in the direction of the long axis of the dog-bone. This extensional motion maximizes the stress to the 10 mm long and 4 mm diameter gauge section of the dog-bone. With fatigue cycling that exhibits a fully-reversing load of 300 MPa, approximately one third of the yield strength of Mar-M247 at room temperature. This assured that cyclic loading would not produce macroscopic plastic deformation, which was confirmed by measurements of the dog-bone length before and after the fatigue testing.

Inherently a statistical process, fatigue life may be sensitive to many different material, specimen preparation, and testing conditions. This fact makes interrupted tests difficult at planned intervals of total fatigue life, and makes measurement of signals indicating crack initiation, propagation, and growth particularly important. In an earlier test under identical cycling and loading conditions, a dog-bone was cycled until failure to ascertain a general fatigue lifetime. This information was then used to interrupt a second dog-bone specimen at 5 intermediate points between 40–98% of overall life as summarized in Table 4.1.

Table 4.1: Ultrasonic fatigue experimental iterations

Step ID	Cycles (Millions)	Percent of Life (%)
UF1	5.0	40.6
UF2	8.5	69.1
UF3	10.0	81.3
UF4	11.0	89.4
UF5	12.0	97.6
UF6	12.3	100.0

4.2.2 Creep Experiments

To impart creep deformation to the dog-bone specimen, a uniaxial tensile load was applied via specimen grips to the recessed ends of the specimen shoulder, detailed in Figure 4.3. All creep iterations were conducted with the specimen loaded to 300 MPa inside of a clam-shell furnace at a constant 950 °C in air. These testing conditions were selected to simulate temperatures experienced by aerospace turbine engine components [80], with an aggressive load applied to facilitate a more rapid test. Section 3.4 provides further details about the creep frame and test setup, including photographs of the specimen and grips loaded inside of the clam-shell furnace, before and immediately after a creep test was interrupted. Elongation of the specimen during the creep test was monitored via a creep-resistant scaffolding that aligns with the specimen grips and translates the change in specimen length to two digital extensometers positioned outside of the clam-shell furnace. With the goal of studying how the evolution of creep damage affects resonance, a single dog-bone specimen was iteratively crept six times—denoted C1, C2, ..., C6—for a total creep strain of 8.8% after the C6 iteration as detailed in Table 4.2.

Table 4.2: Experimental creep strain increments

Step ID	Strain increment (%)	Total strain (%)
C1	0.27	0.27
C2	0.93	1.20
C3	1.43	2.63
C4	2.09	4.72
C5	1.41	6.13
C6	2.68	8.81

4.2.3 RUS Measurements

After each creep and fatigue iteration the specimen was removed from the experimental setup, and nondestructively evaluated via RUS at room temperature. Note that the application of a small strain gauge to the gauge section of the dog-bone, which was necessary for controlling the fatigue experiment, had a minimal affect on the resonance behavior. However, to be certain that artifacts of the experimental setup were not considered when investigating the changes in resonance due to fatigue damage, all of the resonance data was collected from the dog-bone after application of the strain gauge, including the baseline response.

The RUS setup was developed and custom-built by the Vibrant Corporation, with extensive details about the equipment discussed in Section 3.3, a cursory description of the measurement setup specific to the dog-bone specimen geometry is detailed here. Figure 4.5 depicts how the dog-bone specimen rests directly on four custom-built omnidirectional piezoelectric transducers (PT) with hemispherical SiC tips that together are referred to as the "PT cradle". The cradle is configured such that a dummy and drive PT are parallel to each other on one side of the cradle, with two receive PTs on the opposite side of the cradle to support the specimen. No coupling exists between the specimen and the PT cradle beyond the force of gravity. The drive PT is excited with a swept sinusoidal signal generated by the transceiver in 3 Hz steps. When the drive frequency

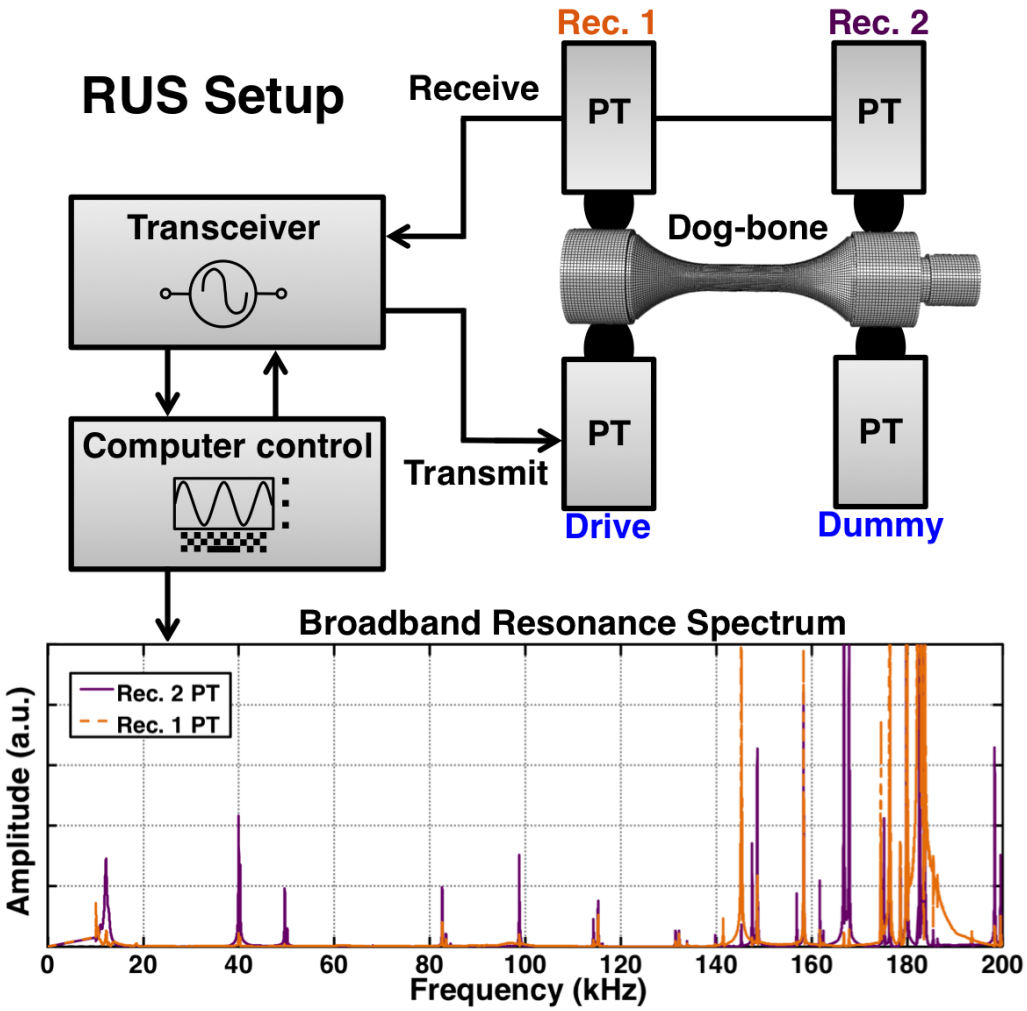

Figure 4.5: Experimental RUS setup utilized in this study to measure f_R of dog-bone specimens, detailed in [146]. The drive piezoelectric transducer (PT) excites the specimen to resonate with amplified deflections that the receive PTs (Rec. 1 PT and Rec. 2 PT) measure, yielding a broadband resonance spectrum.

nears a f_R of the specimen it will begin to resonate and generate amplified deflections that are measured by the two receive PTs contacting the specimen, indicated as Rec. 1 PT and Rec. 2 PT in Figure 4.5. The receive PTs convert vibrations back into an electrical signal that is returned to the transceiver, recorded, and plotted as a function of the drive frequency to yield a broadband resonance spectrum plot as depicted at the bottom of Figure 4.5.

A list of f_R that are characteristic of the test specimen were collected from the com-

bined broadband signal of the two receive PT. For the PT cradle configuration used in this study, the signal amplitudes are not reliably measured from one scan to the next because the relative position of the specimen may vary slightly between measurements and the dog-bone is free to deflect from the PT cradle. For this reason, and to minimize the chance of missing a low-amplitude peak due to any particular specimen placement, the specimen was removed and replaced on the cradle between every scan. Three broadband measurements were collected at each creep/fatigue increment with the average peak frequency used for all comparisons to modeled data. Measurements of f_R were very repeatable and routinely agree to within 0.02% for all modes, which is consistent with values in the literature for similar equipment and testing conditions [127].

High temperature exposure of a Ni-based superalloy in air, even in the absence of an applied load, will evolve the γ–γ' microstructure and form an adherent oxide scale. Therefore, in order to measure the isolated $\triangle f_R$ produced by high temperature exposure in air, the virgin creep dog-bone was subjected to an isothermal "pre-treatment" of 13 hours at 1080 °C prior to the first creep iteration. This isothermal heat treatment temperature is consistent with an aging heat treatment for the Mar-M247 alloy, and was also selected for the fact that 1080 °C is significantly greater than the 950 °C creep test temperature. Thus accelerating the kinetics of oxidation and microstructural evolution mentioned previously, and theoretically delineating an upper bound to the $\triangle f_R$ effects of a single isothermal heat treatment.

4.2.4 Fatigue Experimental Results

The mode-specific changes in dog-bone resonance frequencies ($\triangle f_R$, Equation (1.2)) resulting from the iterative ultrasonic fatigue tests, as measured from the baseline response, are presented in Figure 4.6. It was found that the $\triangle f_R$ remained relatively consistent over a large portion of the fatigue life. This result is consistent with theory as described

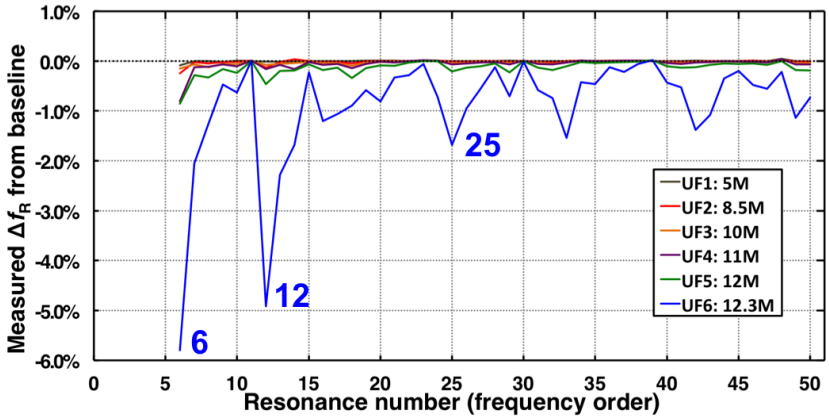

Figure 4.6: Measured $\triangle f_R$ from iterative ultrasonic fatigue test.

in [33], which requires cracks of considerable size in relation to specimen cross section before significant shifts in resonance frequency are discernible. The $\triangle f_R$ data plotted in Figure 4.6 correspond to the ultrasonic fatigue increments (UF#) as detailed in Table 4.1, with the number after the UF# ID indicating the number of fatigue cycles in millions. RUS data for UF6 was collected after 12.3 million cycles, after the dog-bone "failed" as indicated by the fatigue rig being unable to excite the dog-bone to a resonant condition as described in Section 4.2.1.

After the RUS data for UF6 was collected, the failed dog-bone specimen was broken into two pieces in order to observe the fatigue fracture surface. Photographs of the fracture surface are provided in Figure 4.7, demonstrating that the fatigue fracture had progressed across approximated 40% of the cross-sectional area of the dog-bone gauge section. It appears the fatigue crack initiated at an internal defect near the center of the region with dark contrast located near the bottom of the fracture surface.

4.2.5 Creep Experimental Results

The isothermal pretreatment (denoted PT1) and iterative creep tests conducted on the dog-bone specimen affected $\triangle f_R$ as shown in Figure 4.8 (a). The first five of the 50 lowest-frequency modes have been omitted from further analysis due to measurement

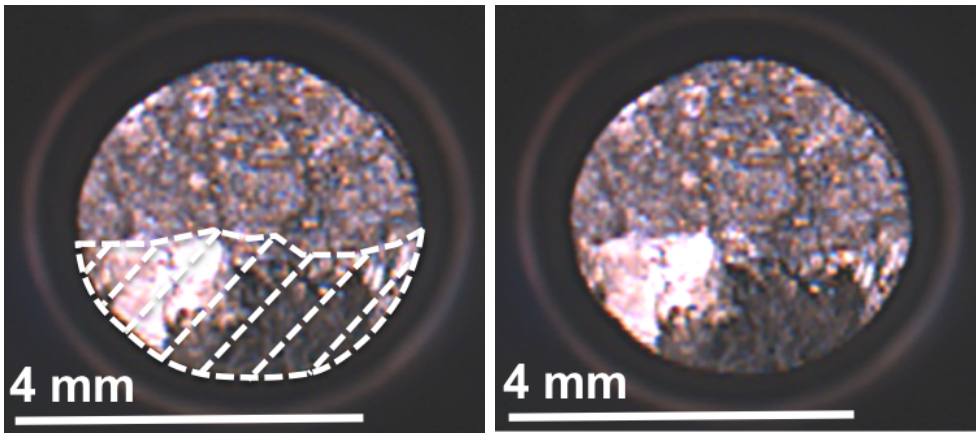

(a) (b)

Figure 4.7: Picture of dog-bone fatigue crack surface across approximately 40% of the gauge section (a) marked in white and (b) unmarked.

variability exceeding 0.02%; such variability is often observed [33], and is likely the result of specimen-cradle coupling effects [147]. The expanded inset Figure 4.8 (b) demonstrates how several resonance modes exhibited a slight increase in f_R as a result of the 13 hour 1080 °C pretreatment. Additionally, mass measurements of the specimen before and after the isothermal pretreatment indicated no appreciable change that would affect $\triangle f_R$. Thus surface oxidation and microstructural evolution have an insignificant effect on resonance under the investigated conditions—especially with respect to creep damage mechanisms—and are therefore omitted from further investigation.

Figure 4.8 (a) shows how greater amounts of creep strain result in a more-negative $\triangle f_R$ for most modes, consistent with a bar-like geometry specimen that increases in length due to plastic straining. Generally low-frequency modes are more affected than modes higher in the frequency regime; modes 12–13 and 16–17 appear to be most affected. Other modes e.g. 23–24 and 37–38 are affected very little by the evolution of creep strain in the dog-bone specimen.

One unexpected observation highlighted in Figure 4.8 (b) is the measured $\triangle f_R$ after the C1 creep iteration whereby the specimen experienced primary creep of nearly 0.3% strain before the test was halted. The average response of modes 5–50 was an increase

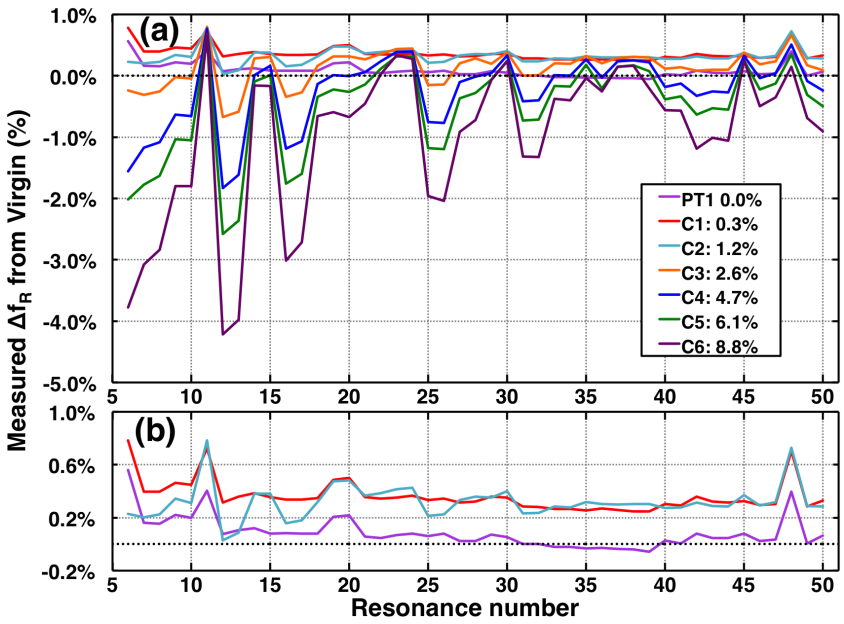

Figure 4.8: Measured $\triangle f_R$ for a dog-bone specimen subjected to: an aging pretreatment (PT1), and six subsequent creep iterations (C1–C6); all plotted in (a), with the first three increments detailed in (b) with an expanded ordinate axis.

in $\triangle f_R$ by approximately 0.4%. This global positive shift in f_R was also observed to occur in sibling Mar-M247 dog-bones after the first creep iteration. While a mechanism responsible for this global positive $\triangle f_R$ has not been identified, some possibilities are discussed in Section 4.4.2.

Beyond the geometry change induced by creep deformation, surface cracking is an additional mechanism of damage expected to affect resonance. Figure 4.9 (a)–(d) are light-optical micrographs that show the gauge section of the dog-bone following testing. Figure 4.9 (a) shows the blue-gray adherent oxide formed during the isothermal pretreatment (13 hour 1080 °C pretreatment), while Figure 4.9 (b) shows the same region after the C6 (8.8% creep strain) iteration. Note the development of surface cracks perpendicular to the loading direction, horizontal for all micrographs, after the C6 creep iteration. After collecting the C6 RUS data, the dog-bone was sectioned longitudinally to assess the penetration depth of the surface cracks and the extent of internal damage. Figure 4.9 (c) provides a cross-sectional view of almost the entire length of the gauge section. With

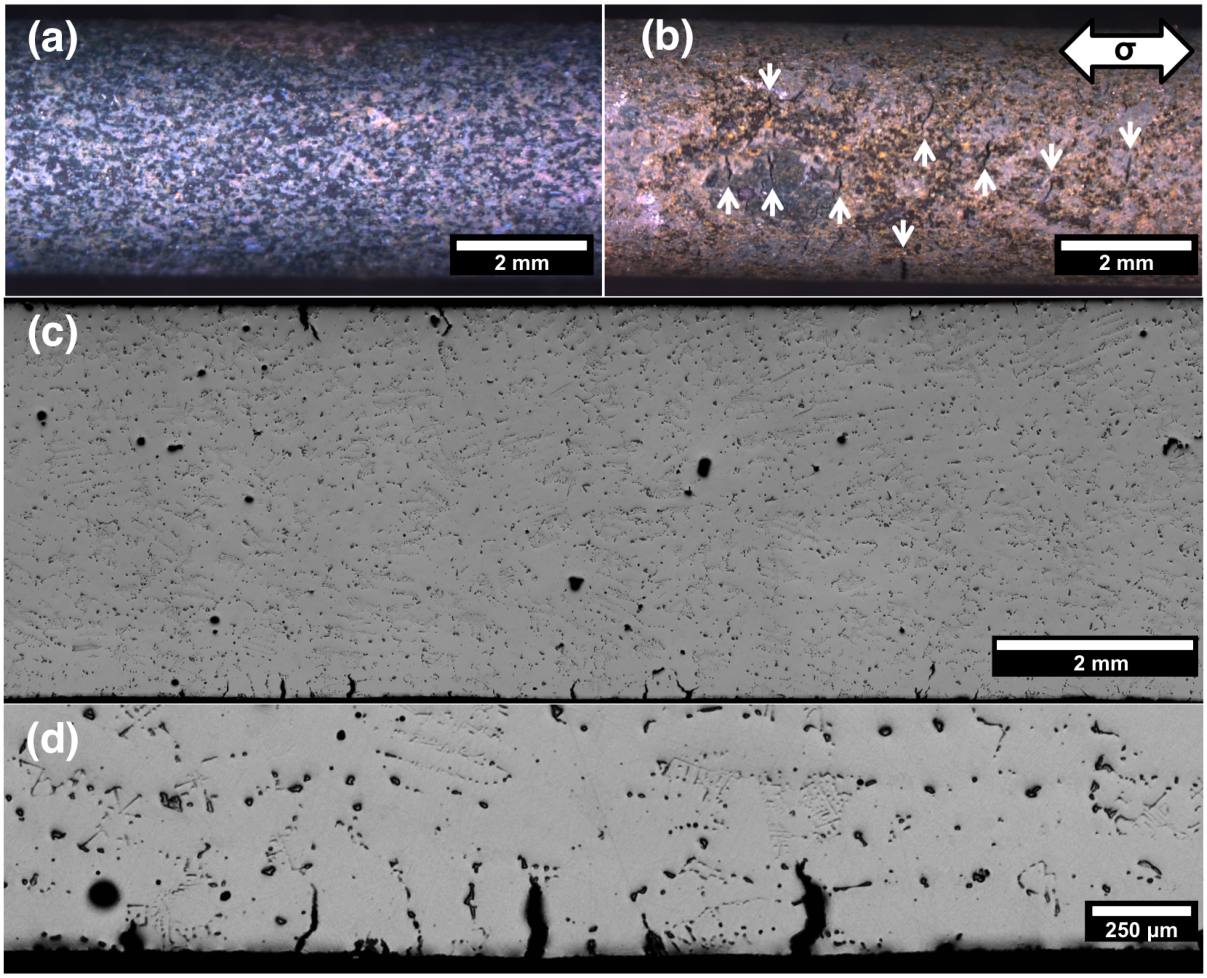

Figure 4.9: Light optical micrographs from the dog-bone gauge section after PT1 with 0% strain (a), or after 8.8% creep strain (b)–(d); the loading axis being horizontal. (a) and (b) show the evolution of surface oxide and cracks—marked with white arrows. Micrograph (c) depicts nearly the entire cross-section of the gauge which emphasizes the superficial nature of the cracks. Higher magnification of the surface is provided in (d), where except for a few large and highly circular pores, the remaining small features in dark contrast are identified to be script or blocky metal-carbides.

the exception of a few large circular casting pores, the small internal features in dark contrast are metal-carbides with blocky or script morphology. No metal-carbide interface separation was observed. Finally Figure 4.9 (d) provides a magnified view of the near-surface damage whereby many cracks are observed penetrating 200 µm into the gauge section and likely contribute to the accelerated tertiary creep rate observed during the C6 iteration.

4.3 FE Modeling Methods and Results

4.3.1 Material Properties for Modeling Resonance

Since low-order resonances cause deflections over large volumes of the resonating body, these modes effectively probe the average elastic response material [148]. This fact is important to consider when building a FE model for predicting f_R of a specimen comprised of a polycrystalline multi-phase material such as Ni-based superalloys. A FE model-based analysis by Nygards [87], discussed in detail in Section 2.1.3, suggests that the polycrystalline Mar-M247 material used in this study can be effectively modeled as elastically isotropic. This is due to the grain structure, depicted in Figure 4.1, consisting of more than 15 grains through-thickness and no apparent texture. The assumption of homogeneous isotropic elastic properties here greatly simplifies FE model design, but it is always important to consider the validity of such an assumption as discussed in Chapter 2, because there are many cases where isotropy cannot be assumed.

Isotropic elastic properties can either be: measured, referenced from a reputable source in the literature, or calculated from single crystal elastic constants (C_{ijkl}) via polycrystalline averaging scheme as discussed in Section 2.1.3. Here, a rule-of-mixtures (ROM) average was made from referenced C_{ijkl} values of Mar-M247's constituent γ [95] and γ' [125] phases assuming a 0.55 volume fraction of γ'. Then these ROM average C_{ijkl}

were converted to an isotropic Young's modulus: E = 216 GPa and Poisson's ratio: ν = 0.313 via Gairola and Kroner's 3rd order polycrystalline average (Equation (2.36)) [92]. With a density of 8700 kg/m^3 per [80] the material properties of the model are fully defined for predicting f_R.

4.3.2 Model of the Dog-Bone Specimen

Abaqus CAE 6.12 [149] was used to model the dog-bone and predict the f_R of the specimen before and after damage. The virgin dog-bone model, with basic dimensions specified in Figure 4.3 and a detailed schematic provided in Section 3.5.2, was discretized into a FE mesh containing approximately 150,000 3D linear wedge and hexahedral elements inside the Abaqus environment [149]. Then the Lanczos eigensolver was used to determine the first 50 lowest-frequency resonance modes to establish the baseline response. After the baseline response was characterized, damage was imparted to the model to determine $\triangle f_R$ as a function of damage.

4.3.3 Results from Virgin Dog-Bone Model

A baseline response of the virgin dog-bone is produced using the modeling methods as described above, with the first 50 f_R provided in Table 4.3. The dog-bone model predicted mode-shapes that are similar to those of a resonating bar or rod, which are described in detail by Migliori and Sarrao [33] and Zadler et al. [46]. This chapter uses similar nomenclature, classifying the resonance mode-shape of the first 50 modes as one of four distinct mode-types: longitudinal bending, extensional, torsional or transverse bending. Figure 4.10 plots these four fundamental mode-types with exaggerated deflection characteristics, while the actual deflections produced by a typical RUS measurement are too small and fast to be resolved by the naked eye. Longitudinal and transverse bending modes consist of non-axisymmetric flexural motion of the longitu-

dinal or transverse axis of the dog-bone, respectively. While torsional and extensional modes are generally axisymmetric, with torsional modes consisting of pure shear motions while extensional modes exhibit predominately longitudinal breathing motions [33, 46]. All resonance modes are either a fundamental mode, i.e. the first-order mode of a specific mode-type, or a higher-order resonance of fundamental modes.

Table 4.3: FE model predicted f_R and mode-type for virgin Mar-M247 dog-bone.

Mode no.	**Frequency** (kHz)	**Mode type**	**Mode no.**	**Frequency** (kHz)	**Mode type**
1	3.1861	b	26	145.49	b
2	3.1861	b	27	155.31	r
3	4.0673	t	28	155.31	r
4	12.384	b	29	160.81	t
5	12.384	b	30	162.05	e
6	19.058	e	31	162.51	b
7	39.183	b	32	162.51	b
8	39.183	b	33	172.05	b
9	49.145	b	34	172.05	b
10	49.145	b	35	176.13	r
11	65.288	t	36	176.13	r
12	82.334	b	37	176.42	r
13	82.334	b	38	176.42	r
14	84.633	t	39	182.90	b
15	98.731	e	40	182.90	b
16	114.22	b	41	185.23	e
17	114.22	b	42	191.33	t
18	116.44	e	43	197.37	b
19	131.23	b	44	197.37	b
20	131.23	b	45	206.78	b
21	133.18	t	46	206.78	b
22	139.89	t	47	207.48	e
23	145.00	r	48	216.73	t
24	145.00	r	49	217.95	e
25	145.49	b	50	218.36	b

Mode-types: longitudinal bending (b), torsional (t), extensional (e) and transverse bending (r).

When the FE models contain orthogonal symmetry about the long axis of the dog-bone, the longitudinal bending modes occur in "degenerate pairs". This means that two distinct longitudinal bending modes exist with same f_R and the same non-axisymmetric flexural motion, except the modes vibrate orthogonal to each other. Such degeneracy is also exhibited by transverse bending modes. With instances of degenerate modes becoming more prevalent as the elastic properties or the specimen geometry exhibit higher symmetries. For example, assuming a material with cubic elastic symmetry that is aligned with the major axes of the specimen geometry: a sphere would exhibit more degenerate modes than a cube, a cube would exhibit more degenerate modes than a rectangular parallelepiped, and a completely asymmetric geometry would exhibit no degenerate modes. The same logic is applicable to the various elastic symmetries as discussed in Section 2.1.2.1.

Interestingly, the degenerate modes predicted by the models are often not observed in measurements due to natural material inhomogeneities and geometry imperfections that disrupt the symmetry required for degeneracy. In discussing the potential NDE capability of RUS for evaluating the cylindricity of bearings, Migliori and Darling point out that a break in cylindrical symmetry of only 1 part per million is sufficient to disrupt the degeneracy of bending modes enough to measure two distinct peaks [150]. In these instances, the measured bending modes occur as a pair of discrete peaks in close proximity, with the degree of separation often correlated to the extent of asymmetry by simple NDE with RUS frameworks [50].

4.3.4 Methods of Modeling Fatigue Cracks

The FE model representing a dog-bone specimen with a fatigue crack is detailed in Figure 4.11 (a)–(c). First, a fatigue crack was modeled at the center of the 10 mm dog-bone gauge section as Figure 4.11 (a) demonstrates. The fatigue crack is modeled perpendicu-

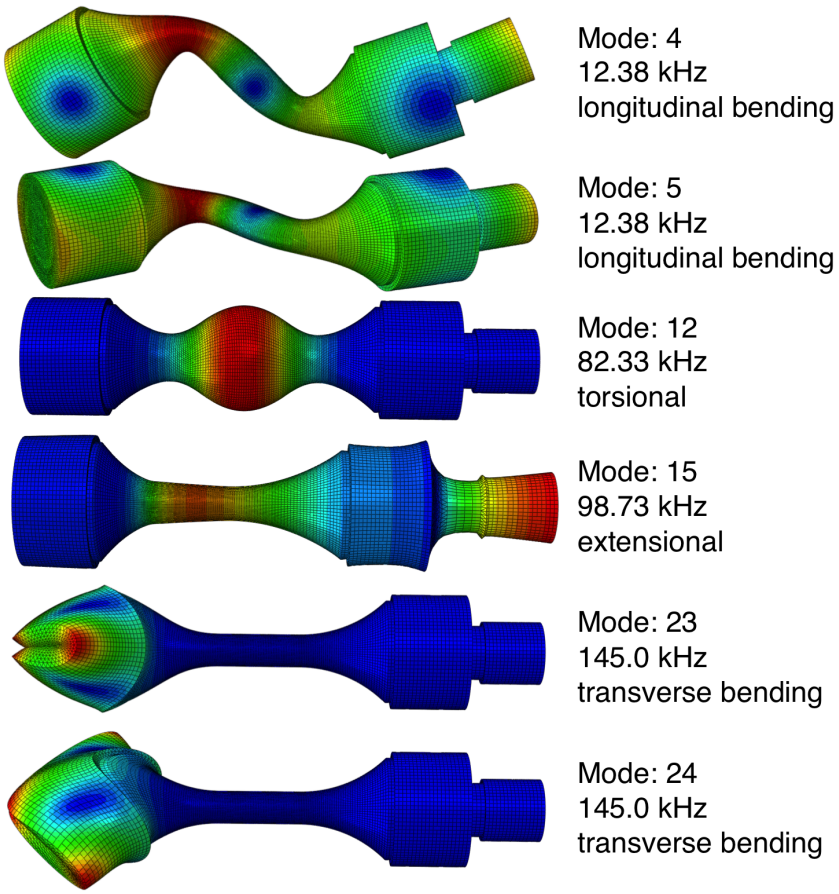

Figure 4.10: Exaggerated FE model depictions of the four low-frequency dog-bone mode-types, with the resonance mode number, f_R, and mode-type to the right of each mode. Note that all bending modes occur in degenerate pairs.

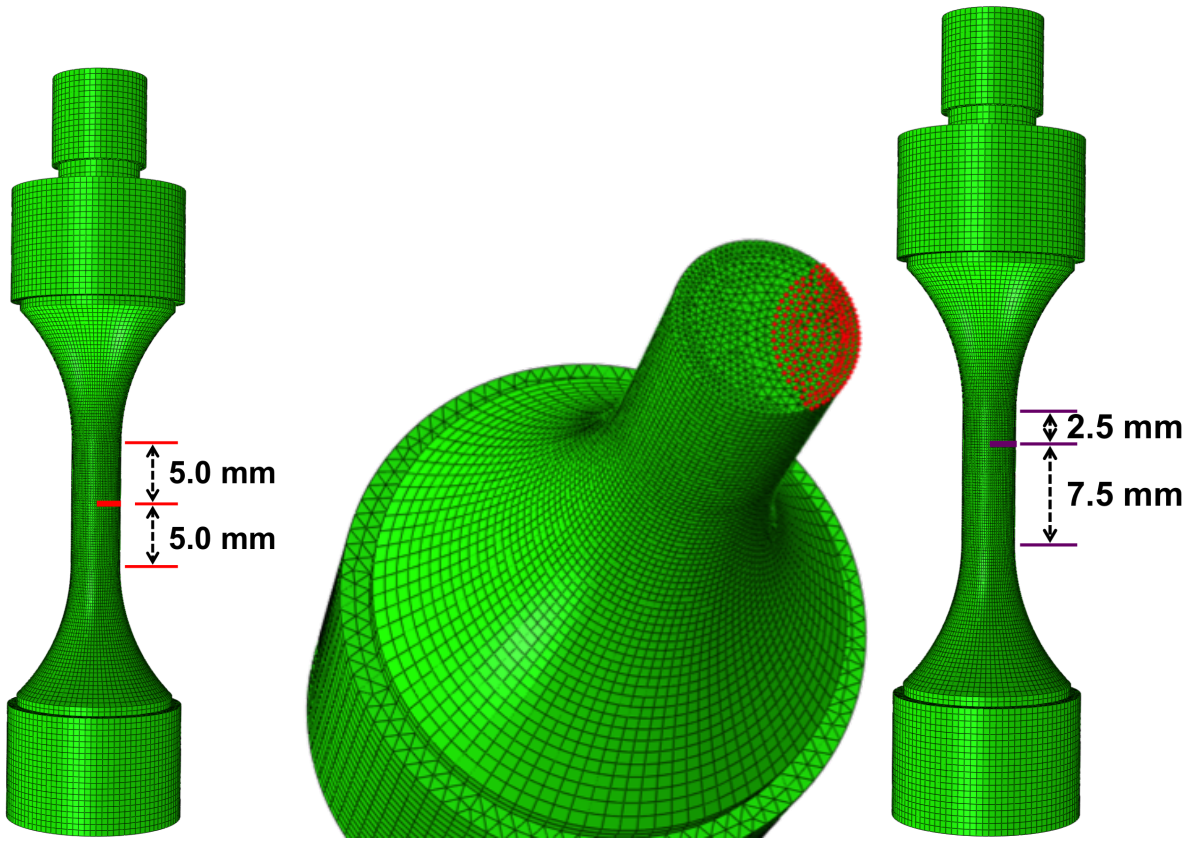

Figure 4.11: FE model of dog-bone specimen with a fatigue crack located at (a) the center of the gauge section, with a (b) cross sectional depiction of the crack shape highlighted in red, as well as a (c) secondary location of the fatigue crack 2.5 mm above the center of the gauge.

lar to the long axis of the dog-bone, consuming approximately 40% of the cross-sectional area in accordance with the observations detailed by Figure 4.7. Figure 4.11 (b) details the geometry of the modeled crack surface, with the FE nodes marked in red representing the elements where tie constrains were removed from neighboring elements to simulate the presence of a crack. Additionally, the same fatigue crack was also modeled at 2.5 mm above the center of the dog-bone gauge section as detailed by Figure 4.11 (c), with important implications for the predicted $\triangle f_R$ response.

4.3.5 Results from Fatigue Crack Model

The FE model predicted $\triangle f_R$ as a result of the two fatigue crack scenarios are provided in Figure 4.12. One of the key differences between the $\triangle f_R$ response as a result of changing the vertical location of the crack along the dog-bone gauge section is: it changes which resonance modes are most affected. Ignoring the first 5 modeled modes because they were not measured, the three most affected modes when the crack was centered on the dog-bone gauge section are modes 6 (extensional), 16 (longitudinal bending), and 30 (extensional). When the crack was moved 2.5 mm above center, mode 6 (extensional) was still among the top three most affected modes, but now mode 12 (longitudinal bending) and mode 25 (longitudinal bending) were most affected. One similarity between the $\triangle f_R$ results of the two models is the extent of degenerate mode splitting. Longitudinal bending modes, 7/8, 9/10, 12/13, 16/17, 25/26, etc., were all degenerate pairs according to the virgin model. But as a result of the symmetry disrupting fatigue cracks, these modes now have distinct f_R as indicated by the $\triangle f_R$ results. Of the four mode-types, extensional, torsional, and longitudinal bending all appear to exhibit considerable sensitivity to the presence of a crack, while the transverse bending modes are almost completely unaffected. This result might not be particularly surprising considering the localized deflection characteristics of the low-order transverse bending modes, as depicted in Figure 4.10. All together, these initial FE model results are promising for the potential use of RUS. Not only for identifying the occurrence of a fatigue crack, but also the potential of providing size and location information about the crack.

4.3.6 Methods of Modeling Creep Damage

The dog-bone shape change due to creep was modeled with a nonlinear plastic analysis which entails a straightforward FE implementation and yields a similar deformed geometry as creep. Specifically, a power-law hardening elastic-plastic constitutive law was

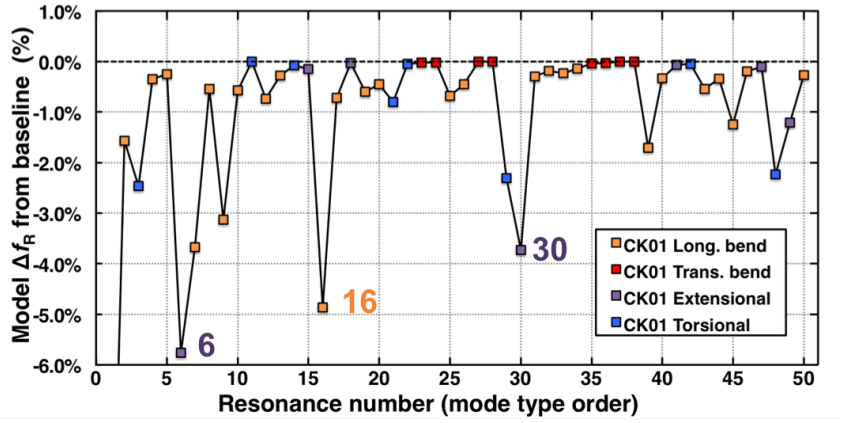

(a)

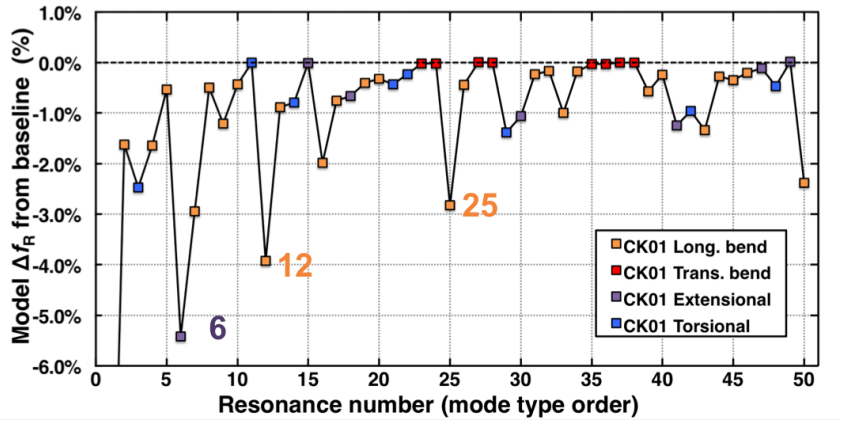

(b)

Figure 4.12: Modeled $\triangle f_R$ due to a fatigue cracks perpendicular to the long axis of the dog-bone specimen at (a) the center of the gauge section and (b) 2.5 mm above the center of the gauge section.

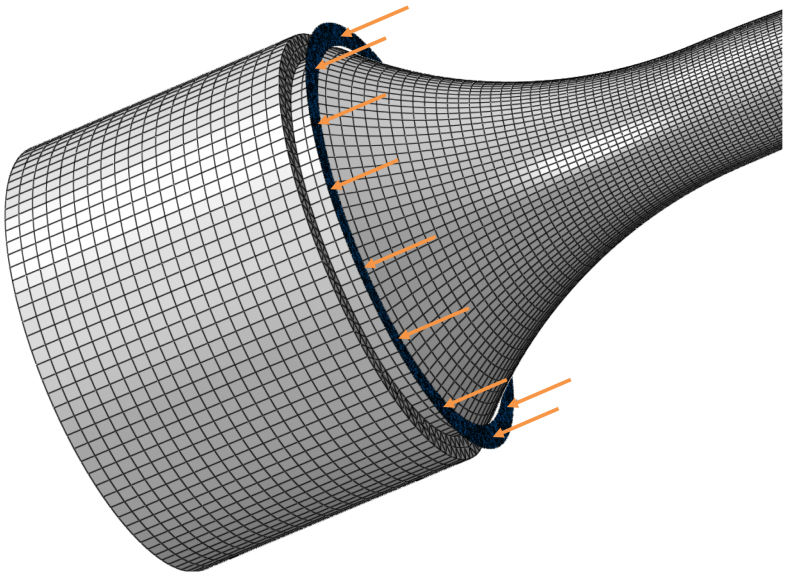

Figure 4.13: FE dog-bone model with a non-deforming ring of material above the recessed end of the dog-bone shoulder. The non-deforming ring is lowered onto the shoulder, in the direction the arrows indicate, to load the specimen similar to experiments.

employed, and is represented in one dimension with:

$$\epsilon = \frac{\sigma}{E} + \frac{\alpha\sigma}{E}\left(\frac{|\sigma|}{\sigma_y}\right)^{m-1}, \tag{4.1}$$

where σ_y is the yield strength, σ is stress, ϵ the total mechanical strain (elastic and plastic), α yield offset, and m is the hardening exponent [149]. The three dimensional constitutive law additionally requires a Poisson's ratio and fully defines the material with nonlinear elastic-plastic constitutive behavior [149]. Since the RUS measurements are collected from an unloaded dog-bone specimen with no elastic strains, the yield strength in the constitutive law was set at an arbitrarily low value while the remaining parameters were as follows: $E = 216$ GPa, $\alpha = 0.002$, $m = 10.0$, and $\nu = 0.313$.

Once populated with material properties, the dog-bone model was loaded in uniaxial tension to produce a strained geometry corresponding to the six strain levels from the experimental work detailed in Table 4.2. Simulating the conditions of the experimental creep setup, the dog-bone was loaded with a non-deforming ring around the recessed

shoulder grips as illustrated in Figure 4.13. As the non-deforming ring contacts the dog-bone, deformation is imparted according to the constitutive material behavior per Equation (4.1). Figure 4.14 depicts a cross-sectional view of the specimen before and after 8.8% strain. Displacement magnitude maps overlay the deformed dog-bones (center and right), as measured with respect to the loading direction (LD) and transverse direction (TD). The LD dog-bone shows uniform elongation within the gauge section, while the TD dog-bone depicts contraction of the gauge cross-section.

4.3.7 Results from Creep Damage Model

The deformed dog-bone model was used as the input geometry for the Abaqus Lanczos eigensolver [149]. As before, the first 50 resonance modes were calculated and the $\triangle f_R$ with respect to the virgin dog-bone model determined as a function of creep strain. FE models were run for each of the six creep increments outlined in Table 4.2. Plots reporting the $\triangle f_R$ for the C2 and C3 creep iterations, 1.2% and 2.6% strain respectively, are provided in Figure 4.15. Mode-type is classified based on the model predicted mode-shapes and denoted by the color of the symbol. Note the different abscissa label between Figure 4.15 (a) and (b). *Frequency order* plotting highlights mode-order switching in the frequency regime while *mode-type order* plots correct for mode-order switching and focus attention on how varying levels of damage affects $\triangle f_R$. Both plotting methods are valid because $\triangle f_R$—by definition in Equation (1.2)—are calculated with respect to the baseline frequency for each distinct resonance mode (i.e. mode-type). Ultimately mode-type order is preferred for depicting how varying levels of damage affect a given resonance mode and will prove useful for comparing measured and modeled $\triangle f_R$ data as demonstrated in Section 4.4.

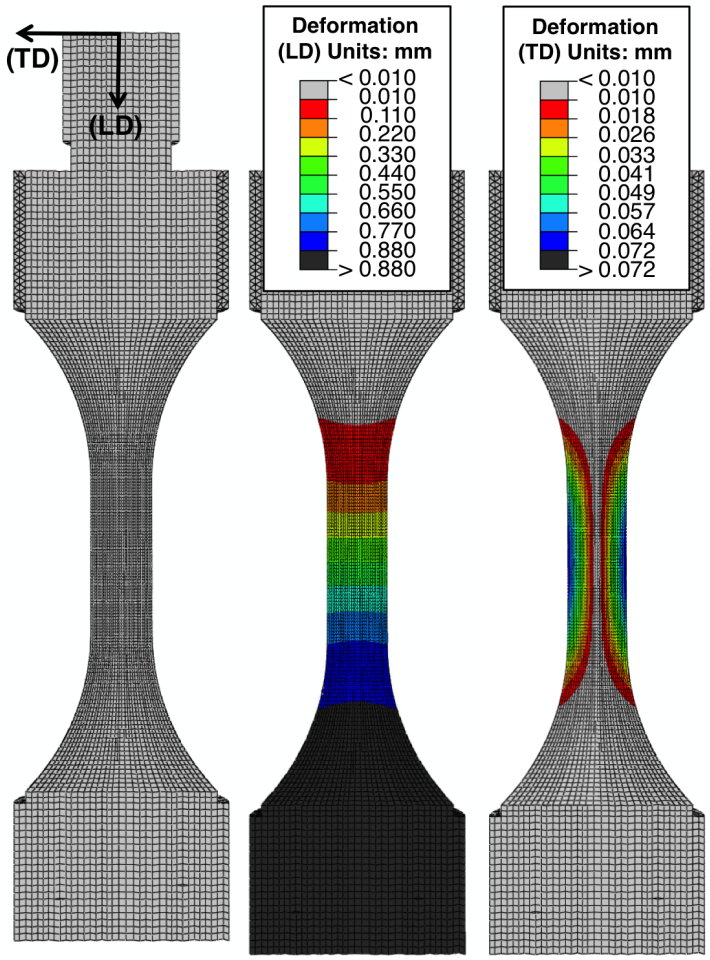

Figure 4.14: Deformation maps from the dog-bone cross-section showing the magnitude of displacement before (left) and after (center and right) 8.8% strain. Elongation along the loading direction (LD) is mapped on the center dog-bone, while the gauge constriction in the transverse direction (TD) on the right. The deformed dog-bone shape is shown to scale, note the key values are in mm and are an order of magnitude smaller in the TD.

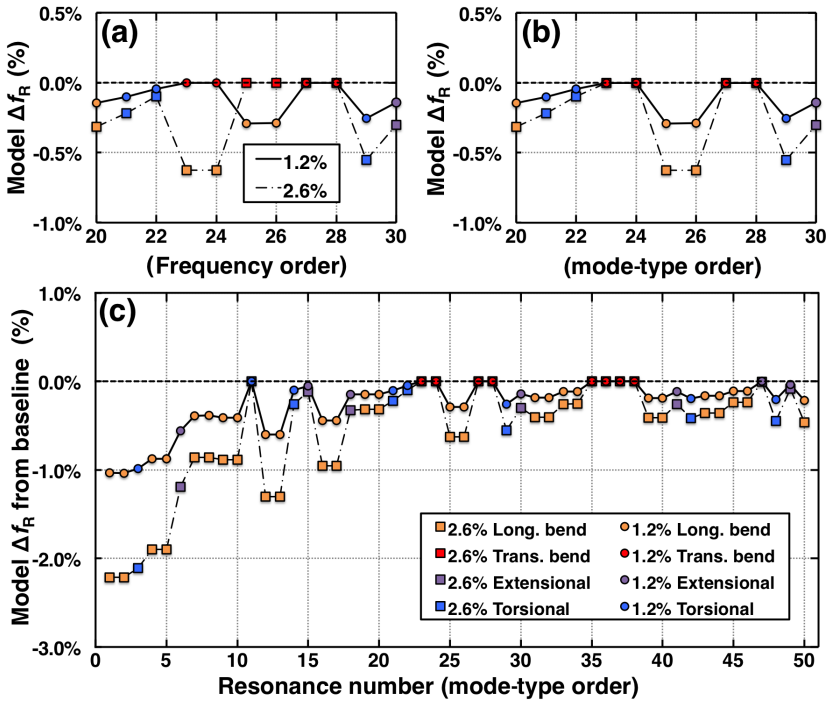

Figure 4.15: Modeled $\triangle f_R$ for a dog-bone with a C2 (1.2%) and C3 (2.6%) creep strain geometry. Plots (a) and (b) show the difference between frequency order and mode-type order respectively, while (c) demonstrates the $\triangle f_R$ trends with increasing creep strain for the first 50 resonances in mode-type order.

4.3.8 Methods of Modeling Surface Cracks

The FE model representing surface cracks is depicted in Figure 4.16. The blue elements represent crack surfaces where tie constrains were removed from neighboring elements across the crack face to simulate half-penny shaped cracks. The first FE model contained 20 cracks that were distributed in five planar cross-sections normal to the loading direction, four cracks per plane, and a planar spacing of 2.5 mm. Each of the 20 cracks were identical and covered 4.8% of the gauge cross-section.

An orthogonally symmetric crack distribution like the 20 crack model described above ascribes a high degree of symmetry to the crack distribution. Indeed a more-random distribution of cracks would certainly be expected to form experimentally, supported by Figure 4.9. Therefore a second model for investigating the $\triangle f_R$ associated with an asymmetric distribution of cracks was also created by randomly removing four of the 20 cracks described previously. One crack was removed from 4 different cross-sections as demonstrated in Figure 4.16, providing a second 16 crack FE model with an asymmetric crack distribution.

4.3.9 Results from Surface Cracks Models

The effect of cracks on the resonance behavior is evaluated as before, by submitting the cracked dog-bone model to the eigensolver and comparing the results to the baseline dog-bone model without cracks. Figure 4.17 details the 20-crack model results with square symbols and the 16 crack model with circles. A cursory observation indicates that the $\triangle f_R$ between the two different crack scenarios are quite similar in character, except for two predictable differences. First, the magnitude of the $\triangle f_R$ for all modes of the 16 crack model are smaller than the corresponding 20 crack model—as fewer cracks result in a smaller drop in f_R. Second, it is clear that the bending modes are not degenerate in the 16 crack model, with modes 9/10 and 16/17 particularly evident of this loss in degeneracy

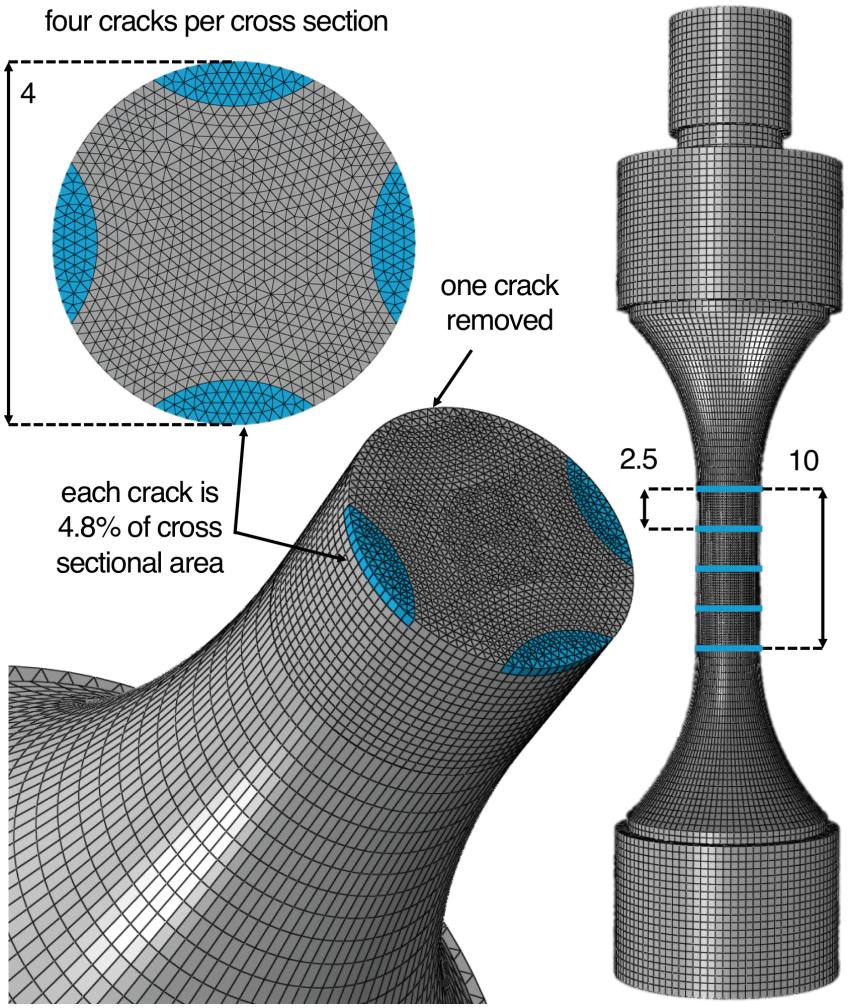

Figure 4.16: FE model of dog-bone specimen surface cracks, each 4.8% of the cross-sectional area of the gauge. Cut-away views on the left detail three or four cracks modeled per crack plane. The five planes of cracks normal to the loading direction are depicted on the right, with 2.5 mm separation between planes of cracks along the 10 mm gauge.

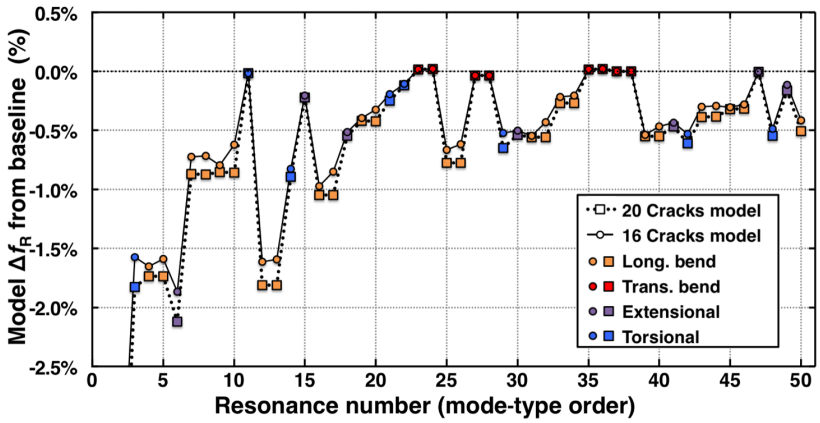

Figure 4.17: FE model predicted $\triangle f_R$ due to a symmetrical distribution of 20 cracks (square points connected by a dashed line), as compared to an asymmetrical distribution of 16 cracks (circle points connected by a solid line).

due to the asymmetrical crack distribution. Degenerate-mode splitting is also observed in the measured data of Figure 4.8, suggesting that damage accumulation is not completely symmetric about the long axis of the dog-bone.

4.4 Discussion: Analysis of Modeling and Experimental Results

Efforts to compare measured and modeled results are important to validate the forward modeling framework and to verify that the modeled damage mechanisms capture the predominant $\triangle f_R$ of the measured specimen. Modeled results are not validated in absolute terms by comparing lists of modeled and measured f_R. Instead, $\triangle f_R$ for the modeled and measured damage mechanisms are compared directly, allowing for validation that the dominant mechanisms affecting resonance are properly identified and modeled, while eliminating specimen or model-specific variations that may affect baseline f_R behavior. Comparing lists of $\triangle f_R$ also eliminates the need for FE modeling efforts to produce a facsimile of a particular experimental specimen. Since natural (and unavoidable) material inhomogeneities and manufacturing imperfects generate a wide distribution of character-

istics for a nominal specimen design, its inevitable that any physical specimen will exhibit some unique baseline characteristics that appear to disagree with the f_R profiles of a modeled specimen. This natural variation can even lead to disagreement in the mode-type order of the modeled and measured datasets, which would almost assuredly confound efforts to directly compare lists of f_R, but which is ameliorated through comparing lists of $\triangle f_R$ results. This is because it is almost impossible to classify RUS measured resonance modes without additional measurements of the resonance mode shape. However, it is much easier for an operator to track measured modes over a period of time where damage is accumulated based on characteristics of the measured RUS spectrum that are difficult to quantify, e.g. peak width, peak shape, interaction with neighboring peaks, and the relative peak amplitudes. Then, in conjunction with modeled $\triangle f_R$ results, the measured modes are more easily identified by their $\triangle f_R$ characteristics, which allowed for baseline mode order disagreement to be identified and corrected as was necessary for analysis of the creep results discussed in Section 4.4.2.

4.4.1 Analysis of Fatigue Models and Measurements

Simply overlaying the measured $\triangle f_R$ results collected after UF6 with 12.3 million fatigue cycles with the FE model predicted results, presented in Figure 4.12, is sufficient for demonstrating which fatigue crack model scenario is most-similar to the measured result. Figure 4.18 (b) with the fatigue crack 2.5 mm above the center of the gauge section demonstrates excellent agreement with the measured results and far superior agreement as compared to Figure 4.18 (a). Even the substantially simplified FE model representation of the cracked dog-bone correctly identifies the resonance modes that are most affected. Though the model under predicts the $\triangle f_R$ magnitude for mode 12 and over predicts the magnitude of mode 25, this disagreement is likely due to the FE model not precisely capturing the crack plane and morphology of the experimental specimen.

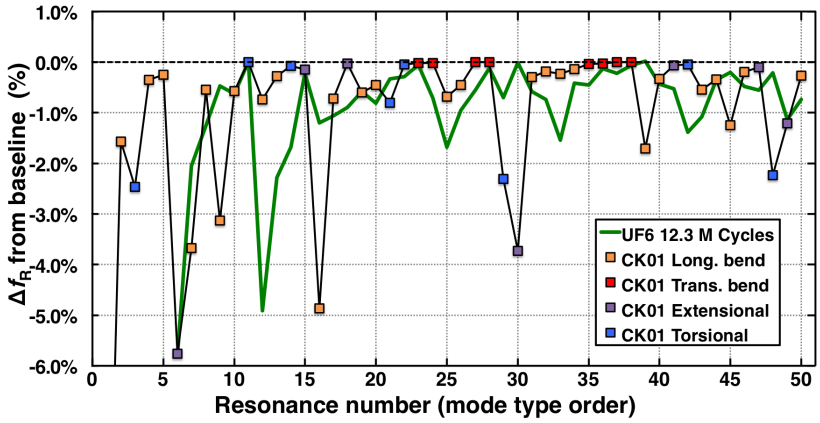

(a)

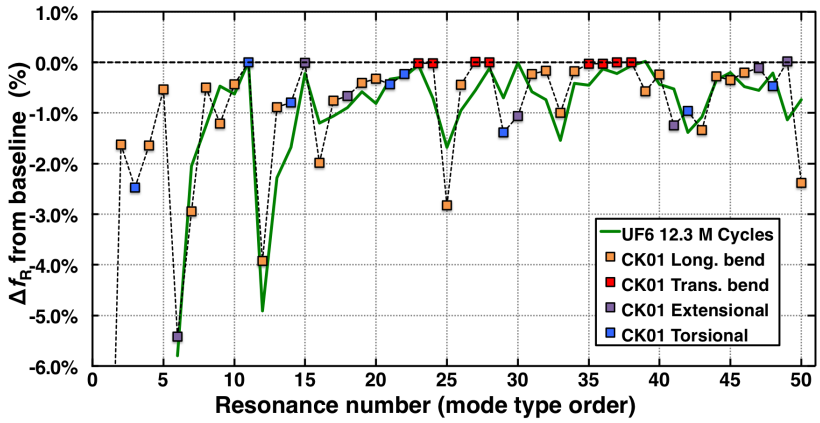

(b)

Figure 4.18: Measured $\triangle f_R$ after the UF6 fatigue iteration overlaid atop the modeled $\triangle f_R$ due to a fatigue crack at (a) the center of the gauge section and (b) 2.5 mm above the center of the gauge section.

Overall, the strong agreement between the measured and the modeled fatigue results validate the FE modeling methods and demonstrate how integrating FE models with RUS measurements can provide mode-type information to measured resonance data.

4.4.2 Analysis of Creep Models and Measurements

Unlike the fatigue analysis discussed previously, analysis of the creep data requires more than simple overlays of measured and modeled $\triangle f_R$ results for validation. This is because the creep specimen experienced multiple concurrent damage mechanisms affecting

resonance. So to assist in the model-to-measure comparison a simple $\triangle f_R$ comparison metric called the "residual" is defined here as:

$$Residual = \Delta f_R^{Measured} - \Delta f_R^{Modeled} \ . \tag{4.2}$$

Then through a progressive process of modeling the predominant outstanding damage mechanism suspected of affecting resonance, the residual between modeled and measured $\triangle f_R$ is reduced until the majority of measured response is accounted for, and the modeling effort is validated. A significant non-zero residual exhibited by a multitude of modes indicates additional mechanisms are operable in the measured specimen, or the model is over/under-predicting the $\triangle f_R$ response. Finally, it is important to remember that RUS measurement error, as reported in Section 4.2, can only be responsible for ±0.02% of the residual, while natural variability in the specimen population is made irrelevant by comparing the dog-bone to itself over time.

Comparing dog-bone creep modeling results to experimentally measured values trough a simple residual analysis and plotting the results for the first 50 resonance modes in mode-type order yields Figure 4.19 (a)–(c). The uncorrected residual in subplot (a) depicts the difference between the measured $\triangle f_R$ of Figure 4.8 and the modeled $\triangle f_R$ from *only* the creep deformation model described in Section 4.3.6. In Figure 4.19 (a), the C1–C5 residuals are generally centered around +0.4–0.5%, with additional scatter of ±0.5% for select modes. Had the shape change associated with creep been the single predominant mechanism affecting resonance, the residuals for C1–C6 would all be centered around 0%. This does not occur because the C1 residual, displayed individually in Figure 4.19 (b), is the result of an anomalous global +0.4–0.5% $\triangle f_R$ as first mentioned in Section 4.2.5. To produce the corrected residual subplot (c), the relatively small global C1 anomaly was removed from the data while *baseline mode order disagreement* was corrected between the measured and modeled data. In fact, agreement of baseline mode order would only

occur if the two baselines had the same frequency order.

Correcting for disagreement between measured and modeled baseline orders is straightforward and justified by a reduction in the sum of squared residuals (SSR), a metric of the total disagreement between measured and modeled $\triangle f_R$. The SSR is calculated as the squared residual for each mode, summed over all modes (6–50), and all creep iterations. The first occurrence of disagreement identified involves modes 27–30 in Figure 4.19 (a). All four modes occur within ±1% of each other in f_R and the SSR is reduced from 0.780% to 0.686% after switching the resonance number of measured modes: 27–28 with 29–30. According to the FE models modes 27–28 are a degenerate transverse bending pair, which we already know are mostly insensitive to the evolution of creep damage, and as a degenerate pair it follows that they would behave similarly and appear in close proximity to each other in f_R. The only additional occurrence of disagreement is between modes 48 and 49, which also occur within ±1% of each other in f_R and reduce the SSR after correcting the disagreement.

The anomalous positive $\triangle f_R$ after C1 would be consistent with either an increase in modulus or a decrease in density, but is not consistent with a change in geometry. While changes in the γ–γ' phase fraction could affect the modulus, a 0.8% increase in Young's modulus would be required for a 0.4% increase in f_R. However, a minimum 10% change in phase fraction would be required due to the γ [95] and γ' phases [125] exhibiting such similar elastic moduli. Such a significant change in microstructure was neither expected nor observed, but was considered as a mechanism to explain the anomalous behavior. Instead of a change in modulus, it is likely that a combination of mechanisms including changes in residual stress and/or dislocation density are responsible. Ultimately, the mechanism/mechanisms responsible for the anomalous C1 behavior remain unclear—warranting further investigation. A possible avenue of investigation could be nonlinear ultrasonic measurements of the dog-bone before and after primary creep, using the ultrasonic fatigue setup. As the dog-bone geometry is designed for both creep and ultrasonic

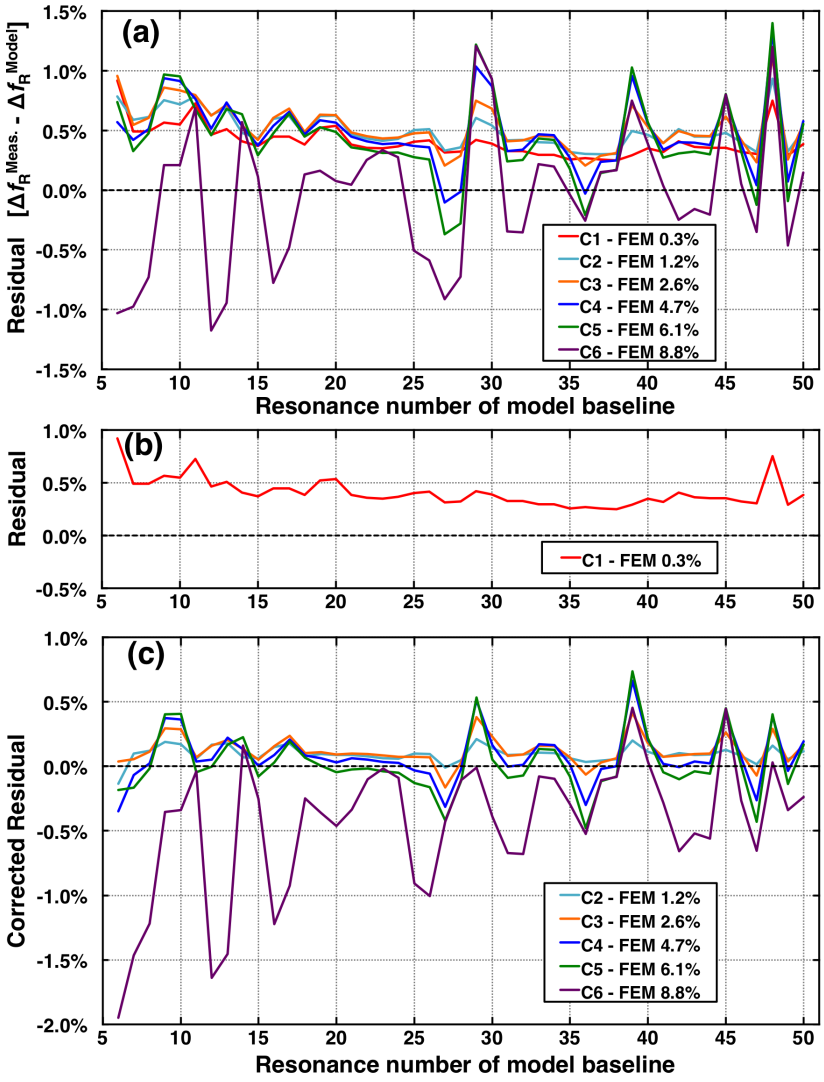

Figure 4.19: Residual plots showing (a) the initial residual values for each mode with the average residual for C1–C5 centered around 0.5% due to (b) the anomalous positive shift of C1. When this C1 residual is set as the new baseline for C2–C6, and mode-order switching corrected for modes 27–30 and 48–49, a corrected residual plot (c) elucidates the good agreement between measured and modeled results for creep iterations C2–C5, and marked divergence of C6.

fatigue, small levels of creep strain should not inhibit the excitation of the 20 kHz extensional mode necessary for nonlinear ultrasonic measurements as detailed by Kumar, Torbet, Pollock, and Jones [133]. Perhaps these measurements, in conjunction with the theory of ultrasonic wave interactions with dislocations proposed by Cantrell [136] could explain the observed behavior through measured changes in: dislocation density, loop length, or average residual stress.

Returning to the corrected residual plot, Figure 4.19 (c), it is clear that the creep geometry change model alone sufficiently predicts the $\triangle f_R$ for most modes of C2–C5, agreeing particularly well up to resonance number 25. However, the C6 residual indicates that the deformation model alone significantly under-predicts the $\triangle f_R$ observed in the measured data after 8.8% strain. To explain the negative residual that remains, an additional damage mechanism must be considered. Notably, this negative residual coincides with the observation of extensive surface cracking depicted previously in Figure 4.9. To demonstrate that the surface cracks are indeed responsible for the significant negative C6 residual that remains, an overlay of the C6 corrected residual from Figure 4.19 (c) was plotted with the 16 crack FE model from Figure 4.17 to yield Figure 4.20. When combined, the similarity of the C6 residual to the 16 crack model $\triangle f_R$ in both character and magnitude affirms that surface cracks are a dominant mechanism affecting resonance after 8.8% creep strain.

The residual metric is effectively an aggregate value of the damage affecting resonance in the measured specimen which has not been addressed by the current FE damage models. A substantial unexplained residual will hinder NDE efforts by requiring damage mechanisms exhibit $\triangle f_R$ with a magnitude larger than that of the residual, on a per-mode basis. For example, consider the band of modes 11–24 which exhibit relatively small residuals and multiple modes sensitive damage. Scanning such a band of frequencies would likely be desirable as part of an NDE framework. Considering modes 11–24 of C2–C5, residuals vary between a low of -0.09% (for C5 mode 24) to a high of 0.24% (for

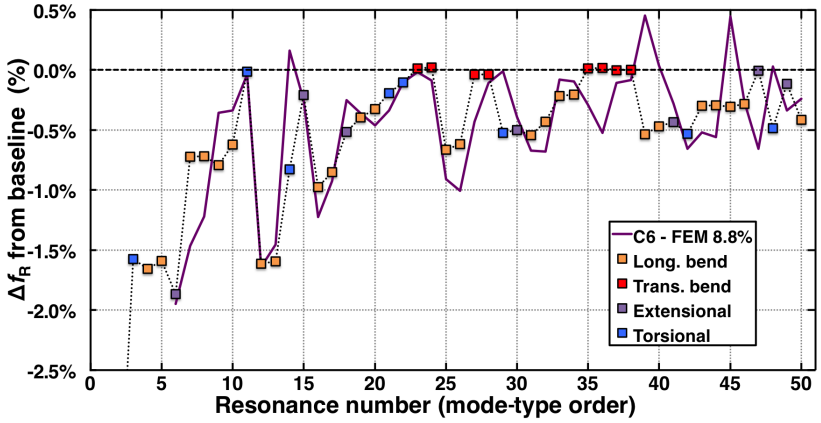

Figure 4.20: FE model of $\triangle f_R$ from 16 cracks along the dog-bone gauge section overlaid with the C6 corrected residual.

C3 mode 17), giving a range of 0.33%. With the conservative assumption that the $\triangle f_R$ of a diagnostic mode must exceed 0.33% before it is reliably detectable, the detectability limit for creep in the current study would equate to a creep strain of 0.66%. According to the FE models, elongation of the 10 mm dog-bone gauge section by 0.66%—an increase in gauge length of only 0.066 mm—would produce a -0.33% $\triangle f_R$ for modes 12–13. Therefore, even by conservative estimates the overall dog-bone specimen need only increase in length from 59.400 to 59.466 mm before creep elongation is reliably detected.

4.4.3 Distinguishing Characteristics of the FMF for NDE

The forward modeling framework proposed by this work combines RUS measurements and FE models for expanded NDE capabilities beyond historical methods (Section 1.3.1) in three fundamental ways. First, unlike other RUS efforts cited in the literature [46,150–152], the intent of this study was not to minimize the absolute error between measured and modeled f_R. Instead, the dog-bone was compared to itself in order to demonstrate how f_R changed over time—rendering natural population variability that confounds statistical sorting methods inconsequential. Such *part-to-itself* inspection procedures increase measurement sensitivity by eliminating the requirement that damage affects a $\triangle f_R$ greater

than the combined natural population variability and measurement uncertainty.

The second point distinguishing this work is that inclusion of FE models make it possible to inform measured resonance spectra with mode-type information and identify specific resonances that are particularly sensitive to individual damage mechanisms. For example, consider modes 14–17 in Figure 4.15 (c) and Figure 4.17 that include: a torsional mode (14), an extensional mode (15), and a longitudinal bending mode pair (16–17). Longitudinal bending modes are affected greatly by the creep elongation and surface crack formation, with degenerate peak splitting consistent with damage disrupting the symmetry of the specimen. Alternatively, modes 14 and 15 are both relatively insensitive to the accumulation of creep strain, while mode 14 is substantially affected by surface cracks. Identification of diagnostic modes that are sensitive to individual or multiple concurrent damage mechanisms can be particularly useful for NDE of large component populations, as selectively measuring diagnostic modes from the broadband spectrum can greatly reduce RUS scan time.

The third major distinction of the proposed NDE framework is the potential for quantitative evaluation of damage. Even with optimal experimental controls, quantifying how damage affects resonance based solely on empirical methods is—and will likely remain—difficult. This is because damage like creep manifests as multiple mechanisms that each affect resonance in a complex manner. While results from the fatigue analysis indicate that the $\triangle f_R$ response due to a crack are highly dependent on both the size and the location of the crack on the specimen. Using FE models and virtual studies, each damage mechanism can be modeled and evaluated for its individual impact on resonance behavior under a variety of circumstances limited only by the parameterization of the FE model. Instead of imparting fatigue cracks to a population of dog-bone specimens to understand the spacial dependence of the $\triangle f_R$ response, parameterizable models constructed as described here would provide far superior information to NDE efforts. Then these individual mechanisms can be combined with other concurrent mechanisms

to study their combined effect, while always having a precise description of the current damage state—which would not be available to NDE frameworks without a modeling component.

4.5 Conclusion

Mechanical damage in polycrystalline Ni-based superalloy Mar-M247 has been evaluated non-destructively with RUS measurements as part of a broad FE-based forward modeling framework for expanding the nondestructive damage evaluation capabilities of RUS. FE models afford the opportunity to isolate the individual creep damage mechanisms affecting resonance, e.g. surface cracks and geometry changes, while informing RUS measurements of crept and fatigued dog-bone specimens with valuable mode-type information. Instead of empirical studies for understanding the $\triangle f_R$ response as a function of damage, virtual studies should: require fewer specimens for validation, allow for more specific and detailed analyses, provide a framework for evaluating similar mechanisms in alternative specimen geometries, and ultimately lead to a generalizable quantitative framework. The FMF established herein overcomes many historical limitations of RUS for NDE, and leads to the following conclusions.

- Studies indicate the size, location, and distribution of cracks that develop during typical fatigue or creep loading significantly impact the $\triangle f_R$ response and produce significant degenerate mode splitting.

- Lower-frequency longitudinal bending modes were the most effective (diagnostic) modes for NDE of mechanical damage in the dog-bone specimen due to their sensitivity (magnitude $\triangle f_R$), prevalence in the lower-frequency regime, and measurement reliability.

- FE models only need refinement until f_R align to within approximately ±1% of

an average virgin measurement, as a residual analysis can correct for mode-order disagreement when present.

- The deformed shape of a crept specimen was shown to be the dominant mechanism affecting resonance, while surface cracking contributed significantly to changes in resonance when they appeared after the accumulation of 6.1% strain.

- Once diagnostic modes are identified, measurements can focus on small segments of the broadband to: reduce scan time and exclude regions with large residuals that may hinder detectability.

- RUS for NDE of difficult-to-measure material parameters, coupled with physical damage models, holds great potential for investigating the mechanistic underpinnings and evolution of life-limiting damage mechanisms.

Chapter 5

Forward Modeling Framework for NDE of Grain Structure Defects

Chapter Abstract

Like the FMF for evaluation of mechanical damage presented in the previous chapter, this chapter, and the publications upon which this chapter are based[1], details how the nondestructive evaluation capability of RUS can be extended through FE-based forward models for detection and quantification of recrystallization in single crystal Ni-based superalloys. Experiments use plastic deformation imparted through shot peening as the thermodynamic driving force for the single crystals of Mar-M247 to recrystallize during subsequent heat treatments. FE models, using self-consistent elastic properties and variable depths of surface recrystallization, show excellent agreement with RUS measured results which allows for the effect on resonance to be isolated and quantified. Once validated, the FMF is applied to single crystal turbine blade models to study the potential effectiveness of RUS for detecting recrystallization in these complex geometry parts. Forward models demonstrate that even small volumes of recrystallized material along thin regions of the turbine blade trailing edge—a likely location for residual stress accumulation from casting—produce significant $\triangle f_R$ characteristics that should be detectable with RUS scans before and after heat treatment.

[1] [55] B.R. Goodlet, L.H. Rettberg, and T.M. Pollock. "Resonant Ultrasound Spectroscopy for Defect Detection in Single Crystal Superalloy Castings," *Superalloys 2016* pp. 303-312. [doi:10.1002/9781119075646.ch33]

[57] L.H. Rettberg, B.R. Goodlet, and T.M. Pollock. "Detecting Recrystallization in a Single Crystal Ni-base Alloy using Resonant Ultrasound Spectroscopy," *NDT&E International*. 83 (2016) pp. 68-77. [doi:10.1016/j.ndteint.2016.05.004]

5.1 Introduction

Advanced casting methods have enabled the fabrication of Ni-based superalloy turbine blades with weight-saving geometries and serpentine internal cooling passages that permit operation at higher thermal and mechanical loads [80, 153]. However, these complex single crystal airfoil designs are prone to grain structure defects that may arise during the directional solidification process, e.g. stray grains or misoriented single crystals [80]. A typical single crystal superalloy casting yield for aviation turbine blades may be as low as ~70% due to defects such as misorentation, high-angle boundaries and recrystallization, with defect criteria being defined by a variety of manufacturer specifications [80]. Residual stresses and plastic strains induced during solidification as a result of metal shrinkage around rigid cores, or impact damage during mold removal may also initiate recrystallization during subsequent heat treatments [154]. Recrystallization, stray grains, and blades with crystal orientations rotated away from the desired [001] axis are all of particular concern due to their deleterious impact on both creep and fatigue properties [154–156]. Process controls that minimize the occurrence of these life-limiting grain structure defects and effective nondestructive evaluation tools to reliably detect defective components before entering service are critical.

5.1.1 Alternatives for NDE of Recrystallization

There are a variety of nondestructive techniques for evaluating grain structure in Ni-based superalloys including: etching and visual inspections [157], x-ray diffraction, radiography and tomography [158, 159], and ultrasonic methods [33, 160]. Visual inspections after etching are commonly employed to identify high-angle grain boundaries, stray grains, recrystallization, and freckles that are present on the surface [157], however they can be subjective and prone to error, and are incapable of assessing defects below the sur-

face. X-ray methods based on diffraction include the classical Laue technique to produce diffraction spots for a quantitative determination of single crystal orientation [158]. X-ray computed tomography and radiography methods generally rely on absorption contrast and require more expensive and brighter beam sources [159]. Ultrasonic methods are more affordable than x-ray methods and more quantitative than a visual inspection. Pulse-echo ultrasonics [161] and ultrasonic array [160] both demonstrate potential as quantitative inspection techniques for grain structures, but they are typically local inspection tools tailored to identify small flaws in particular regions of a specimen. Only through ultrasonic resonance can one sample the full volume of a specimen with a single measurement [33], potentially enabling the detection of bulk, subsurface, and surface grain defects with a single measurement.

5.1.2 Influence of Recrystallization on Resonance

As a direct result of elastic anisotropy (Equation (2.31)), a single crystal casting will exhibit different resonance characteristics as compared to a polycrystalline casting of the same material. The larger the elastic anisotropy, the greater the divergence of resonance characteristics. Conversely, a material with an $A = 1$ would exhibit the same resonance characteristics irrespective of grain structure, and would not be a candidate material to detect recrystallization with RUS. Except for W which is very nearly isotropic, no single crystals exhibit perfectly isotropic elasticity [72], though polycrystalline materials without a preferred crystallographic texture are often isotropic [82].

Understanding the elastically anisotropic nature of single crystal Ni-based superalloys is key to understanding how RUS could be helpful in diagnosing recrystallization. When a material recrystallizes, new grains are nucleated with crystallographic orientations that are different than the parent single crystal. With Section 2.1.4 explaining how crystallographic orientation affects directionally dependent elastic properties, it is clear that as

these new grains grow and consume the surrounding material, the effective elastic constants are changing as well. If the recrystallized grains are oriented in a direction that is more complaint to normal loads, then the directional Young's modulus ($E_{[hkl]}$) would decrease. While this decrease would cause resonance modes that are dependent on $E_{[hkl]}$, e.g. extensional modes, to exhibit a negative $\triangle f_R$ according to:

$$f_R \propto \sqrt{\frac{E_{[hkl]}}{\rho}} \ . \tag{5.1}$$

The same basic relationship holds for other resonance modes as well, like torsional modes which are largely dependent on shear moduli. Following the simplified example given above, recrystallization will inevitably cause changes in crystal orientation that affect the local value of the directionally dependent shear modulus ($G_{(mno)[hkl]}$), which will lead to $\triangle f_R$ according to:

$$f_R \propto \sqrt{\frac{G_{(mno)[hkl]}}{\rho}} \ . \tag{5.2}$$

A more detailed discussion of this subject is provided in Section 5.6.2 of this chapter, along with values of $E_{[hkl]}$ and $G_{(mno)[hkl]}$ calculated for Mar-M247, and supporting experimental and modeling results.

5.2 Experimental Methods

5.2.1 Materials and Specimen Preparation

Starting from a 7.62 cm long by 1.27 cm diameter bar, machined per the specifications in Figure 3.10, of polycrystalline Ni-based superalloy Mar-M247—cast as a single crystal—with nominal composition provided in Table 3.4. The single crystal bar was shot peened[2] by GE Power & Water at a peening gas pressure capable of producing an 11 mil Almen

[2]Courtesy of Jesse Keller, Art Peck, and Jon Schaeffer of GE Power & Water

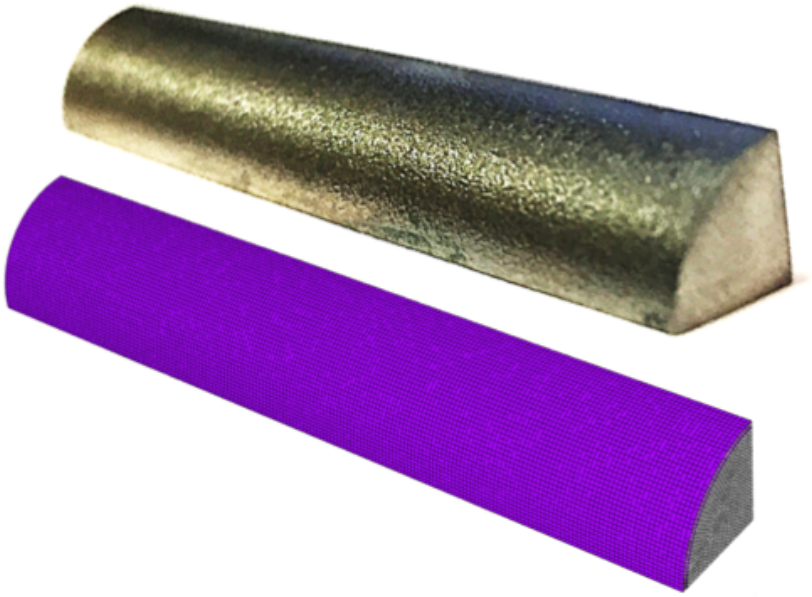

Figure 5.1: Shot peened quarter-cylinder specimen of single crystal Mar-M-247 above its FE model counterpart with a highlighted 400 µm layer of recrystallization.

strip deflection, which is twice that of a typical surface treatment in order to ensure that recrystallization would occur on subsequent heat treatments. Fixturing allowed for complete circumferential coverage during shot peening, but resulted in the incomplete peening of less than 1.3 cm of material at the top and bottom of the bar. Therefore, it was shortened to 5.08 cm by removing 1.27 cm from both ends with a wire EDM. Now with a uniform shot peening applied to the circumferential surface of the bar, it was sectioned longitudinally into four equal pie pieces, again via wire EDM, yielding 4 test specimens herein referred to as quarter-cylinder specimens. Except for the dimpled surface depicted in Figure 5.1, there was no appreciable change in the geometry of the bar after shot peening, nor was there any appreciable change in shape after sectioning the bar into quarter-cylinder specimens. The shallow EDM damage layer was removed from the flat faces of the quarter-cylinder specimen using 600-grit sandpaper prior to initial RUS measurements for establishing the baseline f_R response.

5.2.2 Recrystallization Heat Treatments

After acquiring a baseline f_R response of the shot peened quarter-cylinder specimen, it was iteratively heat treated at a solution treatment temperature of 1225 °C using an open air tube furnace. The ends of the tube furnace were closed using alumina blocks and end-caps, except when loading and unloading the specimen, to ensure optimal furnace temperatures were maintained. The quarter-cylinder specimen was inserted into the center of the tube furnace for times of 2, 5, 10, 20, 80, 160 and then 320 minutes, followed by air cooling to room temperature between each iteration. RUS measurements were conducted between each heat treatment after the specimen fully cooled to room temperature as verified by a k-type thermocouple contacting the specimen. Note that because elastic moduli are temperature dependent properties, RUS measurements should always be conducted at a consistent temperature when evaluating $\triangle f_R$ over time.

5.2.3 RUS Measurement Considerations

Resonance frequencies are collected from broadband RUS scans of the quarter-cylinder specimen using a measurement setup provided by the Vibrant Corporation as depicted in Figure 5.2, with further details provided in Section 3.3. Figure 5.2 shows the quarter-cylinder specimen resting on a cradle of four omnidirectional piezoelectric transducers (PTs); one drive PT, two receive PTs and a dummy PT for supporting the specimen. The drive PT is driven with a swept sinusoidal frequency from the transceiver across the 1-200 kHz broadband using a 3 Hz step size and a 5 ms dwell requiring a few minutes to complete the scan. When the drive frequency nears a f_R of the specimen, a standing elastic wave characteristic of mechanical resonance will form across the specimen and constructively interfere to generate amplified deflections hundreds to thousands of times greater than the drive amplitude. These amplified deflections are then recorded by the two receive PTs, with amplitude plotted as a function of the drive frequency to yield a

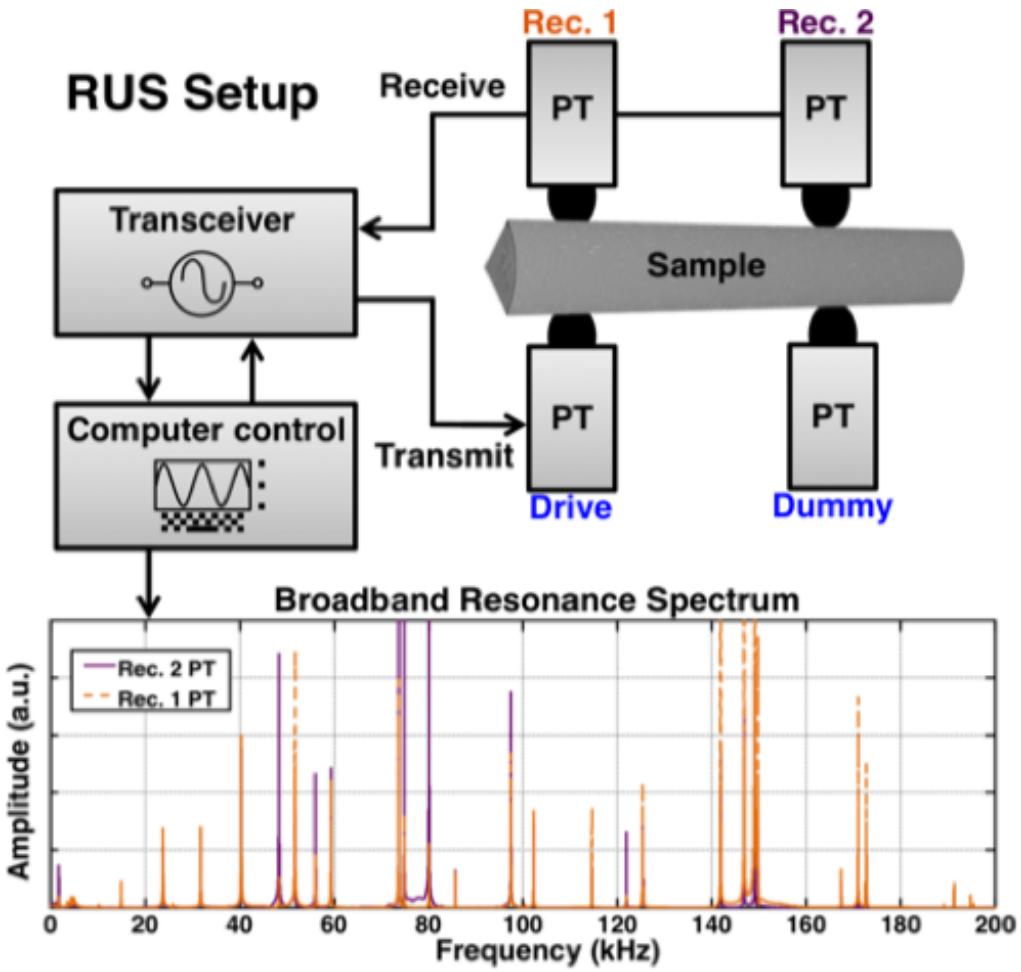

Figure 5.2: RUS experimental setup for the quarter-cylinder specimen, supported by the piezoelectric transducer cradle and actuated by the transceiver with a computer controller to produce a broadband RUS spectra.

broadband resonance spectrum plot as depicted at the bottom of Figure 5.2.

Once the broadband RUS spectra were collected, a list of the first 30 f_R is extracted using automated peak picking software available on the computer controller connected to the transceiver. These data are then independently verified by the operator before being transfered from the collection computer for further analysis. In an effort to ensure that no resonance modes were missed, all f_R reported and used as part of this investigation are mean values from 3 broadband scans. Table 5.1 provides the mean and the standard deviation of the first 30 f_R collected from the quarter-cylinder specimen. With the

specimen removed and replaced on the PT cradle after each broadband measurement to ensure that any random specimen-transducer coupling minimally biases the f_R results.

Table 5.1: Mean and standard deviation (sd) for the first 30 resonance modes of the quarter-cylinder specimen, based on 3 broadband RUS scans.

Mode No.	**Frequency** (kHz) mean ± sd	**Mode No.**	**Frequency** (kHz) mean ± sd
1	6.992 ± 0.011	16	102.069 ± 0.002
2	9.222 ± 0.020	17	108.846 ± 0.002
3	18.303 ± 0.042	18	122.852 ± 0.009
4	23.991 ± 0.003	19	126.547 ± 0.003
5	32.569 ± 0.000	20	128.677 ± 0.000
6	34.485 ± 0.003	21	143.364 ± 0.002
7	37.049 ± 0.043	22	152.284 ± 0.006
8	44.168 ± 0.017	23	156.391 ± 0.000
9	54.345 ± 0.002	24	156.714 ± 0.003
10	64.056 ± 0.006	25	176.205 ± 0.005
11	68.108 ± 0.019	26	182.100 ± 0.006
12	73.234 ± 0.006	27	184.723 ± 0.003
13	77.131 ± 0.005	28	185.583 ± 0.003
14	94.376 ± 0.015	29	206.668 ± 0.012
15	95.708 ± 0.002	30	210.991 ± 0.008

5.3 Experimental Results

5.3.1 Metallographic Analysis

For purposes of validating the FE model and linking the measured and modeled results, the 1225 °C heat treated quarter-cylinder specimen was ground, polished, and etched after the 320 minute heat treatment to reveal the depth of the surface recrystallization. Optical micrographs in Figure 5.3 show a variable-depth recrystallization front, marked with a white dashed line in the bottom micrograph, progressing inward from the free surface at the top of the micrograph. The recrystallization depth was measured at 100 µm

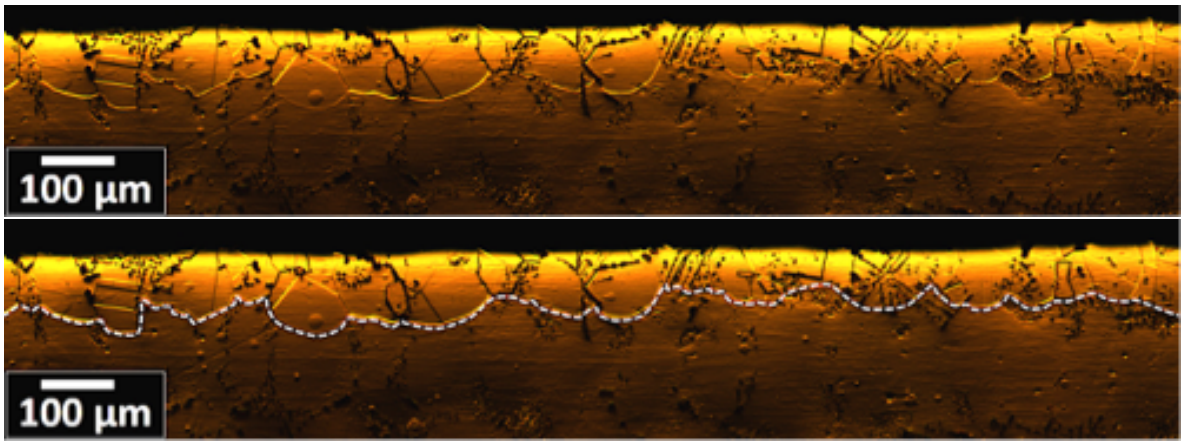

Figure 5.3: Optical micrographs of the quarter-cylinder specimen after shot-peening and iterative heat treatments at 1225 °C for up to 320 minutes. The two micrographs are identical except for the white dashed line delineating the recrystallized layer, determined to have an average depth of 80 µm.

intervals across the entire etched surface of the specimen for approximately 500 individual measurements at an average depth of 80 µm.

Mode-specific changes in resonance frequency ($\triangle f_R$), as defined by Equation (1.2), describe how each resonance mode changes in percentage terms from the baseline f_R response. In this case the baseline condition is the fully prepared quarter-cylinder specimen in the as-shot peened state, prior to any heat treatments. Figure 5.4 plots the measured $\triangle f_R$ of the shot peened quarter-cylinder specimen after the iterative heat treatments at 1225 °C. As the figure makes clear, a majority of the modes exhibit a positive $\triangle f_R$, while the remaining modes have a negative $\triangle f_R$ with a regular periodicity that gives the data a characteristic saw-tooth pattern. The magnitude of the $\triangle f_R$ response increases as a function of heat treatment time, indicating that the mechanism affecting resonance requires a finite amount of time at 1225 °C. The mechanism is most active at early times exhibiting half of the total $\triangle f_R$ response after the 5-minute treatment; and is basically exhausted after the 160-minute treatment.

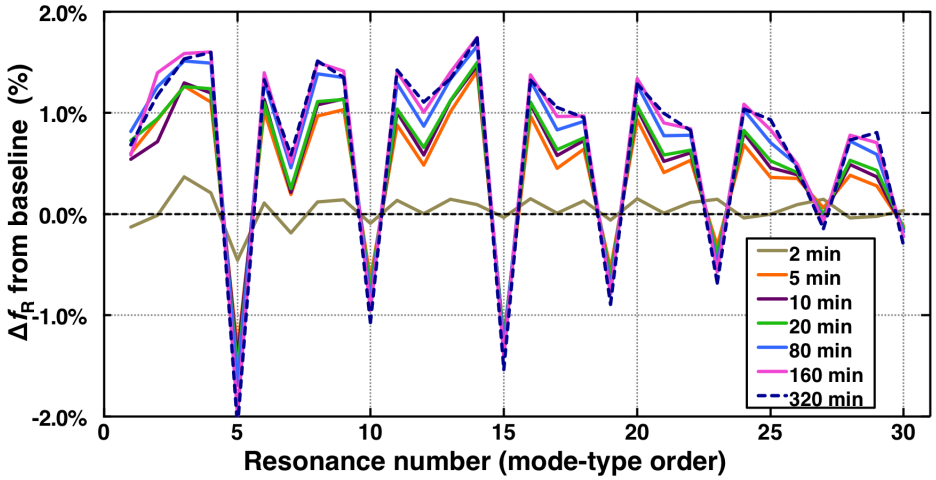

Figure 5.4: Measured $\triangle f_R$ for shot-peened quarter-cylinder specimen heat treated iteratively 1225 °C.

5.4 Modeling Methods

Figure 5.1 is the quarter-cylinder specimen along with a finite element (FE) model of the specimen depicted with a 400 µm layer of recrystallization marked by purple elements. A detailed view of the quarter-cylinder specimen model, containing approximately 150,000 linear hexahedral elements, is provided in Figure 5.5. The recrystallization depth is varied in the model by assigning either single crystal elastic properties or polycrystalline elastic properties to the finite elements. The refined mesh at the surface allows for recrystallization to be modeled at depths of 25 to 400 µm, with each layer containing at least 5 elements through thickness. A simple mesh sensitivity study on the FE model verified that further refinement of the mesh did not affect the results.

5.4.1 Self Consistent Elastic Properties

It is important that self-consistent elastic properties be used between the single crystal and polycrystalline regions of the FE model, so as to capture only the relevant effect of recrystallization on resonance [57]. Self-consistency is maintained by using the single

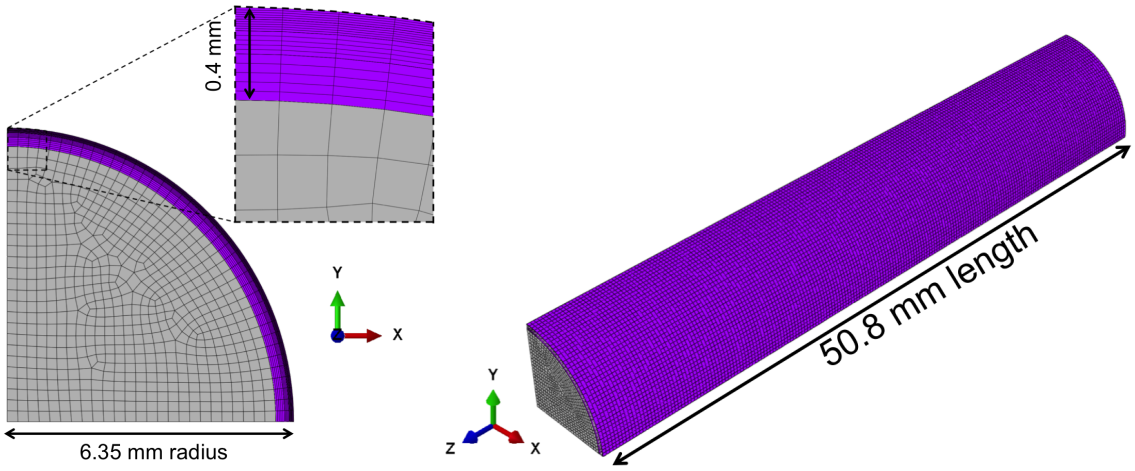

Figure 5.5: Depiction of quarter-cylinder specimen FE mesh with the elements marked in purple representing a layer of surface recrystallization 400 µm thick.

crystal stiffness values (C_{11}, C_{12}, and C_{44}) and a self-consistent polycrystalline averaging scheme (e.g. Equation (2.36), as discussed in Section 2.1.3) to calculate the two isotropic moduli. The significant elastic anisotropy (A, Equation (2.31)) that necessitates higher-order polycrystalline averages for calculating realistic isotropic shear moduli (G) is the same material property that describes the extent to which a single crystal bar will exhibit different f_R characteristics as compared to an identical bar comprised of an aggregate of randomly oriented grains. Ni has an $A_{Ni} \approx 2.5$ [93] while the isotropic assumption applied to polycrystalline aggregates stipulates $A_{isotropic} = 1.0$, effectively removing a degree of freedom from the elastic body. Specifically, $A_{Ni} \approx 2.5$ means that there is a factor of 2.5 between the tetragonal shear modulus (C', Equation (2.34)) and the trigonal shear modulus (C_{44}) [88]. While the differential between the tetragonal and the trigonal shear moduli is what the isotropic averaging schemes must rationalize, because cubic symmetry materials have two directionally dependent shear moduli while isotropic materials have just one.

Table 3.6 summarizes the single crystal stiffness values used to model the single crystal Mar-M247. These single crystal elastic constants were themselves calculated using a simple rule of mixtures calculation assuming a volume of 45% γ with properties from [95],

and 55% γ' with properties from [125]. The preferred polycrystalline averaging scheme for modeling Ni-based superalloys is that of Gairola and Kröner [92], using Equation (2.36) to define the shear modulus (G_{GK}) and Equation (2.32) for the common definition of bulk modulus (K) in cubic materials. Then once K and G_{GK} are determined, simple conversions provided by Equation (2.11) and Equation (2.12) yield an isotropic Young's modulus and Poisson's ratio (E_{GK} and ν_{GK}), which define the constitutive behavior of the polycrystalline regions of the Abaqus FE model with self-consistent elastic properties. The final isotropic elastic constants use for modeling are summarized Table 3.7.

5.4.2 Validation of Homogeneous Representation of Recrystallization

In addition to self-consistent elastic properties, an assumption about the surface recrystallization layer needs to be evaluated before moving forward. As Kuhn and Sockel discuss, the Gairola-Kröner averaging scheme "takes into account the grain interactions in a macroscopically isotropic polycrystalline aggregate of cubic crystals" [93]. However, its not obvious nor safe to freely assume that the thin layer of recrystallized material, often only a couple of grains through thickness, should be modeled as a homogeneous layer of isotropic elastic properties. In an effort to determine whether a homogenized isotropic layer sufficiently captures the elastic behavior of surface recrystallization, the following modeling study was devised.

A cylindrical sub-volume of material was modeled with both a homogeneous and a discrete-grain representation of surface recrystallization to test the validity of the homogeneous assumption being applied to the recrystallized Mar-M247 material. If the homogenization represented by Figure 5.6a is valid, then it should yield similar $\triangle f_R$ results to a discrete grain approach illustrated by Figure 5.6b, when both RX scenarios are compared to the single crystal baseline. Particularly, the low-order resonance modes should

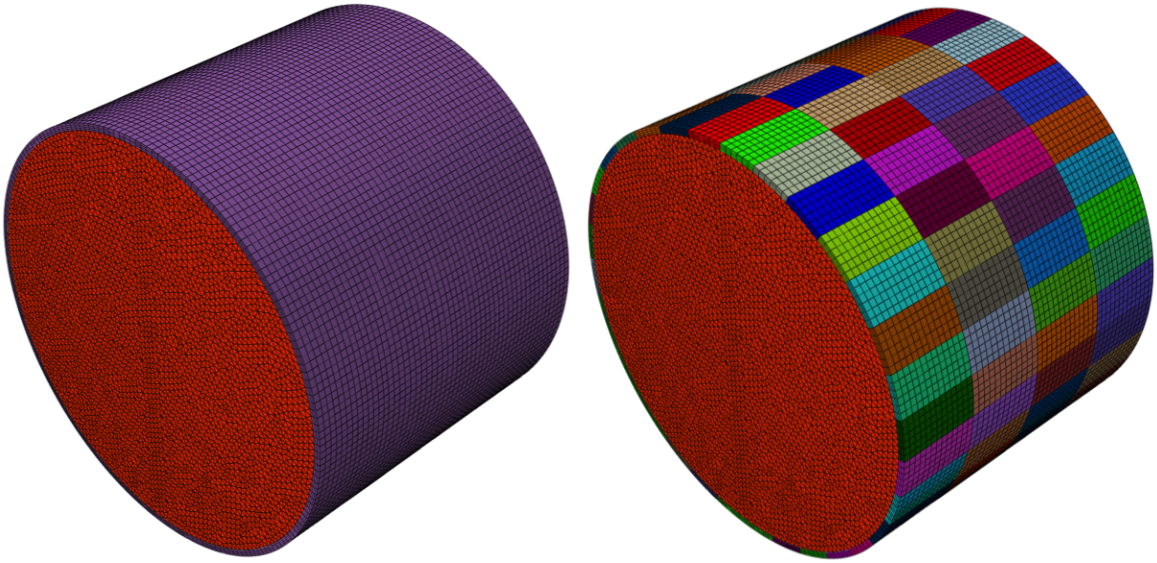

(a) isotropic homogenized layer (b) 4×32 discrete anisotropic grains

Figure 5.6: FE models used for a modeling study to determine whether (a) a homogenized isotropic layer sufficiently models surface recrystallization or if (b) a discrete grain modeling approach is required.

track closely because these are the modes that are ultimately going to be used as part of an NDE framework. While higher-order modes may be more sensitive to local variations in properties and lead the homogeneous isotropic model to deviate from the discrete grain model.

The discrete-grain model is comprised of a layer of 128 single crystal grains arranged in a grid that has 4 grains spanning the length of the cylinder, 32 grains about the circumference, and one grain through thickness. The orientation of each of the 128 grains was assigned from a list of Euler angles representing a random orientation distribution. Note the color of each grain in Figure 5.6b was arbitrarily assigned to aid viewing, not as an indication of grain orientation like inverse pole figure (IPF) coloring schemes. While Figure 5.6a demonstrates the recrystallized layer modeled as a homogeneous volume with isotropic Gairola-Kröner average moduli. Both approaches model a recrystallized layer thickness that is 5% of the specimen radius.

Results of the modeling study are provided in Figure 5.7, wherein the $\triangle f_R$ predicted

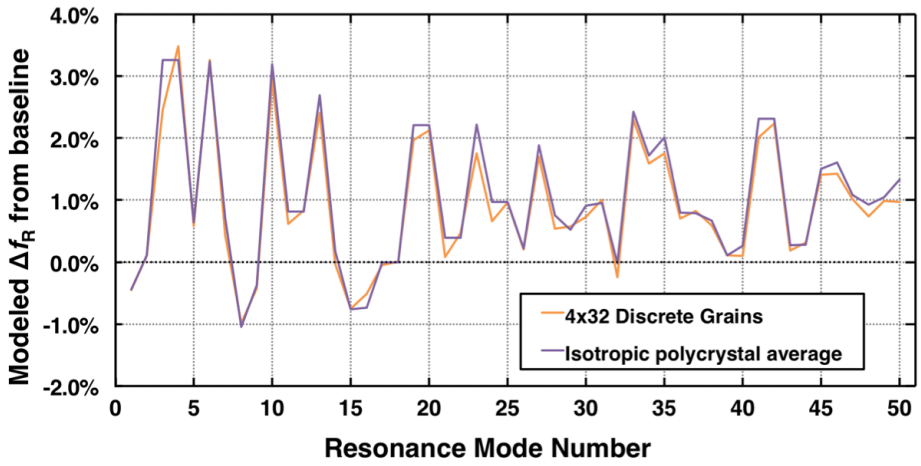

Figure 5.7: FE model study of $\triangle f_R$ for the homogeneous isotropic case and the discrete grain case in very good agreement with each other. This result indicates that homogenized isotropic properties originally modeling bulk aggregates can also be applied to thin layers of surface recrystallization.

for the first 50 modes of the cylindrical sub-volume modeled according to the two recrystallization scenarios can be directly compared. Clearly the $\triangle f_R$ predicted by the two representations are very similar for the first 50 resonance modes, which gives good confidence for the use of a isotropic homogenization procedure to represent a thin layer of surface recrystallization. Essentially the two modeling approaches simulate recrystallization using two extreme representations. The physically accurate representation would likely fall somewhere between the $\triangle f_R$ predicted by the relatively-coarse 128 discrete grain model and the $\triangle f_R$ predicted by the infinitely-refined grains implicit in the isotropic model. While the disagreement between the two models indicates the extent to which error is potentially introduced by the isotropic assumption for the current case of recrystallization consuming 5% the radius of the specimen. This potential error is very small compared to the magnitude of the $\triangle f_R$ response resulting from recrystallization itself, and therefore is neglected.

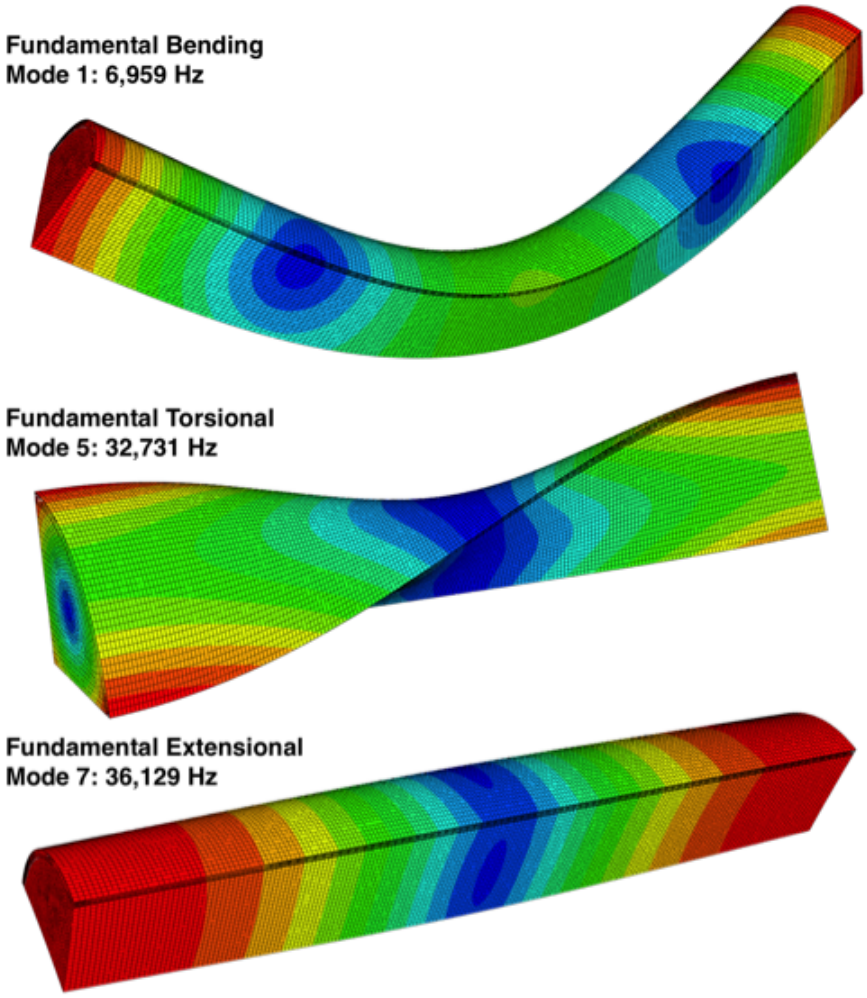

Figure 5.8: Magnified deflection character plots of the three fundamental mode-types observed in the low-frequency regime of the resonance spectrum.

5.4.3 Modal Analysis

In addition to predicting f_R, FE models inform RUS measurements with valuable mode-type information that may be useful for explaining which individual modes will be affected by recrystallization, and in what direction the $\triangle f_R$ response is likely to be. As for all specimen geometries, the low-frequency resonance modes of the quarter-cylinder specimen can either be characterized as a fundamental mode, or as a higher-order resonance of fundamental modes. The three fundamental mode-types observed to occur at low frequencies for the quarter-cylinder specimen are: extensional, torsional, and (longitudinal) bending; depicted in Figure 5.8 by plotting a magnified representation of the deflection characteristics upon resonance. Torsional modes are expected to be particularly sensitive to shear moduli, while bending and extensional modes to be predominantly dependent on the Youngs modulus. By observing how these modes are affected by recrystallization, it should be possible to infer how the elastic properties of the quarter-cylinder specimen are changing, with the magnitude of the change correlating to the volume of single crystal material that is recrystallized.

5.5 Modeling Results

The baseline response for the single crystal quarter-cylinder specimen is summarized in Table 5.2, which also provides the mode-type assigned to each resonance. From this baseline response, the model predicted $\triangle f_R$ associated with recrystallization depths of 25, 50, 100 and 200 µm from the surface are plotted in Figure 5.9. Like-modes are compared to each other as a function of recrystallization depth, as allowed by the modal analysis which matches modes based on their deflection character, not their current position in the frequency regime. Mode shape information is plotted over the 200 µm recrystallization results in Figure 5.9, but the mode-shape information applies to all FE model results.

Table 5.2: Modeled f_R and mode-type for the single crystal quarter-cylinder specimen.

Mode no.	**Frequency** (kHz)	**Mode type**	**Mode no.**	**Frequency** (kHz)	**Mode type**
1	6.9591	b	16	104.066	b
2	9.3166	b	17	106.813	e
3	18.595	b	18	124.497	b
4	24.343	b	19	128.607	t
5	32.731	t	20	131.210	b
6	35.039	b	21	140.464	e
7	36.129	e	22	154.097	b
8	44.774	b	23	158.587	t
9	55.308	b	24	159.443	b
10	65.253	t	25	172.254	e
11	69.008	b	26	183.898	b
12	71.873	e	27	186.371	t
13	78.561	b	28	188.181	b
14	95.884	b	29	201.551	e
15	97.323	t	30	210.368	t

Mode-types: longitudinal bending (b), torsional (t), extensional (e).

Clearly the torsional modes exhibit a negative $\triangle f_R$, while the extensional and bending modes exhibit a positive $\triangle f_R$ due to recrystallization of the quarter-cylinder specimen. This observation follows with previous statements that: bending and extensional modes are most-sensitive to changes in the local Youngs modulus, while torsional modes are affected by local changes in shear modulus. Now we can surmise that recrystallization as modeled leads to a reduction in the shear modulus of the specimen, and a concomitant increase in the Young's modulus, with the changes in resonance scaling as a function of the depth of recrystallization.

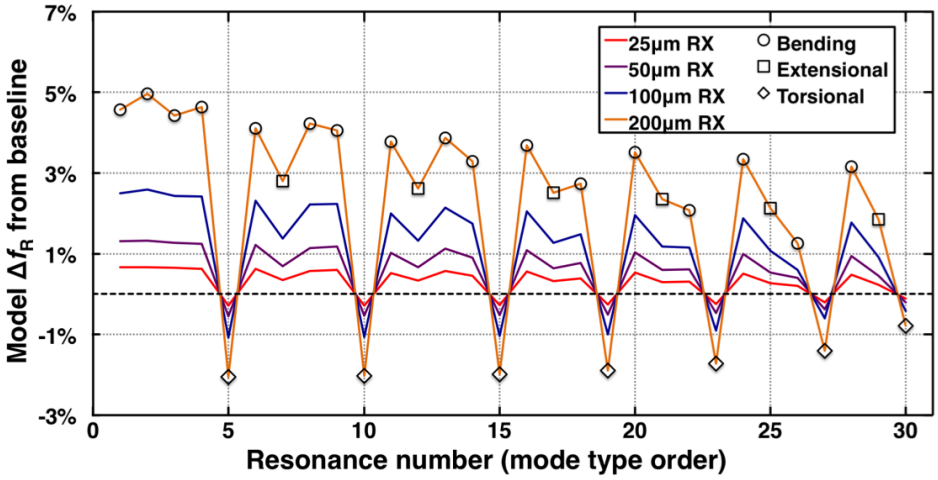

Figure 5.9: FE model predicted $\triangle f_R$ due to surface recrystallization on the quarter-cylinder specimen. Mode type information is plotted along with the 200 µm recrystallization results, and applies to all model results presented in mode type order.

5.6 Discussion of Measured and Modeled Results

5.6.1 FE Model Validation

The preferred technique for validating FE models as part of a FMF is to compare measured and modeled $\triangle f_R$ results for known levels of damage, not f_R results directly. This is because the f_R results will inevitably exhibit some disagreement as a result of irrelevant differences in the baseline resonance behavior of the virgin specimen and the virgin model, complicating efforts to compare lists of f_R. While most of the irrelevant differences between the modeled and the measured baselines are removed when $\triangle f_R$ are determined. This assures us that the modeled-predicted $\triangle f_R$ data contain only the effect of the mechanism being modeled, and no others. In an effort to minimize the $\triangle f_R$ produced by alternative mechanisms, previous studies have shown that multiple-hour isothermal heat treatments of Mar-M247 in air can affect small $\triangle f_R$ in the absence of any shot peening [162]. While iterative isothermal heat treatments for 1 hour or less exhibit negligible $\triangle f_R$ magnitudes on the order of the RUS measurement precision. Since the measured

$\triangle f_R$ results presented in Figure 5.4 indicated that the dominant mechanism affecting resonance appears to have arrested by the end of the 160-minute heat treatment at 1225 °C. In addition to the tiny differences between the 160-minute and 320-minute treatments exhibiting characteristics consistent with heat treatment effects, and not the recrystallization mechanism currently being considered. It was decided that the modeled $\triangle f_R$ results should be compared to the $\triangle f_R$ measured after the 160-minute treatment, instead of after the final 320-minute treatment.

The metallographic analysis shown in Figure 5.3 indicated a final RX depth at an average of 80 µm. Therefore measured $\triangle f_R$ data after the 160-minute treatment are compared to modeled data corresponding to 80 µm in Figure 5.10. This comparison demonstrates excellent agreement of measured data to model results corresponding to a simple FE model that is only accounting for the recrystallization mechanism. Additionally, the excellent agreement shown by Figure 5.10 validates the use of self-consistent Gairola and Kröner [92] average moduli to represent an isotropic polycrystalline layer of recrystallization atop a parent single crystal.

Figure 5.10: Comparison of $\triangle f_R$ due to recrystallization indicating very good agreement between the 160-minute measurement and the 80 µm recrystallization model.

5.6.2 Discussion of Observed Changes in Resonance

For this and subsequent discussions it is useful to again consider directionally dependent engineering moduli such as Young's modulus ($E_{[hkl]}$, Equation (2.37)) and the shear modulus ($G_{(mno)[hkl]}$, Equation (2.38)), explained in detail in Section 2.1.4. These engineering moduli recast the elastic behavior of cubic single crystals in terms of crystallographic direction whereby $[hkl]$ represent the direction of the applied load and (mno) stipulates the plane normal upon which the load is applied (as necessary for defining shear loading) [98]. Using Equation (2.37), and the single crystal stiffness values for Mar-M247 in Table 3.6, the directional Young's moduli according to crystallographic direction are determined and summarized in Table 5.3.

Table 5.3: Directional Young's moduli for single-crystal Mar-M247, calculated using single crystal elastic constants provided in Table 3.6.

Directional Moduli	**Value (units)**
$E_{[100]}$	115.6 GPa
$E_{[110]}$	218.8 GPa
$E_{[111]}$	311.5 GPa

As the single crystal bars of Mar-M247 were solidified with a nominal [001] growth direction, the directional moduli clearly show they were cast with their long axis parallel to the most compliant direction for normal strains and the least compliant to shear strains. This behavior holds true for all single crystal Ni-based superalloys solidified in the preferred [001] growth direction, while [111]-oriented crystals would be the least compliant to normal loads. This means that any recrystallized grain would exhibit an orientation that is less compliant, and thus contribute to a positive $\triangle f_R$ for all bending and extensional modes which are particularly sensitivity to $E_{[hkl]}$.

The opposite is true for torsional modes, which are sensitive primarily to shear moduli. According to Table 5.4, $G_{(mno)[hkl]}$ is greatest against shear stresses on {001} crystallo-

Table 5.4: Directional shear moduli for single-crystal Mar-M247, calculated using single crystal elastic constants provided in Table 3.6.

Directional Moduli	Value (units)
$G_{\{001\}<\perp>}$	126.7 GPa
$G_{\{111\}<\perp>}$	53.27 GPa
$G_{(110)[1\bar{1}0]}$	41.30 GPa
$G_{(110)[001]}$	126.7 GPa

graphic planes at a value of 126.7 GPa. This explains why recrystallization results in a negative $\triangle f_R$ for all torsional modes in Figure 5.9.

5.6.3 Secondary Mechanisms for Frequency Shifts

Such strong agreement between the recrystallization model and the RUS measurements, despite the omission of secondary mechanisms potentially affecting resonance like oxidation or dislocation recovery, results in a negligible unexplained residual (Equation (4.2)). This is in contrast to the FMF study of creep damage (discussed in Chapter 4) which required the inclusion of secondary mechanisms (i.e. cracks) to explain the residuals remaining after the primary (shape change) mechanism was modeled [56]. Nevertheless, it is worth considering secondary measurements that may influence this measurement. While it could be argued that modes 1–3 exhibit a significant residual, previous RUS investigations using contacting piezoelectric transducers to excite and record f_R often report poor measurement repeatability for the first few lowest-frequency modes [33, 37]. It has been suggested that vibration coupling between the specimen and the transducers is the cause of this repeatability issue, which is exacerbated by the relatively large deflections exhibited by the lowest-frequency modes [147]. As such, these modes are commonly excluded from NDE investigations [56], and from inversions estimating elastic properties [37].

A number of physical changes in the material are possible as a result of the 1225 °C

heat treatment including recrystallization, surface oxidation and spallation, and changes in the dislocation substructure. Dislocation reorganization and recovery mechanisms operating in bulk materials have been argued to result in a slight modulus increase [163], affecting a positive $\triangle f_R$ through the relationship described by Equation (5.1). While oxidation of the superalloy and spallation of the oxide can slightly change the geometry and mass of the specimen, measurements of the specimen mass between each heat treatment indicate that the $\triangle f_R$ resulting from these mechanisms would be insignificantly small. What is most likely to affect a $\triangle f_R$ beyond the dominant mechanism of recrystallization is actually the heat treatment effect on the superalloy itself leading to changes in the $\gamma - \gamma'$ microstructure. As demonstrated in [162], solution heat treatments applied to fully aged (polycrystalline) cylinders of Mar-M247 can lead to a negative $\triangle f_R$ from 0.1 to 0.2%, while aging treatments resulted in the opposite $\triangle f_R$ response. However these heat treatment effects are seen as inconsequential to the current study because the they only affect an appreciable $\triangle f_R$ after long exposures at high temperatures, after the recrystallization mechanisms appears to be exhausted, exhibiting $\triangle f_R$ that are an order of magnitude smaller than the effect produced by the recrystallization, and thus are not intimately studied as part of this FMF.

5.6.4 Quantitative NDE

Given the simple FE models of RX described above have been validated with experimental results, and no appreciable residual exists. Then matching modeled results (of known RX depth) to RUS measurements collected from intermediate heat treatment iterations can provide quantitative measures of RX depth at these intermediate times. Figure 5.11 demonstrates this quantitative NDE ability by comparing the $\triangle f_R$ measured after the 20-minute 1225 °C heat treatment to a FE model of RX depth at a depth of 50 µm. This measure to model comparison again demonstrates excellent agreement without a signif-

icant residual, and is a testament to the capability of simple FE models for expanding the quantitative NDE potential of RUS. While additional model results could easily be fit to other intermediate times to provide a nondestructive measure of recrystallization kinetics.

Figure 5.11: Validated RX models can nondestructively quantify RX depth at intermediate times, with 50 µm of RX predicted after the 20-minute heat treatment at 1225 °C.

5.7 Extensions of the FMF

5.7.1 Extension to Materials Science Investigations

The FMF for NDE with RUS can be extended in a straightforward manner to inform manufacturing process control variables, monitor damage evolution of complex geometry components during their service lifetimes, or inform physics-based damage models and fundamental science investigations. For an example of the latter, consider application of the recrystallization FMF for characterizing a duplicate single crystal Mar-M-247 quarter-cylinder specimen heat treated at 1150 °C, instead of 1225 °C as before. Figure 5.12 details the measured $\triangle f_R$ results for this second quarter-cylinder specimen iteratively heat treated at 1150 °C, clearly exhibiting slower recrystallization kinetics and less than half

the average recrystallization depth after the 160-minute heat treatment as compared to the 1225 °C specimen detailed in Figure 5.4. Using the framework provided, a study of recrystallization kinetics as a function of heat treatment temperature could be accomplished in straightforward manner. The 5.08 cm long quarter-cylinder specimens could be sectioned into multiple smaller specimens, providing opportunities to study different experimental controls as well as statistical significance for repeated conditions. Metallographic analysis of select samples would assure model validation, though it wouldn't be necessary for a majority of the specimens, which could save a considerable amount of time on specimen preparation efforts. While multiple bars could be shot-peened at different peening pressure to evaluate the deformation threshold necessary for initiation of recrystallized grains.

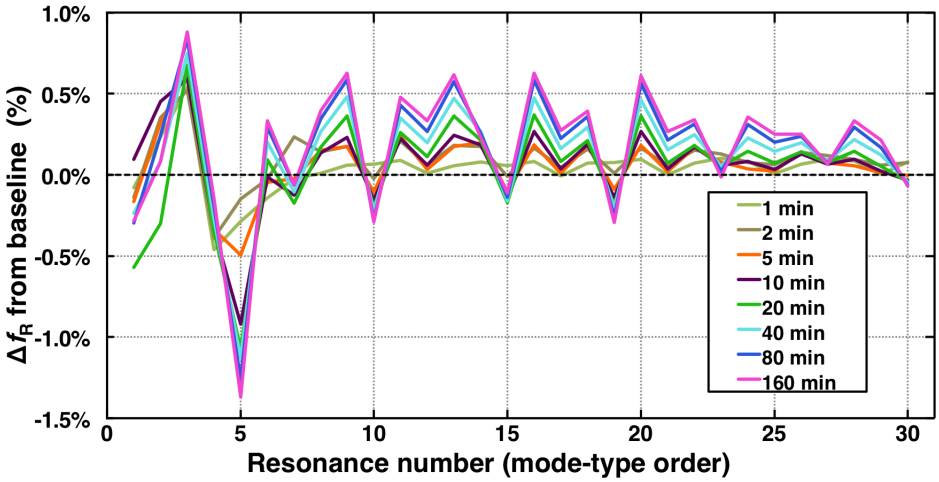

Figure 5.12: Measured $\triangle f_R$ for shot-peened quarter-cylinder specimen heat treated iteratively at 1150 °C.

In addition to studying different treatment conditions on Mar-M247, the FMF discussed in this chapter has also been applied to a second-generation single crystal superalloy René N5 specimen that underwent an identical shot peening treatment as described above. Interestingly, after a single solution treatment at 1215 °C the René N5 specimen exhibited an average recrystallization depth of 178 µm [57]. This depth is over twice the final recrystallization depth experienced by the Mar-M247 specimen, treated itera-

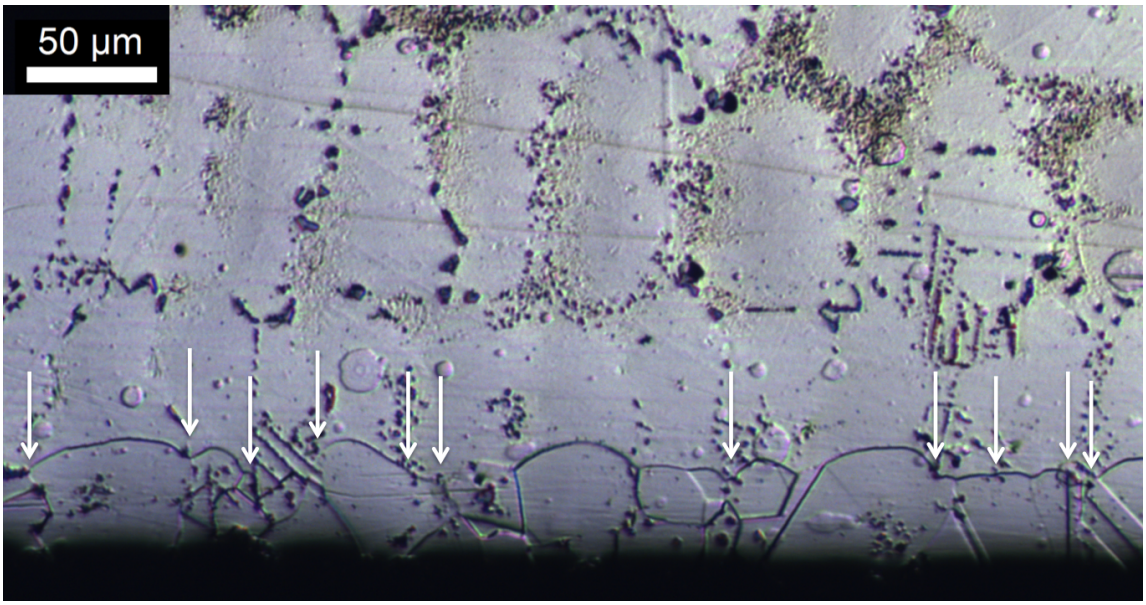

Figure 5.13: Micrograph of Mar-M247 specimen, heat treated at 1225 °C, with a recrystallization front pined by carbides as indicated by arrows.

tively at a higher temperature of 1225 °C temperature. Simply comparing René N5 and Mar-M247, it is clear there is a strong compositional dependence to the propensity of an alloy to recrystallize. Clearly, further work in this area would be necessary to provide a definitive explanation for the difference in behavior noted here. But the presence of a higher volume fraction of carbides in Mar-M247, as is typical for a polycrystalline Ni-based superalloy, is suspected to play a role in inhibiting boundary motion during recrystallization. This is further supported by Figure 5.13 showing a micrograph of the 1225 °C Mar-M247 specimen with arrows indicating locations along the recrystallization front that appear to be pinned by carbides. As many opportunities exist for RUS to quickly and nondestructively provide quantitative information about sub-surface grain structures and recrystallization of single crystal Ni-based superalloys, future materials science investigations are possible in a higher throughput manner.

5.7.2 Extension to Complex Geometries

Extending the FMF to complex geometries is important to gain understanding about the potential measurement sensitivity of RUS for diagnosing grain structure defects like recrystallization in actual components like turbine blades. For this effort a notional blade geometry is used which contains many features of a modern single crystal first stage turbine blade: an airfoil, platform, shroud, fir-tree slots, and an internal cooling passage. Figure 5.14a details the notional blade geometry, with the wire-frame depiction in Figure 5.14b showing the internal cooling passage that runs through the entire blade. Figure 5.15 details how the blade model was subdivided into discrete sections, which allows for different material properties or crystallographic orientations to be assigned for parametric sensitivity studies of recrystallization or stray grains.

For a parametric study of recrystallization along the trailing edge (TE) of a single crystal turbine blade, single crystal Mar-M247 elastic properties from Table 3.6 were first assigned to the entire turbine blade detailed in Figure 5.14 to establish a baseline response. Then as Figure 5.15 outlines, TE sections were assigned polycrystalline properties (Table 3.7) to simulate a region of recrystallization, one section at a time. As before, the models are evaluated with the Lanczos Eigen frequency solver [149], providing $\triangle f_R$ predictions for the first 20 resonance modes, plotted in Figure 5.16a for sections TE 1–TE 3 and Figure 5.16b for TE 4–TE 6. From these results, it appears that the location of the recrystallized volume along the trailing edge affects which modes are most sensitive, but the general saw-tooth pattern to the $\triangle f_R$ plots is consistently observed. As a first order approximation it can be said that each TE section consists of 1% of the total turbine blade volume, which affects a characteristic saw-tooth $\triangle f_R$ pattern with a range of 1%. Some modes exhibit a positive $\triangle f_R$, while others exhibit a negative $\triangle f_R$, likely a result of resonance modes exhibiting deflections with greater bending or torsional character, respectively.

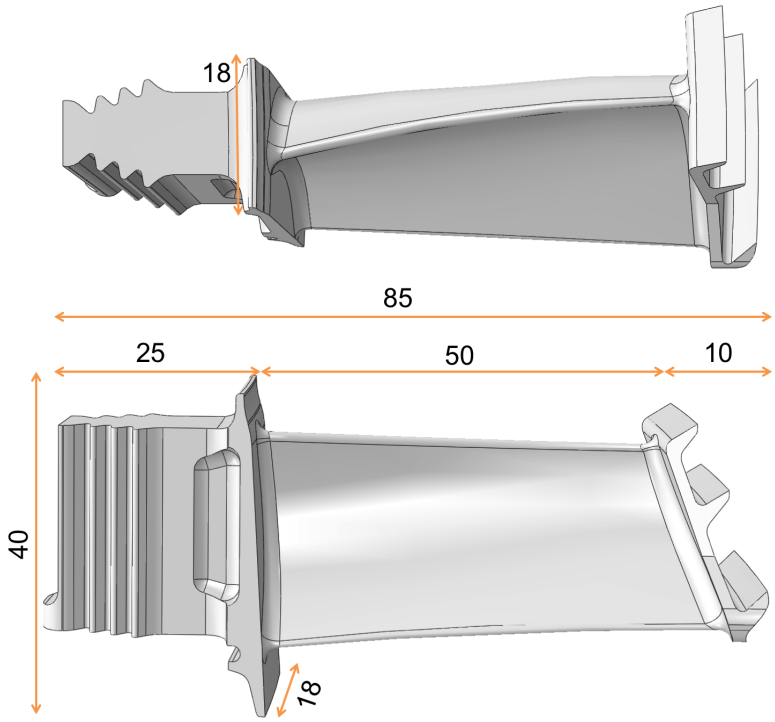

(a) Solid fill

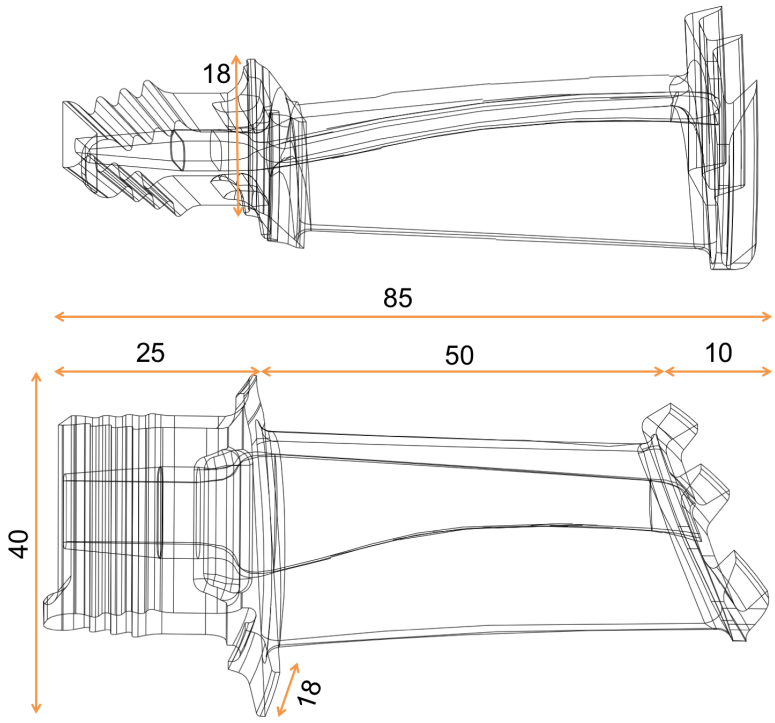

(b) Wire frame

Figure 5.14: Turbine blade model with (a) solid fill showing the surface features and (b) a wire frame depiction showing the contours of the internal cooling passage.

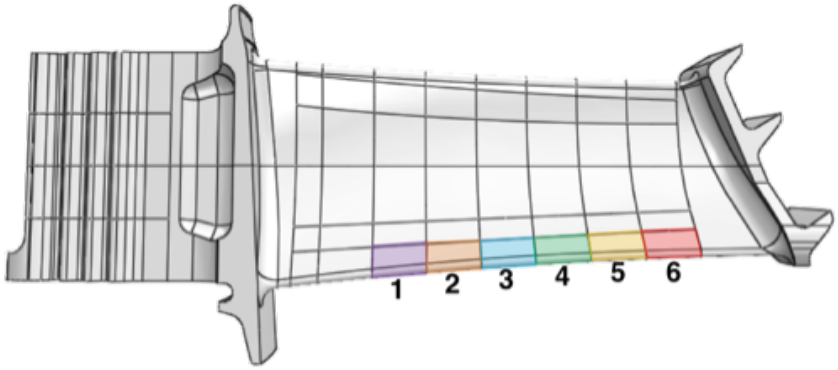

Figure 5.15: Turbine blade model subdivided into sections with trailing edge sections numbered and color coded.

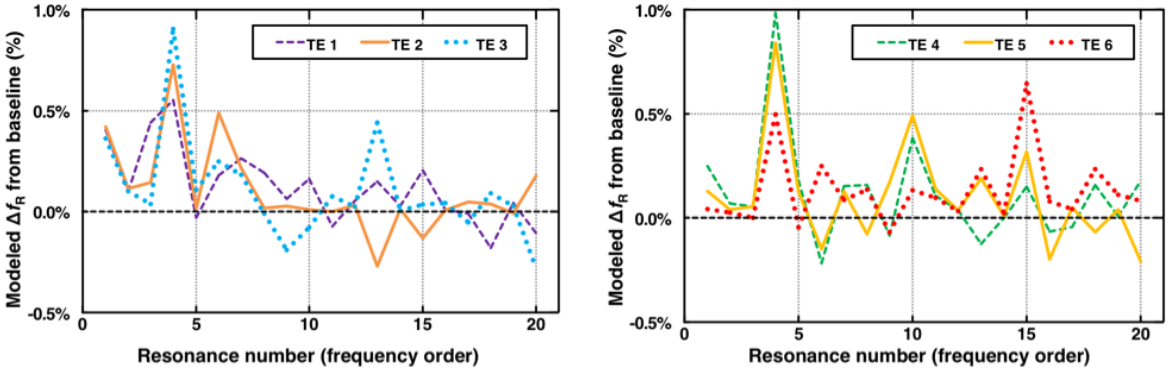

(a) Modeled $\triangle f_R$ for TE sections 1-3

(b) Modeled $\triangle f_R$ for TE sections 1-3

Figure 5.16: Modeled $\triangle f_R$ for recrystallization on turbine blade geometry trailing edge (TE) sections located at positions (a) 1–3 and (b) 4–6

5.7.2.1 Modal Analysis of Complex Geometries

A cursory modal analysis reveals that some similar mode types exist between the quarter-cylinder specimen geometry and the turbine blade geometry. Specifically, Figure 5.17a demonstrates how mode 2 exhibits torsional, mode 4 exhibits bending, and mode 7 exhibits extensional deflection characteristics. However, modal analysis in complex geometry components is not a simple task because mode-type classification based on observing the exaggerated deflection character predicted by the FE models can be quite subjective. Without objective metrics for classifying modes in complex geometries, it can be difficult to consistently identify modes and establish the general behavior of particular mode-

types. Particularly, the development of a uniform naming convention applicable to a variety of complex geometries remains a challenge that hinders modal analysis and limits the ability to apply knowledge gained from one analysis to another. But given that FE analysis provides a detailed map of nodal displacements for each resonance mode, classifications schemes based on objective (numerical) descriptions of mode shapes are very likely possible, despite the difficulty of classifying modes by their physical appearance.

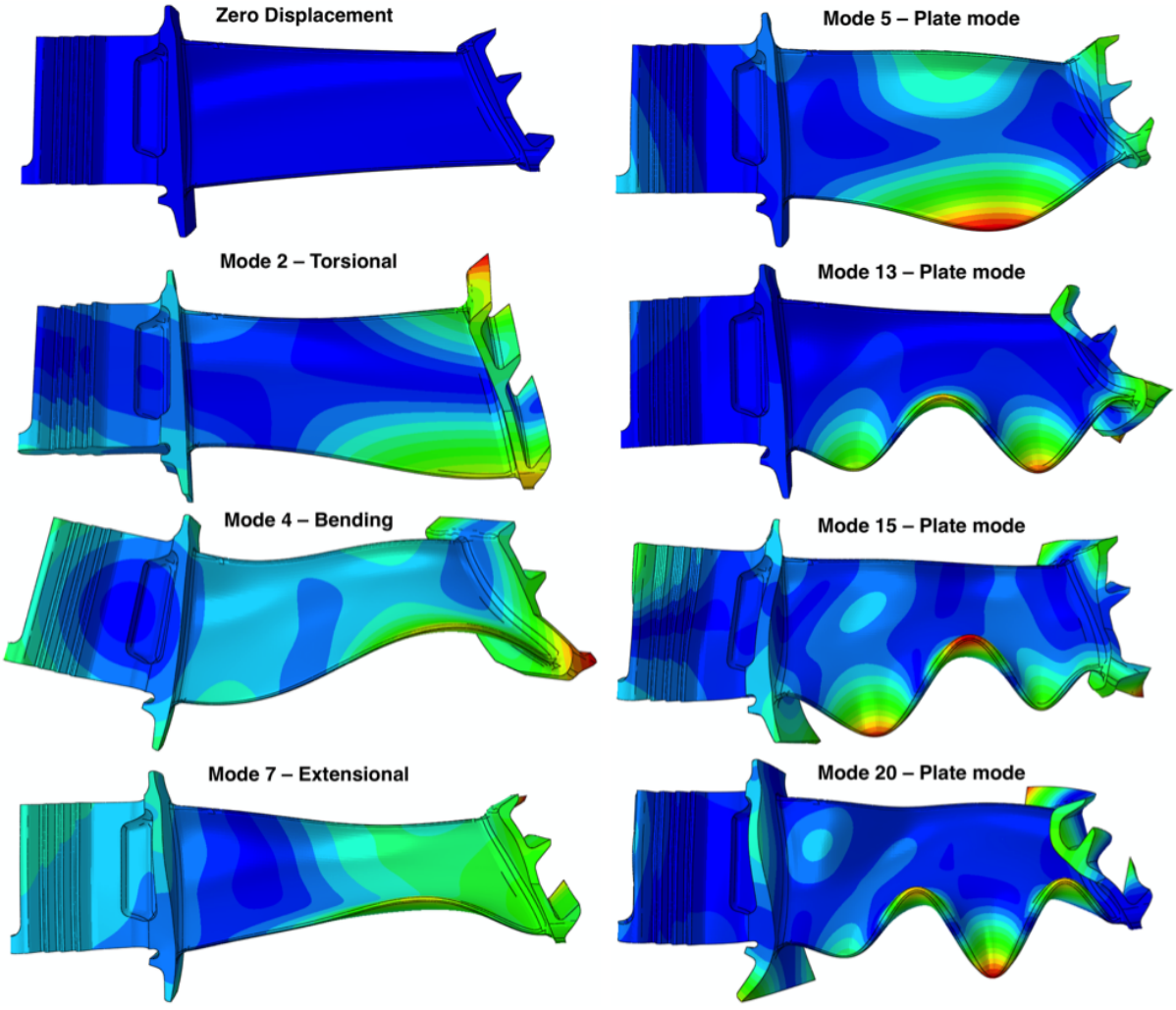

(a) Fundamental modes (b) Plate modes

Figure 5.17: Resonance mode shapes plotted with (a) fundamental torsional, bending, and extensional characteristics and (b) turbine blade specific "plate modes".

As an example, Figure 5.17b details a set of four turbine blade resonances predicted

with the FE model that do not conform well to previously identified mode-types. These modes exhibit bending and torsional characteristics, and appear to be related to each other such that a unique mode type classification is warranted. The designation "plate modes" is due to the fact that modes with a similar appearance have been observed in plate geometries, whereby sinusoidal deflections arise along thin exterior sections of the plate. These plate modes are common at low frequencies for the given turbine blade model, and exhibit a strong positive or negative $\triangle f_R$ that depends on the location of recrystallization along the TE of the airfoil. In fact, these modes appear to be quite diagnostic of defects along the trailing edge of the blade, and with further study it may be possible to identify specific regions that contain damage based on which plate modes are most affected. A rigorous modal analysis was not conducted for the turbine blade model results, therefore Figures 5.16a and 5.16b focus on the first 20 resonance modes where mode order switching is less likely. Note that failing to account for mode order switching would result in modeled $\triangle f_R$ that appear smaller than they actually are, which could obscure resonances that are particularly diagnostic of damage.

5.8 Conclusion

Simple finite element models have been developed and validated with RUS measurements to establish a forward modeling framework for quantitative evaluation of recrystallization in single crystal castings. FE models employ self-consistent elastic properties between the recrystallized and single crystal regions, with the recrystallized material modeled as a homogeneous isotropic volume with Gairola and Kröner [92] average properties. This homogenization greatly simplifies the modeling procedure as compared to a discrete grain approach, while producing modeled $\triangle f_R$ that are in very good agreement with measured results. The FMF was experimentally validated with Mar-M247 single crystal quarter-cylinder specimens, shot-peened to induce recrystallization on subsequent 1225 °C heat

treatments. Validation and a residual analysis determined recrystallization to be the single dominant mechanism affecting resonance in the measured specimen. While secondary mechanisms affecting resonance during high temperature exposure, e.g. annealing of imparted dislocations and surface oxidation, were deemed to have a negligible impact on resonance. Finally, the validated FMF is extended to complex geometry models, demonstrating the viability of RUS for detecting grain structure and casting defects in a variety of single crystal components. Demonstrating great potential for evaluation of small volumes of recrystallization along thin regions of turbine airfoils—where residual stresses from casting are high, and deformation induced recrystallization is more likely. Finally, a list of key conclusions from the work described in this chapter are provided below:

- FE models with self-consistent elastic properties provide an accurate description of the influence of recrystallization on resonance, and form the basis of a FMF for extending the predictive capability of RUS for NDE.

- Recrystallization in [001] single crystals of Ni-based superalloys introduce local changes in crystal orientation, which affect the elastic properties and result in $\triangle f_R$ with a characteristic saw-tooth pattern.

- Modal analysis confirms that recrystallization in [001] single crystals cause modes with bending and extensional characteristics to exhibit a positive $\triangle f_R$, while torsional modes exhibit a negative $\triangle f_R$.

- As demonstrated by the models and the experiments, the magnitude of the $\triangle f_R$ scale with the volume fraction of recrystallized material, which is key to quantitative assessments.

- Small volumes of recrystallization in a notional turbine blade geometry, on order of 1% the total volume of the blade, result in significant and characteristic $\triangle f_R$ that are two orders of magnitude greater than the reported RUS measurement sensitivity.

Chapter 6

Development of an Inverse Modeling Framework for Materials Characterization with RUS

Chapter Abstract

In this and the following chapter, Bayesian modeling and Hamiltonian Monte Carlo (HMC) are utilized to formulate a novel inverse modeling framework (IMF) capable of simultaneously estimating anisotropic elastic properties and crystallographic orientation of a specimen, from only a list of measured resonance frequencies collected via resonance ultrasound spectroscopy (RUS). This chapter, and the publication upon which this chapter is based[1], provides the first-ever demonstration of a full-Bayesian IMF to tackle the problem of RUS inversion of elastic properties, and the second-ever to simultaneously estimate crystal orientation after Sarrao et al. reported doing so in 1994 [36]. But with no subsequent demonstrations or reports of replication in well over 20 years, a different (more robust) approach is developed here through parameterizing crystal orientation as a unit quaternion, while the second-generation IMF code (CmdStan-RUS) detailed in the next chapter is the first open-source code of its kind. Together, these advances lead to substantially simplified experimental and computational procedures that form a broadly applicable IMF capable of accurately quantifying the elastic properties of materials, including low-symmetry single crystals. Finally, the IMF developed in this chapter is experimentally validated with RUS data collected from two parallelepiped specimens of structural metal alloys: polycrystalline Ti-6Al-4V (Ti-64) and single crystal Ni-based superalloy CMSX-4.

[1] [47] B. Bales, B.R. Goodlet, W.C. Lenthe, L. Petzold and T.M. Pollock. "Bayesian Inference of Elastic Properties with Resonant Ultrasound Spectroscopy," *Journal of the Acoustical Society of America* 143 (2018) pp.71-83. [doi:10.1121/1.5017840]

6.1 Introduction

Modern experimental procedures for RUS are discussed in great detail by Migliori et al. [33, 38, 126], but generally involve excitation of a specimen with vibrations from a piezoelectric element that is in physical contact with the specimen. When the drive frequency of the piezoelectric element approaches a natural vibrational mode frequency of the specimen, a resonance condition develops from constructive interference of opposite-traveling elastic waves to generate a standing wave throughout the specimen [33]. This standing wave leads to deflections of the specimen surface that are magnified in amplitude, potentially thousands of times greater than the drive amplitude, and are easily recorded by a second contacting piezoelectric element [33, 34]. When collecting a broadband RUS measurement the lowest-frequency mode is first identified, then the specimen is excited through a continuous range of greater frequencies until a desired quantity of modes are collected. These characteristic resonance frequencies are then provided to an inversion algorithm for estimating elastic properties. Today, the greatest impediment to broad application of resonance methods for elastic property evaluation are not empirical, but computational in nature.

Beyond inverting elastic properties with RUS data, crystallographic orientation can also be determined, as briefly detailed by Sarrao et al. [36]. The IMF developed here incorporates the ability to simultaneously estimate elastic properties and crystal orientations when the crystal reference frame is misaligned with the specimen reference frame. Simply machining a single crystal specimen along the crystal growth direction is insufficient, as only a few degrees of misalignment can lead to unacceptably large uncertainty in modulus estimates. X-ray diffraction methods are most often employed to measure the crystallographic orientation of an RUS specimen [33, 36], but this adds considerable complexity and cost to experimental methods as well as an additional source of measure-

ment error. Sarrao et al. [36] were first to report inverting crystal orientation and elastic moduli simultaneously, and rightly note the added value provided by such a capability. However, little guidance is offered towards reproducing their results beyond instructing the reader to proceed with "proper caution" by performing the inversion with "slower convergence steps". The present research details an alternative and robust approach for simultaneously estimating crystal orientation and elastic properties.

6.1.1 Computational Considerations for Inversion

While straightforward theoretically, there is considerable difficulty in the practical implementation of a RUS inversion framework. First, no general analytical solution exists for the computation of resonance frequencies for a 3D volume of material. Therefore, approximate (numerical) methods must be employed [33]. Meaningful contributions of numerous researchers over many decades including Holland (1968) [12], Demarest (1971) [13], Ohno (1976) [15], and Visscher et al. (1991) [19] have culminated in a generalized numerical approach for solving the forward problem based on variational methods. The xyz method of Visscher et al. is applicable to most simple specimen geometries and requires minimal computational resources [19], given that all of the requisite information about the specimen geometry and material properties are provided. Ultimately, the viability of any IMF for evaluating elastic properties from RUS measurements depends on an efficient and accurate forward calculation method [33].

As the resonance frequencies of a specimen are dependent on its shape, elastic constants, density, external forces, and the orientation of the elastic body, the deconvolution of unknown parameters from resonance frequencies is far from a trivial task. In fact, no closed form solution to this problem exists whereby unknown attributes of the specimen geometry or material properties are computed directly from a measured list of resonance frequencies [33]. Therefore, inverse methods are employed to find values for

the unknown parameters that bring a forward calculation of resonance frequencies into sufficient agreement with the resonance frequencies measured via RUS. Historically, elastic property inversion of RUS data has been accomplished via least square optimization algorithms [33, 43, 46]. For this task, the Levenberg-Marquardt (LM) algorithm popularized by Migliori et al. [33, 38] combines a modified Newton method with the steepest descent algorithm [36, 38, 43] to perform the inversion.

The least squares approach for overdetermined systems is popular due to its computational simplicity, but often suffers from a lack of robustness to outliers in the data set [164]. Another unfortunate characteristic of optimization-based inversion methods is that different initial parameterizations (i.e. "best guess" elastic moduli and optimizer-specific parameters) can lead the optimization algorithm to alternative solutions, while "poor" initial guess values may preclude convergence entirely [26, 51]. This problem is not unique to the LM algorithm, e.g. similar concerns exist when genetic algorithms are used [51, 165, 166].

An ideal IMF would be robust to uncertainty in the initial parameterization, noise in the measured data, misidentified modes, as well as missing or spurious modes; and would consistently converge to the correct solution. Ogi et al. [27] demonstrate an optimizer-based inversion framework capable of reliable convergence without the benefit of quality initial guess moduli. But their framework first requires proper mode identification via laser Doppler interferometry mapping of resonance mode shapes [27]. Indeed collecting additional data may simplify the inversion procedure, as would preparing a specimen with its crystal axes aligned with the specimen axes. But these methods only complicate experimental procedures while adding considerable cost. Ogi et al. go on to conclude that "correct mode identification is essential for successful, optimum determination of material coefficients" [27]. However, as this chapter will demonstrate, mode identification, quality initial guess moduli, and x-ray measurements of crystal orientation are by no means essential elements of a robust RUS inversion framework.

6.1.2 Implications of a Bayesian Approach to Inversion

A considerable downside to Bayesian techniques is the increased computation time, as the number of forward calculations necessary for HMC sampling of the posterior distributions is significantly greater than optimizer-based methods. A single optimization may require 10^2–10^4 forward problem evaluations, though the count is highly dependent on the quality of the initial guess values and the optimization algorithm used—with no guarantee of convergence or estimates of uncertainty. Alternatively, collecting a significant number of independent samples for performing a Bayesian inference may require upwards of 10^6 forward problem evaluations across all of the HMC chains—with remarkably robust convergence behavior given the model is not ill-defined. Ultimately, this chapter will demonstrate how the combination of fast and accurate forward calculations (employing the xyz algorithm [19]), conducted using modern computational resources, and efficient posterior sampling via Hamiltonian dynamics provide the necessary speed-ups for performing a Bayesian inference with a modern desktop computer in 10–50 hours.

As alluded to previously, most classic RUS inversions provide only point estimates of elastic constants; that is, single number estimates for each parameter in the RUS model regardless of the amount or precision of data. Point estimates are unsatisfactory in many inverse problems because they do not give information about how well a fit worked or how well a parameter is known. Bayesian techniques can be used to avoid these problems by systematically estimating uncertainty. It is very reasonable that a point estimate produces answers that are "good enough" in controlled experiments, but it is difficult to develop confidence in the methods for experiments where prior knowledge is sparse.

In a manner similar to that of Bernard et al. [101], the approach developed here improves upon classical RUS inversion by reformulating the problem as a Bayesian inference and characterizing the unknown parameters through sampling the resultant poste-

rior distribution. The capability to simultaneously estimate the orientation and elastic properties of elastically anisotropic bodies offers further improvement to classical RUS inversion techniques, simplifying specimen preparation procedures and eliminating a potential source of measurement error. Key advantages and disadvantages of a Bayesian formulation will be highlighted, along with experimental and computational considerations helpful for replication. Ultimately this work intends to demonstrate robust convergence behavior irrespective of initial parameterization and easy-to-interpret uncertainties for all parameter estimates.

6.2 Experimental Methods

6.2.1 Specimen Preparation

Regular parallelepiped specimens of fine-grained polycrystalline Ti-6Al-4V (Ti-64) and single crystal Ni-based superalloy CMSX-4 were machined via wire EDM (electrical discharge machining) then carefully ground with 800-grit sandpaper to remove the superficial EDM damage layer. The Ti-64 specimen measured 7.753 x 9.057 x 13.199 mm, with a mass of 4.0795 g and a calculated density of 4402 kg/m^3. The CMSX-4 parallelepiped dimensions were 11.959 x 13.953 x 19.976 mm with a mass of 29.0041 g and a calculated density of 8701.4 kg/m^3. With randomly oriented grains, the Ti-64 specimen exhibits isotropic elastic symmetry while the single crystal CMSX-4 material possesses cubic symmetry. Minimizing geometric defects during specimen fabrication and precise measurement of the geometry and mass are important for minimizing the uncertainty in the HMC parameter estimates; with a "good" parallelepiped geometry, according to Migliori et al., exhibiting dimensional errors less than 0.1% [38]. The only notable divergence between this work and the typical specimen fabrication procedures outlined by Migliori and Sarrao [33] is that no attempt was made to align the axes of the parallelepiped to the

crystallographic axes of the CMSX-4 material. As orientation and elastic constants will be determined simultaneously through inversion, any arbitrary misorientation between the crystal and specimen axes is allowed.

6.2.2 Resonant Ultrasound Spectroscopy

6.2.2.1 RUS Experimental Setup

RUS data were collected using commercially-available RUS equipment developed by the Vibrant Corporation consisting of three primary components: a transceiver, a piezoelectric transducer (PT) cradle, and a computer control unit; each with further details provided in Chapter 3. Figure 6.1 shows the configuration of the PT cradle as used to measure the CMSX-4 specimen, comprised of three custom-built omnidirectional piezoelectric transducers held in a tripod configuration with adjustable optical table fixtures affixed to a vibration-damped breadboard. The PTs were custom built and consist of a cylindrical brass housing encasing a piezoelectric element, electrical leads, and a wear-resistant hemispherical silicon carbide tip. The parallelepiped specimens freely rest upon the silicon carbide-tipped transducers, with no couplant necessary to facilitate the transmission of vibrations between the transducers and the specimen [33, 34].

The "drive PT" in Figure 6.1 is driven with a swept sinusoidal signal from the transceiver to excite the specimen to resonate, while two "receive PTs" convert vibrations from the specimen back to an electrical signal that is returned to the transceiver and computer control unit for analysis. As a principle of mechanical resonance, a standing elastic wave develops throughout the specimen when the drive frequency approaches a resonance frequency of the specimen. With the magnitude of the vibrations amplified by hundreds to thousands of times the driving force amplitude, depending on the ultrasonic attenuation (i.e. damping characteristics) of the material [33, 34]. Plotting the signal registered by the two receive PTs as a function of the drive frequency yields

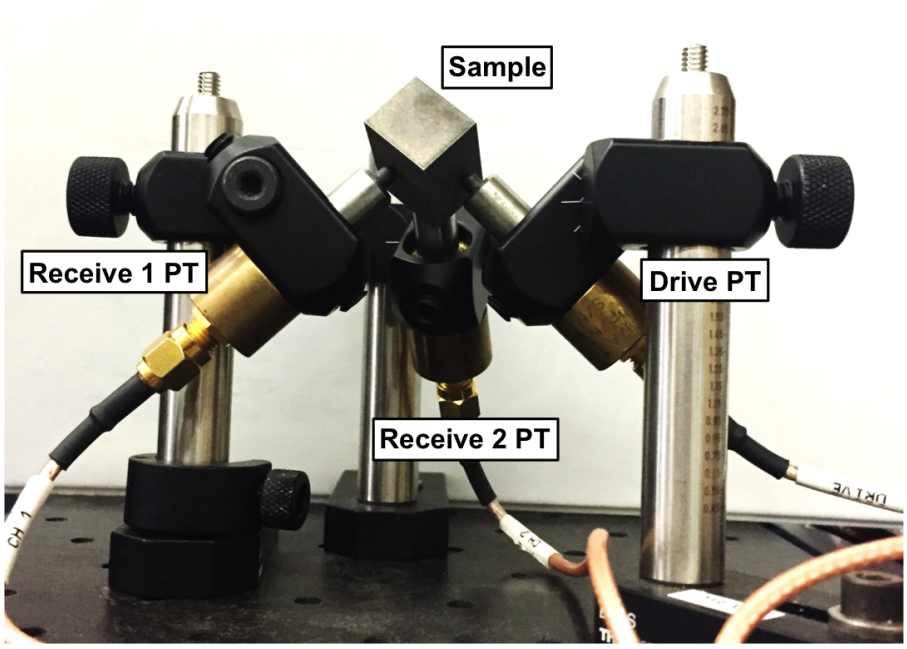

Figure 6.1: Piezoelectric transducers configured into a cradle supporting the CMSX-4 parallelepiped specimen.

a broadband RUS spectrum plot, with each peak indicating the frequency of a unique resonance mode. Figure 6.2 shows a broadband resonance spectrum plot collected from the CMSX-4 specimen, with 53 resonance modes across the 200 kHz broadband.

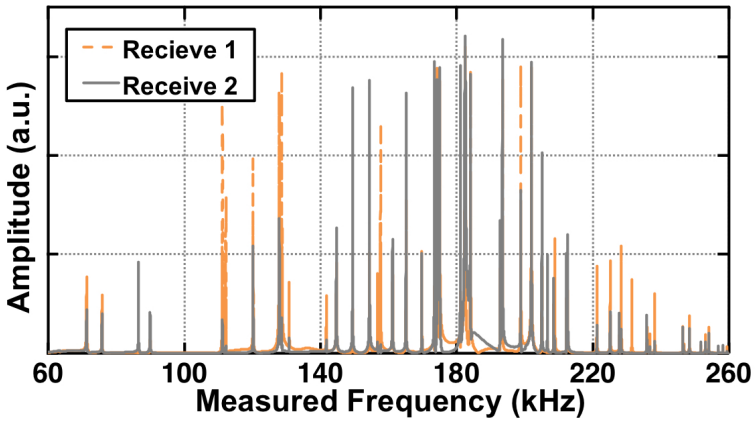

Figure 6.2: RUS broadband spectrum plot collected from the CMSX-4 specimen.

6.2.2.2 RUS Measurement Considerations

It is important to minimize the magnitude and the variability of any external forces on the specimen while collecting RUS data because these external forces can interfere with the free vibrations of the specimen and affect the frequencies that are measured [38,167]. Configuring the piezoelectric transducers into a fixed cradle as detailed by Figure 6.1 serves to minimize contact force variability between the specimen and the transducers across multiple measurements and specimen sizes. However, as the specimen is free to deflect away from the PT cradle during resonance the signal amplitude information is generally unreliable. For this reason the broadband RUS data plotted in Figure 6.2 are given with arbitrary units (a.u.). When amplitude information is necessary, to measure acoustic attenuation for instance, parallelepiped specimens are often pinched between two (often planar) PTs [167]. Note that the corners of a parallelepiped are the optimal location for excitation and measurement of resonance frequencies [38]; but for the purpose of determining elastic constants the cradle configuration has proven itself simple and effective.

6.2.2.3 RUS Data Collection

Broadband RUS spectra were collected at room temperature and at standard atmospheric pressure in accordance with ASTM standard practice 2534-15 [49]. The broadband scans ranged from 60–260 kHz for the CMSX-4 specimen and from 100–375 kHz for the Ti-64 specimen. Distillation of the broadband resonance spectrum into a list of resonance frequencies was automated for consistency and verified through inspection as the data were collected. Missing or spuriously identifying a mode can greatly confound the process of determining elastic constants [33], therefore considerable attention was directed towards ensuring that measured lists of resonance frequencies accurately reflect the specimen from which they were collected. Occasionally a resonance peak will be obscured by a higher-

amplitude peak in close proximity, but rarely are modes completely missed by both receive PTs of the cradle configured as shown in Figure 6.1. Nevertheless, each broadband measurement was repeated five times, with the specimen removed and replaced on the PT cradle after each measurement to ensure that any unintentional specimen-transducer interactions related to specimen placement would not be repeated. From the multiple broadband measurements a single average list of resonance frequencies was created, from which all computations and property estimates were based.

6.2.3 Crystallographic Orientation Measurements

To measure the orientation of the CMSX-4 crystal reference frame, a series of x-ray diffraction (XRD) measurements were collected using a Rigaku Smartlab High-Resolution Diffractometer with motorized RX-RY stage. First, the broad face of the specimen was prepared in accordance with standard metallographic techniques: wet grinding with 1200-grit paper, mechanical polishing via diamond suspension to 0.25 micron, and a final electrochemical etch. Then the specimen was affixed to the RX-RY stage of the diffractometer, which tilted in two orthogonal directions while Bragg peaks were recorded for {100}, {110}, and {111} crystallographic planes. A least squares fit of the stage position, corresponding to the crystal plane normal vectors, determined the crystal orientation: (0.987, -0.00526, -0.158, 0.0164) as a passive unit quaternion (ordered as $wxyz$) and an uncertainty of approximately one degree.

6.3 Computations

The following sections discuss the development of a statistical model for characterizing elastic constants via RUS. Section 6.3.1 applies a variational approach to the forward problem to derive a generalized eigenvalue equation that is evaluated using the Rayleigh-Ritz method. The resulting eigenvalues correspond to the resonance frequencies while the

eigenvectors correspond to the resonance mode shapes of the 3D elastically anisotropic specimen. Then Section 6.3.3 introduces the Bayesian RUS model, with Section 6.3.4 describing how the Bayesian computations are carried out.

6.3.1 Forward Problem

Given an inverse modeling framework requires many fast and accurate forward problem evaluations, the Rayleigh-Ritz method is preferred over the the finite element forward calculations discussed in previous chapters [18,47]. However, this approach also requires the geometry of the specimen be simple enough to describe with a relatively small set of continuous polynomial basis functions. Thus, building to the point where Rayleigh-Ritz methods are applied, the following Lagrangian formulation of the forward problem is derived using Hamilton's variational principle. Following primarily the derivation by Migliori and Sarrao [33], with insights from other sources [18,101,126], it will be shown that the resonance modes of a free vibrating specimen correspond to the the stationary points of its mechanical Lagrangian ($\mathscr{L}$).

Representing the total energy of a specimen of volume V and free surface S, $\mathscr{L}$ can be stated in the simplest terms as the combination of the kinetic and potential energy of the specimen:

$$\mathscr{L} = \int_V \big(KE - PE\big) dV \ . \tag{6.1}$$

The general form of KE and PE are those of a simple harmonic oscillator with a time dependence of the displacements assumed to be $e^{i\omega t}$. Thus the kinetic energy (KE) of the specimen can be defined as

$$KE \ = \ \frac{1}{2} \sum_i \rho \omega^2 \boldsymbol{u}_i^2 \ , \tag{6.2}$$

with ω being the angular resonance frequency, ρ is the density, and $\boldsymbol{u}_i$ is the ith Cartesian

component of the displacement vector of each point in the volume V. As such, these displacements are a function of position ($\boldsymbol{x}$) within V, and are also a function of time (t). With $\boldsymbol{x} = \boldsymbol{x}_i = [x_1, x_2, x_3]$, such that $\boldsymbol{u}_i = [u_1(\boldsymbol{x}, t), u_2(\boldsymbol{x}, t), u_3(\boldsymbol{x}, t)]$. The potential energy (PE) of the specimen is defined as

$$PE \;=\; \frac{1}{2} \sum_{i,j,k,l} C'_{ijkl} \frac{\partial \boldsymbol{u}_i}{\partial x_j} \frac{\partial \boldsymbol{u}_k}{\partial x_l} \tag{6.3}$$

with effective elastic constants C'_{ijkl} and summation on i, j, k, l from 1 to 3, again for the three Cartesian coordinates. Thus the Lagrangian can be restated as:

$$\mathscr{L} = \frac{1}{2} \int_V \left[\sum_i \rho \omega^2 \boldsymbol{u}_i^2 - \sum_{i,j,k,l} C'_{ijkl} \frac{\partial \boldsymbol{u}_i}{\partial x_j} \frac{\partial \boldsymbol{u}_k}{\partial x_l} \right] dV \;. \tag{6.4}$$

6.3.1.1 Variational Approach to the Forward Problem

Now a variational approach, employing Hamilton's principle, is used to find the stationary points (i.e. the extrema) of $\mathscr{L}$. With the displacements $\boldsymbol{u}_i$ allowed to vary arbitrarily in the volume V and over the surface S,

$$\boldsymbol{u}_i \to \boldsymbol{u}_i + \delta \boldsymbol{u}_i \quad \text{and} \quad \mathscr{L} \to \mathscr{L} + \delta \mathscr{L} \;. \tag{6.5}$$

Thus,

$$\mathscr{L} + \delta \mathscr{L} = \frac{1}{2} \int_V \left[\sum_i \rho \omega^2 \big(\boldsymbol{u}_i + \delta \boldsymbol{u}_i \big)^2 - \sum_{i,j,k,l} C'_{ijkl} \frac{\partial \big(\boldsymbol{u}_i + \delta \boldsymbol{u}_i \big)}{\partial x_j} \frac{\partial \boldsymbol{u}_k}{\partial x_l} \right] dV \;. \tag{6.6}$$

Now keeping terms to the first order in $\delta \boldsymbol{u}_i$, with the latter term requiring integration by parts and the Divergence theorem to give $\delta \mathscr{L}$ as:

$$\delta \mathscr{L} = \int_V \left[\sum_i \left(\rho \omega^2 \boldsymbol{u}_i + \sum_{j,k,l} C'_{ijkl} \frac{\partial^2 \boldsymbol{u}_k}{\partial x_j \partial x_l} \right) \delta \boldsymbol{u}_i \right] dV - \int_S \left[\sum_i \left(\sum_{j,k,l} C'_{ijkl} \boldsymbol{n}_j \frac{\partial \boldsymbol{u}_k}{\partial x_l} \right) \delta \boldsymbol{u}_i \right] dS. \tag{6.7}$$

Given the arbitrary nature of $\delta \boldsymbol{u}_i$ in V and on S, it is known that $\delta \mathscr{L} = 0$, while it can also be said that the left and right hand terms in the parentheses of Equation (6.7) must be equal to zero as well. In setting these terms equal to zero it is clear that they have special significance. The left hand term:

$$\rho\omega^2 \boldsymbol{u}_i + \sum_{j,k,l} C'_{ijkl} \frac{\partial^2 \boldsymbol{u}_k}{\partial x_j \partial x_l} = 0 \text{ in } V \tag{6.8}$$

is a statement of the wave equation of motion, first detailed in Equation (2.40), when given as:

$$\sum_{j,k,l} C'_{ijkl} \frac{\partial^2 \boldsymbol{u}_k}{\partial x_j \partial x_l} = \rho \frac{\partial^2 \boldsymbol{u}_i}{\partial t^2} \ . \tag{6.9}$$

The right hand term of the Lagrangian set equal to zero is

$$\sum_{j,k,l} C'_{ijkl} \boldsymbol{n}_j \frac{\partial \boldsymbol{u}_k}{\partial x_l} = 0 \text{ on } S \ , \tag{6.10}$$

and with

$$\sigma_{ij} = C'_{ijkl} \frac{\partial \boldsymbol{u}_k}{\partial x_l} \ , \tag{6.11}$$

represents the stress-free boundary conditions. Therefore, the set of $\boldsymbol{u}_i$ which make $\mathscr{L}$ stationary by satisfying Equations (6.8) and (6.10), are the same set of displacements that correspond to the ω resonance mode frequencies of the resonating specimen with stress free boundary conditions [12, 13, 15, 19, 33].

6.3.1.2 Generalized Eigenvalue Problem and the Rayleigh-Ritz Method

The process of determining the set of displacements which correspond to the stationary points of the Lagrangian is accomplished first by formulating Equation (6.4) as generalized eigenvalue problem, which is then solved numerically with the Rayleigh-Ritz method. First, expanding the displacements vector $\boldsymbol{u}_i(\boldsymbol{x}, t)$ of the specimen as a finite

sum of J basis functions $\boldsymbol{\phi}_\lambda(x_1, x_2, x_3)$, whereby J is determined by the polynomial order (P) of the expansion (per Equation (6.14)). Together with a set of 3J as-yet unknown coefficients $\boldsymbol{\alpha}_{i,\lambda}$, the expansion of $\boldsymbol{u}_i$ is given as:

$$\boldsymbol{u}_i(x, y, z) = \sum_\lambda \boldsymbol{\alpha}_{i\lambda} \boldsymbol{\phi}_\lambda(x, y, z) \ . \tag{6.12}$$

The basis functions ($\boldsymbol{\phi}_\lambda$) are indexed according to $\lambda = (m, n, o)$, while the coefficients of the expansion ($\boldsymbol{\alpha}_{i\lambda}$) are indexed according to $i\lambda = (i, m, n, o)$. For these index values, $i = 1, 2, 3$ per the three Cartesian directions, just as before, while m, n and o are a combination of nonnegative integers that satisfy:

$$m + n + o \leq P \ . \tag{6.13}$$

Thus, P is the maximum polynomial order of the expansion with J potential permutations according to

$$J = \frac{(P+1)(P+2)(P+3)}{6} \ , \tag{6.14}$$

such that typical values of $P = 8,\ 10,\ 12$ lead to $J = 165,\ 286,\ 455$ basis functions.

Earlier implementations ([13, 15]) employed Legendre polynomials for $\boldsymbol{\phi}_\lambda$, giving matrix elements that were easier to compute, but limited in flexibility in describing the geometry of the specimen [33]. Instead, the "xyz-algorithm" of Visscher et al. [19] is used here, which defines the basis functions as a product of powers of the Cartesian x, y, z coordinates:

$$\boldsymbol{\phi}_\lambda = x^m y^n z^o \ = x_1^m x_2^n x_3^o, \tag{6.15}$$

where m, n, and o are the nonnegative integer values referenced in Equation (6.13).

Substitution of Equation (6.12) into Equation (6.4) gives:

$$\mathscr{L} = \frac{1}{2}\int_V \left[\sum_{i,i',\lambda,\lambda'} \delta_{ii'}\rho\omega^2 \boldsymbol{\alpha}_{i\lambda}\boldsymbol{\alpha}_{i'\lambda'}\boldsymbol{\phi}_\lambda\boldsymbol{\phi}_{\lambda'} - \sum_{i,j,k,l,\lambda,\lambda'} C'_{ijkl}\boldsymbol{\alpha}_{i\lambda}\boldsymbol{\alpha}_{i'\lambda'}\frac{\partial\boldsymbol{\phi}_\lambda}{\partial x_j}\frac{\partial\boldsymbol{\phi}_{\lambda'}}{\partial x_l}\right] dV \ , \tag{6.16}$$

where the summation on λ and λ' iterate through the J permutations of λ, e.g. $(0,0,0)$, $(1,0,0)$, $(0,1,0)$, $(0,0,1)$, $(1,1,0)$, etc.

Now transitioning to a matrix representation, with vectors as bold lower-case symbols and matrices as bold upper-case symbols, the stiffness matrix $\boldsymbol{K}$ is defined as

$$\boldsymbol{K} = \boldsymbol{K}_{i\lambda,k\lambda'} = \sum_{j,l} C'_{ijkl}\int_V \frac{\partial\boldsymbol{\phi}_\lambda}{\partial x_j}\frac{\partial\boldsymbol{\phi}_{\lambda'}}{\partial x_l}dV \ . \tag{6.17}$$

while the mass matrix $\boldsymbol{M}$ is defined as

$$\boldsymbol{M} = \boldsymbol{M}_{i\lambda,k\lambda'} = \rho\delta_{ik}\int_V \boldsymbol{\phi}_\lambda\boldsymbol{\phi}_{\lambda'}dV \ , \tag{6.18}$$

with δ_{ik} being the Kronecker delta. Together $\boldsymbol{K}$ and $\boldsymbol{M}$ are substituted into Equation (6.16) to give

$$\mathscr{L} = \frac{1}{2}\omega^2\boldsymbol{a}^T\boldsymbol{M}\boldsymbol{a} - \frac{1}{2}\boldsymbol{a}^T\boldsymbol{K}\boldsymbol{a} \ , \tag{6.19}$$

where $\boldsymbol{a}$ is a column vector of elements $\boldsymbol{a}_i$ that are the coefficients of the expansion given in Equation (6.12), while $\boldsymbol{M}$ and $\boldsymbol{K}$ are matrices whose order J is determined by Equation (6.14). The stationary points of Equation (6.19) are now determined by setting

$$\frac{\partial\mathscr{L}}{\partial\alpha_{i\lambda}} = 0 \text{ when } \delta\mathscr{L} = 0 \tag{6.20}$$

leading to the eigenvalue equation

$$\omega^2\boldsymbol{M}\boldsymbol{a} = \boldsymbol{K}\boldsymbol{a} \tag{6.21}$$

where $\boldsymbol{M}$ and $\boldsymbol{K}$ are symmetric and $\boldsymbol{M}$ is positive-definite. From this point, traditional numerical techniques (like commercial eigenvalue solvers) can be used to solve Equation (6.21) for the sets of eigenvalues and eigenvectors that represent the resonance mode frequencies and the resonance mode shapes of the specimen, respectively. Finally, differentiating Equation (6.21) with respect to the estimated parameters is necessary for the Hamiltonian behavior of the Monte Carlo sampling, which is discussed in Section 6.3.4.1.

6.3.2 Effective Properties Due to Crystal Orientation

Along with estimating the single crystal elastic constants, major advantages are gained through simultaneously estimating the orientation of the crystal lattice with respect to the specimen axes. For example, specimen preparation is substantially simplified because a parallelepiped can be cut from a parent single crystal without regard for the crystal reference frame orientation, as long as the effective elastic constants (C'_{ijkl}) are properly incorporated into the forward model. If the rotation from the specimen axes to the crystal axes is represented as a passive unit quaternion (q, Equation (2.53)) with elements $wxyz$, and C_{pqrs} are the elastic constants of an aligned specimen, then the effective elastic constants of the rotated specimen, C'_{ijkl} can be computed as follows:

$$q = \begin{bmatrix} w^2 + x^2 - y^2 - z^2 & 2(xy - wz) & 2(xz + wy) \\ 2(yx + wz) & w^2 - x^2 + y^2 - z^2 & 2(yz - wx) \\ 2(zx - wy) & 2(zy + wx) & w^2 - x^2 - y^2 + z^2 \end{bmatrix} \tag{6.22}$$

$$C'_{ijkl} = q_{ip} q_{jq} C_{pqrs} q_{kr} q_{ls} \ . \tag{6.23}$$

For more information about unit quaternions, how they are relate to Euler Angles and other parameterizations, a well as further discussion about the effects of crystal orientation on C'_{ijkl}, see the discussion provided in Section 2.3.2.2 and Section 2.3.4.

6.3.3 Building a Statistical RUS Model

Viewing the forward problem from a Bayesian perspective, experimental data is modeled as:

$$X_1, X_2, \ldots, X_N = f(C_{11}, C_{12}, ...) + \xi \tag{6.24}$$

where $X_1, X_2, ..., X_N$ are the set of N measured resonance modes, f is the forward model which computes the resonance modes of the specimen given the necessary elastic constants, and ξ is a noise term that represents the combined uncertainty in fabrication and measurement of the specimen.

Since the the noise (ξ) in Equation (6.24) was modeled as a random variable, the outputs $(X_1, X_2, \ldots, X_N)$ are also random variables. Assuming the noise of each mode is normally distributed with mean zero and a variance of the standard deviation (sd) squared, the probability of measuring a set of resonance modes $(X_0, X_1, \ldots, X_N)$ given the elastic constants (C_{11}, C_{12}, etc.) can be written using the forward model, f, as:

$$P(X_0, X_1, \ldots, X_N | C_{11}, C_{12}, \ldots) \sim \mathcal{N}(f(C_{11}, C_{12}, \ldots), \sigma^2) \ . \tag{6.25}$$

This equation, usually written in shorthand as $P(X|\theta)$, is known as the likelihood, and is the probability of measuring a set of data given some fixed parameters. For an inverse problem, it is the opposite relation, $P(\theta|X)$, or the probability that parameters take certain values given the measured data. $P(\theta|X)$ is known as the posterior distribution, and in a Bayesian interpretation represents the uncertainty in a set of parameters given the data. The posterior can be computed from the likelihood and any prior knowledge

about the parameters by using Bayes' rule:

$$\underbrace{P(\theta|X)}_{Posterior} = \frac{\overbrace{P(X|\theta)}^{Likelihood}\overbrace{P(\theta)}^{Prior}}{\underbrace{P(X)}_{PriorPredictive}} . \tag{6.26}$$

The $P(\theta)$ term is called the prior because it is specified to contain the prior beliefs about the probabilities of certain parameters (which could be as simple as requiring a parameter to be positive, or something much more complicated). $P(X)$ is the prior predictive distribution. It can be computed from the likelihood and the prior ($P(X) = \int P(X|\theta)P(\theta)d\theta$), but for the Monte Carlo computations here can be regarded as a normalization constant and ignored.

If the model and data match well, the posterior distributions on the parameters will be tight, and it will be easy to extract estimates for the parameters. However, from the outset, it is unclear how informative the posterior will actually be. It is possible, for instance, to have higher confidence in one parameter than another, or to have multiple values of a parameter that give equally likely explanations for the data. Because of this uncertainty, it is important to compute the full posterior $P(\theta|X)$ and work with confidence intervals rather than just returning a single estimate.

Returning to Equation (6.24), the IMF developed here and in the following chapter assumes the noise (ξ) is distributed normally about every resonance mode with a single variance (i.e. the scale of the noise does not change for each mode). The primary justification for picking this model comes a-posteriori by checking that the model explains the data well with few outliers. Of course such a check is not always so simple, as the standards for "explaining the data well" and the definition of an outlier are very application specific. In this chapter, the RUS measurement noise (presumably from inconsistent placement of the specimen on the transducer cradle or specimen transducer interactions) was much smaller than the noise inherent to the specimen itself (presumably

from specimen fabrication). Unfortunately, specimen fabrication is not easily repeatable in a manner that would allow for multiple independent samples, making it difficult to ever fully justify these assumptions.

Following the assumptions stated above, given that one set of resonance modes is available, every measurement goes towards estimating the lumped variance parameter. Thus the complete likelihood can be stated as:

$$P(X|\theta) = \prod_i \frac{1}{\sqrt{2\pi\sigma_i^2}} e^{\frac{(f_i(\theta)-X_i)^2}{2\sigma_i^2}} \tag{6.27}$$

where $f_i(\theta)$ is the i^{th} computed resonance mode. By collecting many independent resonance mode measurements, the estimates for θ can be tightened to suitable levels.

The prior term ($P(\theta)$) can be used to specify prior information about a parameter. For instance, it makes sense to assume that the C_{11} elastic constant is positive, somewhere between zero and a few hundred gigapascals. This can be expressed by a uniform prior distribution $P(C_{11}) = \mathcal{U}(0 \text{ GPa}, 500 \text{ GPa})$. Likewise, perhaps a parameter is known to some precision, in which case a normal prior like $P(C_{11}) = \mathcal{N}(200 \text{ GPa}, 10 \text{ GPa})$ is reasonable. For the work detailed in this chapter, the prior on the variance parameter was set to $\sigma^2 = \mathcal{U}(0 \text{ kHz}, \infty \text{ kHz})$.

6.3.4 Computing the Posterior (Hamiltonian Monte Carlo)

Given a likelihood and prior, it is trivial to use Bayes' theorem to write out an expression for the posterior. However, evaluating this expression is difficult because the dimension of θ can be large and the cost of evaluating the likelihood high. It is possible, though, to approximate the posterior by drawing samples from it using Monte Carlo techniques.

The Monte Carlo technique used in this dissertation is Hamiltonian Monte Carlo (HMC). To understand the results it will be useful to quickly review the characteristics of HMC and Markov Chain Monte Carlo (MCMC) methods in general. Perhaps the

most common MCMC method is Metropolis Monte Carlo (Metropolis MC). In physics terms, Metropolis MC generates a sequence of samples $s_0, s_1, \ldots, s_N$ that represent states drawn from a thermodynamic equilibrium. The Metropolis algorithm, like all MCMC methods, proceeds sequentially. That is, state s_{i-1} is used to generate s_i. The jump from s_{i-1} to s_i is chosen randomly, and the decision to keep or reject the new state s_i is made based on the difference in an energy function $\Delta\Phi = \Phi(s_i) - \Phi(s_{i-1})$, representing the transition energy from state s_{i-1} to state s_i. If the Metropolis algorithm accepts and rejects are handled properly in accordance with the energy function Φ, then the sequence of states generated by the process will have physical meaning with regards to the thermal equilibrium of the simulated system.

In statistical applications, the sequence of states, $s_0, s_1, \ldots, s_N$, is replaced with a sequence of parameterizations, $\theta_0, \theta_1, \ldots, \theta_N$, and Φ is set equal to $\log P(X|\theta)P(\theta)$, the log of the joint distribution. A common pitfall for newcomers is wondering what role $\int X$ plays in this. X is the measured data. It is fixed, and does not change. Sampling only happens over the parameters ($\int \theta$) in the joint distribution. With this choice of Φ, the Metropolis Monte Carlo method will generate a sequence of parameterizations where each parameterization, θ, is drawn from a distribution proportional to the true posterior. These samples can then be used to approximate the true posterior.

Application of Metropolis MC is mostly limited for computational reasons. In practice, Metropolis MC does not efficiently explore parameter space due to how it randomly selects new parameterizations with very little regard to the problem at hand. Hamiltonian Monte Carlo addresses this issue where possible by using the gradient of $\log P(X|\theta)P(\theta)$ to select new states more intelligently. Compared to Metropolis MC (and many other MCMC methods), HMC generates posterior samples much more efficiently. The need for the derivatives of $\log P(X|\theta)P(\theta)$ limits HMC's applicability in general, but the necessary derivatives are available in the forward model used here. A key parameter for HMC is the time step, which will determine how efficiently the chain can move around

parameter space. The time step cannot be too large though, or the HMC chain will go unstable and always reject new states.

The Hamiltonian Monte Carlo algorithm used in this chapter was taken from [168], with adaptations for orientations by [169]. For this HMC algorithm, the use of multiple steps sizes (as detailed in [168]) were critical for achieving efficient sampling. While the IMF used in the next chapter employs the default sampler in Stan (an open-source probabilistic programing language [60]) which automatically determines the optimal step size, and other HMC parameters without the need for user input.

6.3.4.1 Necessary Derivatives

The gradient of $\log P(X|\theta)P(\theta)$ is derived here. All derivatives are computed with the chain rule. $P(\theta)$ is assumed equal to one to simplify the math (the non-negativity constraint on sd^2 is controlled with a parameter transformation [60]).

6.3.4.2 Elastic Constants

With $P(\theta)$ equal to one, the $\log P(X|\theta)P(\theta)$ term is simplified to $\log P(X|\theta)$. Using the chain rule to write the partial derivative of the log-likelihood with respect to the parameter C_{11} gives the sum:

$$\frac{\partial logP(X|\theta)}{\partial C_{11}} = \sum_i \frac{\partial logP(X|\theta)}{\partial \omega_i} \frac{\partial \omega_i}{\partial C_{11}} \tag{6.28}$$

where ω_i is the i^{th} resonance mode, or the i^{th} index of $f(\theta)$. The partial derivative with respect to ω_i is easy to compute (given the likelihood in Equation (6.27)):

$$\frac{\partial logP(X|\theta)}{\partial \omega_i} = \frac{-(\omega_i - X_i)}{\sigma^2} \ . \tag{6.29}$$

The partial derivative of ω_i with respect to C_{11} (or any elastic constant) requires derivatives of the eigenvalues (the ω_i^2s) of Equation (6.21). Given a number of distinct eigenvalues (ω_i^2) and orthonormal eigenvectors (ν_i), the derivative of the i^{th} eigenvalue can be computed as in [170]:

$$\frac{\partial \omega_i^2}{\partial C_{11}} = \nu_i^T \frac{\partial K}{\partial C_{11}} \nu_i \tag{6.30}$$

$$\frac{\partial \omega_i}{\partial C_{11}} = \frac{1}{2\omega_i} \frac{\partial \omega_i^2}{\partial C_{11}} = \frac{1}{2\omega_i} \nu_i^T \frac{\partial K}{\partial C_{11}} \nu_i \ . \tag{6.31}$$

The partial derivatives of the eigenvalues requires derivatives of the stiffness matrix from Equation (6.21). These can be obtained from the construction in Equation (6.17):

$$\frac{\partial K_{i\lambda,k\lambda'}}{\partial C_{11}} = \sum_{j,i=1}^{3} \frac{\partial C_{ijkl}}{\partial C_{11}} \int_V \frac{\partial \boldsymbol{\phi}_\lambda}{\partial x_j} \frac{\partial \boldsymbol{\phi}_{\lambda'}}{\partial x_l} dV \ , \tag{6.32}$$

while $\frac{\partial C_{ijkl}}{\partial C_{11}}$ arises from the specific symmetry of the system. For a cubic crystal, C_{ijkl} is defined as Equation (2.29), while $\frac{\partial C_{ijkl}}{\partial C_{11}}$ is given as:

$$\frac{\partial C_{ijkl}}{\partial C_{11}} = \begin{bmatrix} 1 & 0 & 0 & 0 & 0 & 0 \\ 0 & 1 & 0 & 0 & 0 & 0 \\ 0 & 0 & 1 & 0 & 0 & 0 \\ 0 & 0 & 0 & 0 & 0 & 0 \\ 0 & 0 & 0 & 0 & 0 & 0 \\ 0 & 0 & 0 & 0 & 0 & 0 \end{bmatrix} . \tag{6.33}$$

Combining Equation (6.29), Equation (6.31), Equation (6.32), and Equation (6.33) give the necessary expression for $\frac{\log P(X|\theta)}{\partial C_{11}}$. This can be repeated for the other elastic constants as well.

Finally, instead of estimating the three cubic stiffness parameters: C_{11}, C_{12}, and C_{44} directly, a simple parameter transformation was employed for improved mobility and

HMC sampling. The transformed parameter space: C_{11}, A, and C_{44} was used herein, with A being the Zener anisotropy ratio [88]:

$$A = \frac{2C_{44}}{C_{11} - C_{12}} \ , \tag{6.34}$$

as first discussed in Section 2.1.3.

6.3.4.3 Noise term (σ)

The partial derivative of the log-likelihood with respect to the noise term σ is given by:

$$\frac{\partial log P(X|\theta)}{\partial \sigma} = -\frac{N}{\sigma} + \sum_{i}^{N} \frac{(\omega_i - X_i)^2}{\sigma^3} \ . \tag{6.35}$$

6.3.4.4 Lattice-Specimen Orientations

As stated in Section 6.3.1, the lattice-specimen orientation is parameterized as a passive unit quaternion. Though this complicates the calculations slightly as compared to Euler angles, parameterizing the problem with Euler angles produced unsatisfying results. With Euler angles, due to the degrees of freedom collapsing around the poles, it was difficult to determine whether the orientations were converging.

Quaternions, though expressed in four dimensions (w, x, y, z), live on a three dimensional manifold characterized by:

$$w^2 + x^2 + y^2 + z^2 = 1 \ . \tag{6.36}$$

In other words, not all combinations of four real numbers make a valid quaternion. In order to sample correctly on this manifold, the Geodesic HMC algorithm in [169] is used. Without going into detail, Byrne [169] adjusts random momentum generation and timestepping in HMC to keep the quaternion parameters on the manifold (Equa-

tion (6.36)). Further details about the implementation and use of quaternions are provided in Section 2.3.2.2.

Computing the partial derivatives of the log-likelihood with respect to an orientation parameter, for instance w, is the same as for an elastic constant up to the term $\frac{\partial C_{ijkl}}{\partial w}$ (simply replace C_{11} with w in Equation (6.29), Equation (6.31), and Equation (6.32)). These require partial derivatives of Equation (6.17) and Equation (6.22):

$$\frac{\partial C_{ijkl}}{\partial w} = \frac{\partial q_{ip}}{\partial w} q_{jq} C'_{pqrs} q_{kr} q_{ls} + q_{ip} \frac{\partial q_{jq}}{\partial w} C'_{pqrs} q_{kr} q_{ls} + q_{ip} q_{jq} C'_{pqrs} \frac{\partial q_{kr}}{\partial w} q_{ls} + q_{ip} q_{jq} C'_{pqrs} q_{kr} \frac{\partial q_{ls}}{\partial w} \tag{6.37}$$

$$\frac{\partial q}{\partial w} = 2 \begin{bmatrix} w & -z & y \\ z & w & -x \\ -y & x & w \end{bmatrix} . \tag{6.38}$$

6.4 Results

6.4.1 Polycrystalline Ti-64

Polycrystalline Ti-64 elastic constants were inverted using the geometries given in Section 6.2.1 along with the first thirty measured resonance modes. While the fine grain microstructure and random crystallographic texture of the Ti-64 material would lead one to guess the elastic symmetry to be isotropic, an isotropy assumption was not enforced. The standard deviation of the noise was constrained to be positive. The initial conditions for the sampler were chosen as (C_{11} = 2.0, A = 1.0, C_{44} = 1.0, σ = 5.0). The final inverted parameters are given in Table 6.1 along with reference values from Fisher and Renken [171]. Note that Fisher and Renken [171] provide single crystal stiffness values for pure titanium, which are commonly accepted as sufficient for Ti-64. These elastic constants were then converted to isotropic moduli using a Voigt-Reuss-Hill average scheme [89]. Clearly the inverted value of $A = 1.000 \pm 0.002$ demonstrates the Ti-64

material is effectively isotropic.

Table 6.1: Summary of estimated parameters for Ti-64 specimen alongside reference values.

Parameter	**Reference** [171]	**Bayesian Estimate** (mean ± sd)
C_{11}	1.651×10^{11} Pa	$(1.703 \pm 0.015)\times10^{11}$ Pa
C_{44}	4.330×10^{10} Pa	$(4.492 \pm 0.001)\times10^{10}$ Pa
σ	—	$(0.414 \pm 0.058)\times10^{3}$ Hz
A	1.000[1]	1.000[2] ± 0.002

[1] The reference anisotropy ratio is equal to 1 as a result of the Voigt-Reuss-Hill [89] polycrystalline average.
[2] The estimated anisotropy ratio was allowed to vary.

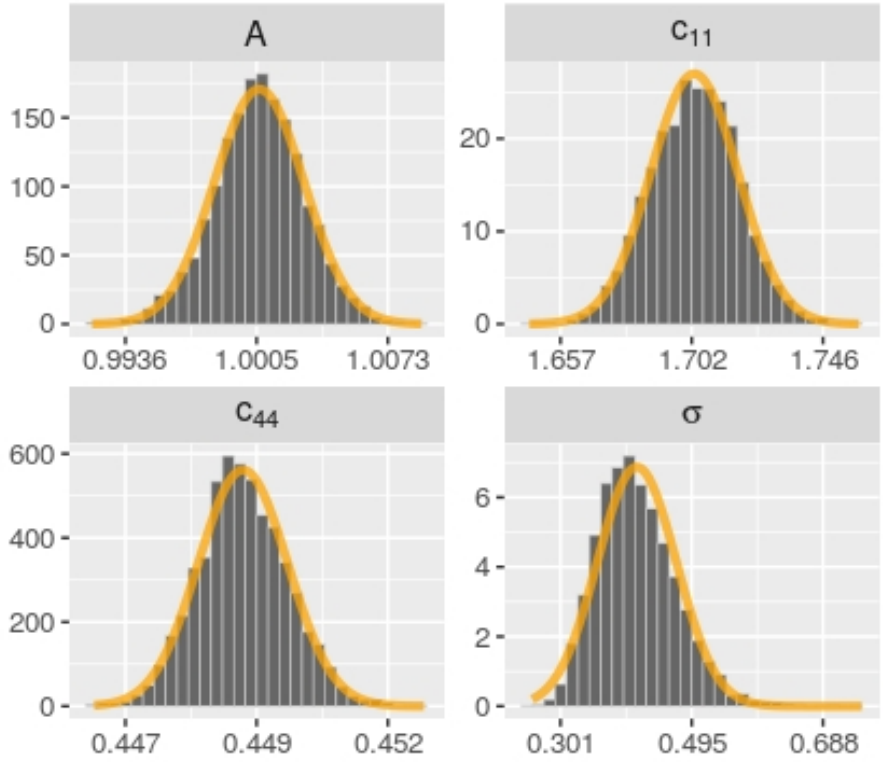

Figure 6.3: Approximate posterior distributions for the Ti-64 specimen (normalized to a PDF scale) for C_{11}, A, C_{44}, and σ computed from four thousand HMC samples. Normal PDF fits are superimposed to justify the use of mean and standard deviation to characterize the posteriors.

The full estimated posterior distributions for the four parameters (two elastic con-

stants, the anisotropy ratio, and the noise term, σ) are shown in Section 6.4.1. All the parameters (C_{11}, A, C_{44}, and σ) are well approximated by the superimposed normal distributions. This (visually estimated) quality of the fits justifies the use of mean and standard deviation, summarized in Table 6.1.

In Bayesian modeling, the two basic tools for validating an inversion are traceplots, which are plots of the sequence of states sampled by the MCMC sampler, and posterior predictive distribution plots. The traceplots for the last four thousand posterior samples for the Ti-64 specimen are plotted in Section 6.4.1. Extracting information from a traceplot is fairly straightforward. If the distribution of samples in the traceplot is stationary for a long period of time, the chain is assumed (but not guaranteed) to be sampling from the true posterior. Traceplots are usually the easiest place to detect modeling problems. If, for instance, a parameter enters an invalid range or shows a bimodal tendency, it is usually easy to spot in the traceplots. The traceplots in Section 6.4.1 show nothing unusual, suggesting that the samples themselves come from the true posterior of the model.

The second tool for validating a Bayesian modeling process are the posterior predictive distributions. The posterior predictive distributions are the distributions generated if samples from the approximated posterior distribution are used to generate new resonance modes. The quality of fit can be evaluated by comparing the posterior predictive distributions to the measured resonance modes. In the context of RUS measurements, evaluating the "quality of fit" means making sure there are not many outliers in the data (for instance, by making sure 95% of the data is within the 95% posterior predictive intervals) and identifying any systematic biases in the posterior predictive means. One example of this would be if the first ten posterior predictive resonance modes were all estimated with mean frequencies less than their respective measured modes. Errors should appear random. Any structure suggests a problem in the model or the data. For RUS, this could include missing or spurious resonance modes as part of the measured

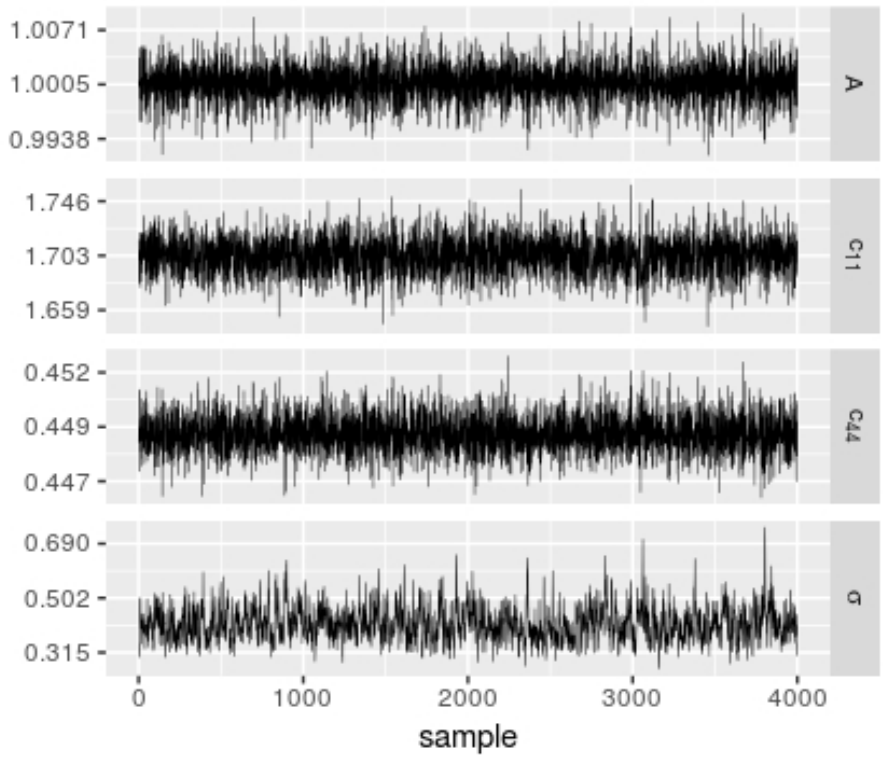

Figure 6.4: Traceplots (last four thousand samples) for the estimated parameters for the Ti-64 specimen.

Table 6.2: Ti-64 specimen measured and posterior predictive modes, (mean ± sd).

Mode	**Measured** (kHz)	**Q Ave.**[1]	**Posterior**[2] (kHz)
1	109.076 ± 0.027	3,832	108.86 ± 0.43
2	136.503 ± 0.083	3,209	135.97 ± 0.43
3	144.899 ± 0.051	3,157	144.42 ± 0.41
4	184.926 ± 0.046	6,482	184.60 ± 0.44
5	188.476 ± 0.029	4,781	187.99 ± 0.43
6	195.562 ± 0.032	6,828	195.56 ± 0.44
7	199.246 ± 0.029	7,016	199.19 ± 0.44
8	208.460 ± 0.078	6,162	208.08 ± 0.43
9	231.220 ± 0.030	7,241	231.63 ± 0.44
10	232.630 ± 0.042	6,759	232.47 ± 0.44
11	239.057 ± 0.033	2,874	239.09 ± 0.45
12	241.684 ± 0.077	7,148	242.24 ± 0.44
13	242.159 ± 0.030	7,367	242.53 ± 0.44
14	249.891 ± 0.079	7,436	249.89 ± 0.42
15	266.285 ± 0.097	7,771	267.20 ± 0.46
16	272.672 ± 0.069	8,376	272.49 ± 0.44
17	285.217 ± 0.037	7,984	285.04 ± 0.45
18	285.670 ± 0.095	8,008	285.65 ± 0.43
19	288.796 ± 0.023	10,400	289.23 ± 0.45
20	296.976 ± 0.060	7,651	296.77 ± 0.42
21	301.101 ± 0.030	8,687	301.60 ± 0.46
22	303.024 ± 0.053	8,854	303.03 ± 0.43
23	305.115 ± 0.058	9,296	305.02 ± 0.44
24	305.827 ± 0.067	9,509	305.26 ± 0.47
25	306.939 ± 0.034	10,706	306.39 ± 0.45
26	310.428 ± 0.024	6,946	310.15 ± 0.44
27	318.000 ± 0.042	11,199	317.51 ± 0.45
28	319.457 ± 0.040	7,600	319.88 ± 0.47
29	322.249 ± 0.053	10,011	322.17 ± 0.42
30	323.464 ± 0.027	9,986	322.93 ± 0.44

[1] The average quality factor (Q Ave.) is provided along with the standard deviation of the measured frequency as an indicator of the quality and repeatability of the RUS measurements.

[2] Estimated means and standard deviations of the posterior predictive distribution were generated using the last two hundred samples from the HMC trajectory (Section 6.4.1). The only mode outside of the 95% posterior intervals is highlighted in gray.

frequency list that will be readily identifiable when compared to the posterior predictive distributions. If a missing mode is identified, the term in the likelihood in Equation (6.27) corresponding to the missing mode is removed (since that data is not available), and the inference rerun for improved results.

The posterior predictive distributions for the Ti specimen are shown in Table 6.2, along with the first 30 measured resonance modes for comparison. As can be seen, all but one measured mode is in the 95% posterior interval and the estimated noise level is on par with what could be expected by measuring other specimens produced with the same specifications. The average quality factor (Q Ave.) and the standard deviation of the measured modes is provided for context about the repeatability and quality of the RUS measurements. As the specimen was removed, rotated, and then replaced on the transducer cradle between each broadband measurement, the standard deviation of the measured frequencies varied more significantly than they would have if the specimen was not removed between measurements. But having successfully identified each of the first 30 modes with an average standard deviation of 0.05 kHz, the procedure is deemed acceptable. While the measurement uncertainty is approximately one-quarter of the noise estimate, itself representing a combination of (measured and modeled) sources.

Given the combined evidence from the traceplots, the posterior predictive distributions, and the posterior distributions themselves, it is reasonable to conclude that the model describes the data well and that statements based on the computed posterior distributions should represent the physical system.

6.4.2 Single Crystal CMSX-4

The single crystal CMSX-4 elastic constants and orientation were inverted using the geometries given in Section 6.2.1 and the first thirty measured resonance modes. Instead of running a single, long HMC chain, the inference was broken into warmup and post-

warmup stages (as described in [172, Chapter 12]). In the warmup stage, four chains are run from a fixed initial condition (C_{11} = 2.0, A = 1.0, C_{44} = 1.0, σ = 5.0) to find reasonable parameter estimates. In the warmup stage the sampler needs to move around very-low probability areas of parameter space, and for stability the HMC timestep must be kept relatively small. After running the chains long enough to reach the high probability region of parameter space, new chains were initialized with larger HMC timesteps to more efficiently explore the posterior. In both stages, multiple chains are run to verify that the HMC is converging to the same solution. While only the samples from the post-warmup stage are used for the inferences.

Table 6.3: Summary of CMSX-4 parameter estimates and 95% posterior interval from each of the four HMC chains of 1000 samples each.

Parameter (units)	**Chain**	**Mean ± sd**	**Posterior int.** 2.5%	97.5%
C_{11} (10^{11} Pa)	1	2.492 ± 0.040	2.418	2.574
	2	2.492 ± 0.041	2.415	2.580
	3	2.493 ± 0.041	2.418	2.578
	4	2.489 ± 0.040	2.417	2.569
	1-4	2.492 ± 0.040	2.417	2.576
C_{44} (10^{11} Pa)	1	1.3145 ± 0.0025	1.3099	1.3196
	2	1.3144 ± 0.0027	1.3089	1.3203
	3	1.3145 ± 0.0026	1.3092	1.3198
	4	1.3143 ± 0.0026	1.3094	1.3194
	1-4	1.3144 ± 0.0026	1.3093	1.3197
A	1	2.8652 ± 0.0075	2.8509	2.8801
	2	2.8651 ± 0.0089	2.8483	2.8831
	3	2.8652 ± 0.0079	2.8493	2.8804
	4	2.8650 ± 0.0078	2.8492	2.8805
	1-4	2.8651 ± 0.0081	2.8493	2.8811
w	1	0.9885 ± 0.0003	0.9879	0.9891
	2	0.9884 ± 0.0003	0.9879	0.9891
	3	0.9884 ± 0.0003	0.9879	0.9891
	4	0.9884 ± 0.0003	0.9879	0.9891
	1-4	0.9884 ± 0.0003	0.9878	0.9891
x	1	0.0000 ± 0.0062	-0.0117	0.0119
	2	0.0002 ± 0.0063	-0.0121	0.0130
	3	-0.0002 ± 0.0061	-0.0114	0.0116
	4	0.0000 ± 0.0063	-0.0124	0.0128
	1-4	0.0000 ± 0.0062	-0.0118	0.0124
y	1	-0.1510 ± 0.0025	-0.1549	-0.1461
	2	-0.1512 ± 0.0025	-0.1552	-0.1460
	3	-0.1511 ± 0.0024	-0.1550	-0.1464
	4	-0.1514 ± 0.0024	-0.1549	-0.1462
	1-4	-0.1512 ± 0.0024	-0.1550	-0.1461
z	1	0.001 ± 0.010	-0.018	0.019
	2	0.000 ± 0.010	-0.018	0.019
	3	0.001 ± 0.010	-0.018	0.019
	4	0.001 ± 0.010	-0.018	0.019
	1-4	0.001 ± 0.010	-0.018	0.019

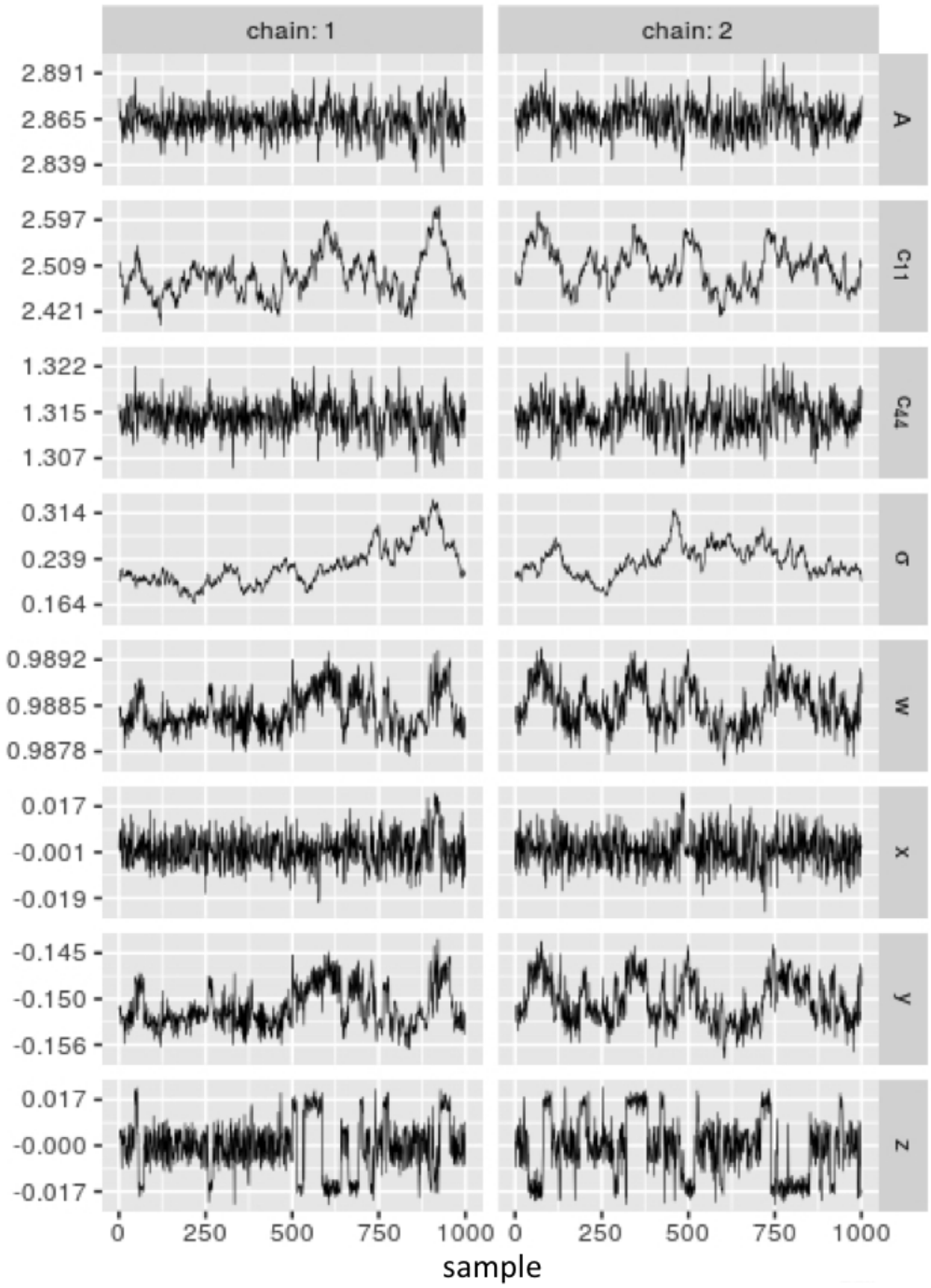
chain: 1
chain: 2
2.891
2.865
2.839
A
2.597
2.509
2.421
c11
1.322
1.315
1.307
c44
0.314
0.239
0.164
σ
0.9892
0.9885
0.9878
w
0.017
-0.001
-0.019
x
-0.145
-0.150
-0.156
y
0.017
-0.000
-0.017
z
0
250
500
750
1000
sample

(a) Chains 1–2

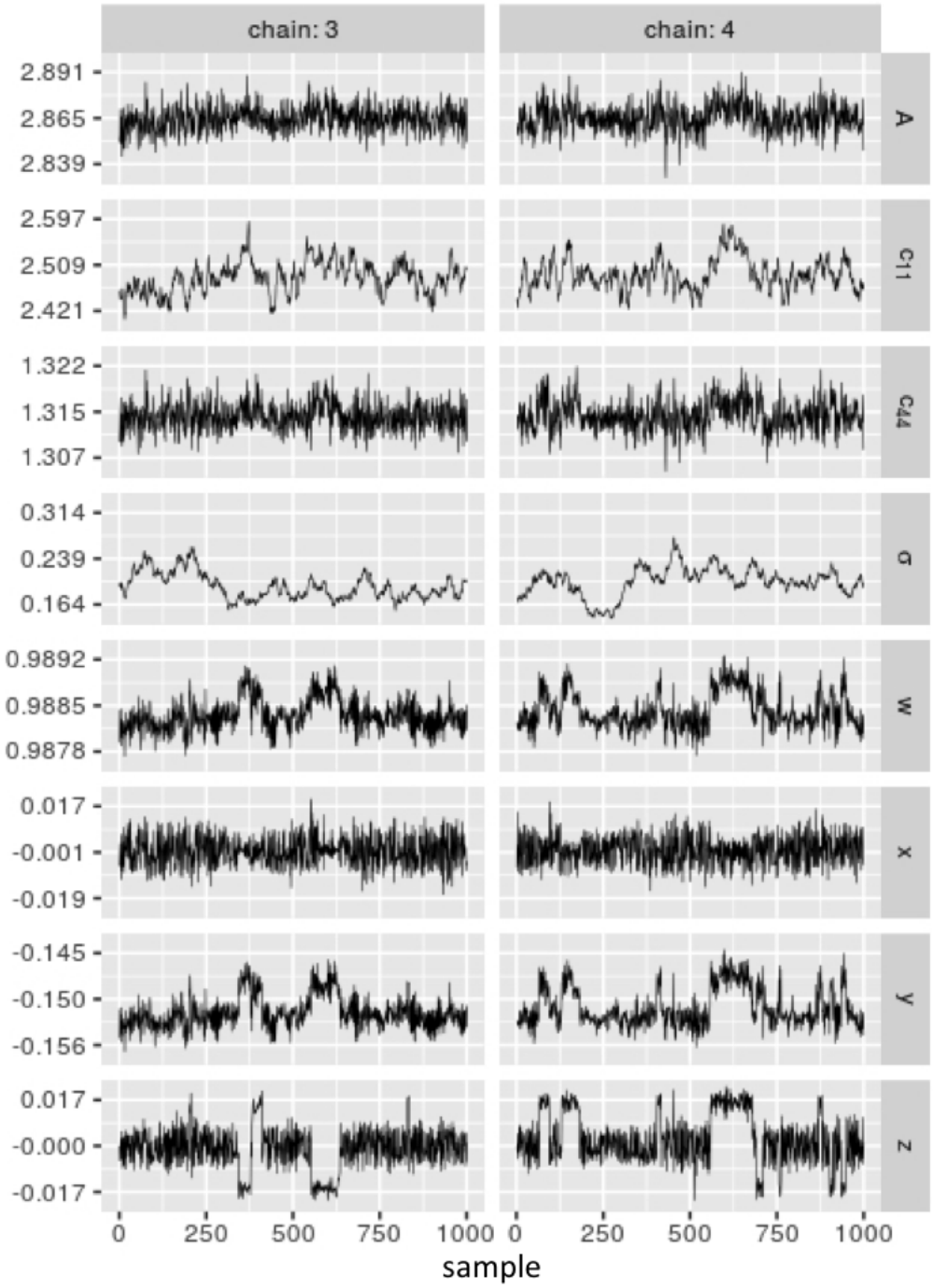

(b) Chains 3–4

Figure 6.5: Warmup traceplots (four independent chains of one thousand samples each) for the estimated parameters in the single crystal CMSX-4 specimen. The rough means of the parameters in these chains were used to initialize four chains with larger time steps to more efficiently explore the posterior.

The warmup traceplots are shown in Figure 6.5, while the post-warmup traceplots are shown in Figure 6.6. As can be seen in these figures, all the chains in both warmup and post-warmup stages are sampling the same region of parameter space. While a key difference between the plots is that the post-warmup chains more aggressively explore the C_{11} and σ parameter spaces (due to the larger HMC timestep). Table 6.3 summarizes the material parameter estimates from each of the four 1000-sample HMC chains, as well as the sum total of the four chains presented in Figure 6.6. The consistency between the mean values of the four chains is a testament to the reliability of the inference, while the standard deviation associated with each mean demonstrates the precision of the parameter estimate. For example, the standard deviations of the C_{11} and C_{44} parameters are 4.0 GPa and 0.26 GPa respectively. This demonstrates the superior precision of the C_{44} estimate as compared to C_{11} estimate, and is consistent with RUS-based elastic property inversions reported previously by Migliori et al. [38].

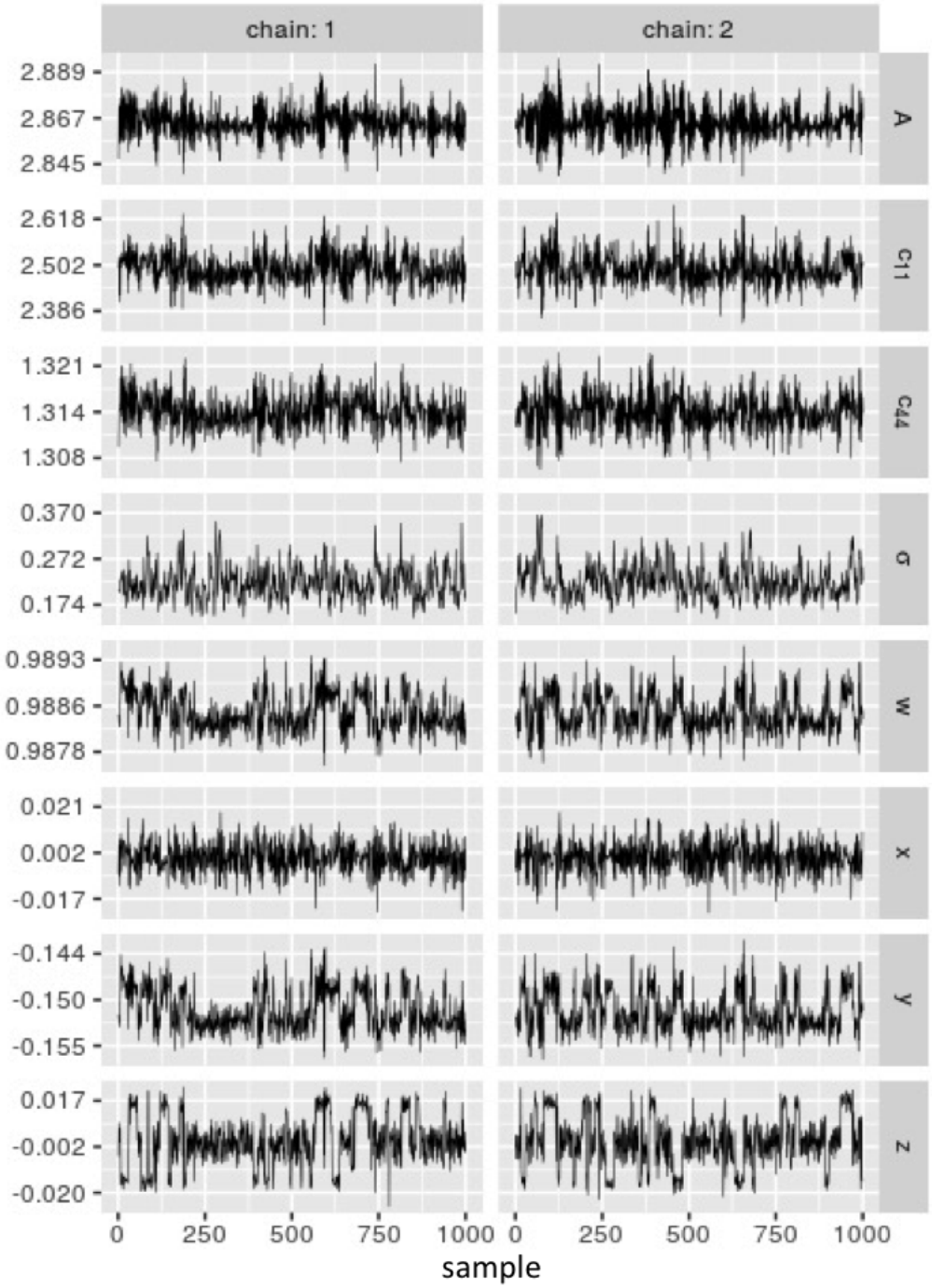
chain: 1
chain: 2
2.889
2.867
2.845
A
2.618
2.502
2.386
c11
1.321
1.314
1.308
c44
0.370
0.272
0.174
σ
0.9893
0.9886
0.9878
w
0.021
0.002
-0.017
x
-0.144
-0.150
-0.155
y
0.017
-0.002
-0.020
z
0
250
500
750
1000
sample

(a) Chains 1–2

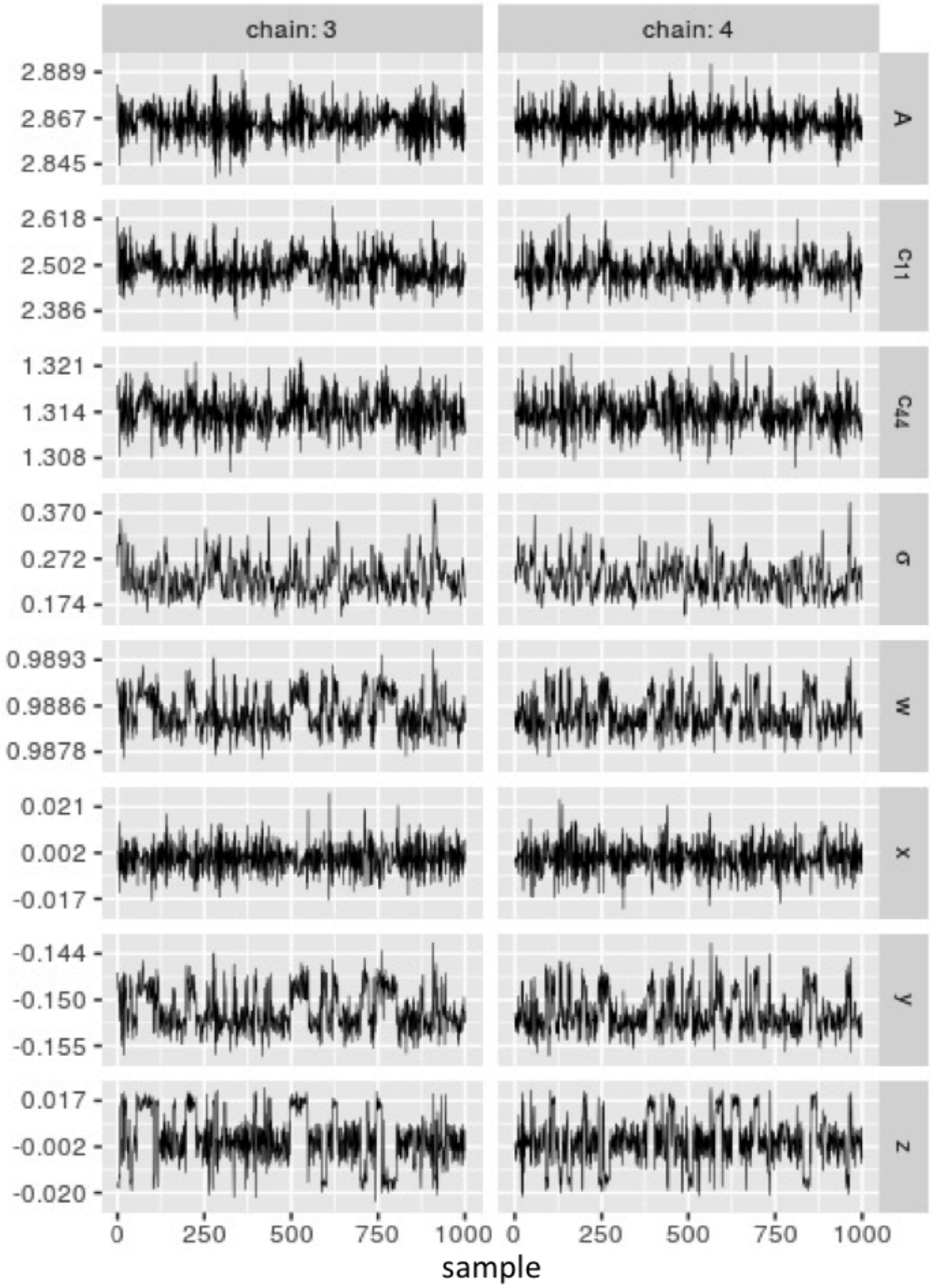

(b) Chains 3–4

Figure 6.6: Sampling traceplots (four independent chains of one thousand samples each) for the estimated parameters of the single crystal CMSX-4 specimen. The elastic constants appear to be unimodal, but the orientation parameters are multimodal.

Table 6.4: CMSX-4 measured and posterior predictive modes (mean ± sd).

Mode	**Measured** (kHz)	**Q Ave.**[1]	**Posterior**[2] (kHz)
1	71.259 ± 0.044	2,279	71.22 ± 0.24
2	75.759 ± 0.025	2,864	75.69 ± 0.23
3	86.478 ± 0.030	3,524	86.46 ± 0.26
4	89.947 ± 0.048	3,077	90.00 ± 0.24
5	111.150 ± 0.033	4,155	111.06 ± 0.26
6	112.164 ± 0.027	4,492	112.01 ± 0.29
7	120.172 ± 0.033	5,048	120.32 ± 0.26
8	127.810 ± 0.042	4,462	127.98 ± 0.25
9	128.676 ± 0.040	4,747	128.64 ± 0.24
10	130.740 ± 0.034	5,342	130.75 ± 0.24
11	141.700 ± 0.037	5,299	141.79 ± 0.25
12	144.504 ± 0.065	5,603	144.36 ± 0.23
13	149.401 ± 0.025	5,918	149.52 ± 0.26
14	154.351 ± 0.026	5,942	154.42 ± 0.25
15	156.782 ± 0.028	6,761	156.97 ± 0.25
16	157.555 ± 0.041	6,123	157.57 ± 0.25
17	161.088 ± 0.063	6,284	160.97 ± 0.24
18	165.103 ± 0.022	6,756	165.21 ± 0.28
19	169.762 ± 0.044	6,995	169.77 ± 0.27
20	173.449 ± 0.050	7,212	173.28 ± 0.26
21	174.117 ± 0.024	6,437	174.13 ± 0.26
22	174.906 ± 0.054	6,916	174.68 ± 0.26
23	181.120 ± 0.042	6,632	181.54 ± 0.25
24	182.459 ± 0.037	7,475	181.87 ± 0.25
25	183.986 ± 0.042	7,837	183.81 ± 0.28
26	192.681 ± 0.032	7,197	192.83 ± 0.24
27	193.436 ± 0.021	7,113	193.71 ± 0.27
28	198.794 ± 0.034	7,249	198.95 ± 0.25
29	201.902 ± 0.032	8,529	201.89 ± 0.27
30	205.015 ± 0.031	8,808	204.85 ± 0.33

[1] The average quality factor (Q Ave.) is provided along with the standard deviation of the measured frequency as an indicator of the quality and repeatability of the RUS measurements.

[2] Estimated means and standard deviations of the posterior predictive distribution were generated using the last two hundred samples from the HMC trajectory (Figure 6.6). There is one mode (highlighted in gray) outside the 95% posterior intervals.

As stated in Section 6.4.1, the posterior predictive distributions elucidate the quality of the fit and are provided for the CMSX-4 specimen in Table 6.4. Alongside these data are the measured frequencies and their standard deviation, as well as the quality

factor for the first 30 resonance modes. As before, the one measured value outside the 95% posterior predictive interval (mode 24) is highlighted in gray, while the average measured standard deviation of 0.03 kHz is approximately one-eighth the value of the noise estimate. Given the relatively small standard deviation associated with each mode, having one of 30 modes outside the 95% posterior predictive interval is not an issue.

Table 6.5: Summary of estimated parameters for the CMSX-4 specimen alongside reference values.

Parameter	**Reference** [98]	**Bayesian Estimate** (mean ± sd)
C_{11}	2.52×10^{11} Pa	$(2.492 \pm 0.040) \times 10^{11}$ Pa
C_{44}	1.31×10^{11} Pa	$(1.314 \pm 0.003) \times 10^{11}$ Pa
σ	—	$(0.229 \pm 0.037) \times 10^{3}$ Hz
A	2.88	2.865 ± 0.008

Estimated posterior distributions of the elastic constants (C_{11}, A, and C_{44}) and the noise parameter (σ) are shown in Figure 6.7. As each parameter exhibits a normal distribution, it makes sense to summarize the parameter estimates by their mean and standard deviation as provided in Table 6.5. Reference CMSX-4 elastic constants from [98] are provided for context, and agree well with the estimates of this chapter.

Due to the symmetry inherent to crystals, in particular cubic crystals, there are numerous symmetrical representations for a given crystal orientation. Therefore it is possible, indeed common, for two orientation quaternions with substantially different component values to represent crystal orientations that are physically very close to each other. In order to visualize the posterior of the crystallographic orientation and produce two dimensional plots, orientation quaternion were transformed into cubochoric coordinates [106] before plotting in Figure 6.8. These plots detail the location of the measured orientation in orange with respect to each of the 4000 HMC sample orientations plotted in black. Although it is not particularly good that the measured crystallographic orientation is away from the bulk of the posterior, uncertainty in the XRD measurement

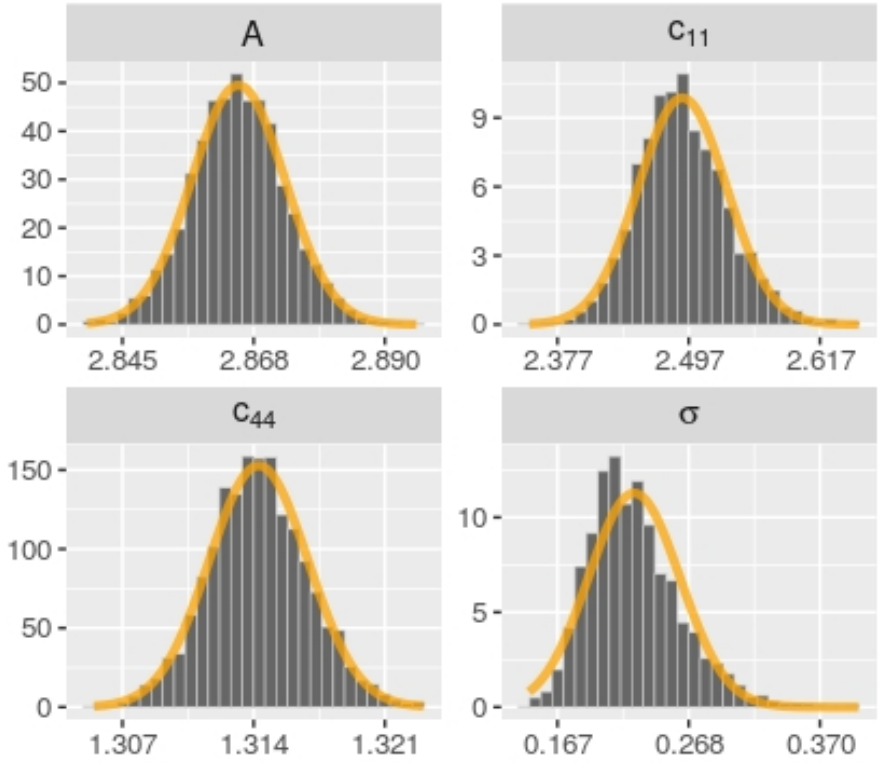

Figure 6.7: Approximate CMSX-4 posterior distributions for C_{11}, A, C_{44}, and noise (σ) parameters, computed from four chains of one thousand HMC samples each. Normal PDF fits are superimposed to justify the use of mean and standard deviation to characterize the posteriors.

of approximately one degree as noted in Section 6.2.3 could easily place the measured orientation within a higher-likelihood region of the posterior; given that a rotation of one degree corresponds roughly to a distance of 0.01 in cubochoric coordinates. Furthermore, the total misorientation angle (in degrees) between the measured orientation and each of the inverted orientations is detailed by the histogram in the bottom right of Figure 6.8. Given the overwhelming majority of misorientation angles were calculated as between 1.0 and 2.5 degrees, our confidence in estimating crystallographic orientation from RUS-measured resonance frequencies is high, with results summarized in Table 6.6

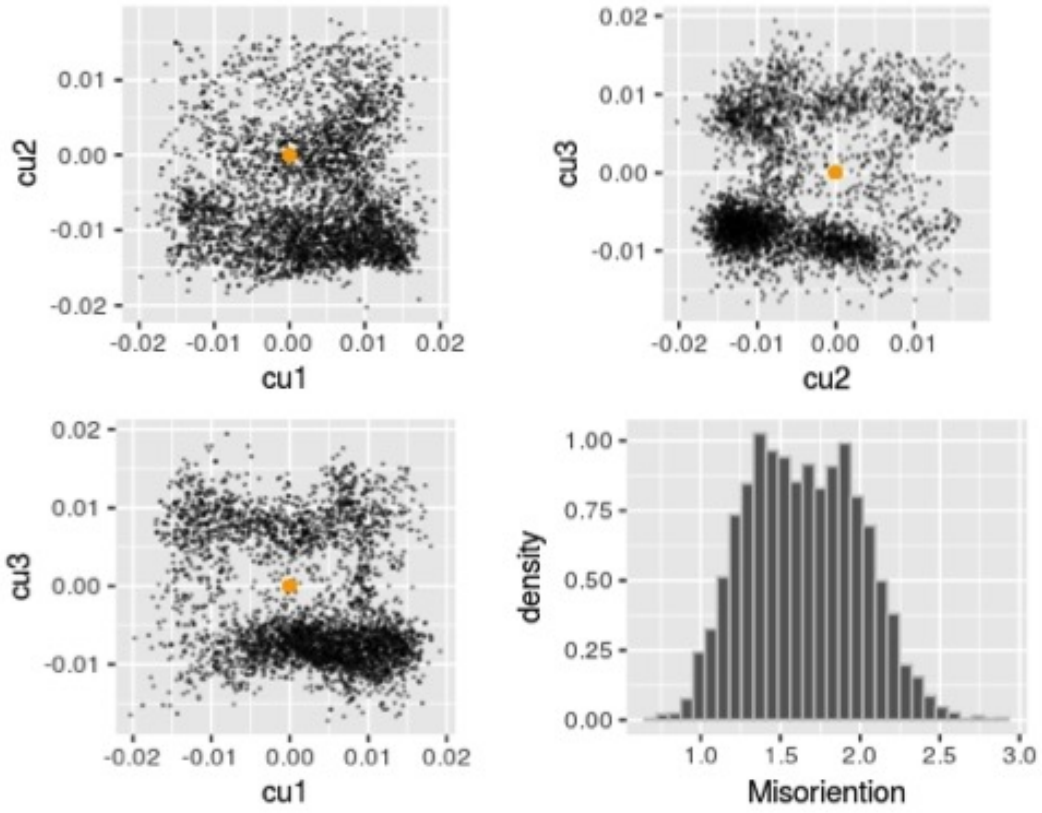

Figure 6.8: Crystallographic orientation posterior plotted in cubochoric coordinates. The distribution of minimum misorientation angle (in degrees) between the measured and estimated orientations is at the bottom. Note that a difference of one hundredth on any cubochoric axis corresponds roughly to one degree of rotation.

To demonstrate that inferring the crystallographic orientation was necessary, an in-

Table 6.6: Summary of CMSX-4 specimen crystal orientation from XRD measurement and Bayesian estimate.

Parameter	**XRD Measurement**	**Bayesian Estimate** (mean ± sd)
w	0.987	0.9884 ± 0.0003
x	−0.005 26	0.000 ± 0.0062
y	−0.158	-0.1512 ± 0.0024
z	0.0164	0.001 ± 0.010

version was run without these degrees of freedom. Figure 6.9 shows the results. As can be seen, C_{11} is not converging to a steady state distribution, and the inversion fails. The scale of σ indicates the fit is not good compared to the inversion with the orientation parameters included.

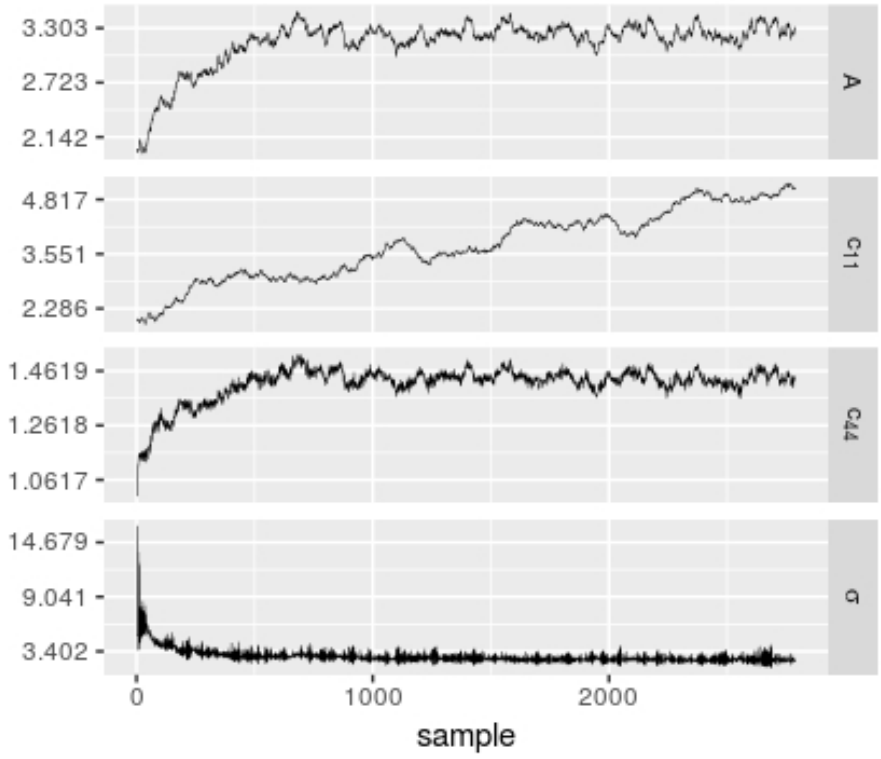

Figure 6.9: Traceplots for the estimated parameters in the single crystal CMSX-4 specimen without including misorientation estimation.

Given that all four warmup and post-warmup chains converge to similar physically realistic solutions and that the posterior predictive distributions align well with the measured data, it is reasonable to conclude that this model describes the data well and that statements based on the computed posterior distributions should represent the physical system. This is confirmed with the reference elastic constants and measured crystallographic orientations.

6.4.3 Computation Efficiency

The Ti-64 inversion ran for approximately eight hours on a quad core Intel i7-2600k desktop computer, while the CMSX-4 inversion took a few days. Each HMC sample takes fifty forward evaluations of the RUS model (so one hundred thousand total for the examples presented here). Since the eigensolve in the forward model evaluation constitutes a large majority of the total evaluation time, it is simple to estimate how long an inversion might take if the forward model is available. If the forward model takes a second to evaluate, the sampler converges to a steady posterior distribution within a thousand HMC samples, and two thousand samples from the posterior are computed, the calculation should take a little under two days.

6.5 Conclusion

A novel and robust RUS inversion framework for characterizing elastic properties and crystal orientation of parallelepiped specimens using a Bayesian modeling approach and Hamiltonian Monte Carlo sampling has been developed. The inversion framework was tested with two experimental datasets for validation: a fine-grained Ti-64 specimen and a single crystal specimen of Ni-based superalloy CMSX-4 with misaligned specimen-crystal reference frames. The Ti-64 specimen exhibited elastic isotropy with C_{11} and C_{44} stiffness constants in agreement with literature values for a Voigt-Reuss-Hill average of

randomly-oriented grains. Inversion of the CMSX-4 data yielded accurate estimates of the three independent elastic moduli in strong agreement with literature values, while the crystallographic orientation was determined to within approximately 2 degrees of XRD measured values. While the current version of the code requires substantially greater computation time as compared to conventional RUS inversion schemes, it also provides the following advantages:

- Built-in uncertainty estimates on all parameters.
- Simultaneous estimation of elastic constants and crystal orientation.
- Simplified requirements for specimen preparation, as misaligned crystal-specimen reference frames are allowed.
- Robustness to common RUS inversion problems like misidentified resonance modes and initial parameterization uncertainty.

Chapter 7

Inverse Modeling Framework for Characterizing Novel Single Crystal Superalloys

Chapter Abstract

While the previous chapter provides the proof-of-concept for RUS Bayesian inference, this chapter, and the publication upon which this chapter is based[1], demonstrates the utility of this powerful and robust inverse modeling framework (IMF). The elastic properties of 9 single crystal γ' containing Co, Ni, and CoNi-based alloys are precisely characterized, many for the very first time. Comparisons are made between the elastic properties of the three alloy classes and among the alloys of a single class, with the following trends observed. A monotonic rise in the C_{44} (shear) elastic constant by a total of 12% is observed between the three alloy classes as Co is substituted for Ni. Elastic anisotropy (A) is also increased, with a large majority of the nearly 13% increase occurring after Co becomes the dominant constituent. Together the five CoNi alloys, with Co:Ni ratios from 1:1 to 1.5:1, exhibited remarkably similar properties with an average A 1.8% greater than the Ni-based alloy CMSX-4. Particular focus is directed towards the distinguishing features and improved capabilities of this next-generation IMF code. Designated CmdStan-RUS [62], this code is released as a custom distribution of the open-source probabilistic programing language Stan [60], and is dedicated to RUS Bayesian inference of elastic properties from rectangular parallelepiped specimens with arbitrary crystal lattice orientations. Parametric studies on the effects of polynomial order, missing modes, resonance mode selection, and orientation estimation are provided as further evidence of the robustness of the IMF.

[1] [58] B.R. Goodlet, L. Mills, B. Bales, M.A. Charpagne, S.P. Murray, W.C. Lenthe, L. Petzold and T.M. Pollock. "Elastic Properties of Novel Co- and CoNi-Based Superalloys Determined through Bayesian Inference and Resonant Ultrasound Spectroscopy," *Metallurgical and Materials Transactions A* 49 (2018) pp. 2324-2339. [doi:10.1007/s11661-018-4575-6]

7.1 Introduction

Propelled by incredible advances in engineering and materials science—and the promise of greater turbine efficiencies and reduced emissions—the operational limits of Ni-based superalloys have been extended to regimes that include periods at over 90% of their melting point [124], all while maintaining considerable mechanical loads in deleterious environmental conditions. Inherent limits exist for future development, as the melting temperature (or more accurately the liquidus and solidus temperatures) is intrinsic to the material and cannot be appreciably increased. This reality has spurred research and development of ordered intermetallic alloys such as NiAl [173], Nb and Mo-based refractory alloys [174–177], and ceramic composites of alumina [178] and silicon carbide [179], all with the goal of supplanting Ni-based superalloys for the most demanding high temperature applications. However, these alternatives often suffer from poor fracture toughness and processing constraints that make their current use costly and limited [174–176, 180], especially considering the safety requirements for use in aerospace.

Given the payoff for increased turbine engine operating temperatures and the limitations of current alternatives to Ni-based superalloys, considerable attention has been directed toward potential intermediate solutions such as $\gamma - \gamma'$ Co-based superalloys [117] and hybrid CoNi-based alloys [118]. The primary motivation for studying these alloys is clear, as the melting point of Co exceeds that of Ni by 40 °C [116]. They also have the benefit of being cast and processed similar to existing Ni-based superalloys, minimizing the cost of development by leveraging existing infrastructure. Of course there are some outstanding issues that must be addressed before these alloys may become technically relevant, including: a low γ' solvus temperature [153], poor oxidation resistance [181], and in some cases a less favorable thermal expansion coefficient for adhesion of protective alumina as compared to Ni-based superalloys [119]. Due to the promise of future oper-

ating temperature improvements, this research focuses on measuring the single crystal elastic constants of select Co and CoNi-based superalloys. Since turbine blades operate under nominally elastic conditions, elastic properties are critically important to design, though have not yet been measured for these new classes of Co-based materials.

7.2 Experimental Methods

7.2.1 Materials

The discovery of a stable $\gamma - \gamma'$ two-phase field in the Co-Al-W ternary in 2006 by Sato et al. [116] with morphologically identical microstructure to Ni-based $\gamma - \gamma'$ superalloys [117] generated considerable interest from the materials science community. Expanding upon the Co-9.2Al-9W at% alloy reported by Sato et al., the first investigations on the mechanical properties of several $L1_2$-containing Co-based alloys demonstrated high potential for turbine material application [118–121]. The Co-based alloys were based primarily on quaternary elemental additions to study a variety of effects including: 2 at% Ta for precipitate strengthening, 2 at% Re for matrix strengthening, 4.5 at% Cr for oxidation behavior, 20 at% Ni for expanded γ' phase field stability, and 1.5-6 at% Mo/V for density reduction [117]. A CoNi-based alloy series explored many of the same alloying effects mentioned previously, but started from a modified base of approximately 30 at% Ni to the Co-Al-W ternary alloy, with variable amounts of: Ta, Cr, Mo, Al, Ni, and C + B. Table 7.1 summarizes the chemical composition of each alloy from the previous investigations that were examined as part of this research, with the distinguishing elemental additions in bold.

Table 7.1: Alloy designations and composition in atomic percent (at%).

Alloy	Co	Ni	Al	W	Ta	Cr	Ti	Mo	Hf	Re	C	B
CMSX-4	9.9	62.9	12.6	2.1	2.2	7.6	1.3	0.4	< 0.1	1.0	-	-
Co-Ternary	79.9	-	9.4	10.7	-	-	-	-	-	-	-	-
Co-2Ta	79.4	-	8.8	9.8	**2.0**	-	-	-	-	-	-	-
Co-6Ti	79.0	-	6.7	8.1	-	-	**6.2**	-	-	-	-	-
CoNi-A	45.9	29.2	9.8	6.3	2.4	6.4	-	-	-	-	-	-
CoNi-A+	45.9	29.2	9.8	6.3	2.4	6.3	-	-	-	-	**0.14**	**0.02**
CoNi-B	44.5	28.2	8.8	6.3	2.1	**10.1**	-	-	-	-	-	-
CoNi-C	**38.1**	**38.0**	9.3	6.9	1.4	6.3	-	-	-	-	-	-
CoNi-D	44.8	30.7	9.6	**4.8**	1.9	6.2	-	**2.0**	-	-	-	-

7.2.1.1 Preparation of Experimental Materials

Prior to conducting any resonance measurements, as-received material was solution heat treated and fully aged. Heat treatment schedules devised for the novel Co and CoNi-based alloys were based on previously measured solidus and solvus temperatures, while the CMSX-4 material was heat treated according to industry standards specifying a step-wise solution treatment and a two-step age [122]. Table 3.3 summarizes the heat treatment schedules for each alloy.

Figure 7.1 demonstrates the consistent microstructure achievable across the three alloy classes by comparing scanning electron microscopy (SEM) micrographs from the Co-6Ti, CoNi-A+, and CMSX-4 alloys in their fully aged conditions. Lower magnification micrographs on the left show aligned dendrites that remain from the directional solidification process, while higher magnification micrographs (center and right) show a significant volume fraction of cuboidal γ' precipitates in a matrix of γ. Microscopy specimens were prepared perpendicular to the nominal [001] growth direction using diamond

suspensions down to 1 μm, then vibratory polished using alumina and colloidal silica to achieve a mirror finish. SEM characterization was completed using a FEI SEM with a field emission gun operating at 15 kV using secondary and backscatter electron detectors.

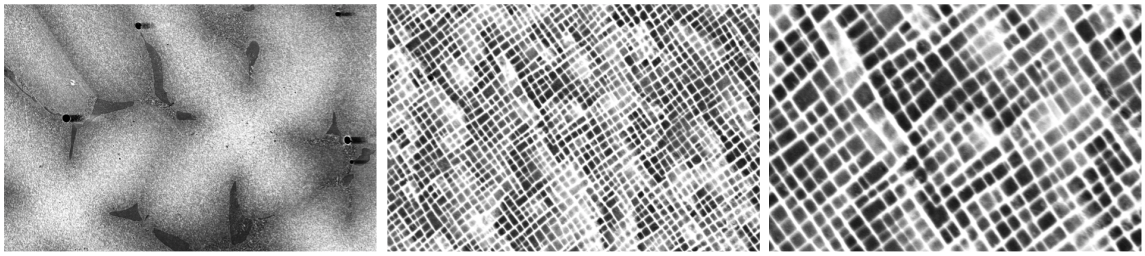

(a) CMSX-4

(b) Co-6Ti

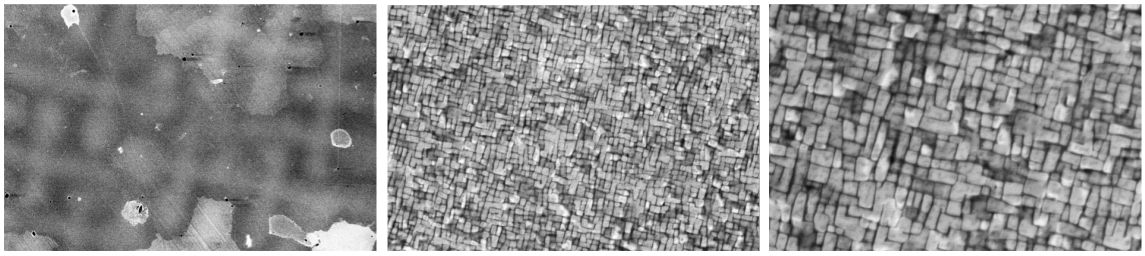

(c) CoNi-A+

Figure 7.1: Backscatter SEM micrographs of the (a) CMSX-4, (b) Co-6Ti, and (c) CoNi-A+ alloys in the solution heat treated and aged condition. Low magnification micrographs on the left show the remnant dendritic microstructure, while higher magnification micrographs in the center and on the right show the cuboidal $\gamma - \gamma'$ microstructure characteristic of superalloys.

7.2.2 Resonant Ultrasound Spectroscopy

7.2.2.1 RUS Specimen Preparation

Two parallelepiped (PP) specimens for each alloy were machined from cylindrical single crystal castings via wire electrical discharge machining (EDM). All PP specimen dimensions were approximately the same at $9 \times 10 \times 11$ mm, though the exact dimensions of each PP varied slightly as the EDM damage layer was removed from each face by hand grinding with 800 grit sandpaper. Precise measurements of the specimen geometry were made with a Mitutoyo outside micrometer with 0.001 mm precision. The mass of each PP was measured with a digital Acculab scale precise to 0.0001 g, and the density was calculated. Note that the $9 \times 10 \times 11$ mm geometry was devised to both minimize the aspect ratio ensuring bending modes sensitive to non-shear moduli occur along each dimension and at relatively low frequencies, and to limit the likelihood of overlapping resonances that are more likely to occur when PP dimensions are nearly equivalent or half-integer multiples of each other.

Analysis of RUS data is substantially simplified when both the single crystal elastic constants and the arbitrary crystal reference frame rotation are determined simultaneously [47]. Otherwise, the specimen must be precisely cut from a parent single crystal of known orientation (typically measured with x-ray diffraction techniques) such that the rotation between the crystal and specimen reference frames is nearly (ideally) zero [33].

7.2.2.2 RUS Measurements

Resonance frequencies were measured with a custom-built experimental setup provided by the Vibrant Corporation as detailed in Section 3.3, which includes a diagram of the setup and plots of broadband resonance spectra in Figure 3.4. The RUS setup included: a desktop computer for control and data visualization, a transceiver to generate

and receive signals, coaxial cables connecting the transceiver to three identical omni-directional piezoelectric transducers (PT) (pictured in Figure 3.5), and a transducer cradle consisting of optical table fixtures affixed to a vibration dampening breadboard (pictured in Figure 3.6). The transducer cradle was designed to fully support the PP specimens along three faces at roughly 90° angles and near the edge of the PP. Note that the corners of a PP specimen are the points of lowest symmetry [13, 38, 128, 129] and provide the lowest elastic coupling/impedance [38, 42] for minimal biasing of the measured resonance frequencies. For the 3 transducer cradle configuration described above, contacting the PP specimen on its faces near the corners was found to provide sufficient signal to noise ratio with minimal variance in frequency for all modes to allow for precise estimates of elastic constants.

All RUS measurements were completed at standard temperature and pressure. To ensure that all of the PP specimen resonance modes were measured, each PP was scanned five times across the range of 70–445 kHz, with the specimen removed, rotated, and then replaced on the transducer cradle after each scan. While this procedure occasionally resulted in a single mode being missed from a broadband scan, each of the first 70 resonance modes were effectively measured for all of the PP specimens investigated in this study. Note that the lowest-frequency modes of the PP specimens investigated in this chapter do not appear to exhibit significantly greater variability in f_R as compared to higher-frequency modes, which is in contrast to reports for the dog-bone specimens investigated in Chapters 4 and 5. The reason for this improved measurement repeatability of was not extensively studied,

Distilling a list of resonance frequencies from each broadband RUS spectrum was partially automated based on: peak amplitude, peak width, separation from neighboring peaks, and the second derivative of the amplitude with respect to frequency. Each of these parameters were set for individual bands (approximately 20 kHz wide) such that the automated process reliably identified most modes. Each scan was then individu-

Table 7.2: Mean and standard deviation (sd) for the first 50 resonance modes of CoNi-A+1, based on 5 broadband RUS scans.

Mode No.	**Frequency** (kHz) mean ± sd	**Mode No.**	**Frequency** (kHz) mean ± sd
1	135.618 ± 0.016	26	286.690 ± 0.013
2	142.851 ± 0.010	27	290.809 ± 0.002
3	144.923 ± 0.010	28	299.620 ± 0.011
4	154.308 ± 0.018	29	304.619 ± 0.013
5	163.844 ± 0.013	30	308.081 ± 0.012
6	164.111 ± 0.008	31	310.982 ± 0.012
7	168.193 ± 0.014	32	320.033 ± 0.015
8	188.061 ± 0.011	33	321.824 ± 0.011
9	202.506 ± 0.010	34	326.095 ± 0.009
10	204.747 ± 0.009	35	332.206 ± 0.013
11	210.693 ± 0.011	36	334.222 ± 0.013
12	211.414 ± 0.012	37	337.300 ± 0.012
13	211.985 ± 0.010	38	341.681 ± 0.011
14	219.423 ± 0.011	39	344.413 ± 0.014
15	220.491 ± 0.014	40	348.664 ± 0.016
16	237.149 ± 0.012	41	354.642 ± 0.012
17	241.558 ± 0.010	42	355.491 ± 0.012
18	244.404 ± 0.016	43	363.661 ± 0.012
19	246.905 ± 0.009	44	367.021 ± 0.012
20	248.223 ± 0.013	45	367.950 ± 0.018
21	259.814 ± 0.014	46	370.402 ± 0.013
22	266.153 ± 0.012	47	373.411 ± 0.012
23	273.195 ± 0.016	48	379.083 ± 0.013
24	275.341 ± 0.013	49	381.878 ± 0.008
25	285.808 ± 0.010	50	383.998 ± 0.011

ally verified for any missing or spuriously identified modes before the frequency list was exported from the collection computer for further analysis. Next, an averaged list of frequencies was created for each PP from the five individual frequency lists, inspecting the standard deviation across the five scans was within 0.1 kHz to assure that no modes were missed or erroneously recorded. An example mode list for PP specimen CoNi-A+1 (referring to CoNi-A+ PP 1, of 2) is provided in Table 7.2, which clearly demonstrates

that measurement precision of ±0.02 kHz (or less) is reliably achieved. This measurement precision is remarkable given that a single broadband scan of 70 resonance modes is collected in less than 10 minutes. Such reliable precision is what makes RUS an ideal measurement technique for estimating elastic constants [33].

7.3 Computational Methods

As there is no direct solution to the general inverse problem of determining elastic properties from RUS measurements, elastic properties must be determined indirectly through least-squares optimization [33, 34, 41] or statistical inference [47] methods. Both of these inversion methods ultimately rely on numerous forward problem evaluations [33, 47], which was covered extensively in Section 6.3.1. Therefore, the computational methods covered by this chapter begin with Section 7.3.1 detailing the inverse problem, with a short summary on traditional optimization-based methods followed by the distinguishing characteristics of a Bayesian approach. Parameter transformations are discussed in Section 7.3.2, including reparameterization of the crystal orientations as a cubochoric vector. Then the statistical RUS model is formulated in Section 7.3.3, which details the Bayesian posterior and necessary assumptions employed by the CmdStan-RUS version of the code [62]. Computation of the Bayesian posterior is accomplished through a self-tuning Hamiltonian Monte Carlo (HMC) algorithm native to Stan [60], with example traceplots, constraints, and initial parameterization discussed in Section 7.3.4. Finally, methods of validation are discussed in Section 7.3.5, where the concept of posterior predictive distributions is introduced, followed by details regarding posterior predictive plots and how they can be used to diagnose some of the more common problems that may arise during RUS Bayesian inference.

7.3.1 Inversion

Inversion of elastic properties from RUS measured resonance frequencies has historically been accomplished using optimization algorithms that yield maximum likelihood estimates (MLE) of the unknown parameters. Some of the more popular optimization algorithms include: the Levenberg-Marquardt (Newton-steepest decent) algorithm popularized by Migliori et al. [33, 38], the derivativeless fixed point iteration (FPI) method used by Plesek et al. [43] for finite element (FE) implementations where derivative information is less accessible, and genetic algorithms as used by Remillieux et al. [51]. Each of these algorithms perform a least-squares regression of an overdetermined system, with more resonance modes being used than parameters being estimated, by iteratively updating an initial guess set of elastic constants to minimize the sum of squared errors (SSE) between a measured and computed list of resonance frequencies [33, 38, 43, 51]. Various convergence criteria are then used to terminate the optimization, typically when successive iterations fail to reduce the SSE or after a desired precision is reached.

Instead of pursuing point estimates of unknown parameters by way of optimization, here we formulate the inverse problem as a Bayesian inference which yields probability distributions for the unknown parameters (elastic constants, crystal orientation, etc.). When the parameter distributions are normally distributed—a characteristic typically verified a posteriori by fitting the distribution as a Gaussian—the mean and the variance of the distribution provide estimates of the parameter value and its uncertainty. While estimating error in the elastic constants from optimization methods is far less straightforward, Migliori and Sarrao [33] discuss an empirical approach to determining uncertainty by exploring the curvature of the (SSE) error surface in the vicinity of the optimization minimum. But this approach only estimates the error in linear combinations of parameters that may be difficult to isolate when the curvature of the error surface is shallow. Confronting these same issues, Spoor [41] employed Monte Carlo methods to

estimate parameter uncertainty in a manner similar to this work by assigning normally distributed random perturbations to his measured resonance modes, then characterizing the distribution of optimization minima to infer uncertainty [41]. Both are meaningful endeavors but involve complicated additional steps beyond the optimization procedures being employed, while uncertainty in the Bayesian estimates are obtained automatically from the posterior distributions.

7.3.2 Scaled and Transformed Parameters

For improved numerical stability and HMC sampling, all single crystal elastic constants are scaled by a common factor of $10^{-11}/Pa$ such that a value of 200 GPa (2.0×10^{11} Pa), is handled by Stan as a scaled unitless parameter: 2.0. Conveniently, the σ (noise) parameter (in units of kHz) and the three cubochoric orientation parameters did not require scaling. Note that the traceplots and histograms present parameters as they are handled by CmdStan-RUS [62], while common units of GPa and kHz are used for tables and result summaries.

In addition to scaling parameters, transformed parameters can improve HMC mobility and efficiency. Superalloys cast as single crystals, with a coherent two-phase microstructure possessing a cube-on-cube orientation relationship between the L_{12} precipitates and the FCC matrix [124], exhibit cubic elastic symmetry that appears homogeneous on the macroscopic scale. This apparent homogeneity occurs whenever the microstructure is orders of magnitude smaller than the wavelength of the resonance modes. In previous work [47], it was observed that the (C_{11}, C_{12}, C_{44}) elastic parameter space led to inferior sampling as the C_{11} and C_{12} parameters were highly correlated. Therefore, the C_{12} parameter was transformed into the Zener anisotropy ratio (Equation (2.31)) [88] such that sampling now takes place over a transformed (C_{11}, A, C_{44}) elastic parameter space [47]. This chapter also uses the (C_{11}, A, C_{44}) parameter space, while any alter-

native elastic symmetry with arbitrary parameter transformations is possible through simple modifications of the CmdStan-RUS input files [62].

7.3.2.1 Crystal Orientations

In the previous chapter (and in Bales et al. [47]), the arbitrary rotation of the crystal reference frame was parameterized as a passive unit quaternion. Unfortunately, parameterization as a unit quaternion confounded the default HMC sampler in Stan [60], the No U-Turn Sampler [182]. Though reparameterizing with cubochoric coordinates ($\boldsymbol{\kappa} = [\kappa_1, \kappa_2, \kappa_3]$), as first introduced in Section 2.3.2.4, resolved this issue. With details about transformations between the various orientation representations (Euler angles, unit quaternions, homochoric and cubochoric vectors) provided in Section 2.3.3 per references [103, 106]. Essentially, $\boldsymbol{\kappa}$ is derived from the homochoric vector ($\boldsymbol{h}$) via an equal-volume transformation from the homochoric ball ($V_{\boldsymbol{h}} = \pi^2$) to the cubochoric cube of edge length $\pi^{2/3}$ [104]. Thus, the three components of a cubochoric vector are valid between the range $-\frac{1}{2}\pi^{\frac{2}{3}}$ to $\frac{1}{2}\pi^{\frac{2}{3}}$. With the important feature of homochoric and cubochoric representations being that they are equal-volume representations of the unit quaternion hemisphere [104]. This ensures that random samples drawn from a homochoric or cubochoric space will uniformly sample that space [103, 104], while offering readily refinable grids that are well suited for implementation in modern computer programming [106].

7.3.3 Building a Statistical RUS Model

Bayes' rule can be presented in its common form [183]:

$$\underbrace{P(\theta|M)}_{Posterior} = \frac{\overbrace{P(M|\theta)}^{Likelihood}\overbrace{P(\theta)}^{Prior}}{\underbrace{P(M)}_{Prior Predictive}}, \tag{7.1}$$

where statements of conditional probability $P(...|...)$, measured data M, and estimated parameters θ, are combined to read "$P(M|\theta)$" as "the probability of the data given the parameters" [184]. To perform a Bayesian inference, a statistical model representing the likelihood is first developed and initialized based on prior knowledge and some observed data. Then new data in the form of previous posterior samples are used to update the prior knowledge in a systematic manner and to inform future posterior evaluations. This iterative learning process minimizes the uncertainty of estimated parameters with regard to the information available and may ultimately allow for precise estimates given enough posterior samples are available and the statistical model accurately describes the problem.

As the statistical RUS model employed in this work was described previously in Section 6.3.3, only a cursory description highlighting key elements and assumptions will be made here. The first assumption is that resonance modes $(m_1,\ m_2,\ m_3,\ \ldots,\ m_N)$, in a frequency ordered list of modes M with length N can be modeled as:

$$M = m_1,\ m_2,\ \ldots,\ m_N = f(L,\ C,\ \boldsymbol{\kappa},\ \rho) + \xi\ . \tag{7.2}$$

The forward model $f(...)$ is a function of the properties of the modeled specimen $(L,\ C,\ \boldsymbol{\kappa},\ \rho)$ and a normally distributed random noise ξ. Concerning the terms of the forward model, $L = (l_1,\ l_2,\ l_3)$ represents the dimensions of the parallelepiped, $C = (C_{11},\ C_{12},\ C_{44})$ are the single crystal elastic constants (with cubic elastic symmetry assumed for this example), $\boldsymbol{\kappa} = (\kappa_1, \kappa_2, \kappa_3)$ are the cubochoric crystal orientation coordinates, and ρ is the mass density of the specimen; collectively expressed as $\theta = (L,\ C,\ \boldsymbol{\kappa},\ \rho)$ for short. ξ is assumed normally distributed about each mode with a single variance equivalent to σ^2 (i.e. ξ is the same for every mode) and represents the combined uncertainty in the model and the measurements [185]. While it is unlikely that the noise is actually the same for every mode, Section 7.3.5 discusses a-posteriori methods by which this and other assumptions

are deemed acceptable.

The formulation of Equation (7.2) means that the resonance modes produced by either the forward model or by measurement are themselves random variables [47, 185]. Thus a statement of the conditional probability of measuring a set of modes M from a specimen with a fixed set of parameters θ may be written in terms of the forward model f as:

$$P(M|\theta) \sim \mathcal{N}(f(\theta), \sigma^2) \ , \tag{7.3}$$

with the tilde ($\sim$) indicating that the statement $P(M|\theta)$ "has the probability distribution of" and $\mathcal{N}$ indicating "a normal distribution" of modes with variance σ^2 about $f(\theta)$. In terms of a Bayesian formulation (Equation (7.1)), $P(M|\theta)$ is the likelihood. With a rigorous treatment of the mathematics and assumptions, a complete statement of the likelihood can be given as:

$$P(M|\theta) = \prod_i \frac{1}{\sqrt{2\pi\sigma_i^2}} e^{\frac{(f_i(\theta)-M_i)^2}{2\sigma_i^2}} \tag{7.4}$$

where i is the index of the computed ($f_i(\theta)$) and measured (M_i) modes [47].

Prior probability distributions ($P(\theta)$ in Equation (7.1)) express prior beliefs about the parameters that can be based on: values cited in literature, previous measurements on the same or similar material, or even based on an intuitive understanding of the natural range a parameter may exhibit. Importantly, priors express knowledge or beliefs about ultimately unknown quantities, they can be estimated from the data itself, and they do not necessarily precede the data in time [186]. Prior probability distributions can be simple expressions like assuming the C_{11} elastic constant ranges between 0 and 500 GPa with uniform probability:

$$C_{11} \ \sim \ \mathcal{U}(0 \ GPa, \ 500 \ GPa). \tag{7.5}$$

Or more informed statements like C_{11} being normally distributed about a mean of 250 GPa with a standard deviation of 50 GPa:

$$C_{11} \sim \mathcal{N}(250\ GPa,\ 50\ GPa). \tag{7.6}$$

Alternative distributions are also available including exponential, Cauchy, Student's-T, and others [60, 61]. With linear combinations of parameters implemented simply as:

$$C_{11} - C_{12} \sim \mathcal{N}(100\ GPa,\ 50\ GPa)\ . \tag{7.7}$$

All of the inferences in this work assumed the same set of weakly informative priors as summarized below:

$$\begin{aligned}
\sigma &\sim \mathcal{N}(0\text{ kHz}, 1.0\text{ kHz}) \\
C_{11} &\sim \mathcal{N}(250\ GPa,\ 75\ GPa) \\
C_{44} &\sim \mathcal{N}(125\ GPa,\ 50\ GPa) \\
A &\sim \mathcal{N}(3.0,\ 0.75) \\
C_{11} - C_{44} &\sim \mathcal{N}(125\ GPa,\ 50\ GPa)\ .
\end{aligned}$$

Ultimately we want to find the posterior distributions that express the probability that of our parameters θ take certain values given a measured set of modes M. We now have the likelihood and the priors, but the prior predictive distributions $P(M)$ are unknown. Fortunately, Bayes' rule can be simplified to:

$$P(\theta|M) \propto P(M|\theta)\ P(\theta) \tag{7.8}$$

when sampling with Markov chain Monte Carlo (MCMC) methods [187] because posterior

samples are generated proportional to the true posterior distribution [60]. Now with a complete formulation of the inverse problem, the Bayesian posterior is computed with HMC.

7.3.4 Computing the Posterior with HMC

Hamiltonian Monte Carlo is a hybrid Markov chain Monte Carlo (MCMC) method [59, 60, 188] that avoids the random walk exploration behavior common to other MC methods [189] by informing the sampler with first-order gradient information [182, 188]. As for the derivatives necessary for Hamiltonian dynamics, they were detailed in Section 6.3.4.1, and are now fully handled within CmdStan-RUS [62]. Like other MCMC methods, HMC involves sequentially building a Markov chain of samples based on memoryless exploration from the current state, with distributions proportional to the true posterior distribution [60]. With zero consideration given to previously accepted states, a proposed state at the end of an exploration period is only added to the chain when it is accepted through a Metropolis update based on the relative probability of the proposed state with respect to the current [59]. The Metropolis update accepts proposed states evaluated with a higher probability than the current state, but may reject a proposed state of lower probability in favor of retaining the current state.

Hamiltonian dynamics provide superior sampling by proposing distant and less correlated samples to the Metropolis update, and are accomplished through introduction of a fictitious momentum term at the beginning of an exploration period [59, 182]. This momentum term can assist in propelling the sampler beyond local minima and bring the sampler towards the steady state region of the posterior. When a proposed state is rejected, a new momentum term is generated and the exploration is restarted from the retained state [59].

7.3.4.1 Initial Parameterization and Constraints

Initial parameterization of the HMC chains are randomly generated from distributions specified by the priors given in Section 7.3.3. The traceplots in Figure 7.2 show the first 100 samples for four independent HMC chains of the CmdStan-RUS inversion of CoNi-C1, (the first parallelepiped of alloy CoNi-C). Clearly the random initial parameterization is only weakly informed by the given priors. For example, the C_{11} parameter initial values range from over 650 GPa for chain 2, to less than 50 GPa for chains 1 and 3. These are by all means "poor initial guess values", from the perspective of RUS inversion literature that consistently cites "good initial guess values" as important for ensuring convergence [26, 33, 41–43, 51]. In fact, the robust convergence behavior of the Bayesian IMF, despite poor initial values and no efforts to identify measured resonance modes, is one of the key contributions of this work.

As the traceplots in Figure 7.2 show, the four HMC chains reach the stationary region of the posterior relatively early (in this case, after less than 100 samples) in the 500 sample warm-up period—despite initial parameterization in extremely low probability regions of the posterior. Only the samples generated after the warm-up period are used to characterize the posterior distributions, so the rate at which the stationary region of the posterior is reached is a secondary concern. Each chain is run for a total of 1500 samples, with the first 500 warm-up samples ultimately discarded, a chain that reaches the stationary region before the warm-up period is complete is deemed a success.

The rapidly converging behavior detailed by Figure 7.2 is not always achieved, though it is by far the most common occurrence. Upwards of 90% of the individual chains reached a common stationary region of the posterior within the first half of the warm-up period. Of the approximately 10% of chains that fail to reach the stationary region, the vast majority of these cases were due to the sampler stalling as it asymptotically approached a constraint specified when parameters are first defined in CmdStan-RUS. Below is a list

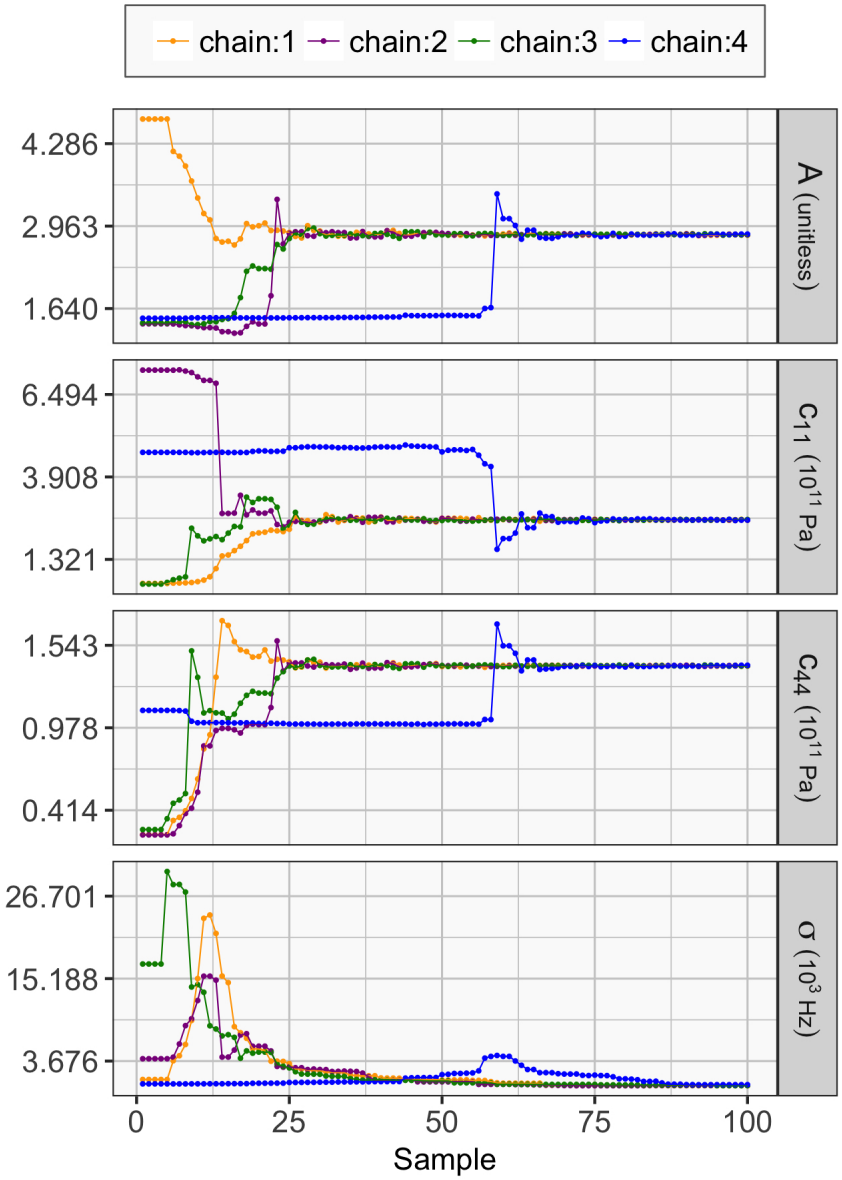

Figure 7.2: Traceplots of the first 100 warm-up samples of four independent HMC chains for the CoNi-C1 specimen demonstrating robust convergence to the stationary region of the posterior from remarkably distant, randomly generated, initial conditions.

of constraints applied:

$$\sigma,\ C_{11},\ C_{12},\ C_{44} \ = \ (0, \infty)$$

$$A \ = \ (1, \infty)$$

$$C_{44}/C_{11} \ = \ (0, 3/2)$$

$$\kappa_1,\ \kappa_2,\ \kappa_3 \ = \ (-1.072515, 1.072515)\ .$$

While all of these constraints are not strictly forbidden, e.g. C_{12} can be negative [190], the stiffness matrix must be positive definite which restricts C_{11}, C_{44}, and all constants along the diagonal to be positive. Instead, these constraints were developed through trial and error to minimally restrict the sampler while also mitigating the occurrence of initial parameterizations that would confound the sampler. Fewer constraints afford fewer opportunities for the sampler to find local regions of parameter space where the posterior probability increases as a constraint is approached. For these reasons it is recommended that implausible yet physically permissible values not be restricted through constraints, but instead discouraged through specifying priors whenever possible as detailed by Section 7.3.3.

7.3.4.2 Verifying Sampling Behavior

The full scales on Figure 7.2 do not allow one to observe the sampling behavior in the stationary region of the posterior. Instead, a detailed view of the last 100 samples of the CoNi-C1 inversion is provided in Figure 7.3. Here one can verify quality sampling by observing: sufficient mixing as each chain freely explores the posterior, no obvious trends (i.e. stationary), no multimodal tendencies, and mostly uncorrelated behavior between subsequent samples of a given chain. Of the four parameters plotted, the noise parameter σ is clearly being sampled with the least efficiency as it exhibits some correlated sampling behavior. Overall, the traceplots provided in Figures 7.2 and 7.3 provide great confidence in our efforts to use HMC to calculate the posterior distributions, with further measures for validation discussed in Section 7.3.5.

After verifying quality sampling, all samples generated after the warm-up period across the various HMC chains are combined to generate histograms for visual summary of the results. Figure 7.4 provides a set of histograms from specimen CoNi-B2 that contain 4000 samples, from 4 combined chains of 1000 samples each, that are typical of the results collected. Fitting with a Gaussian distribution confirms the normal behavior

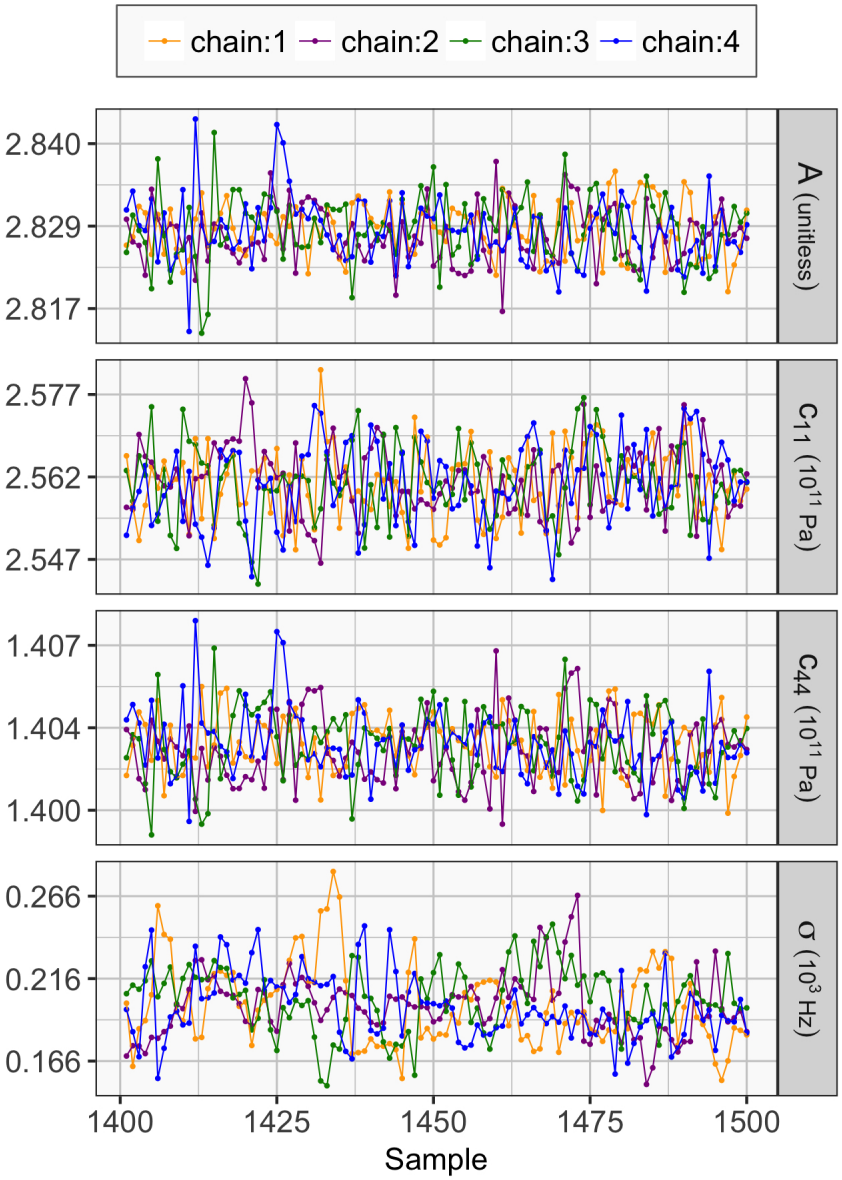

Figure 7.3: Traceplots of the last 100 sampling samples of four independent HMC chains for the CoNi-C1 specimen demonstrating desirable uncorrelated sampling behavior of the stationary region of the posterior for the noise and three elastic parameters.

of the parameter distributions around a single mode, and allows for the distributions to be characterized by their mean and standard deviation (sd). With sd being a direct estimate of the uncertainty, it can be reduced through the generation of additional HMC samples according to $1/\sqrt{N_{eff}}$, where N_{eff} is the number of effective samples [60].

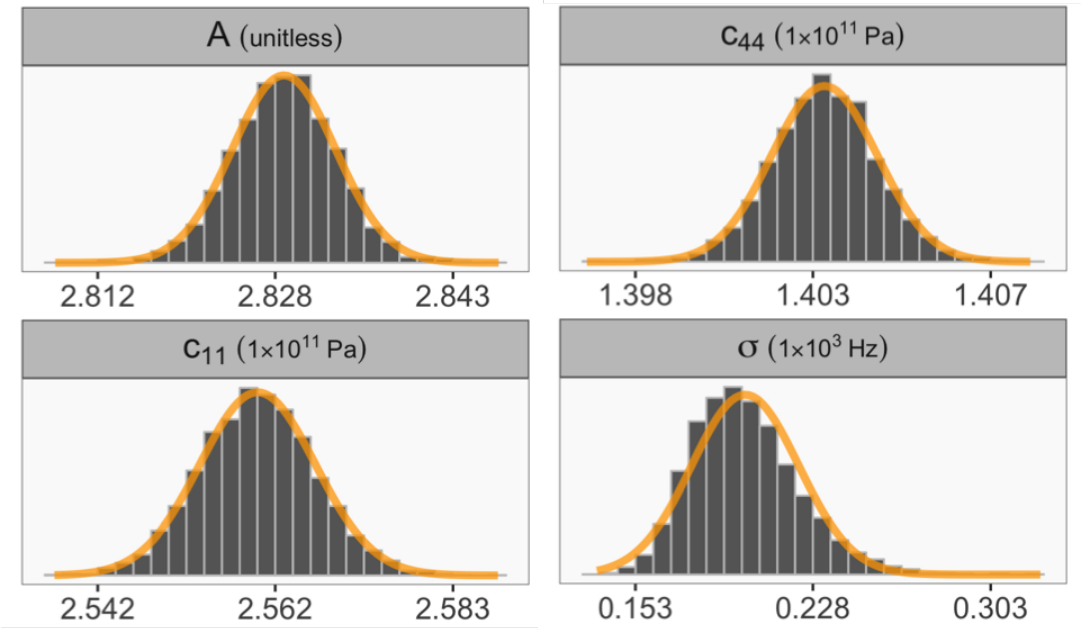

Figure 7.4: Histogram populated with 4000 samples (4 chains of 1000 samples each) for the CoNi-B2 specimen. Gaussian distributions overlay the histograms to demonstrate the parameters are normally distributed and justify describing the distributions with a mean and standard deviation.

7.3.5 Posterior Predictive Distributions and Validation

A check on the posterior predictive distributions as detailed in this section provides essential information for validating results. Posterior predictive distributions are developed by taking posterior samples of the estimated parameters and generating new resonance modes that reflect the implications of the uncertainty in the parameter estimates. Upon inspection, 95% of the measured modes should fall within the 95% intervals, otherwise this suggests that there are likely outliers in the measured data or the model is ill-defined [47].

As a visual aid, posterior predictive plots like those shown in Figure 7.5 are generated. Both plots show the difference between the posterior predictive and the measured mode frequencies, designated as the error on the abscissa, for the first 40 modes of specimen Co-Ternary-B. The length of the bars about each point indicate the 95% intervals. With units of kHz, this interval is not the mode invariant noise parameter σ, instead it represents

the frequency range about which 95% of resonance mode frequencies from the generated posterior predictive distributions exist. With only a 5% chance that a measured mode and a posterior predictive mode would differ by more than the interval indicated, a posterior predictive plot with 40 modes might be expected to exhibit 2 modes with an error beyond the 95% interval. The difference between the plots in Figure 7.5 is the polynomial order used for the forward calculation, with $P = 10$ for Figure 7.5a and $P = 12$ for Figure 7.5b.

For validation, one should inspect the posterior predictive plot to ensure that there is neither an observable trend in the error, nor any discernible patterns or structure that may indicate an ill-defined model. A positive trend in the error of Figure 7.5a is apparent by the first 12 modes exhibiting a negative error, while 6 of the last 7 modes are above the zero line. Additionally, the last two modes of Figure 7.5a lie unusually far beyond the 95% interval, suggesting either the noise is not independent and identically distributed, or there is a problem with the forward calculation. The fact that the unusual behavior exhibited by modes 39 and 40 in Figure 7.5a is not observed in Figure 7.5b is a clear sign that numerical imprecision of the forward calculation is the root cause, and may lead to biased inference results. For these reasons the $P = 10$ results are discounted in favor of the $P = 12$ results. Though it is worth noting that the $P = 10$ inference ran for 20.3 hours, while the $P = 12$ inference ran for 60.9 hours. For situations where computational time is of concern, using fewer resonance modes (N) would allow a smaller P without introducing numerical error into the results.

7.4 Results and Discussion

Table 7.3 summarizes the elastic parameter estimates from two parallelepiped specimens (A and B or 1 and 2) of each alloy composition, measured at room temperature, in the solution heat treated and fully aged condition. Very good agreement is observed between the specimen pairs, with the largest deviation for Co-6Ti. The estimates of the anisotropy

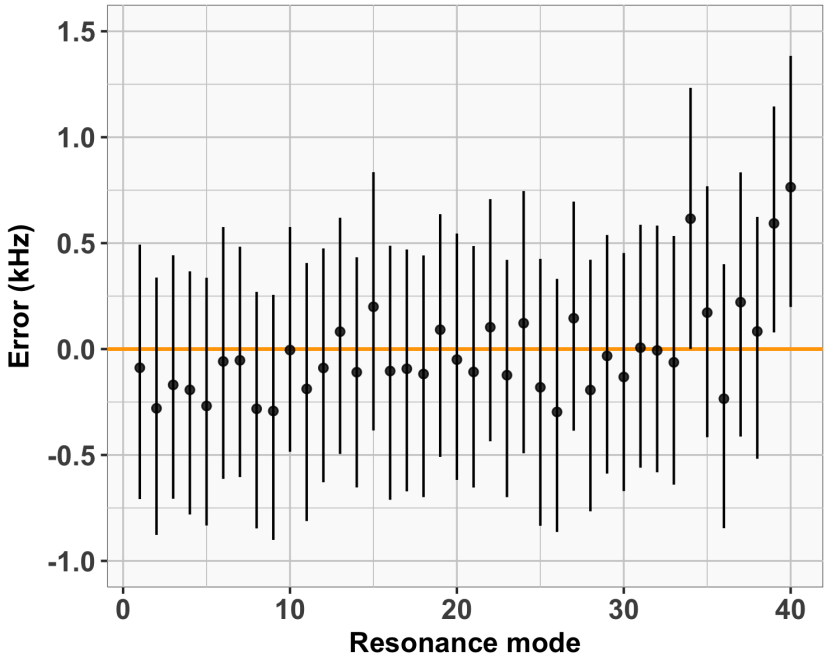

(a) $P = 10$

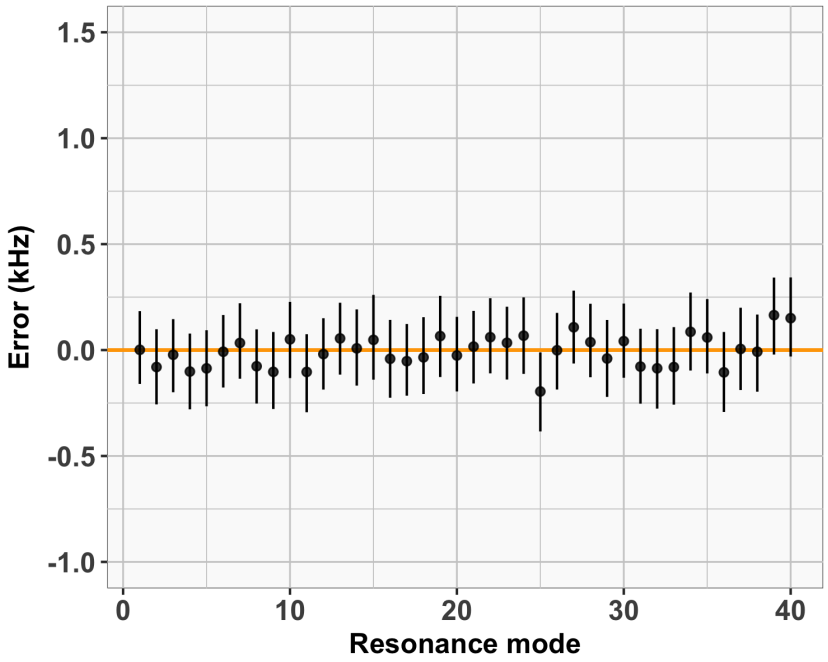

(b) $P = 12$

Figure 7.5: Co-Ternary-B posterior predictive plots demonstrating (a) undesirable trends in the error when $P = 10$, i.e. polynomial order is insufficiently small, and how (b) using $P = 12$ resolves this issue.

ratio (A) for Co-6Ti-A and Co-6Ti-B vary by about 1%, and as a result the estimates of C_{12} (which was not estimated directly) varies by just over 2%.

Table 7.3: Summary of the best inferences of elastic parameters for two parallelepiped specimens of each alloy.

Specimen name	$\mathbf{C_{11}}$ (GPa) mean ± sd	$\mathbf{C_{12}}$ (GPa) mean ± sd	$\mathbf{C_{44}}$ (GPa) mean ± sd	**A** (unitless) mean ± sd
CMSX-4-A	249.0 ± 2.3	157.0 ± 2.4	129.2 ± 0.29	2.811 ± 0.011
CMSX-4-B	248.3 ± 2.0	156.3 ± 2.1	129.6 ± 0.28	2.817 ± 0.0097
Co-Ternary-A	257.3 ± 0.79	164.2 ± 0.83	149.9 ± 0.13	3.219 ± 0.0045
Co-Ternary-B	256.7 ± 0.58	163.4 ± 0.60	150.0 ± 0.10	3.217 ± 0.0035
Co-2Ta-A	258.8 ± 1.8	164.5 ± 1.9	147.7 ± 0.26	3.134 ± 0.0085
Co-2Ta-B	259.3 ± 1.6	165.1 ± 1.7	147.9 ± 0.23	3.141 ± 0.0077
Co-6Ti-A	248.1 ± 1.4	156.8 ± 1.4	145.4 ± 0.24	3.188 ± 0.0086
Co-6Ti-B	250.7 ± 1.8	160.2 ± 1.9	145.2 ± 0.23	3.211 ± 0.0086
CoNi-A1	256.7 ± 0.36	157.6 ± 0.37	142.1 ± 0.08	2.868 ± 0.0029
CoNi-A2	256.4 ± 0.41	157.6 ± 0.41	141.9 ± 0.09	2.873 ± 0.0032
CoNi-A+1	256.7 ± 0.86	157.9 ± 0.90	142.2 ± 0.11	2.880 ± 0.0036
CoNi-A+2	255.9 ± 0.66	157.2 ± 0.70	142.0 ± 0.09	2.880 ± 0.0030
CoNi-B1	257.1 ± 1.3	158.2 ± 1.4	141.6 ± 0.21	2.864 ± 0.0068
CoNi-B2	257.5 ± 1.0	158.7 ± 1.1	141.7 ± 0.17	2.868 ± 0.0057
CoNi-C1	256.0 ± 0.67	156.8 ± 0.70	140.3 ± 0.13	2.828 ± 0.0044
CoNi-C2	256.1 ± 0.75	156.6 ± 0.79	140.6 ± 0.14	2.825 ± 0.0048
CoNi-D1	256.2 ± 0.60	157.2 ± 0.62	141.2 ± 0.09	2.853 ± 0.0029
CoNi-D2	257.8 ± 0.78	158.6 ± 0.82	141.3 ± 0.12	2.849 ± 0.0036

7.4.1 Influence of Alloy Chemistry on Elastic Constants

First consider a comparison between the five CoNi-based alloys in Table 7.3. CoNi-C exhibits the lowest anisotropy of the class at 2.83, while CoNi-A+ exhibits the largest A of 2.88. The C_{44} value of CoNi-C is also the smallest of the CoNi-based alloys, about 1% smaller than the largest C_{44} again belonging to CoNi-A+. CoNi-C is compositionally the most distinct CoNi alloy with 6.6–11.9 at% less Co and 7.3–9.8 at% more Ni likely contributing to its lower C_{12}, C_{44}, and A values. Interestingly, the C_{11} constant barely varies beyond the approximately 1 GPa uncertainty for the 5 CoNi alloys. Overall, the data in Table 7.3 indicate that all of the CoNi alloys are elastically quite similar, while even moderate alloying additions within the CoNi alloy class have only a small effect on elastic constants.

The Co-based alloy class offers an interesting opportunity to compare three alloys with nearly constant Co concentrations, which appeared to be a significant factor in CoNi-based alloys discussed previously. Overall, the elastic constants of the Co-based alloys differ from each other by a greater extent than the CoNi-based alloys, indicating that Co-based alloy elastic constants are more dependent on small to moderate compositional differences than their CoNi-based counterparts. Interestingly, the Co-6Ti alloy was the least stiff of the three Co-based alloys, exhibiting smaller C_{11}, C_{12} and C_{44} elastic constants. The Co-Ternary alloy exhibited the greatest C_{44} and A, while Co-2Ta was marginally stiffer in the C_{11}. With a range varying by 3.3%, the C_{44} parameter changed the most as a result of alloying, followed by the anisotropy ratio varying by 2.2% among the Co-based alloys.

One of the greatest differences between the moduli of the various alloy classes is the anisotropy ratio exhibited by the Co-based alloys. A increased from a low of about 2.81 for the Ni-based alloy CMSX-4 to around 2.86 for the CoNi-based alloys, or approximately +1.8%. A more dramatic increase was observed between the CoNi-based alloys and the

Co-based alloys as A increased by an additional 11%, from an average of 2.86 to an average of 3.17. With a nearly negligible increase between CMSX-4 and the CoNi alloy class, the C_{12} elastic constant exhibited a much more significant increase of about 4–6 GPa (+3%) between the CoNi and the Co-based alloy classes.

Following a similar progression from lowest to highest Co concentration, the C_{44} modulus is observed to consistently increase with increasing Co. Except now the most dramatic increase in C_{44} is between the Ni-based alloy and the CoNi alloys. A smaller, yet still significant, increase exists between the CoNi and the Co-based alloy classes. Quantifying this, the C_{44} modulus increased by 10 GPa (+8%) from CMSX-4 to the CoNi alloy class, before increasing by a more modest 4–8 GPa from the CoNi to the Co-based alloy class.

Initially C_{11} follows a similar trend with increasing Co, with an increase of about 7–8 GPa (or about 3%) between CMSX-4 and the average CoNi-based alloy. However, the C_{11} elastic constant fails to increase much beyond the 256–257 GPa range exhibited by the CoNi alloy class. With approximately 35% more Co than the average CoNi alloy: Co-2Ta exhibits a C_{11} that is only 2-3 GPa higher, Co-Ternary is basically equivalent, while Co-6Ti exhibits a C_{11} that is 7 GPa lower than the average CoNi alloy.

7.4.2 Effect of Heat Treatments on Elastic Properties

In addition to the results summarized in Table 7.3, one alloy from each class was evaluated in the solution heat treated condition to investigate the potential role of changing volume fractions of the FCC and $L1_2$ phases. Specifically, two parallelepipeds of CMSX-4, Co-6Ti, and CoNi-A were solution heat treated, then measured with RUS, aged, and finally measured with RUS again. The results of this heat treatment study are summarized in Table 7.4, with the heat treatment schedules summarized previously in Table 3.3. Clearly, the thermal history does not appreciably affect the elastic properties of the

alloys investigated. While a similar result is reported by Parsa et al. [191] who used RUS to study the effect of heat treatments on the elastic properties of a single crystal Ni-based superalloy with a composition similar to that of CMSX-4. These results suggest that the room temperature elastic constants of the ordered and disordered phases of the Co and CoNi-based alloys are not substantially different from each other, as has been previously reported for Ni-based alloys [98, 192].

Table 7.4: Effect of solution heat treatment and subsequent aging treatment on elastic constants.

Specimen name	$\mathbf{C_{11}}$ (GPa) mean ± sd	$\mathbf{C_{12}}$ (GPa) mean ± sd	$\mathbf{C_{44}}$ (GPa) mean ± sd	**A** (unitless) mean ± sd
CMSX-4-A-SHT	247.1 ± 2.1	155.4 ± 2.2	129.1 ± 0.28	2.813 ± 0.010
CMSX-4-A-Aged	249.0 ± 2.3	157.0 ± 2.4	129.2 ± 0.29	2.811 ± 0.011
CMSX-4-B-SHT	246.1 ± 1.8	154.3 ± 1.9	129.4 ± 0.31	2.819 ± 0.011
CMSX-4-B-Aged	248.3 ± 2.0	156.3 ± 2.1	129.6 ± 0.28	2.817 ± 0.0097
Co-6Ti-A-SHT	248.5 ± 0.77	157.6 ± 0.80	146.0 ± 0.14	3.211 ± 0.0049
Co-6Ti-A-Aged	248.1 ± 1.4	156.8 ± 1.4	145.4 ± 0.24	3.188 ± 0.0086
Co-6Ti-B-SHT	250.1 ± 1.1	159.6 ± 1.1	145.6 ± 0.13	3.218 ± 0.0046
Co-6Ti-B-Aged	250.7 ± 1.8	160.2 ± 1.9	145.2 ± 0.23	3.211 ± 0.0086
CoNi-A1-SHT	255.5 ± 0.70	156.2 ± 0.72	142.2 ± 0.10	2.864 ± 0.0029
CoNi-A1-Aged	256.7 ± 0.36	157.6 ± 0.37	142.1 ± 0.08	2.868 ± 0.0029
CoNi-A2-SHT	256.2 ± 0.43	156.9 ± 0.44	142.2 ± 0.10	2.864 ± 0.0033
CoNi-A2-Aged	256.4 ± 0.41	157.6 ± 0.41	141.9 ± 0.09	2.873 ± 0.0032

7.4.3 Effect of Mode Selection and Polynomial Order

In theory, each specimen has one true set of elastic constants that are probed indirectly by fitting a subset of the lowest-frequency modes, measured via RUS, with an appropri-

ately parameterized model. Though even a well-fitting model may yield biased parameter estimates if the measured data contains outliers, or lacks necessary information about the complete elastic response. Considering that the shape of a specimen influences the types of modes that occur [46], and that the lowest-frequency modes of a specimen are dominated by the smallest (i.e. shear) elastic moduli [26,46], it is logical to be concerned that any small sampling of these lowest-frequency modes might provide incomplete information. Although the definition of a small sampling of modes is not obvious and warrants further attention, it is noted in Section 7.2.2.1 that the $9 \times 10 \times 11$ mm parallelepiped geometry was intentionally devised with these concerns in mind.

One obvious way to mitigate the potential of a non-representative sampling of resonance modes being used for a given inversion is to simply use more modes. This assumes that a larger sampling of the lowest-frequency resonance modes would be less influenced by any single outlier mode, more likely to contain a variety of mode types, and include resonances that are sensitive to the larger moduli that influence higher-frequency modes. Of course there are a couple of potential problems with this strategy that need to be mentioned. First, the larger the number of modes used (N), the more likely it is that the list contains a missing or spuriously identified mode that could confound the inversion. Fortunately, with the transducer cradle configuration as described, and the fact that each inference is based on an average of 5 individual broad measurements, missing or spurious modes are quite rare occurrences. Furthermore, Section 7.4.4 demonstrates how a missing mode is readily identifiable using posterior predictive plots, allowing for the measured mode list to be corrected. A second and potentially less obvious issue is that the accuracy of the forward model generally decreases as the order of the resonance modes increase, necessitating a higher polynomial order (P) and substantially greater evaluation time. This is all motivation for a study of inference results as a function of N and P.

Table 7.5 summarizes the parameter estimates from a series of Bayesian inferences of

specimen CoNi-A+2 using various N and P values. The first takeaway is that consistent results are achieved despite the choice of N, with the best results from the perspective of the lowest uncertainty achieved when $N = 40$. Recalling Figure 7.5 and the discussion in Section 7.3.5, it is apparent that $P = 10$ is insufficient when $N = 40$, thus $P = 12$ is exclusively used for inferences when $N > 30$. The case where $N = 30$ provides an interesting comparison as both $P = 10$ and $P = 12$ inferences were conducted. As this comparison makes clear, $P = 12$ leads to more precise parameter estimates, but the mean values are not appreciably different. A similar observation comes from the $N = 60$ and $N = 70$ inversions where the uncertainty due to an insufficiently small P, as determined through careful inspection of the posterior predictive plots, contributes to slightly worse precision. Fortunately, the accuracy appears minimally affected when numerical error is introduced by an insufficiently small P.

7.4.4 Impact of Missing or Spurious Modes

A common issue that confounds RUS inversion efforts are missing or spuriously identified modes from a broadband RUS measurement. This is particularly problematic when the mode is of lower-frequency and near the beginning of a frequency ordered list because it displaces every subsequent mode in the list. When prior information about the elastic properties of a specimen is absent and no mode shape measurement capabilities are available, it is almost impossible for one to be certain that a given measured list of modes is complete and without error. Furthermore, conducting an inversion (either an optimization or a Bayesian inference) from a measured frequency list with a missing mode may lead to erroneous elastic property estimates, or unsatisfactorily large uncertainty bounds. Fortunately, by estimating the noise parameter (σ) as part of the Bayesian inference and conducting the validation checks discussed in Section 7.3.5, missing or spurious modes are readily identifiable. Then the spurious mode can easily be excluded to

Table 7.5: Summary of parameter estimates as a function of the number of modes used for specimen CoNi-A+2. Note the results highlighted in gray are only provided for explanatory purposes as they are either biased by numerical error (i.e. insufficient polynomial order) or insufficient data.

Modes used	**Poly. order**	**Noise** σ (kHz) mean ± sd	$\mathbf{C_{11}}$ (GPa) mean ± sd	$\mathbf{C_{12}}$ (GPa) mean ± sd	$\mathbf{C_{44}}$ (GPa) mean ± sd	**A** (unitless) mean ± sd
1-10	10	0.24 ± 0.15	256.7 ± 4.6	158.0 ± 4.7	141.7 ± 0.85	2.869 ± 0.022
1-15	10	0.134 ± 0.041	255.3 ± 1.7	156.5 ± 1.8	142.0 ± 0.30	2.875 ± 0.0080
1-20	10	0.135 ± 0.029	256.9 ± 1.3	158.2 ± 1.3	142.1 ± 0.14	2.880 ± 0.0040
1-25	10	0.180 ± 0.032	255.8 ± 1.5	157.2 ± 1.5	142.1 ± 0.15	2.882 ± 0.0044
1-30	10	0.216 ± 0.033	257.4 ± 1.5	158.9 ± 1.6	141.9 ± 0.16	2.880 ± 0.0051
1-30	12	0.152 ± 0.025	256.9 ± 1.1	158.3 ± 1.1	142.0 ± 0.12	2.882 ± 0.0037
1-35	12	0.144 ± 0.020	256.4 ± 0.90	157.8 ± 0.94	142.0 ± 0.099	2.880 ± 0.0032
1-40	12	0.138 ± 0.018	255.9 ± 0.66	157.2 ± 0.70	142.0 ± 0.095	2.880 ± 0.0030
1-45	12	0.210 ± 0.024	256.3 ± 1.0	157.7 ± 1.1	141.9 ± 0.13	2.879 ± 0.0042
1-50	12	0.218 ± 0.023	256.5 ± 0.98	158.0 ± 1.0	141.8 ± 0.12	2.878 ± 0.0041
1-60	12	0.242 ± 0.024	255.6 ± 1.0	157.0 ± 1.1	141.7 ± 0.14	2.875 ± 0.0046
1-70	12	0.336 ± 0.031	255.3 ± 1.2	156.8 ± 1.3	141.6 ± 0.18	2.874 ± 0.0061

correct the measured frequency list and the inversion repeated for significantly improved results.

Table 7.6: Summary of parameter estimates for two inversions of CoNi-D1, each using the first 40 modes, with and without accounting for missing mode 32.

Missing mode 32	**Poly. order**	**Noise** σ (kHz) mean ± sd	$\mathbf{C_{11}}$ (GPa) mean ± sd	$\mathbf{C_{12}}$ (GPa) mean ± sd	$\mathbf{C_{44}}$ (GPa) mean ± sd	**A** (unitless) mean ± sd
yes	12	2.70 ± 0.28	283 ± 25	186 ± 26	147.0 ± 3.3	3.04 ± 0.11
no	12	0.170 ± 0.022	256.4 ± 0.60	157.4 ± 0.62	141.3 ± 0.11	2.856 ± 0.0034

For example, mode 32 of specimen CoNi-D1 was not identified prior to running an $N = 40$, $P = 12$ inversion, with results summarized in Table 7.6. The first indication of a problem with the inversion was the estimate of $\sigma = 2.70 \pm 0.28$ kHz. This noise estimate is an order of magnitude larger than a typical successful inversions, and over 15 times larger than the same inversion after properly accounting for the missing mode. Though a high σ estimate is indicative of an ill-defined model, it does not help with identifying the location of a potentially missing mode. For this, a posterior predictive plot like Figure 7.6 is instrumental, as it clearly indicates the location of the outlier as mode 32. Given that error is defined here as the modeled mode frequency minus the measured mode frequency, an outlier with a negative error indicates a missing mode while a positive error indicates a spurious mode in the measured frequency list.

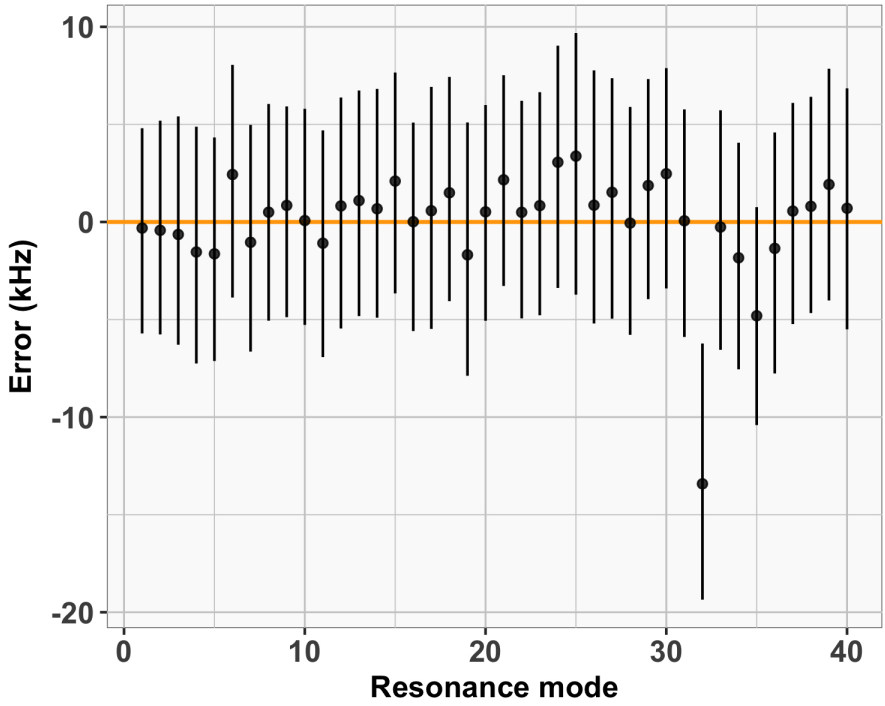

Figure 7.6: Posterior predictive plot of CoNi-D1 demonstrating how such a plot can be used to quickly identify which mode was missed during RUS measurement.

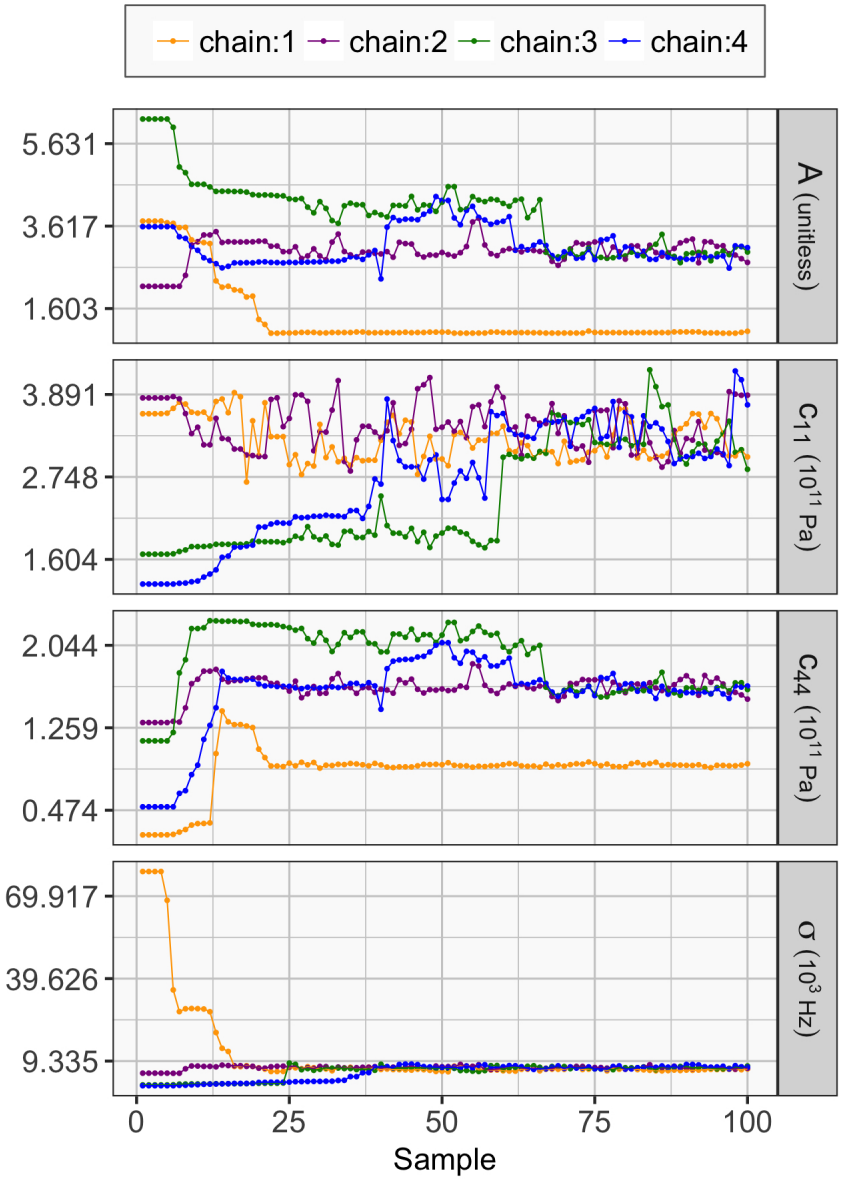

Figure 7.7: Traceplots of first 100 warm-up samples of four independent HMC chains for the CoNi-A1 specimen, without estimating orientation.

7.4.5 Inversion Without Estimating Orientation

To demonstrate the necessity of estimating crystal orientation and elastic properties simultaneously, a previously successful inversion is repeated with the orientation parameters now fixed. CoNi-A1 was selected for this demonstration because the specimen resulted in one of the best inversions as demonstrated by the precise parameter estimates

summarized in Table 7.3. The effect of fixing the three cubochoric orientation parameters enforces the (incorrect) assumption that the crystal and specimen axes are perfectly aligned. However, no attempt was made to measure the crystal axes of the parent single crystal before the parallelepiped specimen was fabricated, so it is extremely unlikely that the axes are indeed aligned. This is a perfect example of an ill-defined model, because there should be no combination of C_{11}, A, and C_{44} that will lead to a forward model evaluation that remotely agrees with the RUS measured data.

First see the traceplots in Figure 7.7, which provide the first 100 warm-up samples of the CoNi-A1 inversion with fixed orientation parameters. Given that the initial conditions are randomly generated, there is an initial period of exploration where the parameter estimates are improved. But unlike the rapid convergence of all four chains to a single stationary region of the posterior as Figure 7.2 shows, the four chains do not agree after the first 100 samples. In fact, the chains never agree on a single set of elastic parameters to explain the measured data, as Figure 7.8 shows by plotting the last 100 samples from the sampling regime, just as Figure 7.3 previously plotted the last 100 samples from a successful inversion of CoNi-C1. Multi-modal tenancies are demonstrated by the elastic parameter estimates of chains 2–4, while the estimate of σ around 7 kHz is over an order of magnitude larger than the successful inversions. Table 7.7 provides a comparison of the two CoNi-A1 inversion results as a summary.

Table 7.7: Summary of parameter estimates for two inversions of CoNi-A1, with and without estimating crystal orientation.

Orientation estimated	**Noise** σ (kHz) mean ± sd	$\mathbf{C_{11}}$ (GPa) mean ± sd	$\mathbf{C_{12}}$ (GPa) mean ± sd	$\mathbf{C_{44}}$ (GPa) mean ± sd	**A** (unitless) mean ± sd
yes	0.124 ± 0.013	256.7 ± 0.36	157.6 ± 0.37	142.1 ± 0.08	2.868 ± 0.0029
no	6.80 ± 0.55	299 ± 61	174 ± 63	158 ± 43	2.7 ± 1.1

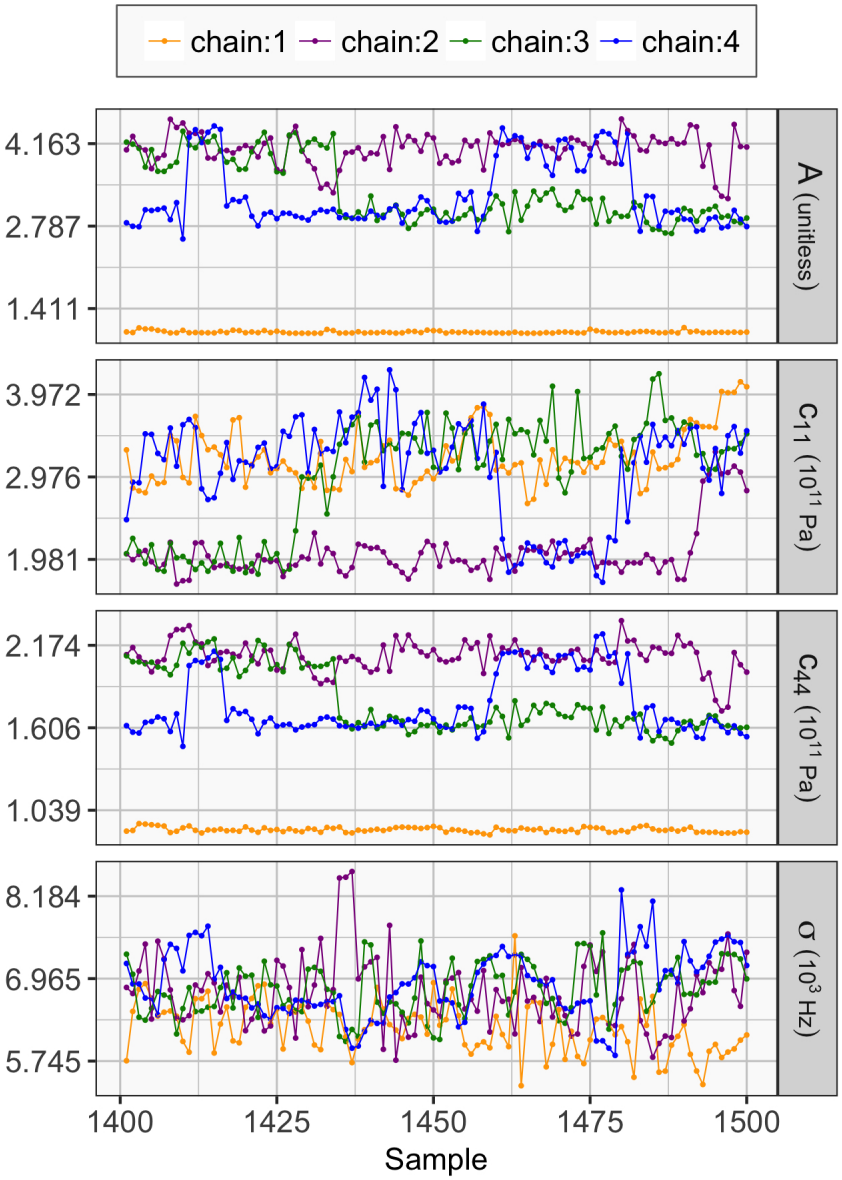

Figure 7.8: Traceplots of last 100 sampling samples of four independent HMC chains for the CoNi-A1 specimen, without estimating orientation.

7.5 Conclusion

CmdStan-RUS [62] is described and demonstrated here for the first time as a versatile and efficient tool for RUS Bayesian inference of elastic properties. This open-source tool offers significant improvements over traditional RUS inversion schemes, from a simplified

implementation to more robust convergence behavior. Notable attributes and advantages are provided below as a summary of the technique:

- No guess values of elastic constants are necessary to initialize an inversion.
- Identifying measured modes and pairing of measured and modeled lists of modes is completely unnecessary.
- Missing or spurious modes are readily identified from posterior predictive plots and easily corrected.
- Random initial parameterization of HMC chains safeguards against biasing results with user specified values.
- Estimating crystal orientation eliminates the need for costly measurements and simplifies specimen fabrication.
- Statistical modeling tools used by CmdStan-RUS are automatically tuned and work reliably without user input.
- Estimating a noise parameter models a real feature of repeated RUS measurements and reduces the chance of biased parameter estimates.
- Multiple HMC chains from markedly different initial conditions converging to a single stationary region of the posterior provides great confidence in results.
- Consistent results have been demonstrated using a range of user-specified polynomial order and mode count.
- A failed HMC chain is rare, trivial to identify, and may be discarded (or rerun) without biasing results.
- Quantification of parameter uncertainty is intrinsic to a Bayesian approach and comes directly from the posterior distributions.

- While only cubic elastic symmetry was considered here, trivial modifications of input files allow for inversions of lower-symmetry materials as well.

Valuable insights have been gained through the application of CmdStan-RUS to estimate the elastic constants of a variety of single crystal Ni, Co, and CoNi-based γ' containing alloys. Excellent agreement is observed, both among independent chains of a single inference and between the estimated parameters of the two parallelepiped specimens of each alloy. This has led to the following conclusions with regard to the elastic constants of the investigated single crystal materials:

- Co-based alloys exhibited elastic anisotropy (A) 11% greater than the CoNi-based alloys and 13% greater than the Ni-based alloy CMSX-4.

- The C_{44} elastic constant was observed to increase monotonically as Ni was replaced by Co for a total average increase of 12% between CMSX-4 and the Co-based alloys.

- The C_{12} elastic constant was only marginally higher for the CoNi-based alloys as compared to CMSX-4, while a 3% increase between the CoNi and the Co-based alloys contributes to the larger A of the Co-based alloys.

- The CoNi alloys exhibited similar elastic properties while Co-based alloys were more sensitive to alloying.

- Heat treatments designed to modify the $\gamma - \gamma'$ microstructure did not appreciably affect the elastic constants of the alloys investigated.

Chapter 8

Discussion, Conclusions, and Recommendations

8.1 Overview

With conclusions specific to the work of each of the main body chapters provided at the end of Chapters 4 to 7, this chapter focuses on broader issues related to the RUS technique. Summarized in two major areas, discussion of the key contributions will focus first on the area of nondestructive evaluation. Herein, NDE procedures employed relatively simple forward models for identifying the mechanisms and extent of damage affecting resonance, with the value of simplicity being broad applicability of the general methods as outlined. The limitations of the FMF ultimately depend on factors such as: the relative impact on resonance of a particular damage mechanism, at a particular location, on a particular specimen, versus the relative impact of resonance-affecting mechanisms that are not modeled or otherwise accounted for. Considering these limitations, discussion concerning the utility of RUS as a NDE tool for evaluating different types of damage is also provided. The second area of focus for this chapter concerns materials characterization using inverse models to accurately and precisely quantify properties. With ultrasonic means providing the most accurate characterization method for determining elastic properties [33,34], along with superior precision and repeatability as compared to static methods [39], the defining features and major contributions of the IMF developed herein are first summarized. Then alternative investigations enabled through the novel features of CmdStan-RUS [62] are discussed, followed by a summary of the major conclusions of this work. The dissertation ends with potential avenues of future work, including a novel high-temperature RUS experimental setup, and opportunities for expanding the IMF characterization potential through modifications of the forward model.

8.2 NDE of Damage with Forward Models and RUS

Chapters 4 and 5 detail the forward modeling frameworks for extending the NDE capabilities of RUS. In this dissertation it has been shown that forward models are necessary to decipher the measured $\triangle f_R$ behavior, and identify the true mechanisms affecting resonance, particularly when multiple modes of damage occur together. Without forward models validated through controlled experiments, it can be difficult to rule out competing explanations, as many different aspects of a specimen can affect its resonance behavior. Consider the example of a first stage turbine blade in an aerospace or power generation turbine engine. These structural parts are often made of Ni-based superalloys because the operating environment requires materials that exhibit considerable strength and stability at high temperatures, ductility for impact damage tolerance, and a degree of oxidation resistance for situations when oxidation/thermal barrier coatings fail.

If, before entering service, a quick broadband resonance spectrum was collected from each turbine blade, then upon any subsequent maintenance overhaul, each blade could again be inspected via RUS, and the $\triangle f_R$ behavior determined. Any obvious outliers could immediately be quarantined for further evaluation. While the $\triangle f_R$ signatures of the remaining blades cross referenced against a database of modeled $\triangle f_R$ results representing individual or multiple concurrent damage mechanisms known to afflict the blades. In Chapter 4 it was shown that cracks and creep elongation each manifested different $\triangle f_R$ signatures which could be independently identified from a complex geometry (dog-bone) specimen subjected creep conditions. While the measured $\triangle f_R$ signature of a fatigued dog-bone indicated not only the presence of a large crack, but indicated the crack was likely some distance away from the center of the dog-bone gauge section, as the measured results more-closely matched the modeled $\triangle f_R$ signature of a crack 2.5 mm above the center of the gauge section. Even these simple cases demonstrate the strength

of RUS as a multi-purpose NDE technique, informed by simple FE models of common modes of damage. With substantial time and cost savings afforded by the implementation of a forward modeling framework, as opposed to strictly empirical methods of diagnosing damage through a series of controlled experiments. This research has highlighted the potential of RUS to detect defects in grain structure as well as mechanical damage, as the next two sections discuss.

8.2.1 RUS for NDE of Mechanical Damage

The RUS for NDE research covered by Chapters 4 and 5 demonstrated many key features that hold considerable promise for future applications. Foremost is the concept of measuring damage evolution over time, based on comparisons to a baseline resonance response, such that mode-specific changes in resonance frequencies ($\triangle f_R$) can be determined for each specimen. This novel paradigm based around calculating the $\triangle f_R$ response independently for each specimen and model has two major implications: it removes the natural variability in f_R exhibited by measured specimens that can hinder NDE investigations attributing causes for specific changes in f_R , and it allows for direct comparison to modeled $\triangle f_R$ results from an ideal model.

Expanding upon this first major implication, in Chapter 4 the forward models of the dog-bone specimen undergoing creep clearly indicated that the shape change mechanism alone was not capable of creating the full $\triangle f_R$ response exhibited by the measured specimen. This was key to demonstrating that secondary damage mechanisms were indeed operable, particularly after the specimen was crept beyond 6% creep strain. With additional FE models affirming that an asymmetrical distribution of many small surface cracks along the gauge section of the dog-bone could be attributed to the unexplained $\triangle f_R$ residual of the measured specimen after the $\triangle f_R$ from the shape change was removed. This ability to discriminate multiple concurrent damage mechanisms is very promising

for the prospect of RUS being applied to NDE service-exposed parts, where operating in extreme environments often leads to the evolution of multiple modes of damage. As long as these modes of damage create a measurable $\triangle f_R$ response, and RUS forward models are capable of reproducing this $\triangle f_R$ response, then NDE efforts can be trained to identify the presence, severity, and type of damage that occurs using rapid, cheap, and nondestructive RUS measurements.

The second major observation was that $\triangle f_R$ should be directly compared to modeled $\triangle f_R$ calculated from an "idealized specimen model", whereby the model does not need to be calibrated to reproduce the measured f_R spectra precisely. Only the IMF deals with aligning measured and modeled f_R spectra themselves, while the FMF is concerned with capturing the mechanisms affecting a change in resonance behavior from a baseline response. By comparing $\triangle f_R$ instead of f_R , the natural fluctuation of variables specific to any real specimen that manifest as a $\pm 1 - 2\%$ variation in f_R from the behavior of ideal model can be safely ignored. For all practical purposes, the FE model only needs to be a "good enough match" to the f_R behavior exhibited by the measured specimen such that the modes of each can reasonably be paired. With the residual analysis previewed in Section 1.3.2 and detailed in Section 4.4.2 useful for correcting any improper pairing that may have occurred due to a mode-order disagreement between the measured and modeled baselines.

The implications of this point for future RUS for NDE efforts is difficult to overstate, as even state-of-the-art NDE investigations prior to this work rarely pursued the opportunity afforded through integration of models with RUS measurements, particularly for rapid assessment of damage in complex geometry parts. This lack of model integration is likely due to the following reasons. First is a commonly held misconception, likely carried over from inversion efforts, whereby minimizing the difference between measured and modeled f_R directly was the key to quantifying properties. Migliori and Sarrao write in their seminal book on RUS that for "simple part geometries, the mode type and

frequency can be calculated, and selection of diagnostic modes can be based on these results. For complex geometries, an empirical approach is the best solution for the development of algorithms to identify specific defects." Advocating for empirical approaches to NDE of complex geometry parts makes sense from the perspective of decades of inverse modeling efforts that have not resulted in any demonstration of an IMF capable of diagnosing the benign causes for a $\pm 1 - 2\%$ variability in f_R typically exhibited by a complex geometry specimen. Without identifying and isolating these benign features, measured and modeled f_R spectra could never be directly compared for purposes of high-fidelity NDE, essentially relegating NDE efforts to empirical methods. But as shown in this dissertation, comparing $\triangle f_R$ results instead of f_R results circumvents this issue entirely. The second reason that has historically inhibited integration of forward models with NDE efforts, which has only recently been surmounted, is that of computational resources. Only in the past decade or so have powerful and affordable computational resources become widely available that are capable of carrying out a series of high-fidelity FE models—entailing numerous specific damage scenarios with a range of severity—with sufficient detail necessary for quantitative NDE of complex geometry parts.

8.2.2 NDE of Grain Structure Defects

The research covered by Chapter 5 of this dissertation has demonstrated that RUS holds immense potential for nondestructive evaluation of single crystal castings like turbine blades, either as part of manufacturing process control or for evaluation of damage accumulated during service in extreme environments. Simple material models representing recrystallized material as a homogeneous isotropic volume with Gairola and Kröner [92] average properties are in excellent agreement with measured results. With the recrystallization mechanism dominating the $\triangle f_R$ behavior with a characteristic saw-tooth pattern, such damage is readily identified. Even when recrystallization occurs in small volumes

in select locations, turbine blade models demonstrate $\triangle f_R$ over an order of magnitude greater than the RUS measurement sensitivity.

Without a baseline RUS response—necessary for calculating a $\triangle f_R$ signature and removing benign part-specific resonance characteristics—forward FE models can still be used to diagnose the cause of anomalous f_R signatures exhibited by newly manufactured parts. For example, one of the most common single-crystal casting defects are stray grains, which form high-angle boundaries that are particularly susceptible to creep damage. Stray grain-containing turbine blades will exhibit substantially anomalous resonance characteristics that make them obvious outliers to even a basic PSS evaluation. Simply measuring the f_R of each blade after removing them from the mold, and comparing these results with an ideal model or a population of peers, could indicate whether a stray grain or substantial geometric defect is present. While this initial scan can then serve as a baseline response for finding smaller defects that may be introduced during subsequent processing (i.e. during solution, aging, or coating treatments). Or for tracking the evolution of damage acquired during service in extreme environments, where impact damage from foreign objects or simply the accumulation of creep strain could provide the driving force necessary for recrystallization to occur—which would be deleterious to the life of the component.

Even sub-surface recrystallization, or recrystallization of the superalloy substrate after a coating is applied, should exhibit characteristic $\triangle f_R$ signatures indicating the presence of recrystallized grains. Both models and measurements in Chapter 5 demonstrate the characteristic saw-tooth pattern for such grain structure defects. In fact, this pattern should be exhibited by any anisotropic [001] single crystal that undergoes recrystallization, as nothing specific to Ni-based alloys makes this analysis possible besides intrinsic elastic anisotropy of the single crystal material. In fact, the surface recrystallization response was so dominant as compared to any other resonance-affecting mechanisms, i.e. dislocation recovery and residual stress relaxation, that simply accounting for the

recrystallized material was sufficient to explain the full $\triangle f_R$ response measured from the quarter-cylinder specimen. This is not to say that residual stress relaxation plays no role in affecting resonance. Just that the $\triangle f_R$ effects resulting from the recovery of dislocations and the relaxation of residual stress imparted via shot-peening ultimately played an insignificant role as compared to the dominant $\triangle f_R$ response attributable to recrystallization.

8.3 Materials Characterization with Inverse Models

First developed in Chapter 6 and expanded upon in Chapter 7, a Bayesian formulation of the RUS inversion problem has been applied to characterize the single crystal elastic properties of novel materials using measured f_R . Capable of simultaneously estimating crystal orientation, the framework is remarkably robust, easy to use, and broadly applicable to material of any elastic symmetry, from isotropic to triclinic. The key consequences of this capability are dramatically simplified experimental and computational procedures for performing the RUS inversion problem, as discussed below.

Experimental procedures are simplified by the fact that reliably estimating the orientation of elastically anisotropic bodies enables RUS inversion without any regard for alignment of the crystal and specimen reference frames. Without this capability, researchers have had to first precisely measure the orientation of a parent single crystal, before machining a rectangular parallelepiped specimen with face normals aligned with the crystallographic axes. Any error in the measurement of the crystal orientation, or specimen manufacturing process, would lead to irreconcilable discrepancies between measured and modeled f_R that ultimately manifest as error in the elastic property estimates. As of this writing, CmdStan-RUS is the only code that has been demonstrated to consistently accomplish this task, and the only such code made freely available to the scientific

community[1].

As for the simplified computational procedure, the Bayesian formulation of the RUS inverse problem—combined with efficient computation of the posterior distributions with HMC—proves remarkably robust in estimating unknown parameters given little, if any, prior information about the parameter values. In fact, this capability is routinely demonstrated by starting multiple independent HMC chains with random initial conditions, and observing the chains rapidly progress towards the same stationary region of the posterior. By comparison, traditional optimization-based approaches are prone to converge to local minima when supplied with poor initial conditions, if they converge at all. For when initial guess values of elastic constants differ substantially from the actual values possessed by the specimen, the frequency order of the measured mode lists will disagree with that of the modeled mode list produced from the guess values. This leads to improper pairing of modes, which underestimates the difference between the measured and modeled mode lists, and can lead the inversion procedure astray. In fact, the issue of identifying measured modes, and subsequent efforts to align measured and modeled mode lists such that inversions can be properly initiated, are so ubiquitously discussed in the literature that one could be excused for believing the problem is universal to RUS inversion. Though recent reports by Bernard et al. [101], in conjunction with the findings of this work, suggests that the problem surrounding quality initial guess values, mode identification, and proper pairing of measured and modeled mode lists may be more appropriately classified as a problem common to optimization-based RUS inversions.

Having two modes improperly paired from a list of 40 modes used for an inversion will not routinely preclude convergence of optimization-based inversions. Though the problem grows more serious with each subsequent misalignment, to a point at which convergence of an optimization-based inversion will become impossible—regardless of the quality of initial guess moduli—without active measures to rectify the misalignment

[1]CmdStan-RUS [62] can be downloaded at: https://github.com/bbbales2/cmdstan-rus

problem. Various solutions to this problem have been proposed over the years, but when one excludes solutions that require the input of additional data, e.g. phase velocity measurements [167] or laser vibrometry measurements of mode shape [26, 27, 85], the remaining options are generally: complicated, reliant on significant input from the user, and far from robust. Remarkably, the IMF as described here performs exceptionally well given zero additional input or feedback from the user. For these reasons the simplified computational procedure of the IMF, in conjunction with the simplified experimental procedures discussed previously, are elevated as key contributions of this work.

8.4 Summary of Major Conclusions

- Models are generally required to predict the resonance characteristics of 3D specimens, while they also provide key information to decipher measured spectra and inform measurements of valuable mode-shape information useful for nondestructive evaluations.

- Nondestructive evaluations should compare mode-specific changes in resonance frequencies ($\triangle f_R$), determined from independent measured and modeled baselines, as doing so removes benign variability in measured specimens and allows for comparisons to idealized models.

- Simple material models that homogenize microstructure-dependent elastic properties are often sufficient for modeling the resonance characteristics of a specimen, as long as self-consistent homogenization schemes are used.

- Bayesian formulation of the inverse problem requires considerably more forward problem evaluations, but the remarkably robust inverse modeling framework provided by such a formulation greatly outweighs the cost of additional computation time.

- The capabilities exhibited by the CmdStan-RUS code exceed those reported by the most capable optimization-based inversion frameworks, routinely estimating elastic constants and crystal orientation parameters with built-in estimates of uncertainty, all without prior knowledge of these quantities or any mode identifying information.

8.5 Extensions of RUS and Future Work

8.5.1 NDE of Recrystallization Kinetics

When the surface recrystallization layer of the quarter-cylinder specimen could be assumed as planar—a fact that was later confirmed by a post-mortem metallographic analysis—simple quantitative evaluations with RUS were capable of accurately predicting the depth of the recrystallized layer, even at intermediate heat treatment times. While not an original goal of this study, the FMF developed herein demonstrates considerable potential as a tool for studying deformation-induced recrystallization kinetics in single crystal materials. Whereby such studies could quickly and easily evaluate the relative impact of chemistry, microstructural conditions, time, temperature, and deformation on the rate and extent of recrystallization. As long as all of the specimens in the study had the same geometry (a quarter-cylinder geometry is in no way a requirement), then only a single series of models varying the recrystallization depth would be required for quantifying the measured $\triangle f_R$ results.

Following a simple procedure where a single crystal plate was progressively shot-peened and specimens removed via wire EDM after sustaining various amounts of deformation, a large population of test specimens could easily be acquired. As long as the specimens are geometrically similar, then they could all be NDE by comparing measured $\triangle f_R$ results to a single ideal specimen model with various depths of recrystallization. Along with the various amounts of deformation induced by peening, selecting different

heat treatment times and temperatures would allow for a large test matrix of independent variables to be evaluated for a given alloy. Using linear interpolation between incremental FE model results, a $\triangle f_R$ trend for each mode as a function of recrystallization depth could be determined and verified with metallography of select specimens. Then using RUS measurements before and after the heat treatments, collected at room temperature because elastic properties are a function of temperature. The recrystallization depth of each specimen at each intermediated heat treatment time could be quickly quantified without considerable trouble. While these or similar methods may also be useful towards investigating the phenomenon of abnormal grain growth in fine-grain polycrystalline materials.

8.5.2 Future Work Characterizing Materials

The items discussed here as possible avenues of future work include only a few of the many possible applications and extensions of the Bayesian IMF described and demonstrated in Chapters 6 and 7. Though for the sake of brevity, only three avenues will be considered here. First is the opportunity to measure high temperature elastic properties of metals using the high temperature RUS setup as pictured in Figure 8.1. This setup includes an induction coil for heating electrically conductive materials, an infrared pyrometer for monitoring the temperature of the specimen, and piezoelectric transducers with six-inch long SiC tips. The extra long SiC tips are not heated by the induction coil and provide the necessary stand-off to both protect the transducer from the heated specimen and to keep the metallic components of the piezoelectric transducers away from the magnetic field concentrated inside the induction coil. Other than the necessity to be vigilant for transducer modes in the resonance spectra—which fortunately are easy to identify as they do not decrease in f_R when the specimen is heated—the general experimental procedures remain the same as previously discussed. While the computational procedure

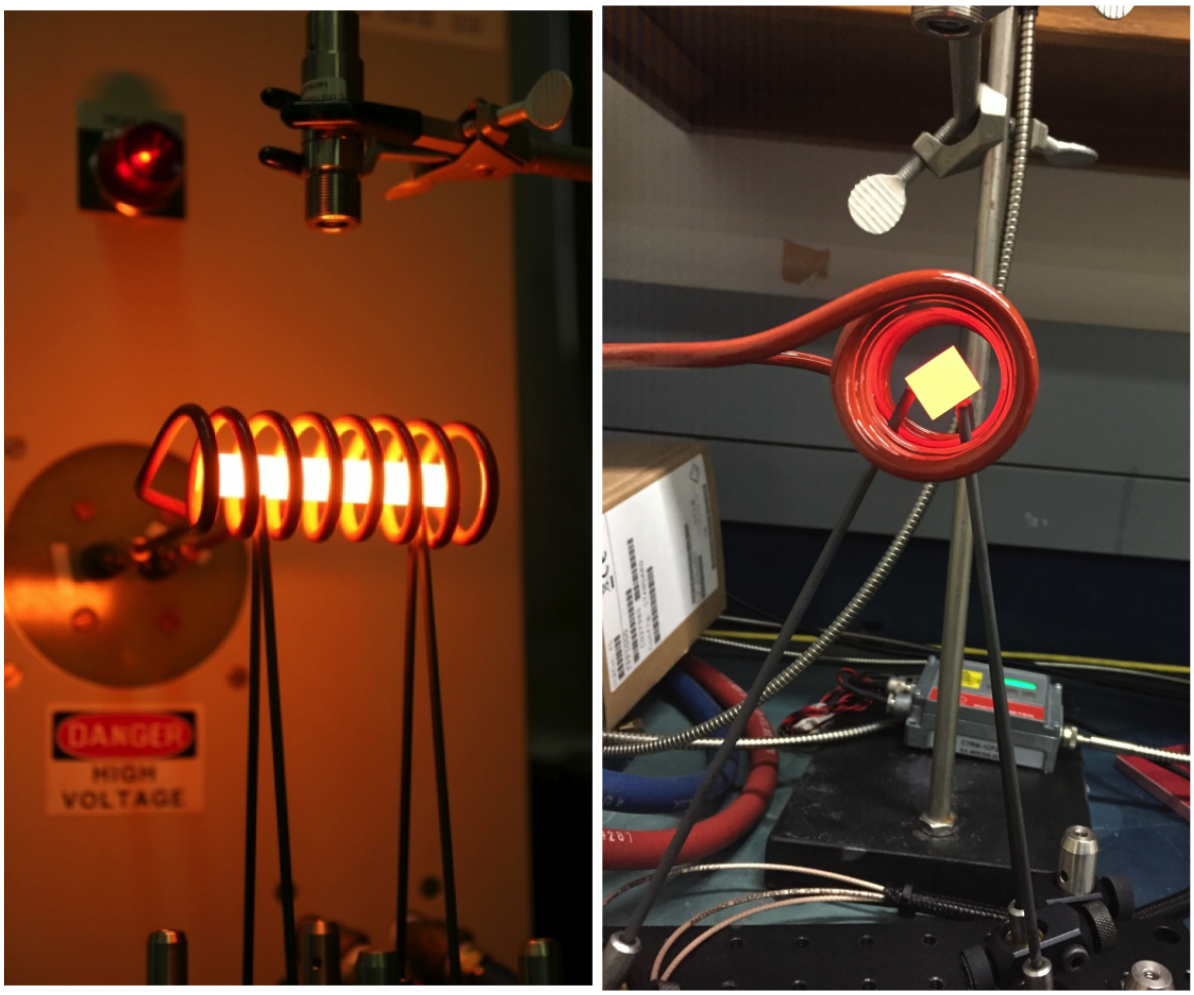

(a) (b)

Figure 8.1: Photographs of the high-temperature RUS setup consisting of an induction coil for specimen heating, piezoelectric transducers with six-inch SiC tips, and an infrared pyrometer as viewed from the (a) side with a cylindrical specimen and (b) as viewed from the front with a parallelepiped specimen.

for inversions also remain the same except for the necessity to account for the change in specimen dimensions as a result of thermal expansion.

The final two avenues of future work pertain to extensions of the CmdStan-RUS code [62], which may be realized through modifying the implementation of the forward problem. Recall that the FMF utilizes FE-based forward models, while the IMF utilizes the Rayleigh Ritz method. This distinction is important, as the computational time savings afforded by the Rayleigh Ritz method decreased the overall evaluation time of

the Bayesian IMF, which is dominated by the speed of the forward calculation. But the Rayleigh Ritz method as implemented in CmdStan-RUS is currently only capable of estimating the properties of rectangular parallelepiped geometry specimens. Without considerable trouble, the code could be modified to accept alternative specimen geometries using modified basis functions provided by Visscher et al. [19], while still maintaining the benefits of a Rayleigh Ritz approach. One specimen geometry that would considerably extend the utility of the CmdStan-RUS code described by Visscher et al. is the "sandwich" geometry, which is essentially a rectangular parallelepiped comprised of two different materials. This specimen geometry would allow for properties to be estimated from bi-layer systems, with many potential applications coming to mind. For example, one could study the elastic properties of thermal barrier coatings as applied to a superalloy substrate, with such systems being of considerable interest to turbine engine manufacturers and researchers alike. Instead, a variety of mechanical testing methods—reliant on relatively complicated experimental procedures—are often used, which provide elastic property estimates with large uncertainties [193]. Whereas CmdStan-RUS could provide estimates of superior accuracy, precision, and estimates of uncertainty. As for the range of possible specimen geometries that would be amenable to such investigations, Gladden suggests a limit of substrate-to-coating thickness of 1000:1 for the context of thin film coatings [194]. While a limit closer to 100:1 seems more practical considering the potential uncertainty in measuring fixed parameters input into the inversion such as coating thickness.

Finally, as alluded to earlier, it is completely possible to replace the Rayleigh Ritz forward model of the IMF with a FE-based forward model capability. This capability would allow for properties to be estimated directly from any arbitrarily shaped specimens, including complex geometry specimens like turbine blades. While it would not be advisable to invert properties from complex geometry specimens when simple geometries are a viable alternative, due to the fact that uncertainty in the specimen geometry will

lower the precision of the parameter estimates. There are many scenarios that fall within the realm of NDE efforts that would greatly benefit from the ability to estimate properties directly from complex geometry specimen. For example, the opportunity to quantify crystal orientation of single crystal turbine blades through inversion holds the potential to eliminate costly x-ray diffraction measurements, while also providing valuable RUS data that may be applied towards future NDE efforts. Given the current structure of the code, a FE-based forward model would increase computation time, though the relative increase would depend on the complexity of the specimen. If the time required for a full Bayesian inference is deemed unacceptable, especially considering the additional time required for FE-based evaluations, optimization methods are also available through the CmdStan-RUS code as described in the Stan user manual [60]. While approximate forward models may also be used to decrease computation time, particularly if the number of unknown parameters is increased. Various techniques could be employed for this such as Gaussian processes (a frequently used technique in Statistics for interpolation), or generalized polynomial chaos (a common method for uncertainty quantification in engineering). Overall, a FE implementation of the forward model would open the IMF to many new possible applications, with the cost of time and added complexity.

In conclusion, the broad applicability of the forward modeling framework, in conjunction with the markedly simplified and robust inverse modeling framework, together greatly expand the nondestructive evaluation and materials characterization capability of the resonant ultrasound spectroscopy technique.

Bibliography

[1] F. Firestone, "The supersonic reflectoscope, an instrument for inspecting the interior of solid parts by means of sound waves," *The Journal of the Acoustical Society of America*, vol. 17, no. 3, pp. 287–299, 1946.

[2] W. P. Mason and H. J. McSkimin, "Attenuation and Scattering of High Frequency Sound Waves in Metals and Glasses," *The Journal of the Acoustical Society of America*, vol. 19, no. 3, pp. 464–473, 1947.

[3] W. P. Mason and H. J. McSkimin, "Energy losses of sound waves in metals due to scattering and diffusion," *Journal of Applied Physics*, vol. 19, no. 10, pp. 940–946, 1948.

[4] R. M. Bozorth, W. P. Mason, and H. J. McSkimin, "Frequency Dependence of Elastic Constants and Losses in Nickel," *Bell System Technical Journal*, vol. 30, no. 4, pp. 970–989, Oct 1951.

[5] W. P. Mason and H. J. McSkimin, "Mechanical properties of polymers at ultrasonic frequencies," *Bell Labs Technical Journal*, vol. 31, no. 1, pp. 122–171, 1952.

[6] H. J. McSkimin, "Measurement of Elastic Constants at Low Temperatures by Means of Ultrasonic Waves- Data for Silicon and Germanium. Single Crystals, and for Fused Silica," *Journal of applied physics*, vol. 6, no. 8, pp. 413–418, 1953.

[7] W. P. Mason, "Physical Acoustics and the Properties of Solids," *The Journal of the Acoustical Society of America*, vol. 28, no. 6, pp. 1197–1206, 1956.

[8] D. B. Fraser and R. C. LeCraw, "Novel method of measuring elastic and anelastic properties of solids," *Review of Scientific Instruments*, vol. 35, no. 9, pp. 1113–1115, 1964.

[9] D. Speiser and K. Williams, *Discovering the Principles of Mechanics 1600-1800: Essays by David Speiser*. Springer Science & Business Media, 2008, vol. 1.

[10] Y. Sato and T. Usame, "Basic study on the oscillation of a homogeneous elastic sphere," *Geophysical Magazine*, vol. 31, no. 1, 1962.

[11] O. L. Anderson, "Rectangular parallelepiped resonanceA technique of resonance ultrasound and its applications to the determination of elasticity at high temperatures," *The Journal of the Acoustical Society of America*, vol. 91, no. 4, pp. 2245–2253, 1992.

[12] R. Holland, "Resonant Properties of Piezoelectric Ceramic Rectangular Parallelepipeds," *The Journal of the Acoustical Society of America*, vol. 43, no. 5, pp. 988–997, May 1968.

[13] H. H. Demarest, "Cube-resonance method to determine the elastic constants of solids," *The Journal of the Acoustical Society of America*, vol. 49, no. 3B, pp. 768–775, 1971.

[14] E. Mochizuki, "Sphere-resonance method to determine elastic constants of crystal," *Journal of Applied Physics*, vol. 63, no. 12, pp. 5668–5673, 1988.

[15] I. Ohno, "Free vibration of a rectangular parallelepiped crystal and its application to determination of elastic constants of orthorhombic crystals," *Journal of Physics of the Earth*, vol. 24, pp. 255–379, 1976.

[16] I. Ohno, S. Yamamoto, O. Anderson, and J. Noda, "Determination of elastic constants of trigonal crystals by the rectangular parallelepiped resonance method," *Journal of Physics and Chemistry of Solids*, vol. 47, no. 12, pp. 1103–1108, 1986.

[17] A. Migliori, W. M. Visscher, S. E. Brown, Z. Fisk, S.-W. Cheong, B. Alten, E. T. Ahrens, K. A. Kubat-Martin, J. D. Maynard, Y. Huang, D. R. Kirk, K. A. Gillis, H. K. Kim, and M. H. W. Chan, "Elastic constants and specific-heat measurements on single crystals of La2CuO4," *Physical Review B*, vol. 41, no. 4, pp. 2098–2102, feb 1990.

[18] A. Migliori and Z. Fisk, "Crystals and ultrasound, old-fashioned materials science," *Los Alamos Science*, no. 21, pp. 182–194, 1993.

[19] W. M. Visscher, A. Migliori, T. M. Bell, and R. A. Reinert, "On the normal modes of free vibration of inhomogeneous and anisotropic elastic objects," *The Journal of the Acoustical Society of America*, vol. 90, no. 4, pp. 2154–2162, Oct 1991.

[20] L. Ostrovsky, A. Lebedev, A. Matveyev, A. Potapov, A. Sutin, I. Soustova, and P. Johnson, "Application of three-dimensional resonant acoustic spectroscopy method to rock and building materials," *The Journal of the Acoustical Society of America*, vol. 110, no. 4, p. 1770, 2001.

[21] A. Wolfenden, *Dynamic elastic modulus measurements in materials.* ASTM International, 1990, no. 1045.

[22] A. V. Lebedev, L. A. Ostrovskii, A. M. Sutin, I. A. Soustova, and P. A. Johnson, "Resonant acoustic spectroscopy at low Q factors," *Acoustical Physics*, vol. 49, no. 1, pp. 81–87, 2003.

[23] S. Siegel, "A Review of Supersonic Methods for Measuring Elastic and Dissipative Properties of Solids," vol. 16, no. 1, pp. 26–30, 1944.

[24] S. Sato, K. Inagaki, V. E. Gusev, and O. B. Wright, "Resonant ultrasound spectroscopy using optical excitation and detection," *Proceedings of the 10th international conference on photoacoustic and photothermal phenomena*, vol. 463, no. 1999, pp. 424–426, 1999.

[25] D. H. Hurley, S. J. Reese, S. K. Park, Z. Utegulov, J. R. Kennedy, and K. L. Telschow, "In situ laser-based resonant ultrasound measurements of microstructure mediated mechanical property evolution," *Journal of Applied Physics*, vol. 107, no. 6, pp. 063 510–1–5, 2010.

[26] P. Sedlák, H. Seiner, J. Zídek, M. Janovská, and M. Landa, "Determination of All 21 Independent Elastic Coefficients of Generally Anisotropic Solids by Resonant Ultrasound Spectroscopy: Benchmark Examples," *Experimental Mechanics*, vol. 54, no. 6, pp. 1073–1085, 2014.

[27] H. Ogi, K. Sato, T. Asada, and M. Hirao, "Complete mode identification for resonance ultrasound spectroscopy," *Journal of the Acoustical Society of America*, vol. 112, no. 6, pp. 2553–2557, 2002.

[28] L. W. Schmerr, *Fundamentals of Ultrasonic Nondestructive Evaluation*, ser. Springer Series in Measurement Science and Technology. Cham: Springer International Publishing, 2016.

[29] H. M. Ledbetter and R. P. Reed, "Elastic Properties of Metals and Alloys: Nickel and Iron-Nickel Alloys," *Journal of Physical and Chemical Reference Data*, vol. 2, no. 1973, pp. 531–618, 1973.

[30] J. Powers and F. Kremkau, "Medical ultrasound systems," *Interface Focus*, vol. 1, no. 4, pp. 477–489, 2011.

[31] F. Uzun and A. N. Bilge, "Immersion ultrasonic technique for investigation of total welding residual stress," *Procedia Engineering*, vol. 10, pp. 3098–3103, 2011.

[32] E. Blomme, D. Bulcaen, and F. Declercq, "Air-coupled ultrasonic nde: experiments in the frequency range 750 khz–2 mhz," *NDT & e International*, vol. 35, no. 7, pp. 417–426, 2002.

[33] A. Migliori and J. Sarrao, *Resonant ultrasound spectroscopy: applications to physics, materials measurements, and nondestructive evaluation.* New York: Wiley-Interscience, 1997.

[34] R. G. Leisure and F. A. Willis, "Resonant ultrasound spectroscopy," *Journal of Physics: Condensed Matter*, vol. 9, no. 28, pp. 6001–6029, Jul 1997.

[35] H. Ogi, H. Ledbetter, S. Kim, and M. Hirao, "Contactless mode-selective resonance ultrasound spectroscopy: Electromagnetic acoustic resonance," *The Journal of the Acoustical Society of America*, vol. 106, no. 2, pp. 660–665, 1999.

[36] J. L. Sarrao, S. R. Chen, W. M. Visscher, M. Lei, U. F. Kocks, and A. Migliori, "Determination of the crystallographic orientation of a single crystal using resonant ultrasound spectroscopy," *Review of Scientific Instruments*, vol. 65, no. 6, pp. 2139–2140, 1994.

[37] G. Li and J. R. Gladden, "High temperature resonant ultrasound spectroscopy: a review," *International Journal of Spectroscopy*, vol. 2010, pp. 1–13, 2010.

[38] A. Migliori, J. Sarrao, W. M. Visscher, T. Bell, M. Lei, Z. Fisk, and R. Leisure, "Resonant ultrasound spectroscopic techniques for measurement of the elastic moduli of solids," *Physica B: Condensed Matter*, vol. 183, no. 1-2, pp. 1–24, Jan 1993.

[39] M. Radovic, E. Lara-Curzio, and L. Riester, "Comparison of different experimental techniques for determination of elastic properties of solids," *Material Science and Engineering A*, vol. 368, no. 1-2, pp. 56–70, Mar 2004.

[40] J. D. Maynard, "The use of piezoelectric film and ultrasound resonance to determine the complete elastic tensor in one measurement," *Journal of the Acoustical Society of America*, vol. 91, no. 3, pp. 1754–1762, 1992.

[41] P. S. Spoor, "Elastic properties of novel materials using pvdf film and resonance ultrasound spectroscopy," Pennsylvania State Univ. Dept. of Physics, Tech. Rep. ADA328037, 1997.

[42] J. Maynard, "Resonant ultrasound spectroscopy," *Physics Today*, vol. 49, no. 1, pp. 26–31, 1996.

[43] J. Plesek, R. Kolman, and M. Landa, "Using finite element method for the determination of elastic moduli by resonant ultrasound spectroscopy," *The Journal of the Acoustical Society of America*, vol. 116, no. 1, pp. 282–287, 2004.

[44] G. Liu and J. D. Maynard, "Measuring elastic constants of arbitrarily shaped samples using resonant ultrasound spectroscopy," *The Journal of the Acoustical Society of America*, vol. 131, no. 3, pp. 2068–2078, 2012.

[45] R. Schwarz and J. Vuorinen, "Resonant ultrasound spectroscopy: applications, current status and limitations," *Journal of Alloys and Compounds*, vol. 310, no. 1-2, pp. 243–250, Sep 2000.

[46] B. J. Zadler, J. H. L. Le Rousseau, J. A. Scales, and M. L. Smith, "Resonant ultrasound spectroscopy: theory and application," *Geophysical Journal International*, vol. 156, no. 1, pp. 154–169, Jan 2004.

[47] B. Bales, B. R. Goodlet, W. C. Lenthe, L. Petzold, and T. M. Pollock, "Bayesian Inference of Elastic Properties with Resonant Ultrasound Spectroscopy," *Journal of the Acoustical Society of America*, vol. 143, no. 1, pp. 71–83, 2018.

[48] E. Maire and P. J. Withers, "Quantitative X-ray tomography," *International Materials Reviews*, vol. 59, no. 1, pp. 1–43, 2014.

[49] "E2534-15: Standard practice for Process Compensated Resonance Testing via swept sine input for metallic and non-metallic parts," West Conshohocken, PA, pp. 1–8, 2015.

[50] "E2001-98: Standard guide for resonant ultrasound spectroscopy for defect detection in both metallic and non-metallic parts," West Conshohocken, PA, pp. 1–7, 1998.

[51] M. C. Remillieux, T. J. Ulrich, C. Payan, J. Rivière, C. R. Lake, and P.-Y. Le Bas, "Resonant ultrasound spectroscopy for materials with high damping and samples of arbitrary geometry," *Journal of Geophysical Research: Solid Earth*, vol. 120, no. 7, pp. 4898–4916, Jul 2015.

[52] S. Bernard, Q. Grimal, and P. Laugier, "Accurate measurement of cortical bone elasticity tensor with resonant ultrasound spectroscopy," *Journal of the mechanical behavior of biomedical materials*, vol. 18, pp. 12–19, 2013.

[53] S. Bernard, Q. Grimal, and P. Laugier, "Resonant ultrasound spectroscopy for viscoelastic characterization of anisotropic attenuative solid materials," *The Journal of the Acoustical Society of America*, vol. 135, no. 5, pp. 2601–2613, 2014.

[54] L. Hunter, "Process compensated resonance testing JT8D-219 1st stage blades," in *4th European Workshop on Reliability of NDE*, Berlin, 2009, pp. 1–26.

[55] B. R. Goodlet, L. H. Rettberg, and T. M. Pollock, "Resonant ultrasound spectroscopy for defect detection in single crystal superalloy castings," in *Superalloys 2016 13th Int. Symp.*, 2016, pp. 303–311.

[56] B. R. Goodlet, C. J. Torbet, E. J. Biedermann, L. M. Jauriqui, J. C. Aldrin, and T. M. Pollock, "Forward models for extending the mechanical damage evaluation capability of resonant ultrasound spectroscopy," *Ultrasonics*, vol. 77, pp. 183–196, 2017.

[57] L. Rettberg, B. Goodlet, and T. Pollock, "Detecting recrystallization in a single crystal Ni-base alloy using resonant ultrasound spectroscopy," *NDT & E International*, vol. 83, pp. 68–77, Oct 2016.

[58] B. R. Goodlet, L. Mills, B. Bales, M.-A. Charpagne, S. P. Murray, W. C. Lenthe, L. Petzold, and T. M. Pollock, "Elastic Properties of Novel Co- and CoNi-Based Superalloys Determined through Bayesian Inference and Resonant Ultrasound Spectroscopy," *Metallurgical and Materials Transactions A*, vol. 49, no. 6, pp. 2324–2339, Jun 2018.

[59] R. Neal, *MCMC using Hamiltonian dynamics*. New York: Chapman & Hall / CRC Press, 2011, ch. 5, pp. 113–163.

[60] Stan Development Team, *Stan Modeling Language User's Guide and Reference Manual, Version 2.15.0*, 2016. [Online]. Available: http://mc-stan.org/

[61] Stan Development Team, *CmdStan Interface User's Guide, CmdStan Version 2.16.0*, 2017. [Online]. Available: http://mc-stan.org/

[62] B. Bales, B. Goodlet, and W. Lenthe, "CmdStan-RUS - a Custom Distribution of the Open-Source Probabilistic Programing Language: Stan," Santa Barbara CA, 2017. [Online]. Available: https://github.com/bbbales2/cmdstan-rus

[63] A. Bower, *Applied mechanics of solids*. Boca Ratton: CRC Press, 2010.

[64] N. W. Tschoegl, "Introductory Concepts," in *The Phenomenological Theory of Linear Viscoelastic Behavior*. Berlin, Heidelberg: Springer Berlin Heidelberg, 1989, pp. 1–34.

[65] W. D. Callister and D. G. Rethwisch, *Materials science and engineering: an introduction*, 7th ed. New York: John Wiley & Sons, Inc., 2007, vol. 94.

[66] H. Seiner, L. Bodnárová, P. Sedlák, M. Janeček, O. Srba, R. Král, and M. Landa, "Application of ultrasonic methods to determine elastic anisotropy of polycrystalline copper processed by equal-channel angular pressing," *Acta Materialia*, vol. 58, no. 1, pp. 235–247, 2010.

[67] F. Larson and A. Zarkades, "Properties of textured titanium alloys," Battelle Columbus Labs, Ohio Metals and Ceramics Information Center, Tech. Rep., 1974.

[68] C. A. Stickels and P. R. Mould, "The use of young's modulus for predicting the plastic-strain ratio of low-carbon steel sheets," *Metallurgical and Materials Transactions B*, vol. 1, no. 5, pp. 1303–1312, May 1970.

[69] G. Davies, D. Goodwill, and J. Kallend, "Elastic and plastic anisotropy in sheets of cubic metals," *Metallurgical and Materials Transactions B*, vol. 3, no. 6, pp. 1627–1631, 1972.

[70] P. Chadwick, M. Vianello, and S. C. Cowin, "A new proof that the number of linear elastic symmetries is eight," *Journal of the Mechanics and Physics of Solids*, vol. 49, no. 11, pp. 2471–2492, 2001.

[71] M. Moakher and A. N. Norris, "The closest elastic tensor of arbitrary symmetry to an elasticity tensor of lower symmetry," *Journal of Elasticity*, vol. 85, no. 3, pp. 215–263, 2006.

[72] P. Vannucci, "General anisotropic elasticity," in *Anisotropic Elasticity*. Springer, 2018, pp. 19–73.

[73] J. Zhao, J. Qiu, and H. Ji, "Reconstruction of the nine stiffness coefficients of composites using a laser generation based imaging method," *Composites Science and Technology*, vol. 126, pp. 27–34, 2016.

[74] L. B. Freund and S. Suresh, *Thin film materials: stress, defect formation and surface evolution*. Cambridge University Press, 2004.

[75] D. Tromans, "Elastic Anisotropy of HCP Metal Crystals and Polycrystals," *International Journal of Research and Reviews in Applied Sciences*, vol. 6, pp. 462–483, Mar 2011.

[76] J. Han, A. Bertram, J. Olschewski, W. Hermann, H.-G. Sockel, J. Hana, A. Bertrama, J. Olschewskia, and H.-g. Sockep, "Identification of elastic constants of alloys with sheet and fibre textures based on resonance measurements and finite element analysis," *Materials Science and Engineering*, vol. 191, pp. 105–111, 1995.

[77] R. Adams and P. Cawley, "A review of defect types and nondestructive testing techniques for composites and bonded joints," *NDT & E International*, vol. 21, no. 4, pp. 208–222, Aug 1988.

[78] J. E. Vuorinen, R. B. Schwarz, and C. McCullough, "Elastic constants of an aluminumalumina unidirectional composite," *The Journal of the Acoustical Society of America*, vol. 108, no. 2, pp. 574–579, 2000.

[79] J. T. Browaeys and S. Chevrot, "Decomposition of the elastic tensor and geophysical applications," *Geophysical Journal International*, vol. 159, no. 2, pp. 667–678, 2004.

[80] R. C. Reed, *The Superalloys*. Cambridge: Cambridge University Press, 2006.

[81] G. Simmons, H. Wang *et al.*, "Single crystal elastic constants and calculated aggregate properties," 1971.

[82] M. J. P. Musgrave, "The propagation of elastic waves in crystals and other anisotropic media," *Reports on Progress in Physics*, vol. 22, no. 1, pp. 74–96, Jan 1959.

[83] N. Nakamura, H. Ogi, and M. Hirao, "Resonance ultrasound spectroscopy with laser-Doppler interferometry for studying elastic properties of thin films." *Ultrasonics*, vol. 42, pp. 491–494, Apr 2004.

[84] T. Richards, "Preferred orientation in non-ferrous metals," *Progress in Metal Physics*, vol. 1, pp. 281–305, Jan 1949.

[85] D. H. Hurley, S. J. Reese, and F. Farzbod, "Application of laser-based resonant ultrasound spectroscopy to study texture in copper," *Journal of Applied Physics*, vol. 111, no. 5, pp. 053 527–1–6, 2012.

[86] S. Spearing, "Materials issues in microelectromechanical systems (MEMS)," *Acta Materialia*, vol. 48, no. 1, pp. 179–196, Jan 2000.

[87] M. Nygårds, "Number of grains necessary to homogenize elastic materials with cubic symmetry," *Mechanics of Materials*, vol. 35, no. 11, pp. 1049–1057, nov 2003.

[88] C. Zener, "Contributions to the Theory of Beta-Phase Alloys," *Physical Review*, vol. 71, no. 12, pp. 846–851, Jun 1947.

[89] R. Hill, "The Elastic Behaviour of a Crystalline Aggregate," *Proceedings of the Physical Society. Section A*, vol. 65, no. 5, pp. 349–354, 1952.

[90] Z. Hashin, "The Elastic Moduli of Heterogeneous Materials," *Journal of Applied Mechanics*, no. 2, pp. 143–150, 1962.

[91] E. Kröner, "Elastic moduli of perfectly disordered composite materials," *Journal of the Mechanics and Physics of Solids*, vol. 15, pp. 319–329, 1967.

[92] B. Gairola and E. Kröner, "A simple formula for calculating the bounds and the self-consistent value of the shear modulus of a polycrystalline aggregate of cubic crystals," *International Journal of Engineering Science*, vol. 19, no. 6, pp. 865–869, Jan 1981.

[93] H. A. Kuhn and H. G. Sockel, "Comparison between experimental determination and calculation of elastic properties of nickel-base superalloys between 25 and 1200 C," *Physica Status Solidi (a)*, vol. 110, no. 2, pp. 449–458, Dec 1988.

[94] H.-A. Kuhn and H.-G. Sockel, "Elastic properties of textured and directionally solidified nickel-based superalloys between 25 and 1200 C," *Materials Science and Engineering: A*, vol. 112, pp. 117–126, Jun 1989.

[95] H. A. Kuhn and H. G. Sockel, "Contributions of the Different Phases of Two Nickel-Base Superalloys to the Elastic Behaviour in a Wide Temperature Range," *Physica Status Solidi (a)*, vol. 119, no. 1, pp. 93–105, May 1990.

[96] F. E. Stanke, "A unified theory for elastic wave propagation in polycrystalline materials," *The Journal of the Acoustical Society of America*, vol. 75, no. 3, pp. 665–681, 1984.

[97] H. Ledbetter, "Monocrystal-polycrystal elastic-constant models," in *Dynamic elastic modulus measurements in materials, ASTM STP 1045*, A. Wolfenden, Ed. Philadelphia: ASTM International, 1990, pp. 135–148.

[98] D. Siebörger, H. Knake, and U. Glatzel, "Temperature dependence of the elastic moduli of the nickel-base superalloy CMSX-4 and its isolated phases," *Materials Science and Engineering: A*, vol. 298, no. 1-2, pp. 26–33, Jan 2001.

[99] D. Antonangeli, M. Krisch, G. Fiquet, J. Badro, D. L. Farber, A. Bossak, and S. Merkel, "Aggregate and single-crystalline elasticity of hcp cobalt at high pressure," *Physical Review B*, vol. 72, no. 13, pp. 134 303–1–7, Oct 2005.

[100] D. Cline, *Variational Principles in Classical Mechanics*. Rochester, NY: University of Rochester River Campus Libraries, Aug 2017.

[101] S. Bernard, G. Marrelec, P. Laugier, and Q. Grimal, "Bayesian normal modes identification and estimation of elastic coefficients in resonant ultrasound spectroscopy," *Inverse Problems*, vol. 31, no. 6, pp. 065 010–1–23, 2015.

[102] E. P. Papadakis, "Physical acoustics and microstructure of iron alloys," *International Materials Review*, vol. 29, no. 1, pp. 1–24, Jan 1984.

[103] D. Rowenhorst, A. Rollett, G. Rohrer, M. Groeber, M. Jackson, P. J. Konijnenberg, and M. De Graef, "Consistent representations of and conversions between 3d rotations," *Modelling and Simulation in Materials Science and Engineering*, vol. 23, no. 8, pp. 083 501–1–17, 2015.

[104] P. G. Callahan, M. Echlin, T. M. Pollock, S. Singh, and M. De Graef, "Three-dimensional texture visualization approaches: theoretical analysis and examples," *Journal of Applied Crystallography*, vol. 50, no. 2, pp. 430–440.

[105] A. Pilchak and J. Williams, "Microstructure and texture evolution during friction stir processing of fully lamellar Ti-6Al-4V," *Metallurgical and Materials Transactions A*, vol. 42, no. 3, pp. 773–794, 2011.

[106] D. Rosca, A. Morawiec, and M. D. Graef, "A new method of constructing a grid in the space of 3d rotations and its applications to texture analysis," *Modelling and Simulation in Materials Science and Engineering*, vol. 22, no. 7, pp. 075 013–1–17, 2014.

[107] F. Zhang, F. Xie, S. Chen, and Y. Chang, "Predictions of Titanium Alloy Properties Using Thermodynamic Modeling Tools," *Journal of Materials*, vol. 14, no. Dec, pp. 717–721, 2005.

[108] R. Ding, Z. Guo, and a. Wilson, "Microstructural evolution of a Ti6Al4V alloy during thermomechanical processing," *Materials Science and Engineering: A*, vol. 327, no. 2, pp. 233–245, Apr 2002.

[109] F. C. Campbell, *Elements of metallurgy and engineering alloys*. ASM International, 2008.

[110] S. Zherebtsov, G. Salishchev, R. Galeyev, O. Valiakhmetov, S. Y. Mironov, and S. Semiatin, "Production of submicrocrystalline structure in large-scale ti–6al–4v billet by warm severe deformation processing," *Scripta Materialia*, vol. 51, no. 12, pp. 1147–1151, 2004.

[111] K. Harris, G. Erickson, and R. Schwer, "MAR M 247 Derivations CM 247 LC DS Alloy, CMSX® Single Crystal Alloys, Properties and Performance," in *5th International Symposium on Superalloys*, M. Gell, C. Kortovich, R. Bricknell, W. Kent, and J. Radavich, Eds., 1984, pp. 221–230.

[112] R. Reed, N. Matan, D. Cox, M. Rist, and C. Rae, "Creep of cmsx-4 superalloy single crystals: effects of rafting at high temperature," *Acta Materialia*, vol. 47, no. 12, pp. 3367–3381, 1999.

[113] D. C. Cox, B. Roebuck, C. M. F. Rae, and R. C. Reed, "Recrystallisation of single crystal superalloy CMSX4," *Materials Science and Technology*, vol. 19, no. 4, pp. 440–446, Apr 2003.

[114] P. Caron and T. Khan, "Evolution of Ni-based superalloys for single crystal gas turbine blade applications," *Aerospace Science and Technology*, vol. 3, no. 8, pp. 513–523, Dec 1999.

[115] A. F. Giamei and D. L. Anton, "Rhenium additions to a ni-base superalloy: Effects on microstructure," *Metallurgical Transactions A*, vol. 16, no. 11, pp. 1997–2005, Nov 1985.

[116] J. Sato, T. Omori, K. Oikawa, I. Ohnuma, R. Kainuma, and K. Ishida, "Cobalt-base high-temperature alloys," *Science*, vol. 312, no. 5770, pp. 90–91, 2006.

[117] T. M. Pollock, J. Dibbern, M. Tsunekane, J. Zhu, and A. Suzuki, "New co-based γ-γ' high-temperature alloys," *JOM*, vol. 62, no. 1, pp. 58–63, Jan 2010.

[118] M. S. Titus, A. Suzuki, and T. M. Pollock, "Creep and directional coarsening in single crystals of new γ–γ cobalt-base alloys," *Scripta Materialia*, vol. 66, no. 8, pp. 574–577, 2012.

[119] R. W. Jackson, M. S. Titus, M. R. Begley, and T. M. Pollock, "Thermal expansion behavior of new co-based alloys and implications for coatings," *Surface and Coatings Technology*, vol. 289, pp. 61–68, 2016.

[120] M. S. Titus, Y. M. Eggeler, A. Suzuki, and T. M. Pollock, "Creep-induced planar defects in L12-containing Co-and CoNi-base single-crystal superalloys," *Acta Materialia*, vol. 82, pp. 530–539, 2015.

[121] Y. M. Eggeler, M. S. Titus, A. Suzuki, and T. M. Pollock, "Creep deformation-induced antiphase boundaries in L12-containing single-crystal cobalt-base superalloys," *Acta Materialia*, vol. 77, pp. 352–359, 2014.

[122] B. C. Wilson, J. A. Hickman, and G. E. Fuchs, "The effect of solution heat treatment on a single-crystal ni-based superalloy," *JOM*, vol. 55, no. 3, pp. 35–40, Mar 2003.

[123] T. Tinga, W. a. M. Brekelmans, and M. G. D. Geers, "Cube slip and non-Schmid effects in single crystal Ni-base superalloys," *Modelling and Simulation in Materials Science and Engineering*, vol. 18, no. 1, pp. 015 005–1–31, 2009.

[124] T. M. Pollock and S. Tin, "Nickel-Based Superalloys for Advanced Turbine Engines: Chemistry, Microstructure, and Properties," *Journal of Propulsion and Power*, vol. 22, no. 2, pp. 361–374, 2006.

[125] F. X. Kayser and C. Stassis, "The elastic constants of Ni3Al at 0 and 23.5 C," *Physica Status Solidi (a)*, vol. 64, no. 1, pp. 335–342, Mar 1981.

[126] A. Migliori and J. Maynard, "Implementation of a modern resonant ultrasound spectroscopy system for the measurement of the elastic moduli of small solid specimens," *Review of Scientific Instruments*, vol. 76, no. 2005, pp. 1–7, 2005.

[127] J. Aldrin, L. Jauriqui, and L. Hunter, "Models for process compensated resonant testing (PCRT) of silicon nitride balls," in *The 39th Annual Review of Progress in Quantitative Nondestructive Evaluation*, vol. 1511, 2013, pp. 1393–1400.

[128] E. Schreiber, O. L. Anderson, and N. Soga, *Elastic constants and their measurement.* New York : McGraw-Hill, 1973.

[129] E. Mochizuki, "Application of group theory to free oscillations of an anisotropic rectangular parallelepiped." *Journal of Physics of the Earth*, vol. 35, no. 2, pp. 159–170, 1987.

[130] J. Heffernan, L. Jauriqui, E. Biedermann, A. Mayes, R. Livings, B. Goodlet, and S. Mazdiyansi, "Process Compensated Resonance Testing Models for Quantification of Creep Damage in Single Crystal Nickel-based Superalloys," *Materials Evaluation*, vol. 75, no. 7, pp. 937–948.

[131] A. Mayes, L. Jauriqui, E. Biedermann, J. Heffernan, R. Livings, J. C. Aldrin, B. Goodlet, and S. Mazdiyasni, "Part-to-Itself Model Inversion in Process Compensated Resonance Testing," in *44th Annual Review of Progress in Quantitative Nondestructive Evaluation*, Provo, UT, 2017.

[132] J. Yi, C. Torbet, Q. Feng, T. Pollock, and J. Jones, "Ultrasonic fatigue of a single crystal Ni-base superalloy at 1000C," *Materials Science and Engineering: A*, vol. 443, pp. 142–149, Jan 2007.

[133] A. Kumar, C. J. Torbet, T. M. Pollock, and J. Wayne Jones, "In situ characterization of fatigue damage evolution in a cast Al alloy via nonlinear ultrasonic measurements," *Acta Materialia*, vol. 58, no. 6, pp. 2143–2154, Apr 2010.

[134] J. H. Cantrell and W. T. Yost, "Nonlinear ultrasonic characterization of fatigue microstructures," *International Journal of Fatigue*, vol. 23, pp. 487–490, 2001.

[135] J. H. Cantrell, "Substructural organization , dislocation plasticity and harmonic generation in cyclically stressed wavy slip metals," *Proceedings of the Royal Society of London A*, no. 460, pp. 757–780, 2004.

[136] J. H. Cantrell, "Nonlinear dislocation dynamics at ultrasonic frequencies," *Journal of Applied Physics*, vol. 105, no. 4, pp. 043 520–1–7, 2009.

[137] T. Courtney, *Mechanical behavior of materials*, 2nd ed. Long Grove, IL: Waveland Press, 2005.

[138] A. Cocks and M. Ashby, "On creep fracture by void growth," *Progress in Material Science*, vol. 27, no. 3-4, pp. 189–244, Jan 1982.

[139] T. Pollock and A. Argon, "Directional coarsening in nickel-base single crystals with high volume fractions of coherent precipitates," *Acta Metallurgica et Materialia*, vol. 42, no. 6, pp. 1859–1874, 1994.

[140] S. Socrate and D. Parks, "Numerical determination of the elastic driving force for directional coarsening in Ni-superalloys," *Acta Metallurgica et Materialia*, vol. 41, no. 7, pp. 2185–2209, Jul 1993.

[141] C. L. Brundidge, D. van Drasek, B. Wang, and T. M. Pollock, "Structure refinement by a liquid metal cooling solidification process for single-crystal nickel-base superalloys," *Metallurgical and Materials Transactions A*, vol. 43, no. 3, pp. 965–976, Mar 2012.

[142] J. Miao, T. Pollock, and J. Jones, "Very high cycle fatigue behavior of nickel-based superalloy René 88DT at 593 C," *International Conference on Very High Cycle Fatigue*, pp. 445–450, 2007.

[143] A. G. Evans, M. Y. He, A. Suzuki, M. Gigliotti, B. Hazel, and T. M. Pollock, "A mechanism governing oxidation-assisted low-cycle fatigue of superalloys," *Acta Materialia*, vol. 57, no. 10, pp. 2969–2983, 2009.

[144] A. Suzuki, M. Gigliotti, B. Hazel, D. Konitzer, and T. Pollock, "Crack progression during sustained-peak low-cycle fatigue in single-crystal ni-base superalloy rené n5," *Metallurgical and Materials Transactions A*, vol. 41, no. 4, pp. 947–956, 2010.

[145] A. Shyam, C. J. Torbet, S. Jha, J. M. Larsen, M. J. Caton, C. Szczepanski, T. M. Pollock, and J. W. Jones, "Development of ultrasonic fatigue for rapid, High temperature fatigue studies in turbine engine materials," in *Superalloys 2004 Tenth Int. Symp.*, K. Green, T. Pollock, H. Harada, T. Howson, R. Reed, J. Schirra, and S. Walston, Eds. TMS, 2004, pp. 259–268.

[146] E. Biedermann, L. M. Jauriqui, J. C. Aldrin, B. R. Goodlet, T. M. Pollock, C. J. Torbet, and S. Mazdiyasni, "Resonance ultrasound spectroscopy forward modeling and inverse characterization of nickel-based superalloys," in *41st Annual Review of Progress in Quantitative Nondestructive Evaluation*, Boise, 2014, pp. 835–844.

[147] A. Yoneda, "Intrinsic eigenvibration frequency in the resonant ultrasound spectroscopy: Evidence for a coupling vibration between a sample and transducers," *Earth, Planets and Space*, vol. 54, pp. 763–770, 2002.

[148] G. Kaplan, T. W. Darling, and K. R. McCall, "Resonant ultrasound spectroscopy and homogeneity in polycrystals," *Ultrasonics*, vol. 49, no. 1, pp. 139–142, Jan 2009.

[149] "Abaqus/CAE Version 6.12-1 User Manual," 2012.

[150] A. Migliori and T. W. Darling, "Resonant ultrasound spectroscopy for materials studies and non-destructive testing," *Ultrasonics*, vol. 34, no. 2-5, pp. 473–476, jun 1996.

[151] K. Flynn and M. Radovic, "Evaluation of defects in materials using resonant ultrasound spectroscopy," *Journal of Materials Science*, vol. 46, no. 8, pp. 2548–2556, Apr 2011.

[152] T. Ichitsubo, H. Ogi, M. Hirao, K. Tanaka, M. Osawa, T. Yokokawa, T. Kobayashi, and H. Harada, "Elastic constant measurement of Ni-base superalloy with the RUS and mode selective EMAR methods," *Ultrasonics*, vol. 40, no. 1-8, pp. 211–215, may 2002.

[153] M. S. Titus, A. Suzuki, and T. M. Pollock, "High Temperature Creep of New L12 Containing Cobalt-Base Superalloys," in *Superalloys 2012*, E. Huron, R. Reed, M. Hardy, M. Mills, R. Montero, P. Portella, and J. Telesman, Eds. Hoboken, NJ, USA: John Wiley & Sons, Inc., Oct 2012, pp. 823–832.

[154] D. Goldschmidt, U. Paul, and P. Sahm, "Porosity Clusters and Recrystallization in Single-Crystal Components," in *Superalloys 1992 (Seventh International Symposium)*, S. Antolovich, R. Stusrud, R. MacKay, D. Anton, T. Khan, R. Kissinger, and D. Klarstrom, Eds. The Minerals, Metals & Materials Society, 1992, pp. 155–164.

[155] J. Meng, T. Jin, X. Sun, and Z. Hu, "Effect of surface recrystallization on the creep rupture properties of a nickel-base single crystal superalloy," *Materials Science and Engineering: A*, vol. 527, no. 23, pp. 6119–6122, Sep 2010.

[156] N. K. Arakere, S. Siddiqui, S. Magnan, F. Ebrahimi, and L. E. Forero, "Investigation of Three-Dimensional Stress Fields and Slip Systems for FCC Single-Crystal Superalloy Notched Specimens," *Journal of Engineering for Gas Turbines and Power*, vol. 127, no. 3, pp. 629–637, 2005.

[157] F. L. Versnyder and M. E. Shank, "The development of columnar grain and single crystal high temperature materials through directional solidification," *Materials Science and Engineering*, vol. 6, pp. 213–247, 1970.

[158] J. Winter, K. Lipetzky, and R. Green, "Optimization of x-ray Techniques for Nondestructive Characterization of Single Crystal Turbine Blades," *MRS Proceedings*, vol. 591, pp. 3–14, Jan 1999.

[159] E. Maire and P. J. Withers, "Quantitative X-ray tomography," *International Materials Reviews*, vol. 59, no. 1, pp. 1–43, 2014.

[160] C. Lane, "The Development of a 2D Ultrasonic Array Inspection for Single Crystal Turbine Blades," 2014.

[161] L. Bond and M. Punjani, "Review of some recent advances in quantitative ultrasonic NDT," *IEE Proceedings A Physical Science, Measurement and Instrumentation, Management and Education, Reviews*, vol. 131, no. 4, pp. 265–274, 1984.

[162] E. Biedermann, L. Jauriqui, J. C. Aldrin, A. Mayes, T. Williams, and S. Mazdiyasni, "Uncertainty quantification in modeling and measuring components with resonant ultrasound spectroscopy," in *42nd Annual Review of Progress in Quantitative Nondestructive Evaluation*, 2015.

[163] A. Granato, A. Hikata, and K. Lücke, "Recovery of damping and modulus changes following plastic deformation," *Acta Metallurgica*, vol. 6, no. 7, pp. 470–480, Jul 1958.

[164] A. Tarantola, *Inverse problem theory and methods for model parameter estimation*. SIAM, 2005.

[165] J. Vishnuvardhan, C. V. Krishnamurthy, and K. Balasubramaniam, "Genetic algorithm reconstruction of orthotropic composite plate elastic constants from a single non-symmetric plane ultrasonic velocity data," *Composites Part B: Engineering*, vol. 38, no. 2, pp. 216–227, 2007.

[166] Y. Zhang, L. O. Hall, D. B. Goldgof, and S. Sarkar, "A constrained genetic approach for computing material property of elastic objects," *IEEE Transactions on Evolutionary Computation*, vol. 10, no. 3, pp. 341–357, 2006.

[167] M. Landa, H. Seiner, P. Sedlák, L. Bicanova, J. Zidek, and L. Heller, "Resonant Ultrasound Spectroscopy Close to Its Applicability Limits," in *Horizons in World Physics, Volume 268*, M. Everett and L. Pedroza, Eds. Nova Science Publishers, 2009, ch. 3, pp. 97–136.

[168] R. M. Neal, "MCMC using Hamiltonian dynamics," in *Handbook of Markov Chain Monte Carlo*, S. Brooks, A. Gelman, G. Jones, and X.-L. Meng, Eds. Chapman & Hall / CRC Press, 2012, ch. 5.

[169] S. Byrne and M. Girolami, "Geodesic Monte Carlo on Embedded Manifolds," *Scandinavian Journal of Statistics*, vol. 40, no. 4, pp. 825–845, Dec 2013.

[170] J. de Leeuw, "Derivatives of generalized eigen systems with applications," *UCLA Department of Statistics Papers*, 2011.

[171] E. S. Fisher and C. J. Renken, "Single-Crystal Elastic Moduli and the hcp bcc Transformation in Ti, Zr, and Hf," *Physical Review*, vol. 135, no. 2A, pp. A482–A494, Jul 1964.

[172] A. Gelman, J. B. Carlin, H. S. Stern, D. B. Dunson, A. Vehtari, and D. B. Rubin, *Bayesian data analysis*. CRC press Boca Raton, FL, 2014, vol. 2.

[173] D. Miracle, "Overview No. 104 The physical and mechanical properties of NiAl," *Acta Metallurgica et Materialia*, vol. 41, no. 3, pp. 649–684, Mar 1993.

[174] T. M. Pollock, "Alloy design for aircraft engines," *Nature Materials*, vol. 15, no. 8, pp. 809–815, 2016.

[175] B. P. Bewlay, M. R. Jackson, P. R. Subramanian, and J. C. Zhao, "A review of very-high-temperature nb-silicide-based composites," *Metallurgical and Materials Transactions A*, vol. 34, no. 10, pp. 2043–2052, Oct 2003.

[176] J. Lemberg and R. Ritchie, "Mo-si-b alloys for ultrahigh-temperature structural applications," *Advanced Materials*, vol. 24, no. 26, pp. 3445–3480, 2012.

[177] J. Perepezko, "Surface engineering of mo-base alloys for elevated-temperature environmental resistance," *Annual Review of Materials Research*, vol. 45, no. 1, pp. 519–542, 2015.

[178] M. Holmquist, R. Lundberg, O. Sudre, A. Razzell, L. Molliex, J. Benoit, and J. Adlerborn, "Alumina/alumina composite with a porous zirconia interphase-processing, properties and component testing," *Journal of the European Ceramic Society*, vol. 20, no. 5, pp. 599–606, 2000.

[179] R. Naslain and F. Christin, "Sic-matrix composite materials for advanced jet engines," *MRS Bulletin*, vol. 28, no. 9, pp. 654–658, 2003.

[180] H. Ohnabe, S. Masaki, M. Onozuka, K. Miyahara, and T. Sasa, "Potential application of ceramic matrix composites to aero-engine components," *Composites Part A*, vol. 30, no. 4, pp. 489–496, 1999.

[181] C. Stewart, R. Rhein, A. Suzuki, T. Pollock, and C. Levi, "Oxide Scale Formation in Novel γ-γ Cobalt-Based Alloys," in *Superalloys 2016*. Hoboken, NJ, USA: John Wiley & Sons, Inc., Oct 2016, pp. 991–999.

[182] M. D. Hoffman and A. Gelman, "The no-u-turn sampler: Adaptively setting path lengths in hamiltonian monte carlo," *Journal of Machine Learning Research*, vol. 15, no. 1, pp. 1593–1623, Jan. 2014.

[183] J. Geweke, "Bayesian model comparison and validation," *American Economic Review*, vol. 97, no. 2, pp. 60–64, 2007.

[184] C. M. Grinstead and J. L. Snell, *Introduction to Probability, 2nd edition.* Providence, Rhode Island: American Mathematical Society, 2003.

[185] D. Higdon, K. Heitmann, E. Lawrence, and S. Habib, *Using the Bayesian Framework to Combine Simulations and Physical Observations for Statistical Inference.* John Wiley & Sons, Ltd, 2010, ch. 5, pp. 87–105.

[186] P. K. Kitanidis, *Bayesian and Geostatistical Approaches to Inverse Problems.* John Wiley & Sons, Ltd, 2010, ch. 4, pp. 71–85.

[187] W. K. Hastings, "Monte carlo sampling methods using markov chains and their applications," *Biometrika*, vol. 57, no. 1, pp. 9–109, 1970.

[188] S. Duane, A. D. Kennedy, B. J. Pendleton, and D. Roweth, "Hybrid monte carlo," *Physics Letters B*, vol. 195, no. 2, pp. 216–222, 1987.

[189] N. Metropolis, A. W. Rosenbluth, M. N. Rosenbluth, A. H. Teller, and E. Teller, "Equation of state calculations by fast computing machines," *The Journal of Chemical Physics*, vol. 21, no. 6, pp. 1087–1092, 1953.

[190] J. Schreuer and S. Haussühl, "Elastic and piezoelectric properties of minerals ii. structureproperty relationships," *EMU Notes in Mineralogy*, vol. 7, pp. 173–198, 2005.

[191] A. B. Parsa, P. Wollgramm, H. Buck, C. Somsen, A. Kostka, I. Povstugar, P.-P. Choi, D. Raabe, A. Dlouhy, J. Müller *et al.*, "Advanced scale bridging microstructure analysis of single crystal ni-base superalloys," *Advanced Engineering Materials*, vol. 17, no. 2, pp. 216–230, 2015.

[192] T. Ichitsubo, D. Koumoto, M. Hirao, K. Tanaka, M. Osawa, T. Yokokawa, and H. Harada, "Elastic anisotropy of rafted Ni-base superalloy at high temperatures," *Acta Materialia*, vol. 51, no. 16, pp. 4863–4869, Sep 2003.

[193] S. R. Choi, D. Zhu, and R. A. Miller, "Mechanical Properties/Database of Plasma-Sprayed ZrO2-8wt% Y2O3 Thermal Barrier Coatings," *International Journal of Applied Ceramic Technology*, vol. 1, no. 4, pp. 330–342, 2004.

[194] J. R. Gladden, "Characterization of Thin Films and Novel Materials Using Resonant Ultrasound Spectroscopy," Ph.D. dissertation, Pennsylvania State University, 2003.